SANDIA REPORT

SAND91—2296 • UC—721
Unlimited Release
Printed December 1992

Brine Inflow Sensitivity Study for Waste Isolation Pilot Plant Boreholes: Results of One-Dimensional Simulations

Stephen W. Webb

Prepared by
Sandia National Laboratories
Albuquerque, New Mexico 87185 and Livermore, California 94550
for the United States Department of Energy
under Contract DE-AC04-76DP00789

Issued by Sandia National Laboratories, operated for the United States Department of Energy by Sandia Corporation.

Available to DOE and DOE contractors from
Office of Scientific and Technical Information
PO Box 62
Oak Ridge, TN 37831

Prices available from (615) 576-8401, FTS 626-8401

Available to the public from
National Technical Information Service
US Department of Commerce
5285 Port Royal Rd
Springfield, VA 22161

NTIS price codes
Printed copy: A11
Microfiche copy: A01

SAND91-2296
Unlimited Release
Printed December 1992

Distribution
Category UC-721

Brine Inflow Sensitivity Study for Waste Isolation Pilot Plant Boreholes: Results of One-Dimensional Simulations

Stephen W. Webb
Fluid Flow and Transport Division 6119

Sandia National Laboratories
Albuquerque, New Mexico 87185

ABSTRACT

Brine inflow to the Waste Isolation Pilot Plant is important in assessing the performance of the repository, and a mechanistic model is needed for performance calculations. Brine inflow experiments are being conducted, and formation parameters such as the permeability and diffusivity are inferred from these data using a simplified one-dimensional radial, uniform property, single-phase Darcy flow model. This model has met with limited success in interpreting some of the recent data. Much of the data could not be satisfactorily fit with the above model because the brine inflow rate increases with time, so a more mechanistic model is being developed based on the TOUGH and TOUGH2 computer codes. These codes are much more complex than the simplified model and include a number of parameters that have not been measured. Therefore, a one-dimensional brine inflow sensitivity study has been undertaken to evaluate the importance of a number of these parameters in influencing the behavior of brine inflow to open boreholes. In addition, two-phase conditions have been included in the study, and the sensitivity of gas inflow rates and the formation pressure and saturation distributions after 1 year are examined. These results should be helpful in determining what additional measurements are necessary to assist in the development of a more mechanistic brine inflow model.

EXECUTIVE SUMMARY

Brine inflow sensitivity studies have been conducted using a one-dimensional model to try to identify the effect of different parameter variations including two-phase conditions on brine inflow measurements. Many of the effects were expected, such as the effect of permeability on the brine inflow rate, and the usefulness of the late-time asymptotic technique in inferring formation permeabilities and diffusivities for single-phase flow. Some of the other effects were a pleasant surprise such as the applicability of the asymptotic method in inferring formation characteristics for two-phase (dissolved gas and some free gas) conditions. Finally, some results indicate that many parameters only influence brine inflow to boreholes at very small times (<1 day).

The general conclusions from this investigation are:

- The late-time asymptotic approach for inferring formation parameters from brine inflow data is reliable (within 10%) in predicting the formation permeability for most single-phase and two-phase conditions. Problems occur for limited brine sources, high initial free gas fractions, and growing DRZs.

- The late-time asymptotic approach is less reliable in evaluating the formation diffusivity, although this parameter is not as crucial as the permeability. Typical errors are within a factor of 2. Again, problems occur for limited brine sources, high initial free gas fractions, and growing DRZs. In addition, for cases with a stationary DRZ, the error in the inferred diffusivity can be about a factor of 10. Use of the outer radius of the DRZ in evaluating the formation diffusivity improves the predictive capability to within a factor of 2.

- Gas inflow rates vary orders of magnitude with variations in the two-phase characteristic curves and free gas fractions. Note that the brine inflow rate variation for these conditions is minimal (within a factor of 2). Therefore, any inference on the free gas conditions in the formation must include knowledge of the two-phase characteristic curves. The presence of a DRZ also affects the gas inflow rate and the distribution of gas in the formation.

- The zone of influence that the borehole measures is often small. After 1 year, for a 0.019-m radius borehole, this distance could be as small as 0.5 m from the center of the borehole for a highly compressible formation or about 1.0 m if there is a significant amount of free gas present.

- The only situation that resulted in the commonly observed increasing brine inflow rate with time is a growing DRZ. Unfortunately, this also is a case where the late-time asymptotic approach did not work and formation parameters cannot be inferred.

- Additional two-dimensional simulations are planned to address other effects such as excavation-borehole interactions and the influence of stratigraphy.

CONTENTS

Figures

Single-Phase Inferred Parameters

Two-Phase Brine Inflow

Two-Phase Inferred Parameters

Tables

INTRODUCTION

Background

Brine inflow to the Waste Isolation Pilot Plant (WIPP) is important in assessing the performance of the repository. The brine may be a significant contributor to the gas generation process, and brine is the principal radionuclide transport mechanism out of the repository (Lappin et al., 1989).

Brine inflow experiments are being conducted (Finley et al., 1992) in which the brine inflow rate to open boreholes is measured. From these data, quantification of the formation parameters such as the permeability and diffusivity (or capacitance) is performed. These parameters are then used in performance assessment calculations to determine the acceptability of the repository performance.

Currently, a simplified one-dimensional, uniform property, single-phase Darcy flow model (Nowak and McTigue, 1987; Nowak et al., 1988) is used in the data reduction procedure to infer the formation parameters. While some scoping calculations have been performed with nonuniform properties, only uniform properties have been used in the data reduction process. The brine flux to an open borehole as prescribed by this simplified model is

$$|q|(R,t) = \frac{k\,P_o}{\mu\,R}\,\frac{4}{\pi^2}\int_0^\infty \frac{\exp\left(-cu^2t/R^2\right)}{J_o^2(u) + Y_o^2(u)}\,\frac{du}{u} \qquad (1)$$

where

- q = brine flux
- R = borehole radius
- t = time
- k = permeability
- P_o = initial brine pressure
- μ = brine viscosity
- c = diffusivity
- u = dummy variable

and J_o and Y_o are Bessel functions.

The asymptotic late-time behavior of this expression (see Appendix A) is

$$\lim_{t_* \to \infty} |q|^{-1}(R,t) = A \ln\left(\frac{4\,c\,t}{R^2\,\Gamma}\right) = A \ln t + B \qquad (2)$$

where

$$A = \frac{\mu R}{2 k P_o} \tag{3}$$

$$B = A \ln \left(\frac{4c}{R^2 \Gamma} \right) \tag{4}$$

with

$$t_* = \frac{c t}{R^2} \tag{5}$$

where $\Gamma = \exp(\gamma)$ and γ is Euler's constant. This expression gives a linear line on a plot of $|q|^{-1}$ vs. ln t. The late-time asymptotic fit seems to be a good representation of the transient behavior, especially at $t_* > 100$ (Appendix A). The inferred values of permeability and diffusivity are

$$k = \frac{\mu R}{2 P_o A} \tag{6}$$

$$c = \frac{R^2 \Gamma}{4} \exp \left(\frac{B}{A} \right). \tag{7}$$

This approach predicts the formation permeability within a few percent, while the inferred formation diffusivity will be overpredicted by about 50%.

This simplified model has met with limited success in interpreting some of the recent data (Finley et al., 1992). Much of the data could not be satisfactorily fit with the above model because the brine inflow rate increases with time. Therefore, the investigation of other phenomena as part of the development of a more mechanistic model for brine inflow is warranted.

The TOUGH (Pruess, 1987) and TOUGH2 (Pruess, 1991) computer codes are the current mechanistic brine inflow models for the WIPP. These codes are more general than the simplified approach, requiring the use of a number of parameters that have not been measured at WIPP. Therefore, to try to understand the potential impact of these parameters, a brine inflow sensitivity study has been undertaken to evaluate their importance in influencing the behavior of brine inflow to open boreholes. Because gas is probably present in the formation along with the brine (Lappin et al., 1989), two-phase conditions have been included in the study, and the sensitivity of gas inflow rates and the formation pressure and saturation distributions after 1 year are examined. For simplicity, the borehole was modeled with a one-dimensional radial model; two-dimensional studies are planned to address other effects such as excavation-borehole interactions and the influence of

stratigraphy. These studies should be helpful in determining what additional measurements are necessary to assist in the development of a more mechanistic brine inflow model.

General Methodology

The brine inflow sensitivity study has been conducted with the TOUGH computer code in which the water properties were modified to approximate brine. The modified properties are:

- Brine Density: As a first approximation, the density of brine is assumed to be 1.2 times the density of water. This assumption implies that brine and water compressibilities are equal, which is not correct. This difference is discussed below.

- Brine Compressibility: Brine compressibility is significantly lower than that of water. Brine compressibility is about 3×10^{-10} Pa^{-1} (Beauheim et al., 1991), while the compressibility of water is approximately 4.5×10^{-10} Pa^{-1} at 27°C and 5 MPa (Weast, 1984) for a difference of 1.5×10^{-10} Pa^{-1}. This value is used to modify the input formation compressibility as discussed later. (After this study was initiated, the compressibility of WIPP brine was measured by McTigue et al. (1991) as $2.40\text{-}2.54 \times 10^{-10}$ Pa^{-1}.)

- Brine Vapor Pressure: The vapor pressure of the brine is assumed equal to 75% of that for pure water (see Appendix B).

- Brine Viscosity: A constant brine viscosity of 1.6×10^{-3} Pa·s is used (Nowak et al., 1988).

- Dissolved Gas: TOUGH uses a value of Henry's constant for air in water of 10^{10} Pa. The solubility of various gases in water and brine has been studied by Cygan (1991). Gas solubility for nitrogen in 5N brine is about a factor of 4 lower than for water at 30°C. Oxygen was not included in the study. Based on this ratio, Henry's constant for air in brine is approximately 4 times that for water, or 4×10^{10} Pa. (Henry's constant is inversely proportional to the gas solubility.) 5N brine is similar to standard Salado brines (Lappin et al., 1989).

The sensitivity study performed with this modified version of TOUGH considers a single-phase and a two-phase base case. Each parameter is varied separately keeping the other base case values constant. Therefore, the coupling between the various factors is not included in the present study. For simplicity, a one-dimensional radial model of nominal 1 m depth has been used.

The base case parameters chosen for this study are:

Borehole Radius	0.019 m
Borehole Depth	1.0 m
Permeability	10^{-21} m^2
Porosity	0.01
Pore Pressure	11 MPa
Effective Radius	Infinite
Compressibility	Fluid Only Incompressible Formation
Dissolved Gas	Air
Dissolved Gas Fraction	0 and 100%
Free Gas	None
Capillary Pressure	Brooks and Corey
Relative Permeability	Brooks and Corey
DRZ	None

Variations of all the parameters listed above have been performed; the values are listed in Appendix C. The total number of simulations involved is 82 (30 single-phase and 52 two-phase). Performance measures are the brine inflow rate (no dissolved gas and dissolved/free gas conditions), gas inflow rate, gas saturation of the inflowing fluid at the borehole conditions, and the fluid pressures and gas saturation profiles in the formation at the end of the simulation, nominally 1 year. The inflow results are per meter depth of the borehole. The borehole pressure is constant at 0.1 MPa, or atmospheric pressure. The inflow rates are based on changes in the masses in the borehole, not on the calculated flow rates; therefore, phase changes that occur in the borehole are properly accounted for.

In addition to the quantitative inflow rates and formation profiles, the late-time asymptotic approach discussed earlier has been evaluated for each case. The inferred values of the formation permeability and diffusivity are compared with the simulation values to determine their usefulness. These predictions are made on a best possible basis because there is no experimental uncertainty or error. Thus, the errors in the inferred parameters are the minimum that could be expected under optimal conditions.

Base Case Results

Before presenting the various parameter variations, it is instructive to discuss the base case results; the parameters are listed above. Nodalization effects are discussed in Appendix D. Figure 1-A shows the brine inflow rate results. The single phase (no dissolved gas or free gas) brine inflow rate into the borehole in Figure 1-A1 drops rapidly during the first 1000 seconds or so. Figure 1-A2 shows the brine inflow rate for the case of brine saturated with dissolved gas (no free gas); the results are very similar to those in Figure 1-A1 in both shape and magnitude. The ratio of the two-phase

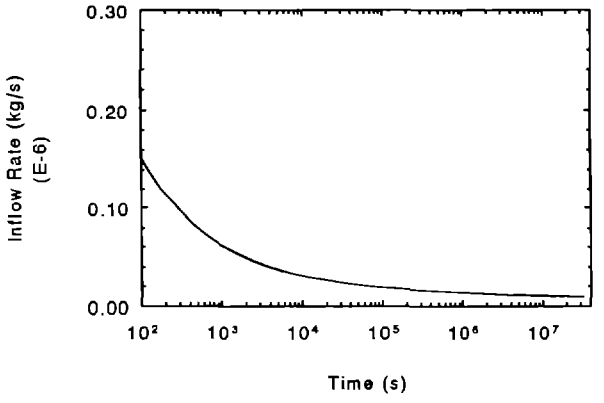

1-A1. Single-phase brine inflow.

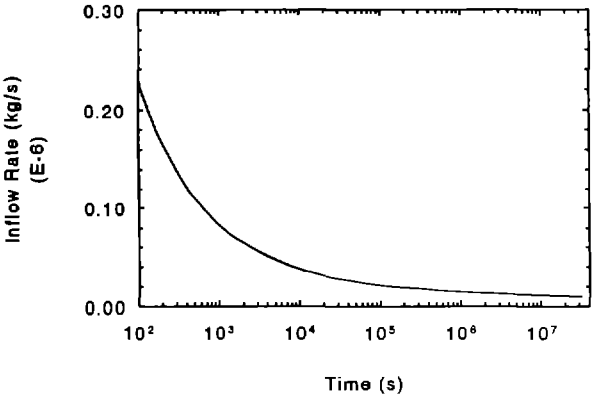

1-A2. Two-phase brine inflow.

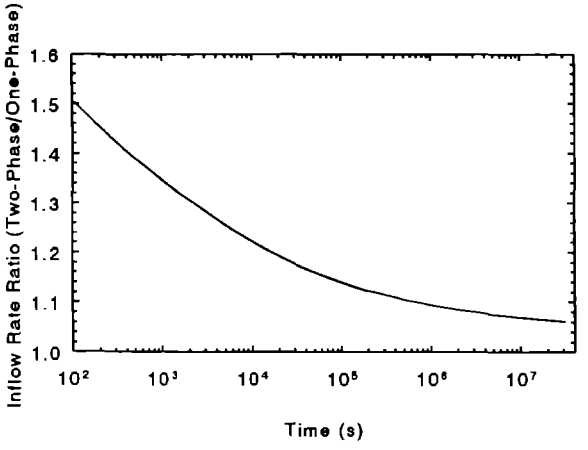

1-A3. Two-phase/one-phase brine inflow ratio.

Figure 1-A. Brine inflow rate base case results.

to single-phase brine inflow rates is given in Figure 1-A3; the maximum increase over single-phase conditions is about 50% on the time scale shown.

As discussed earlier, the late-time asymptotic behavior of the brine inflow rate can be used to infer formation parameters. A straight line is fit to a plot of the inverse of the brine inflow rate versus log time, and the slope is a measure of the formation permeability, while the intercept gives the formation diffusivity. For the base case, the value of t_* of 100 is reached at about 2×10^5 seconds (2 days); after this time, the late-time asymptotic approach is applicable. The results of this analysis for the base case are shown in Figures 1-B1 and 1-B2. A straight line is a good fit to the data after about 10^4 seconds; the R^2 value (correlation coefficient) for these lines is 0.999 or higher. The inferred parameters along with the simulation values are summarized in Table 1. The permeability is well predicted, and the inferred diffusivity is off by up to 50% due to the extrapolation back to 1 second (Appendix A). As discussed in Appendix E, the brine inflow rate is much more sensitive to the permeability than to the diffusivity. Therefore, these inferred values are reasonable measures of the formation parameters.

Table 1. Inferred Base Case Parameters

Permeability (m^2)		
Actual	Inferred	Error
1.0×10^{-21}		
single-phase	1.04×10^{-21}	+4%
two-phase	1.03×10^{-21}	+3%
Diffusivity (m^2/sec)		
Actual	Inferred	Error
2.1×10^{-7}		
single-phase	3.2×10^{-7}	+50%
two-phase	1.6×10^{-7}	-20%

Figure 1-C1 shows the gas inflow rate for the two-phase base case; the behavior is similar to the brine inflow rate with a much lower magnitude. The gas saturation of the inflowing brine at the borehole conditions of 0.1 MPa is given in Figure 1-C2. Even though the gas inflow rate is orders of magnitude less than the brine inflow rate, the gas saturation, or gas volume

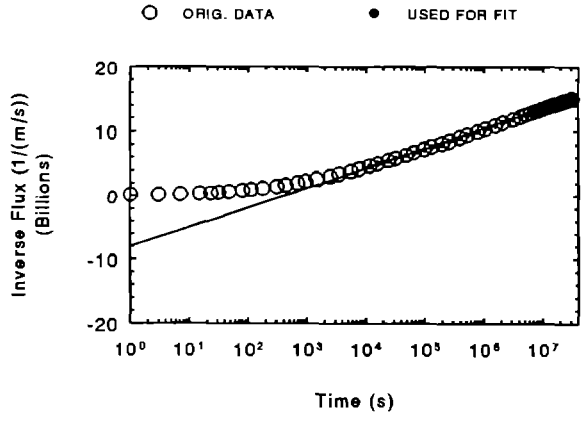

1-B1. Single-phase inverse brine flux.

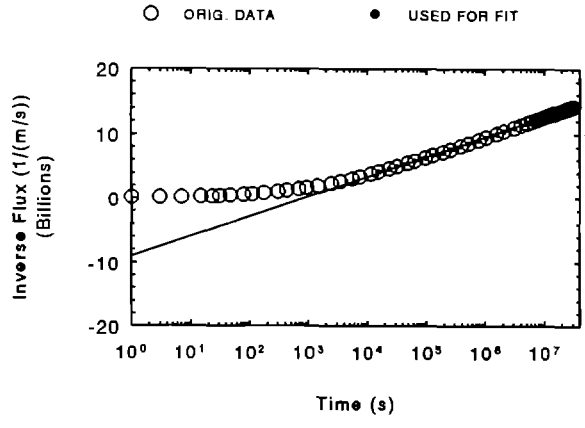

1-B2. Two-phase inverse brine flux.

Figure 1-B. Inverse brine flux base case results.

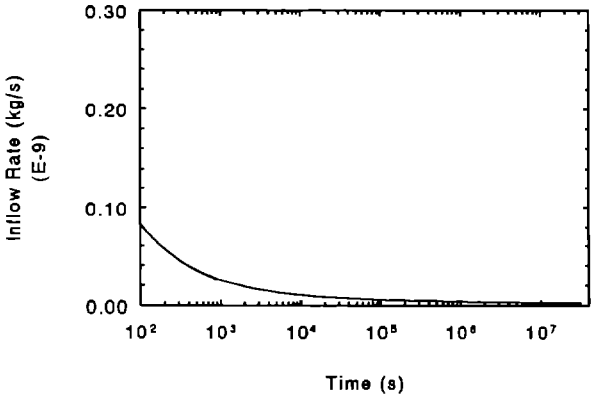

1-C1. Two-phase gas inflow.

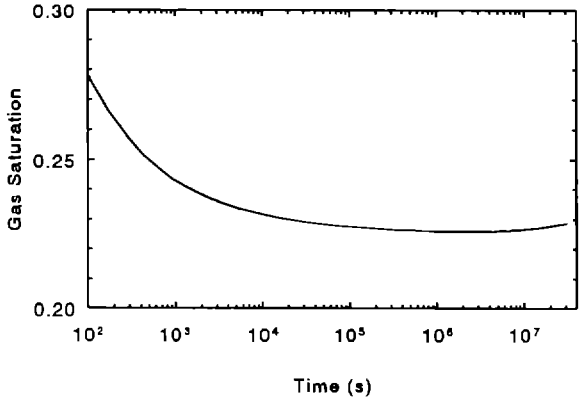

1-C2. Gas saturation of inflowing brine.

Figure 1-C. Gas inflow rate and gas saturation of inflowing brine, base case results.

fraction, at borehole conditions varies from about 0.28 to 0.23 due to the large density difference at the borehole pressure.

Figures 1-D1 and 1-D2 show the brine pressure in the formation at the end of the simulation at 1 year; the pressure is normalized to the far-field brine pressure (P_∞) of 11 MPa. The brine pressure has been affected (<95% of far-field value) out to about 4 meters during this time period; minor differences are noted between the single-phase and two-phase results. Similarly, the gas pressure shown in Figure 1-D3 for the two-phase case is only affected out to about 4 m as well. Note that the gas pressure is higher than the brine pressure due to capillary pressure. Figure 1-D4 gives the gas saturation in the formation. The gas saturation is small in all cases (<~2%), and significant values are essentially confined to within 0.1 m of the borehole.

Due to the large number of cases (82) and the various performance measures, the results are presented in six different sections. The first section contains the single-phase brine inflow rate results; the second section presents the inferred formation parameters from fits to these synthetic (artificial) data. The third and fourth sections give the same results for the two-phase simulations. The fifth section presents gas inflow information. Finally, the sixth section gives the formation pressure and gas saturation distributions at the end of the simulations.

Sensitivity Study Variations

The order of the sensitivity results given in each section is:

- Borehole Parameters
  - Borehole Radius
- Formation Parameters
  - Permeability
  - Pore Pressure
  - Compressibility
  - Porosity (initial value)
- Nonuniform Effects
  - Effective Radius of Brine Source
  - Disturbed Rock Zone Characteristics
- Two-Phase Parameters
  - Solubility
  - Dissolved Gas Fraction
  - Free Gas Fraction
  - Capillary Pressure and Relative Permeability

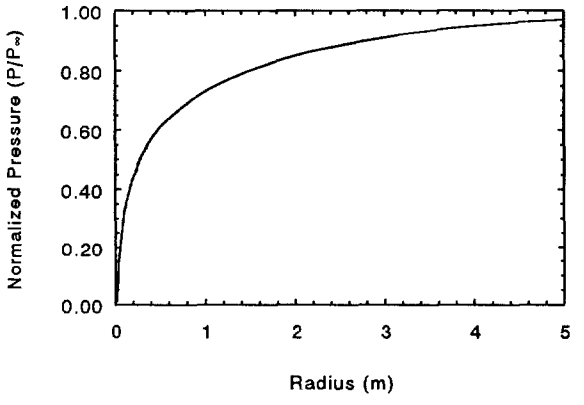

1-D1. Single-phase brine pressure profile.

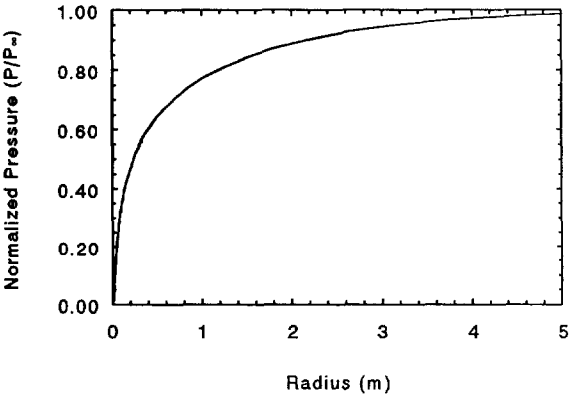

1-D2. Two-phase brine pressure profile.

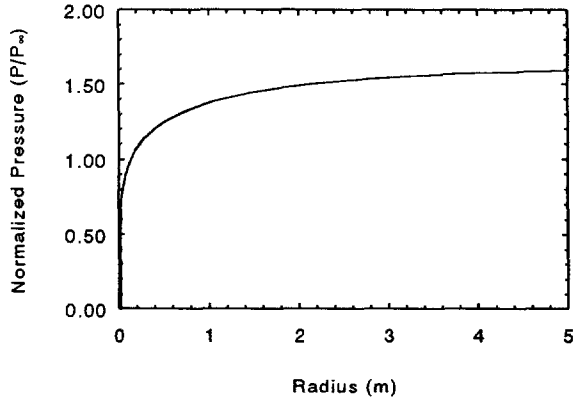

1-D3. Two-phase gas pressure profile.

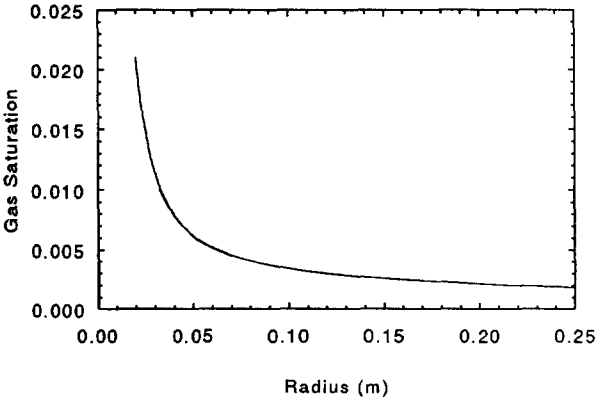

1-D4. Two-phase gas saturation profile.

Figure 1-D. Normalized pressure and gas saturation profiles, base case results at 1 year.

Appendix C lists the numerical values for the various parameters as well as some rationale for their selection. The variations are discussed in detail below.

Borehole Parameters

Variations in the borehole radius are chosen to cover the actual values for boreholes as well as equivalent radii for the repository. The values include 0.019 m (1.5-inch diameter), 0.051 m (4.0-inch diameter), and 0.47 m (36-inch diameter), which are the actual diameters of boreholes in the WIPP. In addition, radii of 1.5 and 4.5 m are included as simplified representations of Room Q and a one-dimensional model of the repository (Nowak et al., 1988). From Equation 1, the brine inflow rate per unit length of borehole is

$$\dot{m} / L = \rho\, q\, A / L = 2\,\pi\, R\, \rho\, q$$

$$= \frac{\rho\, k\, P_o}{\mu}\,\frac{8}{\pi}\int_0^{\infty}\frac{\exp\,(-cu^2 t/R^2)}{J_o^2(u) + Y_o^2(u)}\,\frac{du}{u} \qquad (8)$$

where

$\dot{m}$ = mass inflow rate
L = borehole length
ρ = brine density
A = borehole surface area.

This equation scales directly with $t_* = ct/R^2$. Therefore, for a constant diffusivity, c, the brine inflow rate per unit length of borehole is the same for equal values of t/R^2. The difference in equivalent radius from the actual small boreholes (0.019 and 0.051 m) to the room size values (1.5 and 4.5 m) is exacerbated by the square of the radius ratio. The dramatic difference in the times for the various radii is shown in Table 2. As an example, a time of 1 hour for a radius of 0.019 m is approximately 2.0×10^8 seconds, or 6.4 years, for a 4.5 m radius situation. Similarly, 1000 years on the repository scale is 0.018 years (7 days) and 0.13 years (1 1/2 months) for borehole radii of 0.019 and 0.051 m, respectively. Assuming applicability of the above Darcy flow model, borehole inflow data in the first few days and weeks is necessary for scaling up to the repository behavior during the critical first few hundred years after sealing.

Table 2. Borehole Times*

t/R^2 (s/m^2) =	10^3	10^4	10^5	10^6	10^7	10^8	10^9	10^{10}	10^{11}
R = .019 m	.36s	3.6s	0.6m	6.m	1.h	10.h	4.2d	.11y	1.1y
R = .051 m	2.6s	.43m	4.3m	.72h	0.3d	3.d	30.d	.82y	8.2y
R = 18 in (.46 m)	3.5m	.58h	.24d	2.4d	24.d	.66y	6.6y	66y	660y
R = 1.5 m (Room Q)	.62h	.26d	2.6d	26d	.71y	7.1y	71y	710y	7100y
R = 4.5 m (Repository)	.23d	2.3d	23.d	.64y	6.4y	64y	640y	6400y	64000y

* s = seconds
m = minutes
h = hours
d = days
y = years

Formation Parameters

The variations in the formation parameters are permeability, pore pressure, formation compressibility, and porosity. From equation (8), the brine inflow rate seems to scale directly with the permeability. However, the permeability is also a parameter in the diffusivity, c, or, for an isotropic medium with constant properties (de Marsily, 1986)

$$c = \frac{T}{S} = \frac{K\,L}{S} = \frac{k\,\rho\,g}{\mu}\,\frac{L}{L\,\rho\,\phi\,g\left(\beta_l - \beta_s + \frac{\alpha}{\phi}\right)} \qquad (9)$$

where

T = transmissivity
S = storativity
K = hydraulic conductivity
ϕ = porosity
β_l = liquid compressibility
β_s = solid compressibility
α = porous medium compressibility.

From de Marsily (1986), α_p, the pore compressibility is

$$\alpha_p = \frac{\alpha}{\phi} - \beta_s = \frac{1}{V_p}\frac{dV_p}{dp} \tag{10}$$

where V_p is the pore volume. Using this equation results in

$$c = \frac{T}{S} = \frac{k}{\mu}\frac{1}{\phi\left(\beta_1 + \alpha_p\right)} \tag{11}$$

Thus, the permeability influences the diffusivity; so, from Equation 8, the brine inflow rate does not scale linearly with permeability.

The brine inflow rate scales directly with the pore pressure except for a minor influence of the brine density, ρ, on the pressure and its effect on the diffusivity. However, this effect will be negligible due to the small compressibility of brine.

From equation (11), the pore compressibility, α_p, affects the diffusivity. This pore compressibility can be related to the formation compressibility in Beauheim et al. (1991). The definitions of the specific storage, S_s, are

present:

$$S_s = \frac{S}{L} = \rho\ \phi\ g\left(\beta_1 + \alpha_p\right) \tag{12a}$$

Beauheim et al. (1991):

$$S_s = \rho\ g\left(C_f + \phi\ \beta_1\right) \tag{12b}$$

where C_f is the formation compressibility. Therefore, for equivalence between the two definitions,

$$\alpha_p = \frac{C_f}{\phi}, \tag{13}$$

so equation (11) can be written as

$$c = \frac{T}{S} = \frac{k}{\mu}\frac{1}{C_f + \phi\ \beta_1} \quad . \tag{14}$$

The brine inflow variation in Equation 8 scales with the value of $t_* = ct/R^2$. The effect of the formation compressibility is non-linear due to the dependence of the diffusivity on the inverse of the sum of the compressibilities.

Finally, the porosity influences the diffusivity, which will alter the timing of the brine inflow rate. The brine inflow rate scales directly with the parameter $t/\phi R^2$ for constant values of α_p.

The expression for α_p given by Equation 10 is equivalent to the COM compressibility input parameter employed in TOUGH. The liquid compressibility, β_l, is already incorporated into TOUGH because the fluid density is a function of pressure. From Equation 11, only the sum of the two parameters is important. Therefore, to reflect the difference between brine and water compressibility mentioned earlier, the calculated pore compressibility is reduced by 1.5×10^{-10} Pa^{-1} for input to TOUGH.

Nonuniform Effects

Two different nonuniform effects have been considered. The first case is a limited brine source, or a no-flow boundary at a specified radius. This type of behavior has been inferred from data analysis performed by Beauheim et al. (1991) for some boreholes. This case can also represent brine inflow if there is no far-field brine source. The values were chosen to have an impact on the results.

The second case is that of a DRZ that considers an infinite porous medium with altered properties in the vicinity of the borehole. The DRZ specifications for all the variations are summarized in Table 3. The typical description calls for a uniform increase of the permeability in the DRZ by a factor of 100 and an increase in the DRZ porosity by a factor of 5. The permeability increase is partially based on experimental data in Stormont (1990), while the increase in porosity by a factor of 5 (from 0.01 to 0.05) is suggested by the Koseny-Carmen formula (de Marsily, 1986)

$$k \sim \phi^3 / (1 - \phi)^2 \qquad (15)$$

for a permeability increase of a factor of 100.

A number of variations from this typical description has been studied due to the large uncertainty in the values. The extent of the DRZ has been varied from no DRZ to DRZs of 0.5R, 1.0R, and 2.0R. Other parameters in the DRZ specification have also been varied. The typical model implicitly

Table 3. DRZ Characteristics

Case	ID*	DRZ Zone	Permeability Variation	Misc. Parameters
1	No DRZ	None	-	-
2	0.5R DRZ	0.5 R	factor of 100 step function	DRZ porosity = 0.05
3	1.0R DRZ	1.0 R	factor of 100 step function	DRZ porosity = 0.05
4	2.0R DRZ	2.0 R	factor of 100 step function	DRZ porosity = 0.05
5	Patm	2.0 R	factor of 100 step function	DRZ porosity = 0.05 $P_{initial\text{-}DRZ} = P_{atm}$
6	Constant ϕ	2.0 R	factor of 100 step function	DRZ porosity = 0.01
7	Inc. Δk	2.0 R	factor of 1000 step function	DRZ porosity = 0.05
8	Dec. Δk	2.0 R	factor of 10 step function	DRZ porosity = 0.05
9	McTigue (1989)	2.0 R	factor of 1000 exponential variation z = 2R	DRZ porosity = 0.01
10	Growing DRZ 1R/yr	variable 1R/yr	factor of 100 exponential variation z = 1R	DRZ porosity = 0.01
11	Growing DRZ 2R/yr	variable 2R/yr	factor of 100 exponential variation z = 1R	DRZ porosity = 0.01

*ID as labeled on figures and tables.

assumes no depressurization in the DRZ at the start of the transient. This condition has been varied to specify atmospheric pressure in the DRZ initially. In addition, a variation that did not increase the DRZ porosity over the far-field value is included. Variations in the permeability contrast have also been studied. Cases with an increased contrast (increased DRZ permeability) and a decreased contrast (decreased DRZ permeability) have been specified.

The permeability variation within the DRZ has also been studied. McTigue (1989) specified a DRZ with a total permeability contrast of 1000. The permeability is not uniform in the DRZ and varies according to the relationship

$$k = k_a \exp (D (z - r) / z) \qquad (16)$$

where

D = natural log of the permeability ratio (1000 in this case)
z = characteristic distance for the permeability variation
r = distance into the formation
k_a = undisturbed formation permeability.

The characteristic distance for McTigue's model is two times the borehole radius, or 0.038 m.

Finally, a growing DRZ is considered; growth rates of 1R/yr and 2R/yr have been studied. The permeability contrast within the DRZ is given by the exponential variation (Equation 16) where the characteristic distance is the borehole radius, or 0.019 m. The maximum permeability increase is a factor of 100.

Two-Phase Parameters

If gas exists in the brine, either in the form of dissolved gas or free gas, the amount of gas, the species, and the two-phase characteristic curves are largely unknown. To assess the effects of these parameters, cases with varying gas solubility, dissolved gas fraction, free gas fraction, and two-phase characteristic curves have been investigated.

As discussed earlier, the solubility used in this study is meant to simulate air in brine. Due to the uncertainty in the species and in the solubility, more dissolved gas could be present than assumed. To assess this condition, the gas solubility has been increased up to a factor of 4.

Similar to the solubility, the dissolved gas fraction is unknown. The base case assumes that the brine is saturated with dissolved gas, but the brine may be only partially saturated. Therefore, variations in the dissolved gas fraction are considered.

If brine is saturated with dissolved gas, free gas may exist as well. Free gas fractions up to 50 v/o have been analyzed. For the lower free gas fractions considered (10 v/o and 20 v/o), the gas phase is immobile as determined by the two-phase characteristic curves. Uniform gas distribution and the possibility of gas pockets have been considered for the 10 v/o scenario. The non-uniform distributions of 10 v/o free gas assumed alternating free gas fractions of 0 v/o and 20 v/o of equal volume. To investigate any ordering effect, the cases of G/L (gas/liquid) and L/G (liquid/gas) were studied where the first letter refers to the state of the volume next to the borehole (G - 20 v/o gas; L - 0 v/o gas), and the second letter is the state of the next volume radially outward. The spatial variation is indicated in Figure 2.

Another free gas condition has been analyzed as part of the pore pressure variation. The first pore pressure case assumes brine saturated with dissolved gas at the specified pressure. The second case assumes that the brine is initially saturated with dissolved gas at 15 MPa and is subsequently depressurized, possibly by the existence of the excavation, to the assumed pressure. The amount of free gas due to the depressurization based on the base case capillary pressure curve is:

Pore Pressure	Free Gas
15 MPa	0.
11 MPa	0.00095
6 MPa	0.003
1 MPa	0.0075

These two variations are referred to as dissolved gas and free gas for the pore pressure case.

The two-phase characteristic curves (capillary pressure and relative permeability) have not been measured and are only based on analogue materials. The base case curves are those of Brooks and Corey as summarized in Appendix F. The residual saturation values assumed are 0.2 for the gas and the liquid phase, and the threshold pressure for a permeability of 10^{-21} m^2 is 10 MPa based on the correlation of Davies (1991)

$$P_t = 5.6 \times 10^{-7} \, k^{-0.346} \qquad (17)$$

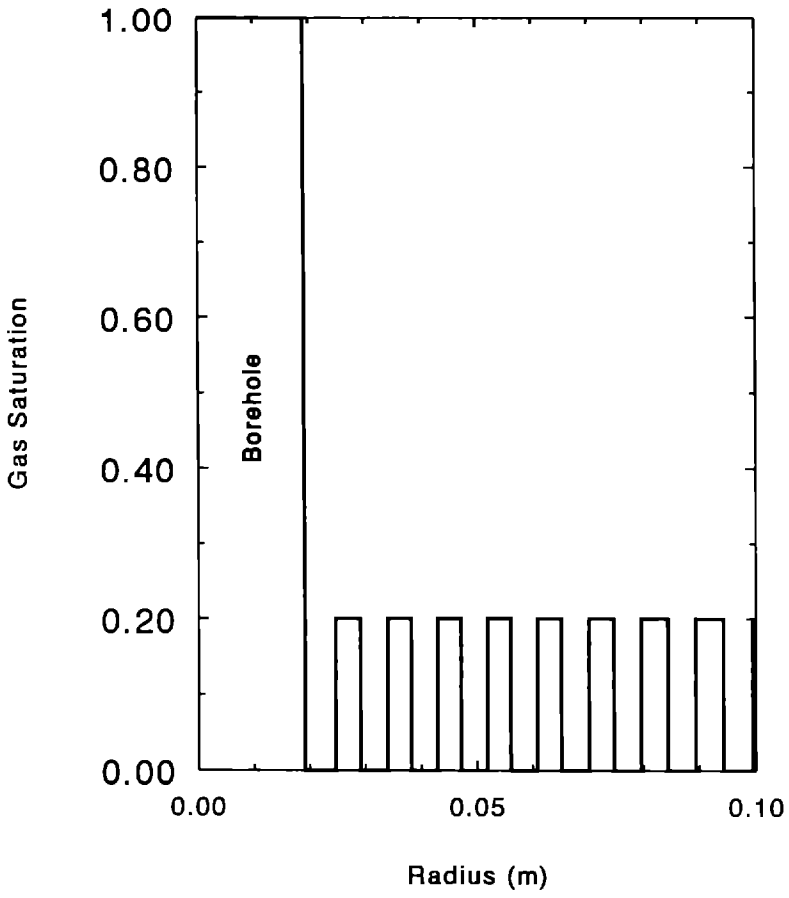

Figure 2. Non-uniform gas distribution.

where P_t and k are the threshold pressure and permeability in MPa and m^2, respectively. The threshold pressure relationship above is used for all the different permeabilities including the variation in DRZs. Thus, for an exponential distribution of permeability, the local threshold pressure varies according to the Davies (1991) correlation. All of the above parameters are highly uncertain, so each has been varied in this investigation.

The value of the threshold pressure determines the magnitude of the capillary pressure curve. The confidence interval for the value given by the correlation is about an order of magnitude. To address this uncertainty, the threshold pressure has been increased and decreased by an order of magnitude. In addition, the limit of zero threshold pressure has been included.

The shape of the capillary pressure curve has also been studied. As proposed by Webb and Chen (1990), the shape of the curve for dissolved gas exsolution may be considerably different than the standard shape as depicted in Figure 3-A. The dissolved gas exsolution shape as well as a uniform capillary pressure curve has been considered.

Variations that affect both the capillary pressure and relative permeability curves include the residual saturations. The default specifications are a value of 0.2 for the liquid and gas residual saturations. Cases where the liquid and gas residual saturations are both 0.0 and both 0.4 have been analyzed.

Finally, the two-phase characteristic curves themselves are highly uncertain. As an arbitrary variation, the curves used by Yucca Mountain called the Sandia functions (Pruess, 1987) have been specified; the two sets of curves are compared in Figures 3-B and 3-C. Although the capillary pressure curves are very similar, the gas relative permeability curves are dramatically different. The relationships for the Sandia functions and the values are summarized in Appendix F. This case has been included to show the possible effect of a different set of curves.

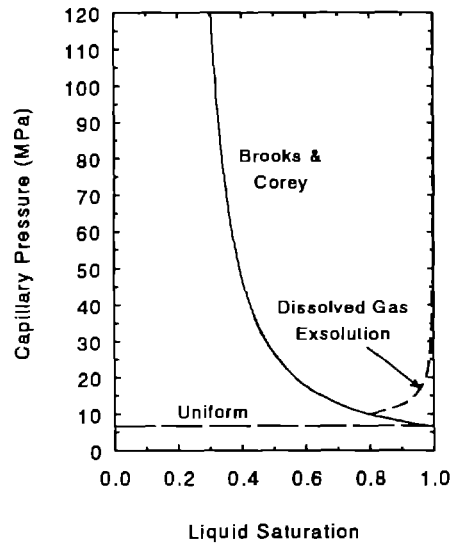

3-A. Capillary pressure curve shape variation.

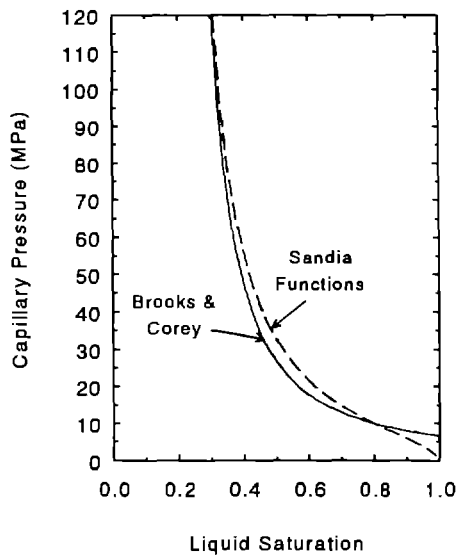

3-B. Capillary pressure curves.

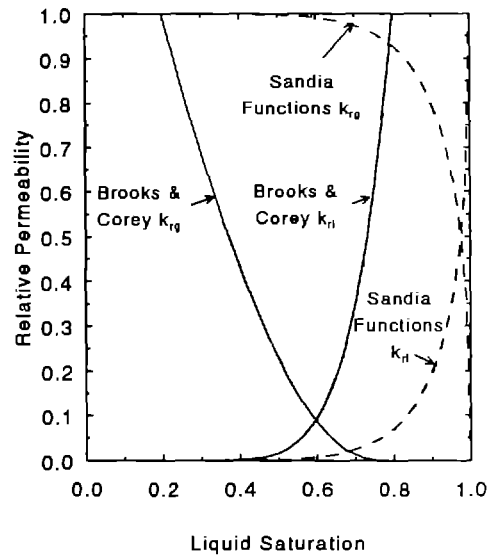

3-C. Relative permeability curves.

Figure 3. Capillary pressure and permeability curves.

RESULTS

Single-Phase Brine Inflow

Figure 4-A1 shows the single-phase brine inflow rate as a function of time and borehole radius. The curves for the various radii have the same mass inflow rate variation simply offset in time. As discussed earlier, by plotting the mass inflow rate as a function of normalized time, t/R^2 ($=t_*/c$), the results for all the radii collapse to a single curve as shown in Figure 4-A2.

Figures 4-B1 to 4-B3 give the brine inflow rate as a function of time and permeability. The inflow rates have greatly different scales depending on the permeability. In addition to differences in the magnitude, the transient behavior is different because the diffusivity is affected. Figure 4-B4 presents the ratio of the brine inflow rate divided by the permeability to that for the base case of permeability 10^{-21} m^2. Due to the change in the diffusivity, the ratio is different than 1.0 even up to 1 year. Thus, changing the permeability alters the magnitude and the shape of the brine inflow rate curve.

The single-phase brine inflow rate as a function of time and pore pressure is presented in Figure 4-C1. The inflow rate variation with time is similar for all the pore pressures. This scaling is shown in Figure 4-C2 where the mass flow rate divided by the pressure difference (pore pressure minus borehole pressure) has been plotted as a function of time; all the curves fall on top of each other.

Figure 4-D1 shows the brine inflow rate as a function of time and formation compressibility. The inflow rate for the three smallest compressibilities (C_f = 0., 10^{-13}, and 10^{-12} Pa^{-1}) are essentially identical. Differences start to be seen as the formation compressibility increases to 10^{-11} Pa^{-1} and higher. While the shape and magnitude of the curves change with the formation compressibility, the result is not dramatic considering the wide variation. Figure 4-D2 shows the normalized effect of the formation compressibility on the brine inflow rate compared to an incompressible formation case. The magnitude of the flow rate can increase by over an order of magnitude at early times. The difference is still significant out to 1 year (factor of about 2 for the highest formation compressibility) and probably much longer.

Figure 4-E1 gives the brine inflow rate as a function of time and porosity. The higher porosity cases show a much higher initial peak for the time period presented. The ratio of the brine inflow rate to that for the base case (ϕ = 0.01) is depicted in Figure 4-E2. The variation in the brine

inflow rate for different porosities persists for the duration of the simulation of 1 year. The mass inflow rate as a function of normalized time (t/ϕ) is presented in Figure 4-E3; the results all fall essentially on one line. The minor differences are due to nodalization effects.

Figure 4-F1 depicts the single-phase brine inflow rate as a function of time and source radius. The inflow rate at late time is a strong function of source radius if the radius is less than about 5.0 m. The limited radius cases continue to decay, whereas the infinite radius result tends to level off. The inflow ratio compared to the base case of an infinite source radius is shown in Figure 4-F2. The ratio keeps dropping for a limited radius; no definitive signal is noted. However, as discussed later, this limited source radius effect can be seen in the late-time fit for inferred parameters.

Figures 4-G to 4-J show the brine inflow rate as a function of time for the various DRZ groups, including the ratio to the base case of no DRZ. Figure 4-G1 presents the brine inflow rate versus time; the initial magnitude is increased significantly if a DRZ is present. From Figure 4-G2, the early-time (100 seconds) brine inflow rate is 30 times that without a DRZ. Late-time brine inflow rate at 1 year is about 25% higher for a 2.0R DRZ than with no DRZ as given in Figure 4-G3.

The early-time brine inflow behavior is significantly different depending on the DRZ porosity and initial pressure condition as given in Figure 4-H1. For the standard DRZ model, the early-time brine inflow rate is much higher than for the constant porosity, initial atmospheric pressure, or no DRZ cases. From Figure 4-H2, the ratio of the brine inflow rate to the case of no DRZ is up to 30 with the standard DRZ, which is reduced to less than 10 for the constant porosity variation. Figure 4-H3 details the early-time behavior as the atmospheric pressure case has a low initial flow rate. The porosity and pressure cases converge to the standard DRZ (2.0R DRZ) case at about 10^4 seconds (3 hours).

Figure 4-I gives the results of changing the permeability contrast from the intact formation to the DRZ. From Figure 4-I1, the inflow rates cross as the magnitude and timing of the inflow rate is affected by the change in permeability contrast. However, after about 3×10^4 seconds, the brine inflow rates for these three cases converge showing little effect of the permeability contrast. Figures 4-I2 and 4-I3 present the ratios to the case for no DRZ detailing the early-time and late-time behavior.

Finally, Figure 4-J gives the single-phase results for the McTigue approach and for a growing DRZ. As expected from the results shown in Figure 4-I, the McTigue permeability variation, which has an exponential variation

in the permeability compared to the step change variation in the base case, has a significant early-time effect on the brine inflow rate in Figure 4-J1 but a small influence later on; the ratios are summarized in Figures 4-J2 and 4-J3. For the growing DRZ cases, the early-time results are equivalent to a case with no DRZ since the DRZ extent is small. Later on, however, at 1 year, the flow rate for the growing DRZ with a 2R/yr rate approaches that for a constant 2.0R DRZ as shown in Figure 4-J3. The results for both growing DRZ cases give slightly increasing brine inflow rates after about 6 months. However, the magnitude of the increase of the inflow rate over the minimum value is small (<1% for 1R/yr and 4% for 2R/yr).

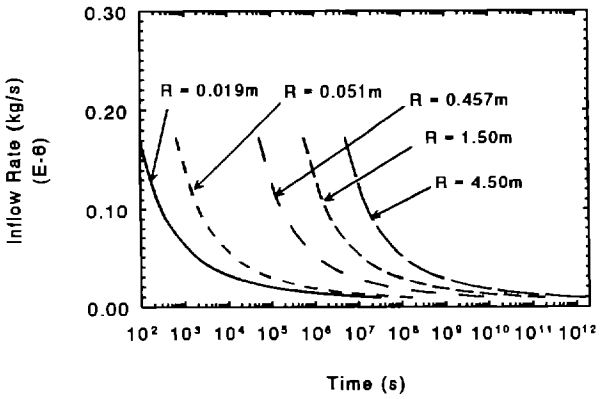

4-A1

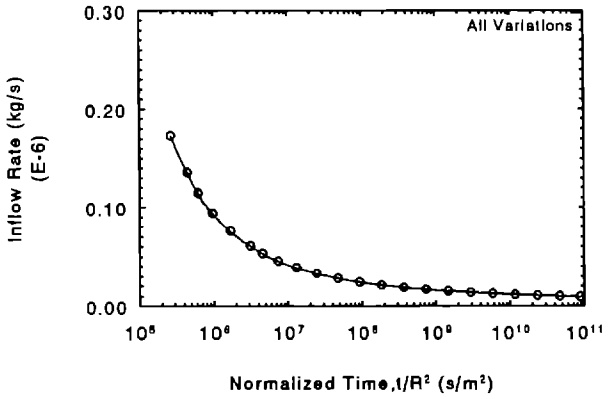

4-A2

Figure 4-A. Results from variation in borehole radius for single-phase brine inflow.

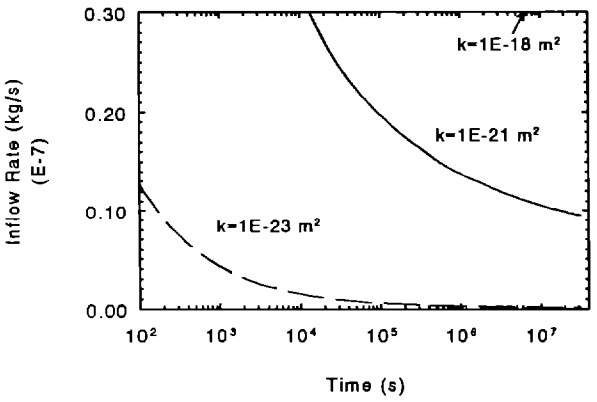

4B-1

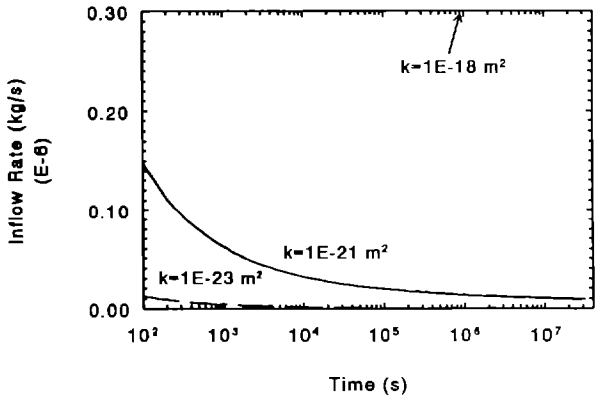

4-B2

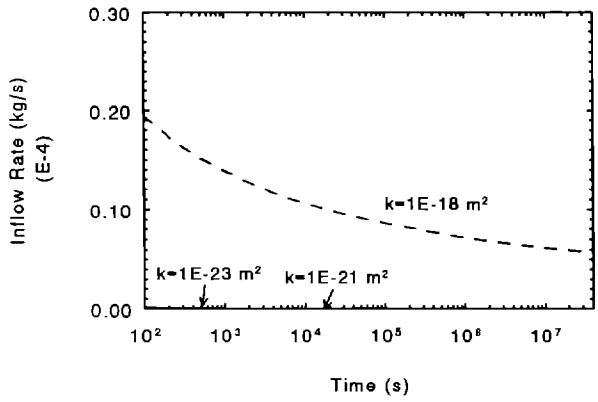

4-B3

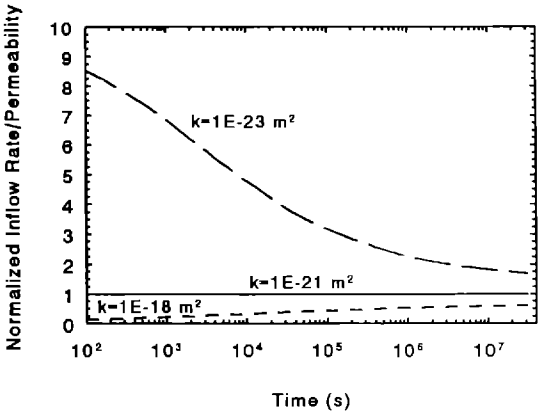

4-B4

Figure 4-B. Results from variation in permeability for single-phase brine inflow.

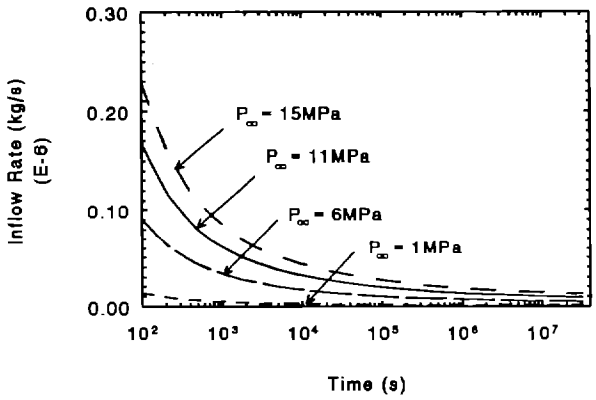

4-C1

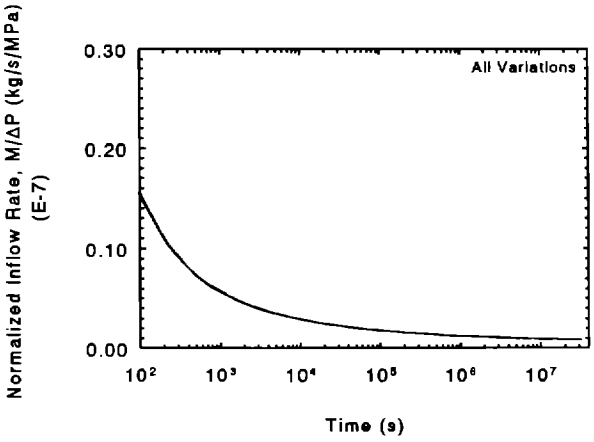

4-C2

Figure 4-C. Results from variation in pore pressure for single-phase brine inflow.

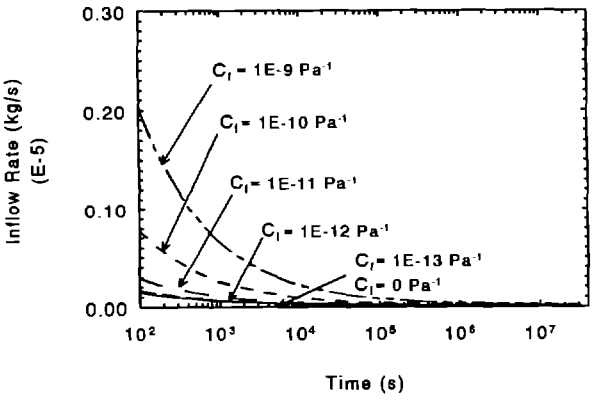

4-D1

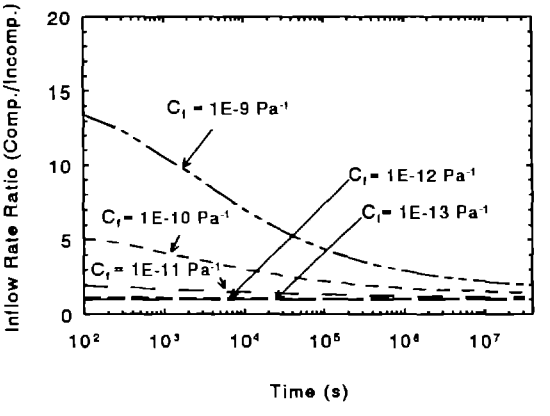

4-D2

Figure 4-D. Results from variation in formation compressibility for single-phase brine inflow.

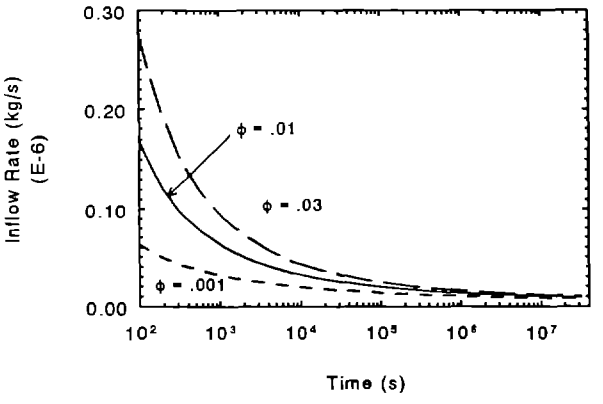

4-E1

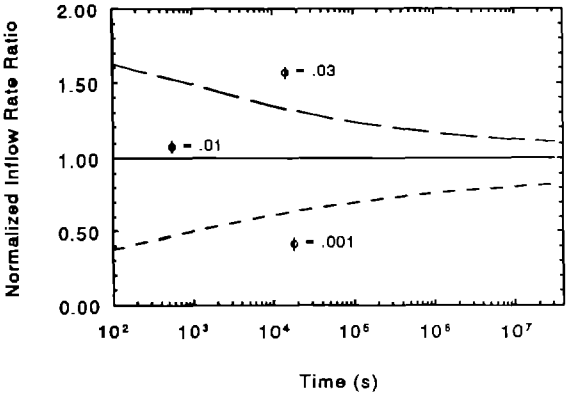

4-E2

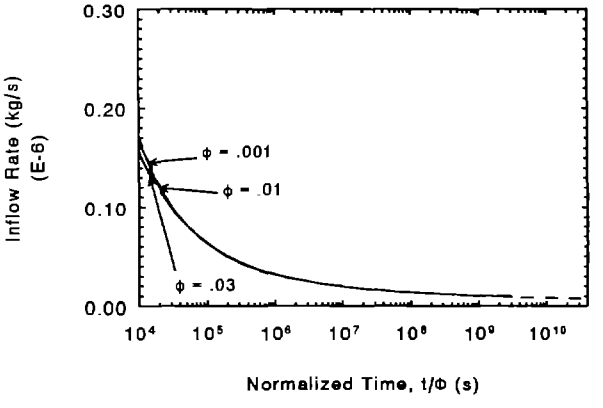

4-E3

Figure 4-E. Results from variation in porosity for single-phase brine inflow.

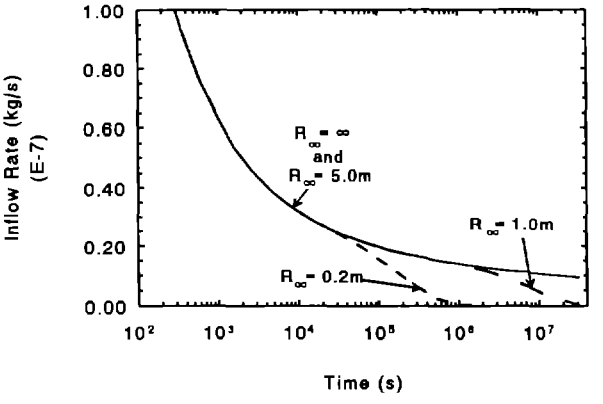

4-F1

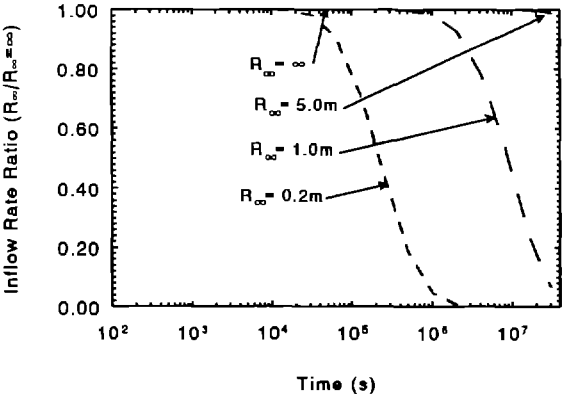

4-F2

Figure 4-F. Results from variation in source radius for single-phase brine inflow.

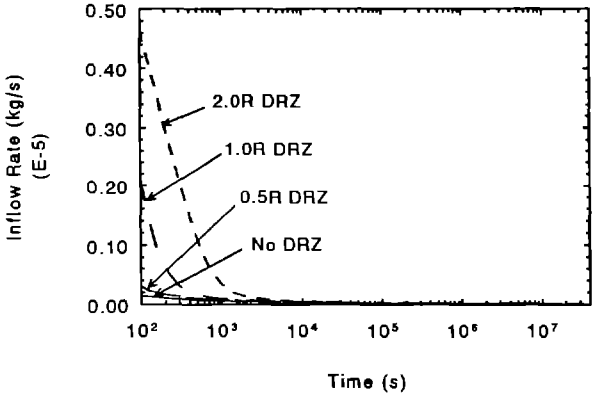

4-G1

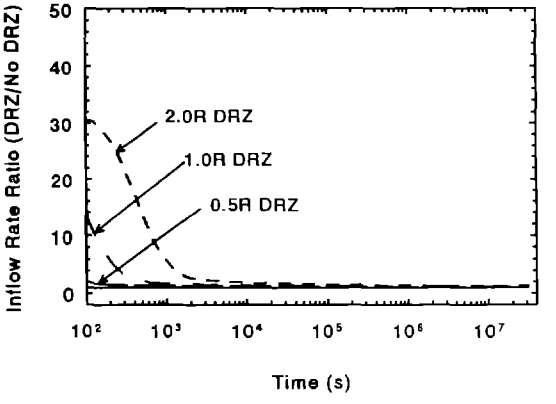

4-G2

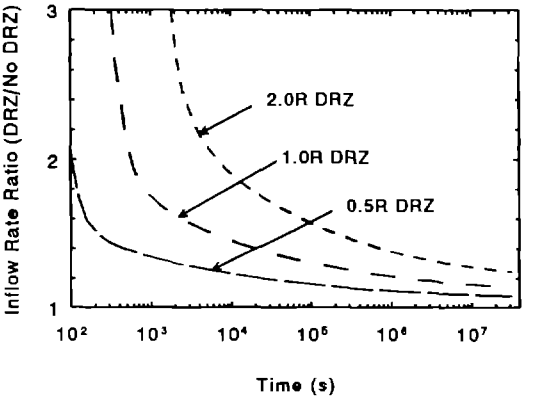

4-G3

Figure 4-G. Results from variation in DRZ distance for single-phase brine inflow.

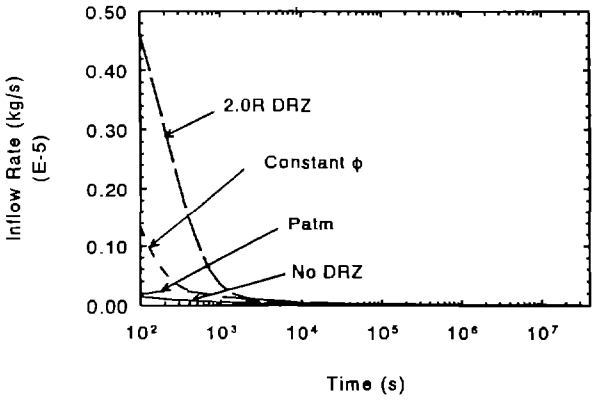

4-H1

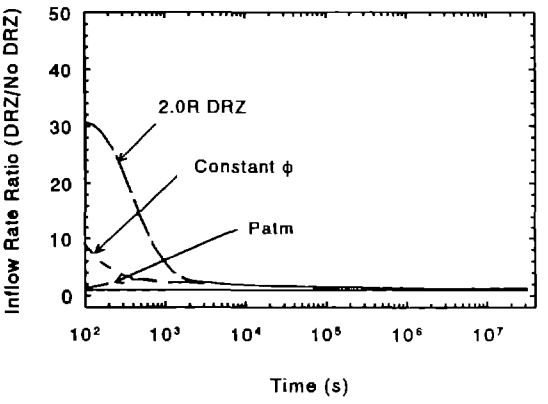

4-H2

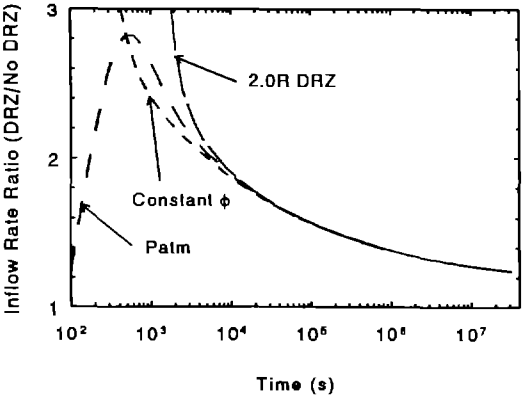

4-H3

Figure 4-H. Results from variation in DRZ porosity and pressure for single-phase brine inflow.

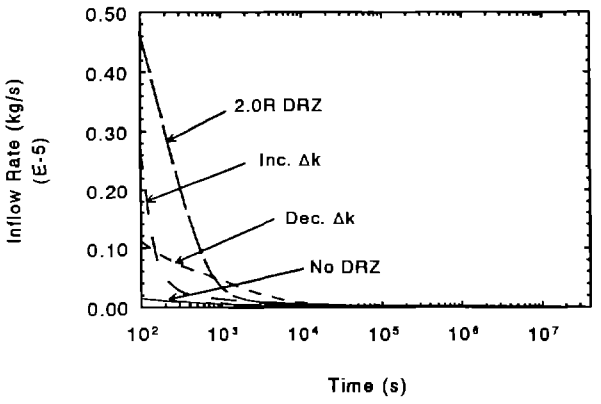

4-I1

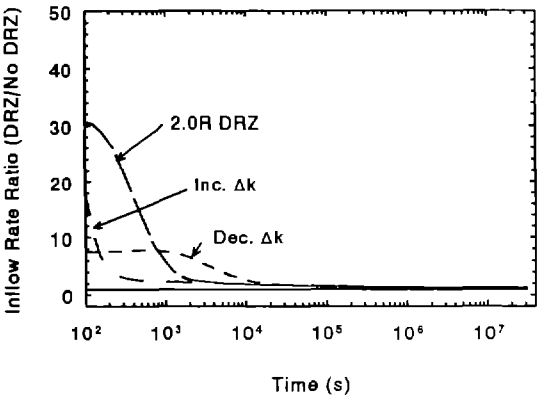

4-I2

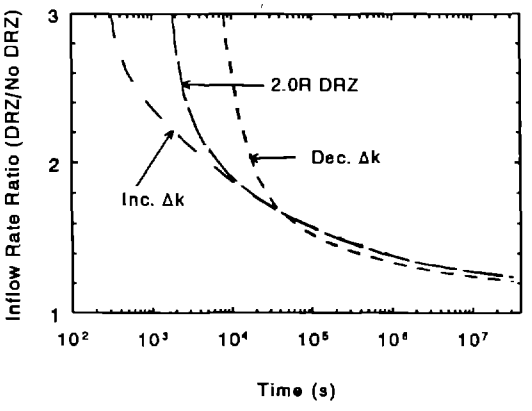

4-I3

Figure 4-I. Results from variation in DRZ permeability contrast for single-phase brine inflow.

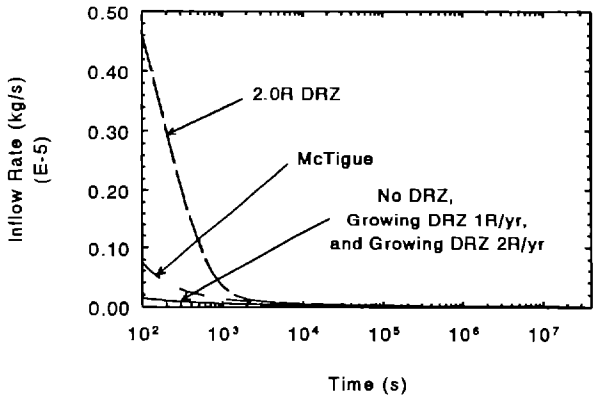

4-J1

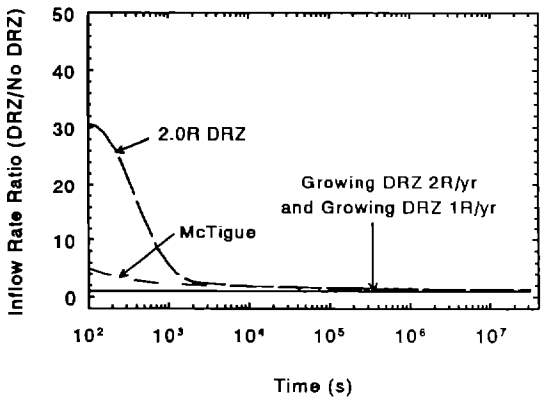

4-J2

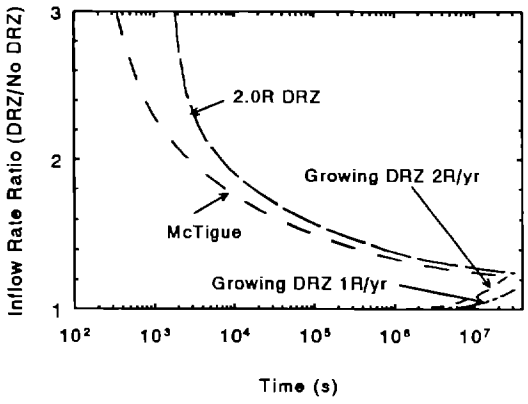

4-J3

Figure 4-J. Results from variation in DRZ permeability distribution for single-phase brine inflow.

Single-Phase Inferred Parameters

The straight-line fits to the inverse brine inflow rate for single-phase conditions are presented in this section. The synthetic data produced by the TOUGH simulations are fit using the late-time asymptotic behavior discussed earlier. The correct diffusivity value is based on single-phase conditions with a fluid compressibility of 3.0×10^{-10} Pa^{-1}. The qualitative behavior of the inverse brine flux and the fits are discussed first, followed by the comparison of the inferred parameters to the simulation values.

Figures 5-A1 and 5-A2 show the fits for the minimum (0.019 m) and maximum (4.5 m) borehole radii considered in this study. For a 0.019-m radius borehole (the base case), the straight-line fit is applicable after about 10^5 seconds, or about 1 day. For the 4.5-m radius case, the corresponding time period is after about 10^{10} seconds (300 years).

Figure 5-B shows results for the permeability variation. For a permeability of 10^{-18} m^2, the straight-line behavior in Figure 5-B1 is appropriate for the entire time. In Figure 5-B2, for a permeability of 10^{-21} m^2, the fit is applicable after about 10^4 seconds, or 3 hours. Finally, in Figure 5-B3, the straight-line fit is reached after about 10^6 seconds, or 10 days, for the lowest permeability of 10^{-23} m^2. The time to approach the late-time behavior is significantly influenced by the permeability.

The fits for different pore pressures are given in Figure 5-C. Since the brine inflow rate scales directly with pore pressure, no variation in the adequacy of the fit is seen. The late-time fits in Figures 5-C1 and 5-C2 are applicable for times greater than 10^5 seconds, or 1 day.

The effect of the formation compressibility on the asymptotic behavior is shown in Figure 5-D. As the formation becomes more compressible, the late-time fit is approached more slowly. For an incompressible formation, the fit in Figure 5-D1 is applicable at about 10^4 seconds (3 hours), while the highest compressibility formation ($C_f = 10^{-9}$ Pa^{-1}), given in Figure 5-D4 approaches this limit at 3×10^6 seconds, about 1 month, or a factor of 300 longer. Figures 5-D2 and 5-D3 show results for intermediate compressibilities for completeness.

Figures 5-E1 to 5-E3 present the porosity variation results. As the porosity increases from 0.001 to 0.03, the minimum time increases from 10^4 seconds to about 10^5 seconds.

The effect of a limited brine source radius is given in Figure 5-F. For an infinite and 5.0-m source radius, the results in Figures 5-F1 and 5-F2 are essentially identical. However, for smaller source radii, namely 1.0 and 0.2

m, the results are dramatically different. For the 1.0-m source radius in Figure 5-F3, the fit is based on 3 points with an R^2 (correlation coefficient) value of 0.92; this compares with an R^2 value of 0.999 or greater for all the other fits. For the 0.2-m source radius (Figure 5-F4), the value of R^2 is meaningless because only two points are involved.

Figures 5-G1 to 5-G4 give the fits for different DRZ distances including zero. The asymptotic times are not appreciably different for the different size DRZs. However, a "kink" in the inverse flux plot is noted before the late-time behavior is reached. This "kink" seems to be indicative of a DRZ, at least for these specifications.

For different initial conditions in the DRZ, the inverse flux data are much different although the time of the fits is similar. For the DRZ at atmospheric pressure, the inverse flux behavior early on in Figure 5-H1 is dramatically different. For a constant value of the porosity, Figure 5-H2 shows a minor difference between it and the standard case (Figure 5-G4) in the shape and extent of the "kink" mentioned above.

Figure 5-I shows the results for various permeability magnitudes in the DRZ. For an increased permeability contrast (higher DRZ permeability), the asymptotic behavior in Figure 5-I1 is approached more slowly than for a decreased permeability contrast given in Figure 5-I2; the time difference is about 2 orders of magnitude as it varies from 10^5 seconds down to about 10^3 seconds.

Finally, Figure 5-J shows the results for the McTigue DRZ model and the two growing DRZ cases. The fit for the McTigue model in Figure 5-J1 is similar to many of the other cases. However, for the growing DRZ cases of Figures 5-J2 to 5-J3, no fit could be generated because the brine inflow rate is increasing slightly (inverse flux decreasing) at the end of the simulation. The effect is clearly seen on the inverse flux plot as the values level out and then turn over.

In addition to the qualitative information from the plots, the fits can be used to quantitatively evaluate the asymptotic method. The results are summarized in Table 4 where the error is defined as

$$\text{Error}(\%) = \frac{\text{Inferred - Actual}}{\text{Actual}} \times 100 \qquad (18)$$

so the error ranges from -100% to $+\infty$%. For the permeability, the inferred values are close (within 10%) in most cases except for the limited brine source cases and the growing DRZ situations. The diffusivity values are considerably in error for these situations as well as for all the other DRZ

cases. As mentioned earlier, brine inflow is much more sensitive to the permeability than to the diffusivity. From results presented in Appendix E, if the permeability is correct but the diffusivity is off by an order of magnitude, the error in the brine inflow is only about 30%. The reason for the poor behavior for the DRZ simulations is that the "effective" radius for brine inflow is no longer the borehole radius. If the outside radius of the DRZ is used, the results are considerably better, as shown in Table 5.

The consistent prediction of the permeability and the low prediction of the diffusivity for the DRZ cases can be explained by looking at Equation 2, or

$$\lim_{t_* \to \infty} |q|^{-1} = A \ln t + B \tag{19}$$

where

$$A = \frac{\mu R}{2 k P_o} \tag{20}$$

and

$$B = A \ln \left(\frac{4c}{R^2 \Gamma} \right). \tag{21}$$

Rewriting in terms of the effective radius of the borehole, R^*, gives

$$\frac{2 \pi L}{|\dot{m}|} = \frac{\mu}{2 k P_o} \ln t + \frac{\mu}{2 k P_o} \ln \frac{4 c}{R^{*2} \Gamma}. \tag{22}$$

Therefore, the permeability does not depend on the effective radius while the diffusivity will vary inversely with the effective radius squared.

For the limited brine source radius, the diffusivity values are more in line with those obtained by McTigue (1989) in his fit to DBT10 data. Perhaps a limited brine source could explain the lower than expected diffusivity values (and higher capacitance values) that have been obtained from brine inflow data. This situation may merit additional study.

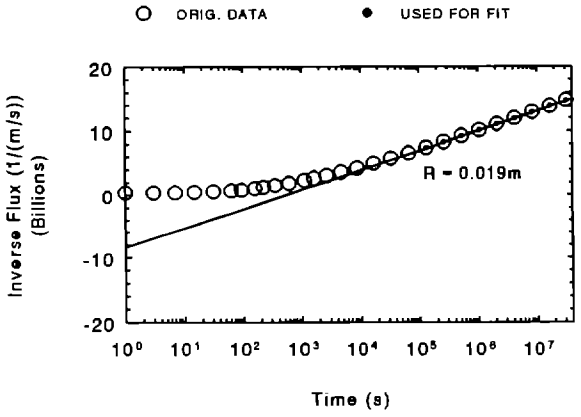

5-A1

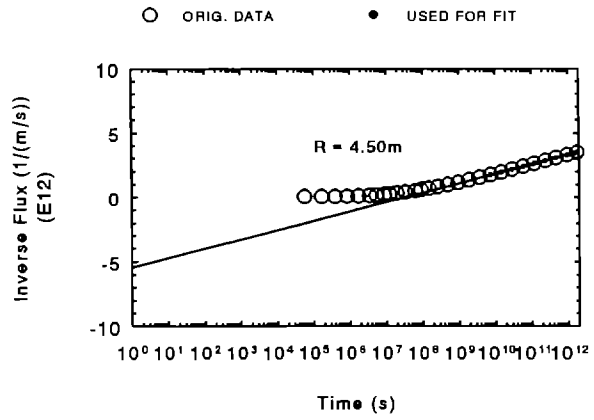

5-A2

Figure 5-A. Results from variation in borehole radius for single-phase inverse brine flux.

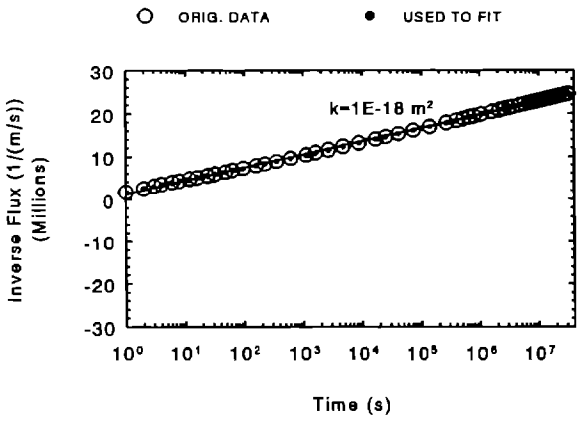

5-B1

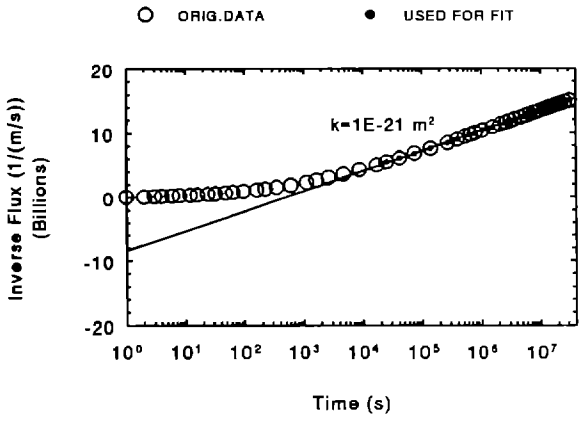

5-B2

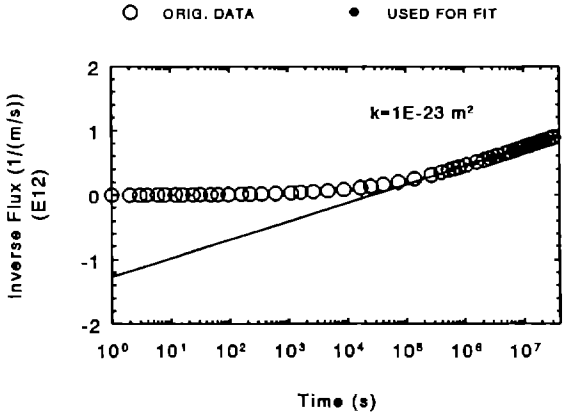

5-B3

Figure 5-B. Results from variation in permeability for single-phase brine inflow.

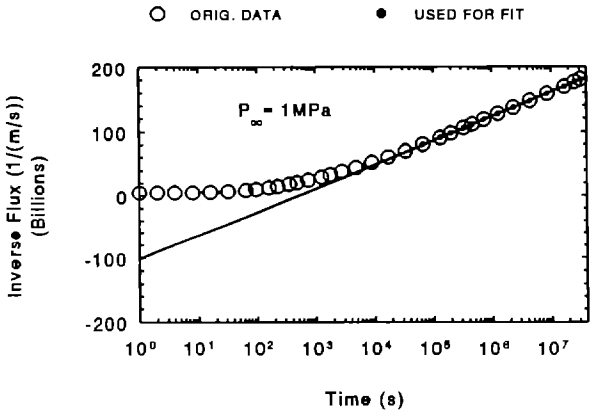

5-C1

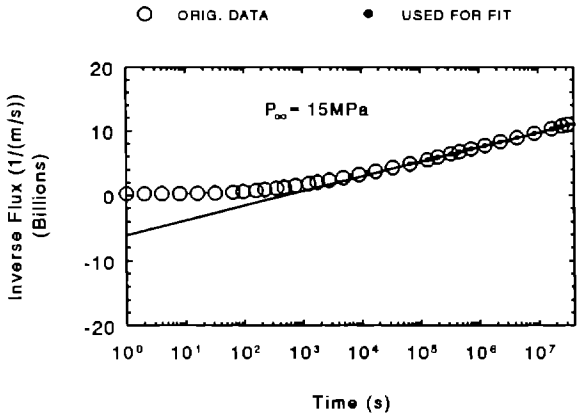

5-C2

Figure 5-C. Results from variation in pore pressure for single-phase inverse brine flux.

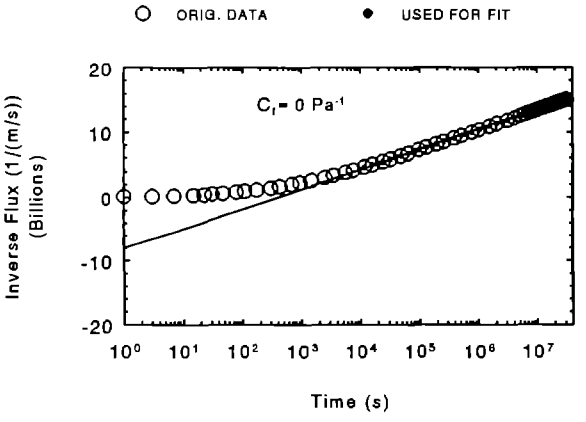

5-D1

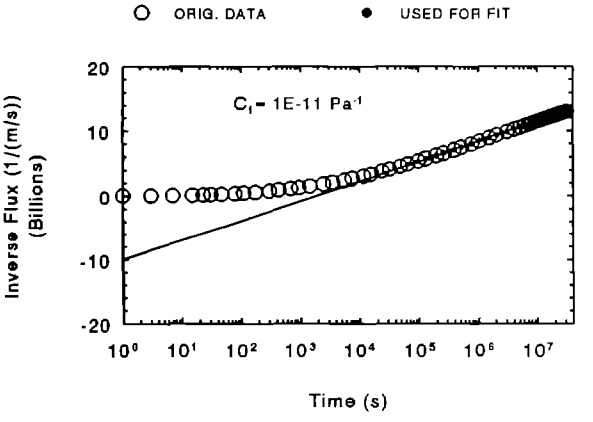

5-D2

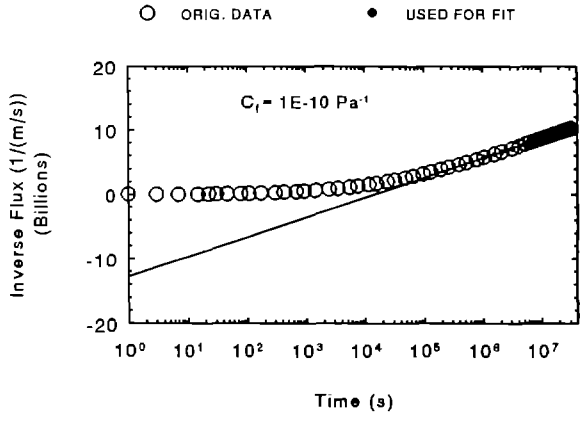

5-D3

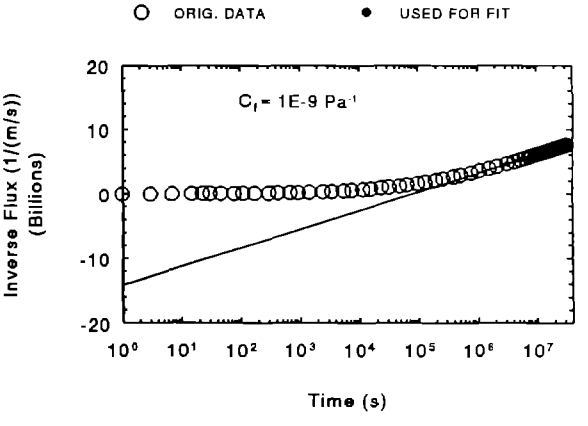

5-D4

Figure 5-D. Results from variation in formation compressibility for single-phase inverse brine flux.

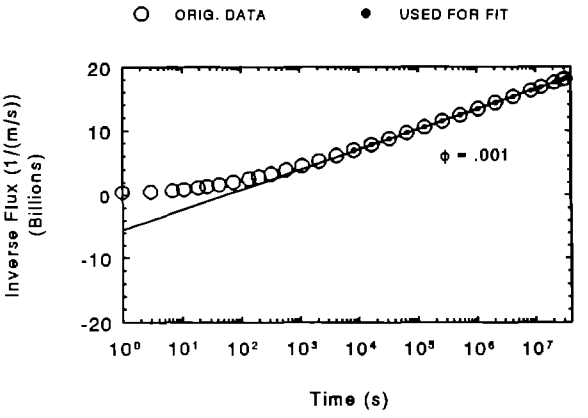

5-E1

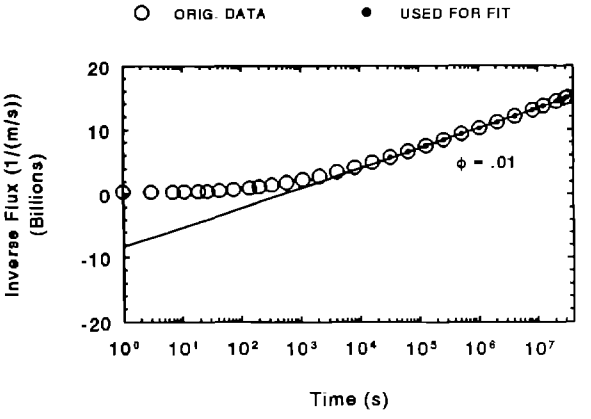

5-E2

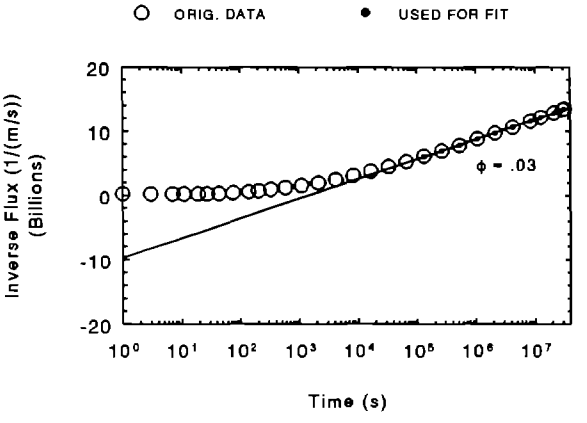

5-E3

Figure 5-E. Results from variation in porosity for single-phase inverse brine flux.

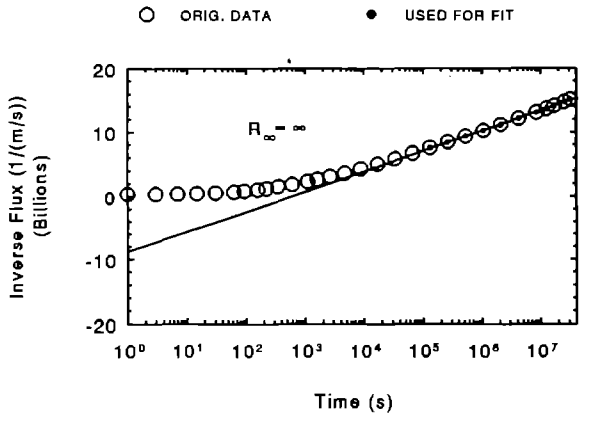

5-F1

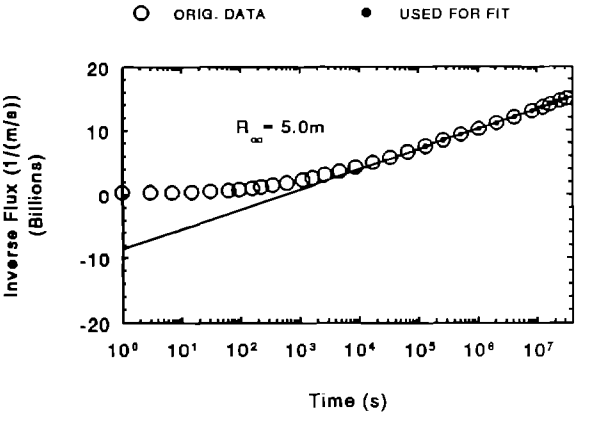

5-F2

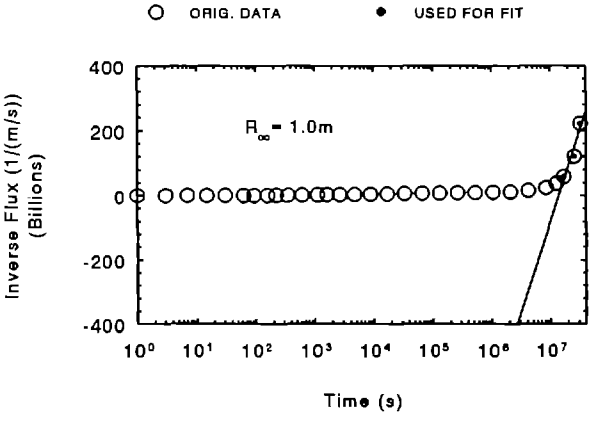

5-F3

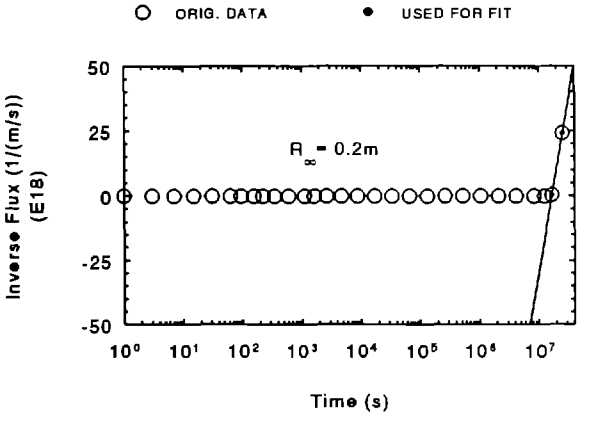

5-F4

Figure 5-F. Results from variation in source radius for single-phase inverse brine flux.

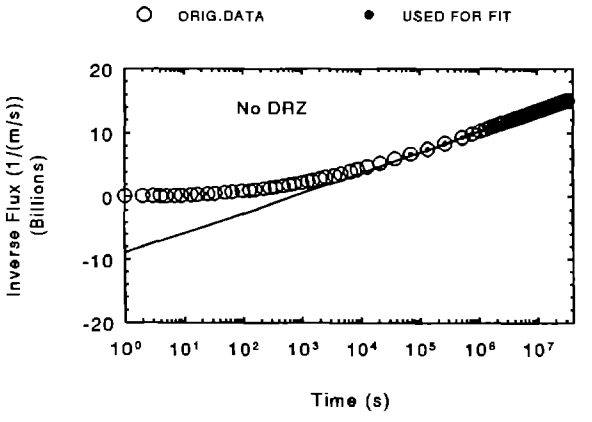

5-G1

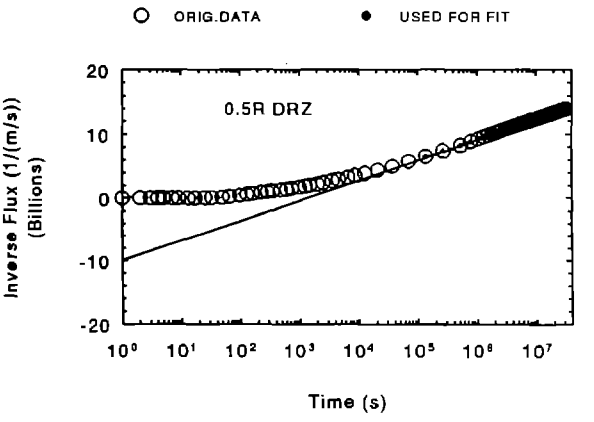

5-G2

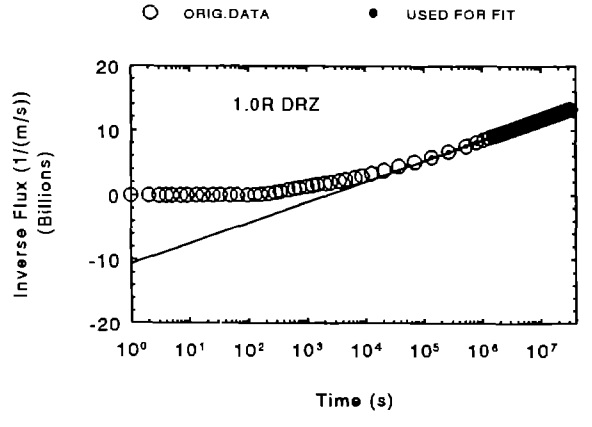

5-G3

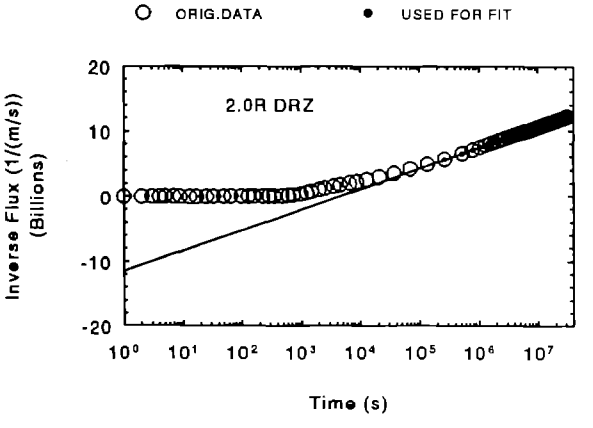

5-G4

Figure 5-G. Results from variation in DRZ distance for single-phase inverse brine flux.

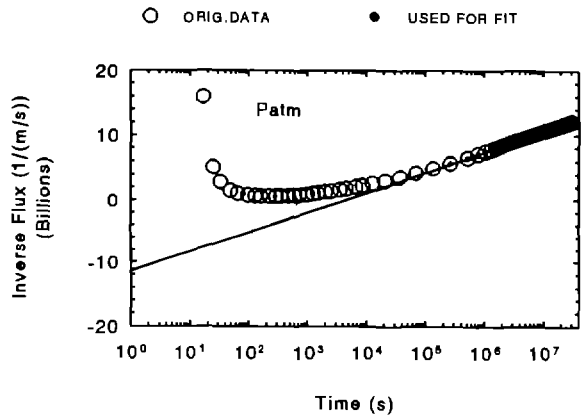

5-H1

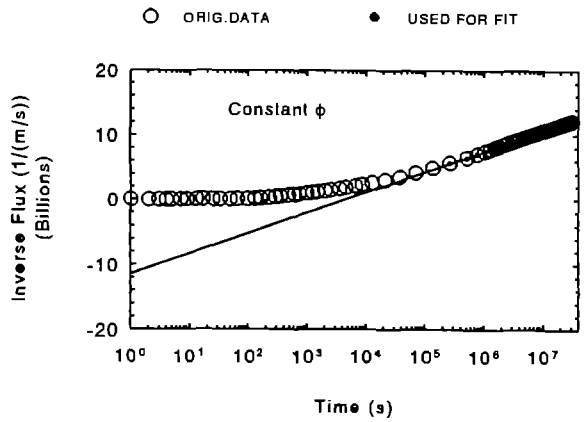

5-H2

Figure 5-H. Results from variation in DRZ porosity and pressure for single-phase inverse brine flux.

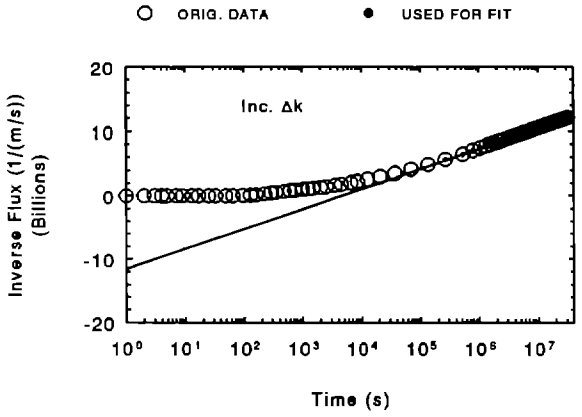

5-I1

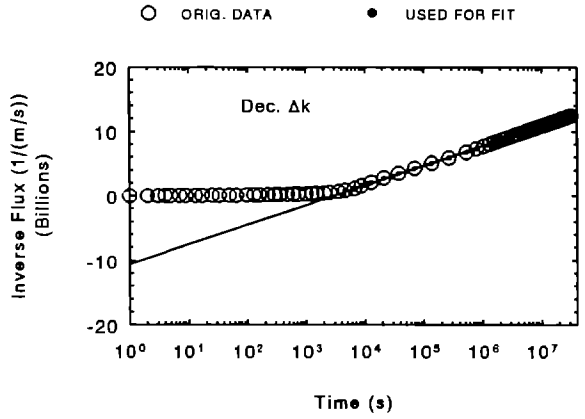

5-I2

Figure 5-I. Results from variation in DRZ permeability contrast for single-phase inverse brine flux.

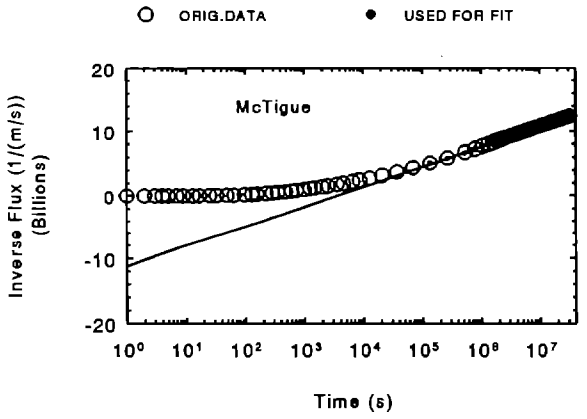

5-J1

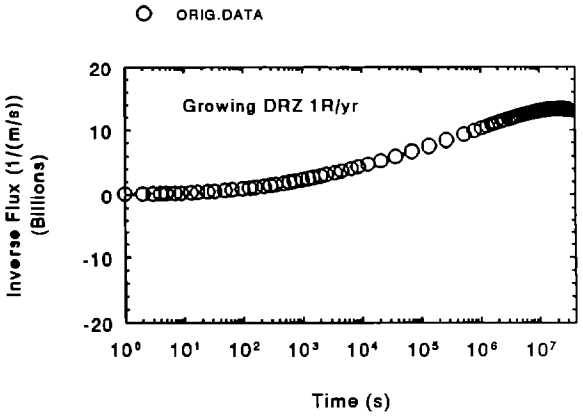

5-J2

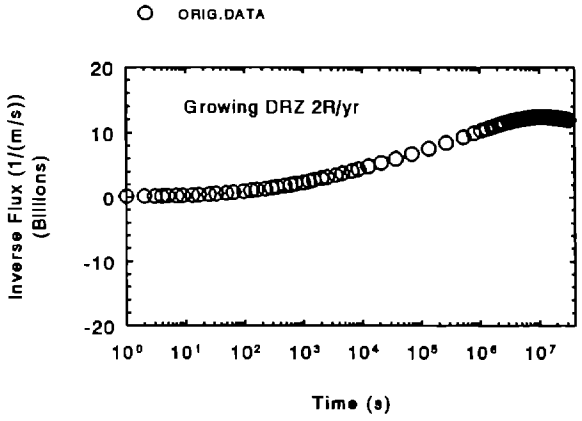

5-J3

Figure 5-J. Results from variation in DRZ permeability distribution for single-phase inverse brine flux.

Table 4. Single-Phase Inferred Parameters

Permeability (m^2)		
Actual	Inferred	Error
1.0×10^{-21} (except as noted)		
Borehole Radius		
R=all	1.04×10^{-21}	+4%
Permeability		
10^{-18} m^2	1.03×10^{-18}	+3%
10^{-21} m^2	1.02×10^{-21}	+2%
10^{-23} m^2	1.11×10^{-23}	+11%
Pore Pressure		
1 MPa	0.94×10^{-21}	-6%
15 MPa	1.03×10^{-21}	+3%
Formation Compressibility		
0 Pa^{-1}	1.03×10^{-21}	+3%
10^{-13} Pa^{-1}	1.04×10^{-21}	+4%
10^{-12} Pa^{-1}	1.04×10^{-21}	+4%
10^{-11} Pa^{-1}	1.04×10^{-21}	+4%
10^{-10} Pa^{-1}	1.04×10^{-21}	+4%
10^{-9} Pa^{-1}	1.10×10^{-21}	+10%
Porosity		
0.001	1.01×10^{-21}	+1%
0.01	1.02×10^{-21}	+2%
0.03	1.02×10^{-21}	+2%
Brine Source		
Infinity	1.01×10^{-21}	+1%
5.0 m	1.01×10^{-21}	+1%
1.0 m	5.6×10^{-24}	-99%
0.2 m	2.4×10^{-32}	-100%
DRZ Characteristics		
No DRZ	1.00×10^{-21}	<-1%
0.5R DRZ	1.00×10^{-21}	<-.5%
1.0R DRZ	1.01×10^{-21}	+1%
2.0R DRZ	1.01×10^{-21}	+1%
Patm	1.01×10^{-21}	+1%
Constant ϕ	1.01×10^{-21}	+1%
McTigue	1.02×10^{-21}	+2%
Inc. Δk	1.01×10^{-21}	+1%
Dec. Δk	1.04×10^{-21}	+4%
Growing DRZ - 1R/yr	No Fit	No Fit
Growing DRZ - 2R/yr	No Fit	No Fit

Table 4. Single-Phase Inferred Parameters (Continued)

Diffusivity (m^2/sec)		
Actual	Inferred	Error
2.1×10^{-7} (except as noted)		
Borehole Radius		
R=all	3.2×10^{-7}	+50%
Permeability		
10^{-18} m^2		
(2.1×10^{-4})	4.0×10^{-4}	+90%
10^{-21} m^2		
(2.1×10^{-7})	3.3×10^{-7}	+60%
10^{-23} m^2		
(2.1×10^{-9})	6.0×10^{-9}	+190%
Pore Pressure		
1 MPa	3.3×10^{-7}	+60%
15 MPa	3.4×10^{-7}	+60%
Formation Compressibility		
0 Pa^{-1}		
(2.1×10^{-7})	3.9×10^{-7}	+90%
10^{-13} Pa^{-1}		
(2.0×10^{-7})	3.8×10^{-7}	+90%
10^{-12} Pa^{-1}		
(1.6×10^{-7})	2.9×10^{-7}	+80%
10^{-11} Pa^{-1}		
(4.8×10^{-8})	8.8×10^{-8}	+80%
10^{-10} Pa^{-1}		
(6.1×10^{-9})	1.1×10^{-8}	+80%
10^{-9} Pa^{-1}		
(6.2×10^{-10})	2.0×10^{-9}	+220%
Porosity		
0.001		
(2.1×10^{-6})	3.0×10^{-6}	+40%
0.01		
(2.1×10^{-7})	3.5×10^{-7}	+70%
0.03		
(6.9×10^{-8})	1.2×10^{-7}	+70%
Brine Source		
Infinity	2.9×10^{-7}	+40%
5.0 m	2.9×10^{-7}	+40%
1.0 m	1.2×10^{-11}	-100%
0.2 m	9.7×10^{-12}	-100%

Table 4. Single-Phase Inferred Parameters (Continued)

DRZ Characteristics		
No DRZ	2.7×10^{-7}	+30%
0.5R DRZ	1.3×10^{-7}	-40%
1.0R DRZ	7.7×10^{-8}	-60%
2.0R DRZ	3.7×10^{-8}	-80%
Patm	3.7×10^{-8}	-80%
Constant ϕ	3.7×10^{-8}	-80%
McTigue	4.7×10^{-8}	-80%
Inc. Δk	3.7×10^{-8}	-80%
Dec. Δk	5.8×10^{-8}	-70%
Growing DRZ - 1R/yr	No Fit	No Fit
Growing DRZ - 2R/yr	No Fit	No Fit

Table 5. Inferred Single-Phase Diffusivity Using Effective Radius

Diffusivity (m^2/sec)		
Actual	Inferred	Error
2.1×10^{-7}		
Borehole Radius		
R=all	3.2×10^{-7}	+50%
DRZ Characteristics		
No DRZ	2.7×10^{-7}	+30%
0.5R DRZ	2.8×10^{-7}	+40%
1.0R DRZ	3.1×10^{-7}	+50%
2.0R DRZ	3.4×10^{-7}	+60%
Patm	3.4×10^{-7}	+60%
Constant ϕ	3.4×10^{-7}	+60%
McTigue	4.2×10^{-7}	+100%
Inc. Δk	3.3×10^{-7}	+60%
Dec. Δk	5.2×10^{-7}	+150%
Growing DRZ - 1R/yr	No Fit	No Fit
Growing DRZ - 2R/yr	No Fit	No Fit

Two-Phase Brine Inflow

The two-phase (brine saturated with dissolved gas including free gas) brine inflow rates are reported in this section. In addition, the ratio of the two-phase brine inflow rate to the single-phase value shown earlier is presented. Unless otherwise noted, all two-phase conditions referred to are from brine initially saturated with dissolved gas; no free gas is assumed.

Figure 6-A1 shows the two-phase brine inflow for the borehole radius variation. As with the single-phase results, the inflow rate can be scaled with t/R^2 as shown in Figure 6-A2. The increase in brine inflow rate for two-phase compared to single-phase conditions is given in Figure 6-A3. The maximum increase is about 1.45, which decreases to about a factor of 1.06.

The two-phase brine inflow rate for the permeability variation is given in Figures 6-B1 to 6-B3, while the brine inflow rate divided by the permeability is shown in Figure 6-B4. The results are similar to the single-phase results as the magnitude and shape of the brine inflow curves are different. The ratio of two-phase to single-phase brine inflow is depicted in Figure 6-B5. The effect of two-phase conditions is a maximum at a permeability of 10^{-21} m^2; the ratio is lower for 10^{-23} m^2 and 10^{-18} m^2. The reason for the maximum influence at the intermediate permeability is due to the gas pressure variation. The capillary pressure magnitude is based on the Davies correlation as discussed earlier. For the low permeability value, the gas pressure remains high enough that any gas coming out of solution occupies a very small volume and has little effect on the liquid pressure. Conversely, for the high permeability value, the gas coming out of solution has essentially fully expanded, so its effect is moderate. For the intermediate permeability, enough gas has come out of solution to keep the gas pressure moderately high, which in turn keeps the liquid pressure higher and increases the brine inflow rate.

For the pore pressure variation, two conditions were investigated. The first condition is brine saturated with dissolved gas at the assumed pore pressure. The second condition is brine saturated with dissolved gas at 15 MPa that is then depressurized to the desired pressure; this variation is intended to approximate conditions from pore pressure reduction due to an excavation. These two variations are referred to as dissolved gas and free gas.

Figure 6-C1 gives the brine inflow rate for the dissolved gas case. Unlike single-phase flow, these results cannot be completely normalized by dividing by the pressure difference, although the results are within about 10% of each other, as shown in Figure 6-C2. Figures 6-C3 and 6-C4 show the

same parameters for the free gas scenario. The normalization does not work as well for the free gas case as the normalized curves are within about 40% of each other. Figures 6-C5 and 6-C6 show the ratio of two-phase brine inflow compared to the single-phase value. The increase is greatest for the lower pore pressures. For dissolved gas, the maximum increase is about 1.65 for 1 MPa pore pressure; the free gas maximum value is about 2.3 for 1 MPa pore pressure. Figure 6-C7 gives the ratio of free gas to dissolved gas brine inflow rate with a maximum ratio of 1.45 for 1 MPa.

The formation compressibility results are given in Figure 6-D. Figure 6-D1 gives the brine inflow rate, and Figure 6-D2 shows the ratio of the inflow rate compared to that for an incompressible formation. For two-phase conditions, the maximum increase in flow rate is a factor of about 9, while the single-phase maximum value shown earlier is about 13. The effect of formation compressibility becomes less important for two-phase conditions than for single-phase flow. Figure 6-D3 presents the two-phase to single-phase brine inflow ratio. The maximum value is about 1.5 for an incompressible formation, which decreases down to 1.0 for the maximum compressibility investigated ($C_f = 10^{-9}$ Pa^{-1}). Therefore, the increase in the brine inflow rate for two-phase conditions is smaller for a more compressible formation. Depending on the formation compressibility, two-phase conditions may or may not influence the brine inflow rate significantly.

Figure 6-E presents the porosity variation results. Figure 6-E1 gives the mass inflow rate, while Figure 6-E2 shows the inflow rate divided by the value for the base case porosity of 0.01. The larger porosity has the higher brine inflow rate. Figure 6-E3 presents the brine inflow rate as a function of normalized time (t/ϕ); the curves for all three porosities basically overlay each other. The two-phase to single-phase brine inflow rate ratio is presented in Figure 6-E4. Except for early-time differences due to nodalization, the ratios for all three cases are the same with a maximum value of 1.5.

Two-phase brine inflow rates for different brine source radii are shown in Figure 6-F1, with the ratio to an infinite radius given in Figure 6-F2. These figures look very similar to those for single-phase flow. However, if the ratio of two-phase to single-phase flow is calculated, the value changes dramatically with time and brine source radius as shown in Figures 6-F3 and 6-F4. For a radius of 0.2 m, the ratio toward the end of the simulation is 10^4 and increasing because the single-phase value is essentially zero. Therefore, if a limited brine source is encountered, the influence of two-phase conditions can be dramatic.

Figure 6-G1 presents the results for different DRZ distances. The presence of a DRZ significantly impacts the early-time (up to 10^4 seconds) brine inflow rate. The ratio of brine inflow with a DRZ to no DRZ is given in Figures 6-G2 and 6-G3 with different scales. For a DRZ distance of 2.0R, the maximum ratio is about 45 at early time and is still about 1.3 after 1 year. The ratio of two-phase to single-phase brine inflow is shown in Figures 6-G4 and 6-G5. The ratio is a maximum of about 25 early, which is largest for the smallest nonzero DRZ distance; the maximum value and the timing may be significantly influenced by the nodalization. For no DRZ, the maximum ratio is about 1.5. Later on, the ratio falls dramatically, approaching the no DRZ values after 10^6 seconds (1-1/2 weeks) for the 2.0R DRZ case.

The results for different DRZ specifications are shown in Figure 6-H. The brine inflow rate in Figure 6-H1 shows that the rate is lower for a constant porosity in the DRZ and is smaller if the initial DRZ pressure is atmospheric. The ratio of the brine inflow with the DRZ to no DRZ is given in Figures 6-H2 and 6-H3. The constant porosity value is about one-half that for the increased porosity (DRZ). The two porosity variations merge at about 3×10^5 seconds (3 days). For the case of initial atmospheric pressure in the DRZ, the ratio remains at 0 up to about 1000 seconds, slowly rising to a maximum of about 2, and merging with the other cases again at about 3×10^5 seconds. Note that the zero brine inflow rate, which lasts about 1000 seconds, is equivalent to about 2-3 months for Room Q. The ratio of two-phase to single-phase brine inflow, which is shown in Figures 6-H4 and 6-H5, is a maximum of about 17 for the standard DRZ, about 9 for a constant porosity, and about 1.5 for the atmospheric pressure variation.

The results for changing the permeability contrast of the DRZ are shown in Figure 6-I. As the permeability contrast increases (the standard model has a contrast of 100); the two-phase brine inflow rate increases dramatically as shown in Figure 6-I1. From Figure 6-I2, the ratio to the base case is a maximum of about 10 for decreased Δk (10), about 45 for the standard model (100), and much greater than 50 for increased Δk (1000). As seen in Figure 6-I3, the values quickly merge at about 10^5 seconds (1 day). The same trend is seen in Figures 6-I4 and 6-I5 for the two-phase to single-phase inflow rates. While the values are considerably different early, the values quickly merge as the far-field parameters dominate.

The McTigue model of the DRZ is compared to the standard model and growing DRZ models in Figure 6-J. The brine inflow rate is lower for the McTigue model than for the standard model, as shown in Figure 6-J1; this behavior is expected due to the lower effective permeability contrast. On this scale, the results for the growing DRZ are the same as for no DRZ. For the growing DRZ cases, the brine inflow rate is actually increasing late in time, increasing by 1% and 8% over the minimum values for the 1R/yr and 2R/y cases, respectively. Figures 6-J2 and 6-J3 present the brine inflow ratio to

that with no DRZ. The standard model and McTigue model have declining ratios; in contrast, the growing DRZ results show an increasing ratio. The growing DRZ ratios are 1.2 and 1.4 for the 1R/yr and 2R/yr growth rates, respectively; the values are still increasing at 1 year. The two-phase to single-phase ratios, given in Figures 6-J4 and 6-J5, show that the McTigue model has a much lower peak than the standard model and merges with the no DRZ results earlier at about 10^5 seconds (1 day). The growing DRZ models have ratios essentially the same as those calculated for no DRZ except at late time, where the ratio for the 2R/yr growth rate is about 1.15.

The predictions for varying the gas solubility are presented in Figure 6-K. Higher values of the gas solubility (higher values of K_H^{-1}) have a minor effect on the brine inflow rate given in Figure 6-K1. As shown in Figure 6-K2, the effect of increasing the gas solubility by a factor of 4 only increases the maximum two-phase to single-phase brine inflow ratio by around 50%, or 1.45 to 2.1.

Figures 6-L1 and 6-L2 show the brine inflow rate and two-phase to single-phase brine inflow ratio for variation of the initial dissolved gas fraction. The inflow rates given in Figure 6-L1 for 0 and 50% dissolved gas fractions are virtually indistinguishable on these plots. Surprisingly, as shown in Figure 6-L2, the brine inflow rate for 50% dissolved gas fraction is below that for single-phase conditions in early time. This behavior is not physical but is related to the numerical solution of the problem as discussed later in this section. At later time, the brine inflow rate for 50% dissolved gas fraction increases above that for no dissolved gas, but the increase is small. Above 50% dissolved gas fraction, the results increase smoothly toward the 100% dissolved gas case.

Figure 6-M1 gives the two-phase brine inflow rate as a function of time for uniform free gas distributions. The highest brine inflow rate is for 10 v/o (volume percent) free gas; the brine inflow rate is lower for no free gas and for 20 v/o free gas. This behavior is due to the fact that for 10 v/o free gas, the free gas increases the effective compressibility of the fluid thereby increasing the late time brine inflow compared to no free gas; the free gas does not flow due to the 20 v/o residual gas fraction in the two-phase characteristic curves. However, for 20 v/o free gas, this effect is offset by the fact that the gas flows above 20 v/o. Therefore, as the fluid depressurizes, the free gas fraction increases above 20 v/o, and the gas flows thereby decreasing the driving force for brine flow compared to 10 v/o. For 50 v/o, the results are not shown because the net brine inflow rate into the borehole is zero; the gas flow rate is so great compared to the liquid flow rate that all the inflowing brine is evaporated by the expanding gas. The effect of varying the free gas distribution is shown in Figure 6-M2. While some difference is noted early for different distributions, the longer

term (>10^5 seconds) brine inflow rate is unaffected by the details for the given non-uniform distribution. Figure 6-M3 gives the brine inflow ratio to that with no free gas; the maximum ratio is about 2.75 for 10 v/o and about 2.4 for 20 v/o. Figure 6-M4 depicts the ratio of the brine inflow rate to single-phase conditions. The brine inflow rate with free gas may be up to 3.5 times higher than for single-phase conditions.

Figure 6-N1 gives the brine inflow rate for capillary pressure magnitude changes. The brine inflow rate increases with decreasing capillary pressure, probably due to the greater volume of gas (lower pressure) for a lower capillary pressure and a resulting more compressible fluid. From Figure 6-N2, the difference in flow rate for changes in capillary pressure magnitude is less than a factor of 2. Figure 6-N3 shows the ratio of the two-phase brine inflow rate for the various cases to that for the base case with single-phase conditions. For variations in the capillary pressure magnitude, the ratio varies from a maximum of about 2.3 for a zero capillary pressure to values less than 1.0 for a high capillary pressure.

Values of the ratio less than 1.0 in Figures 6-L2 and 6-N3 are a numerical artifact. By investigating the source code, these values are the result of some assumptions made in the development of TOUGH that are not important in typical applications. These assumptions are that the density of the liquid phase can be evaluated at the gas phase pressure, and that the presence of dissolved gas does not alter the liquid density. These simplifications only cause differences in the brine inflow rate (maximum 5%) at the highest values of capillary pressure; for the base case, the effect of these assumptions is on the order of 1% or less. Therefore, the assumptions are adequate for WIPP usage in general but must be kept in mind when comparing results using different parameters.

The results for variations in the capillary pressure shape are given in Figure 6-O. The brine inflow results in Figure 6-O1 for the base case and for a uniform capillary pressure curve are essentially the same; these results are due to the low gas saturation valves (high liquid saturation) encountered in the simulation. The brine flow rate is slightly lower for the dissolved gas exsolution case consistent with a slightly higher capillary pressure. Figure 6-O2 shows a maximum difference of less than 25% for the three variations. Figure 6-O3 shows the variation in the ratio of two-phase to single-phase brine inflow rate; the maximum increase is only 50%.

Figure 6-P1 gives the brine inflow rate for the various sets of two-phase characteristic curves studied. Variations in the residual saturations have a small impact on the brine inflow rate as does the effect of a totally different set of curves; the maximum difference is less than a factor of 2 as

shown in Figure 6-P2. Figure 6-P3 depicts the ratio for the different sets of characteristic curves. The ratio in Figure 6-P3 is less than 1.0 for the Sandia functions due to assumptions in TOUGH discussed above, and the variation in the ratio is about a factor of 2.

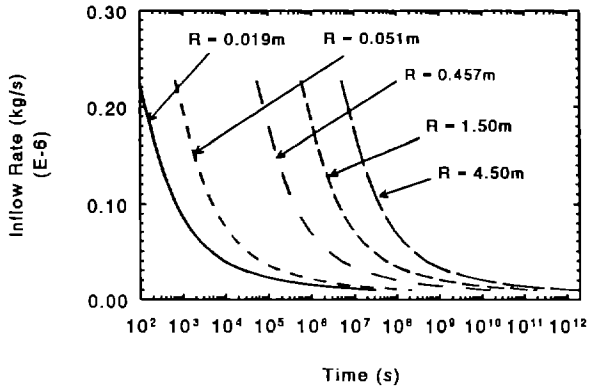

6-A1

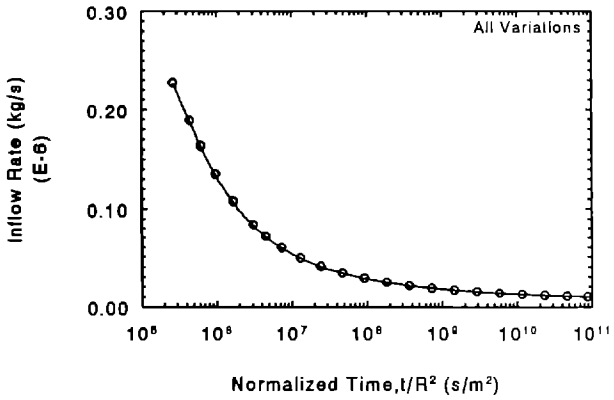

6-A2

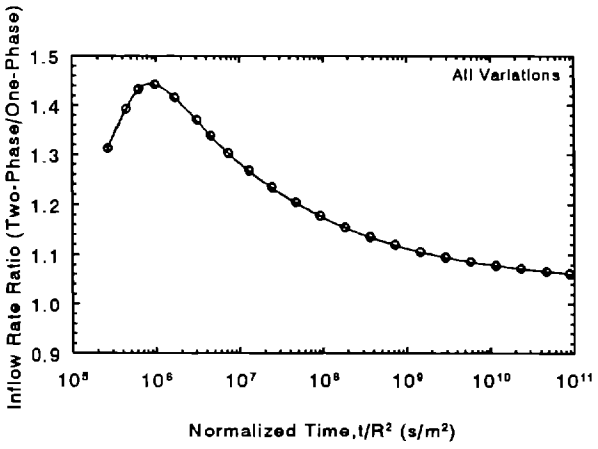

6-A3

Figure 6-A. Results from variation in borehole radius for two-phase brine inflow.

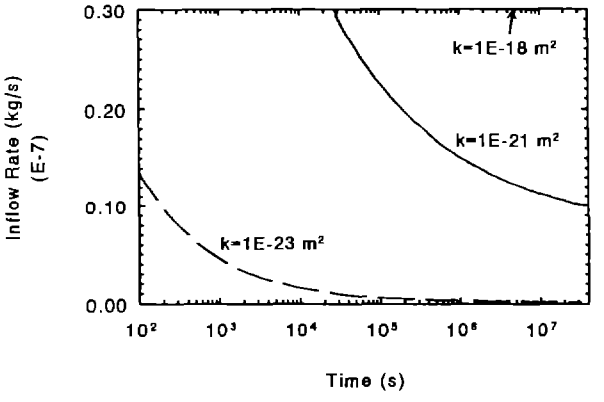

6-B1

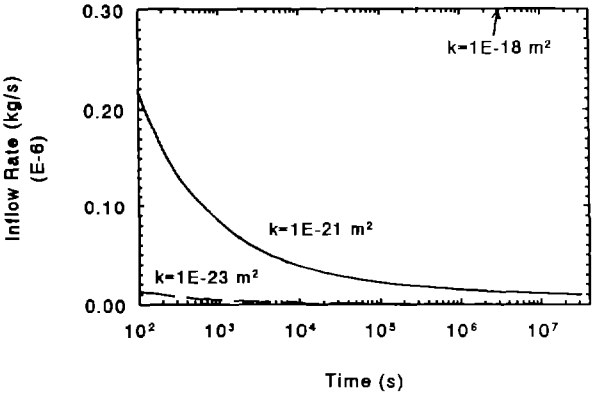

6-B2

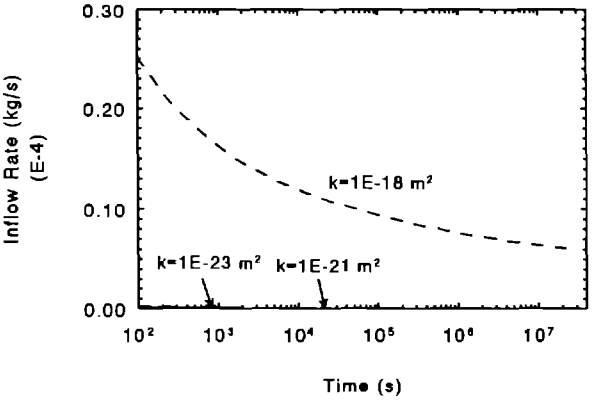

6-B3

Figure 6-B. Results from variation in permeability for two-phase brine inflow.

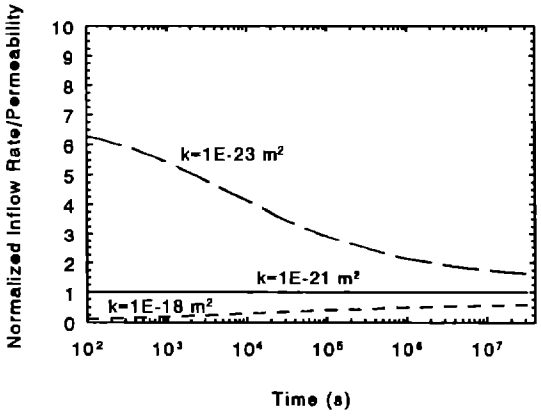

6-B4

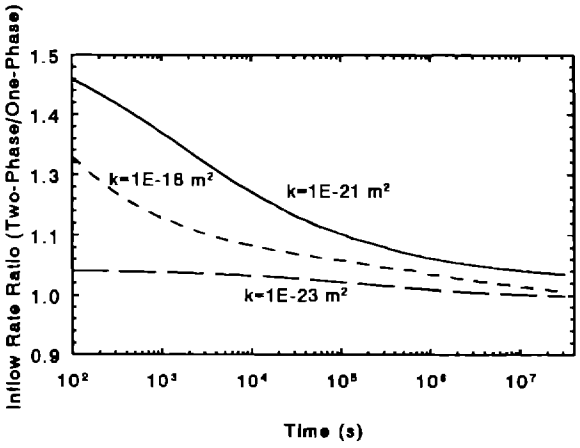

6-B5

Figure 6-B. Results from variation in permeability for two-phase brine inflow (continued).

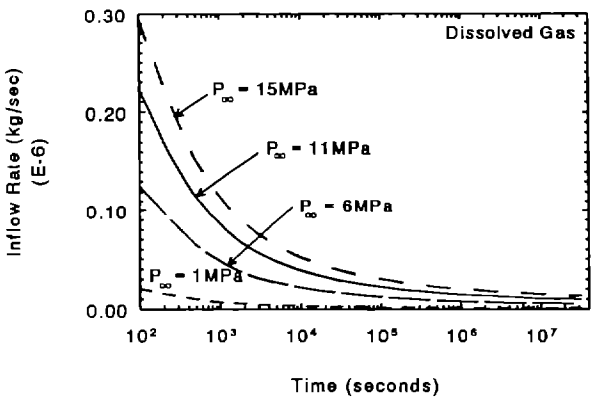

6-C1

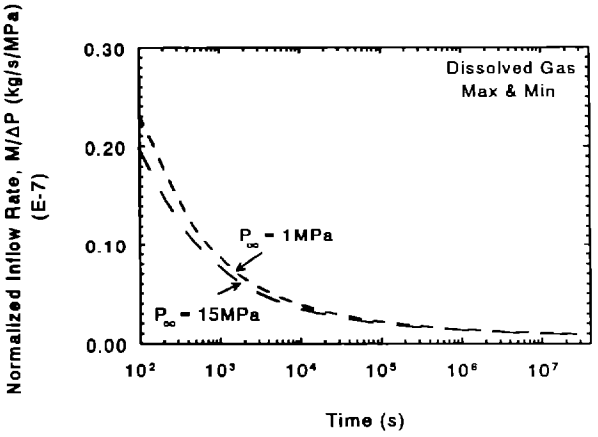

6-C2

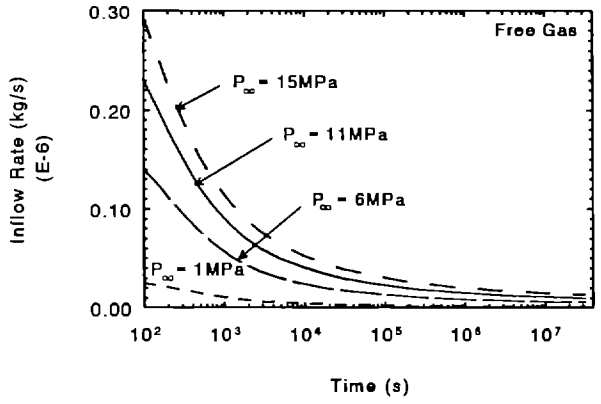

6-C3

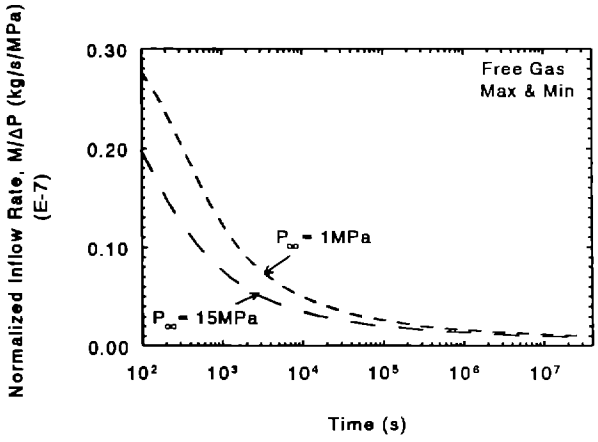

6-C4

Figure 6-C. Results from variation in pore pressure for two-phase brine inflow.

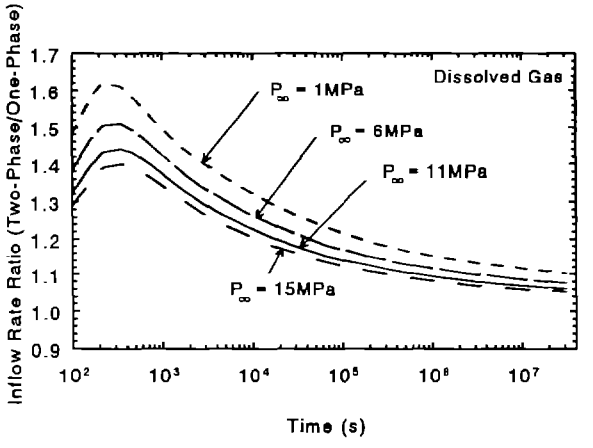

6-C5

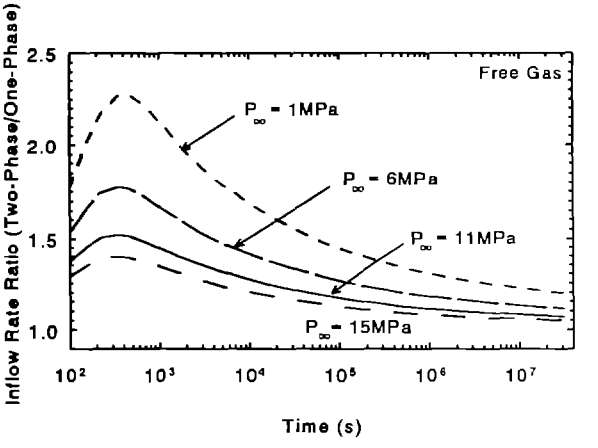

6-C6

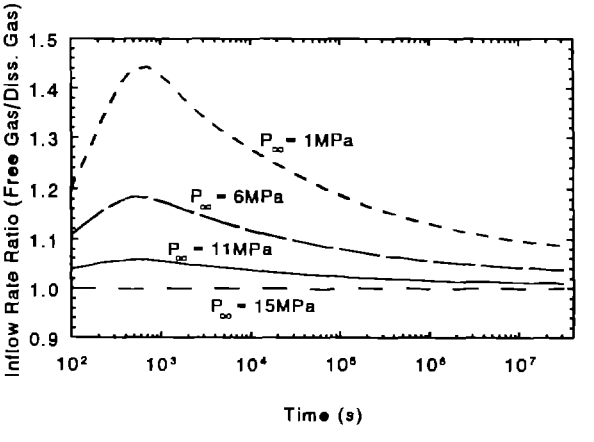

6-C7

Figure 6-C. Results from variation in pore pressure for two-phase brine inflow (continued).

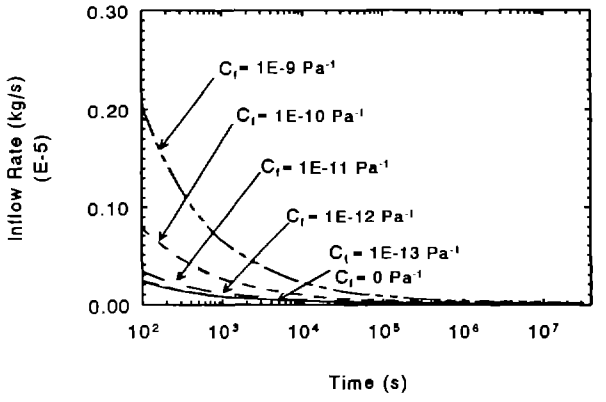

6-D1

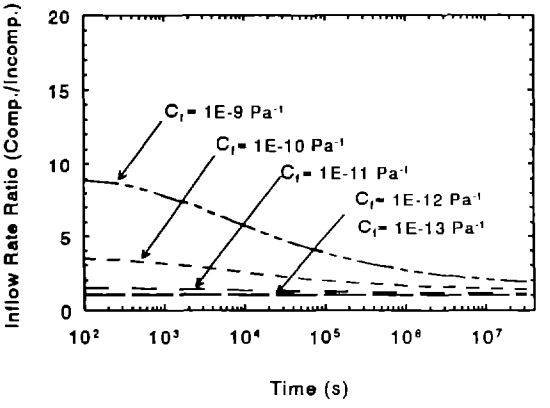

6-D2

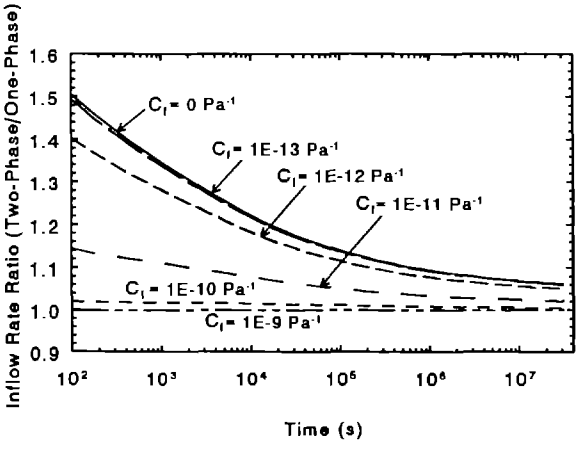

6-D3

Figure 6-D. Results from variation in formation compressibility for two-phase brine inflow.

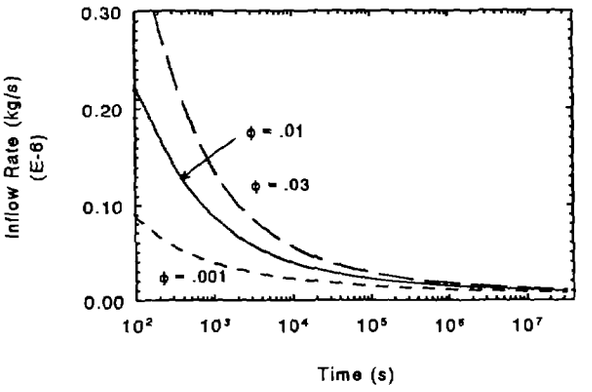

6-E1

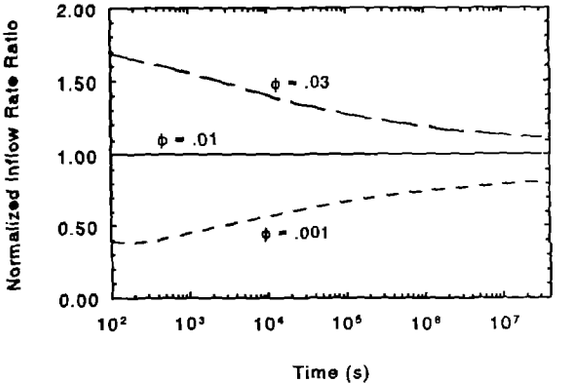

6-E2

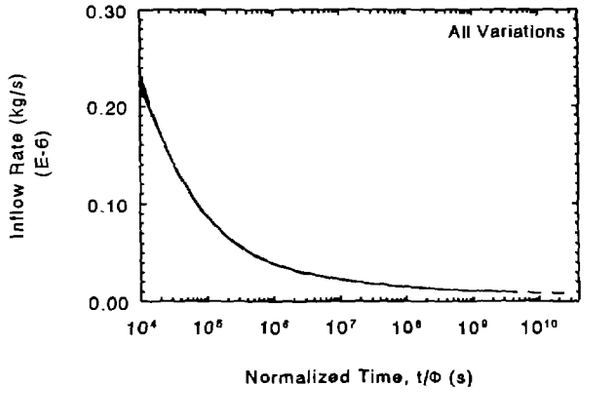

6-E3

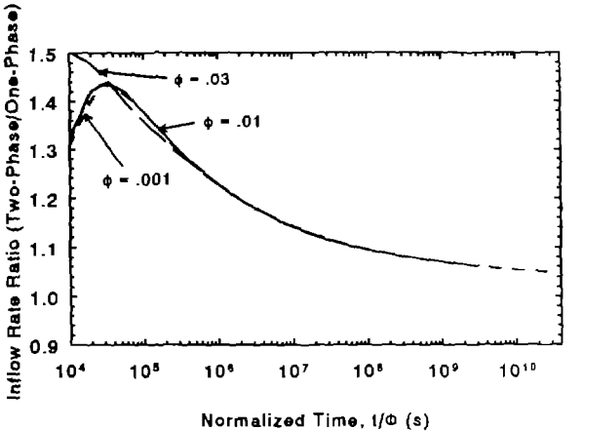

6-E4

Figure 6-E. Results from variation in porosity for two-phase brine inflow.

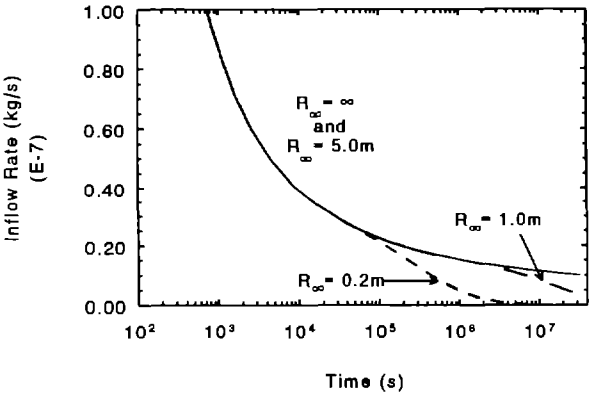

6-F1

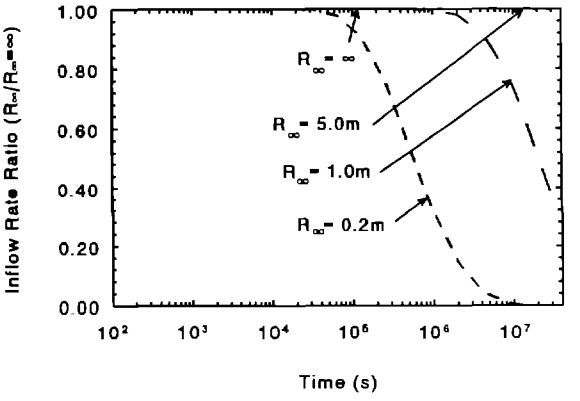

6-F2

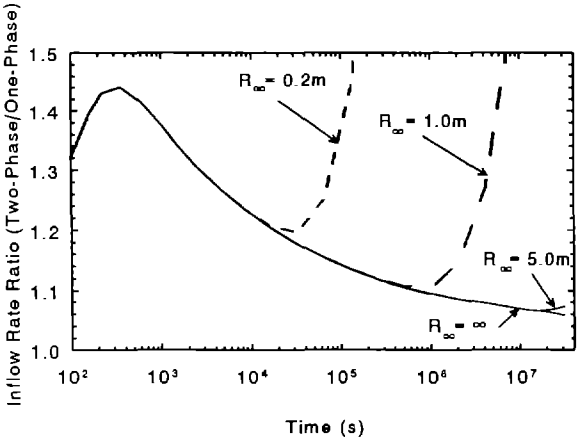

6-F3

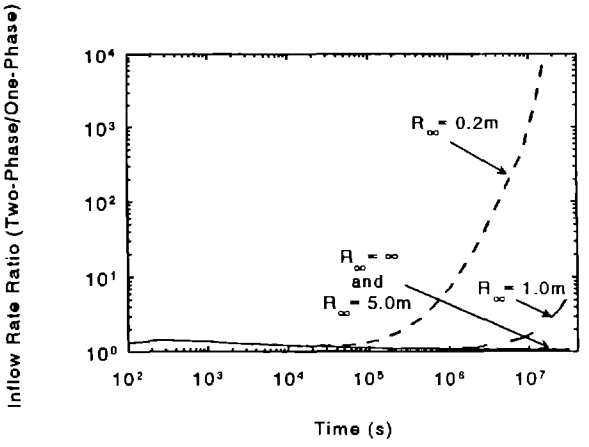

6-F4

Figure 6-F. Results from variation in source radius for two-phase brine inflow.

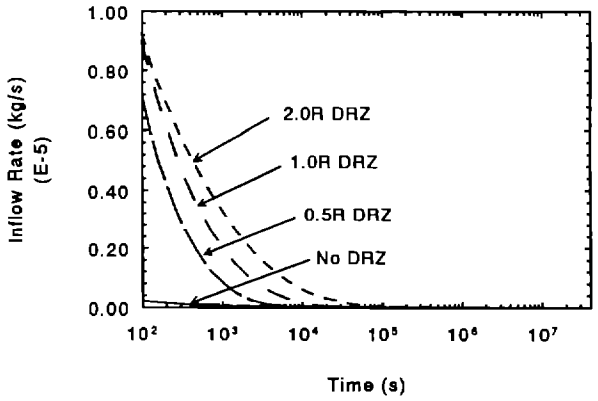

6-G1

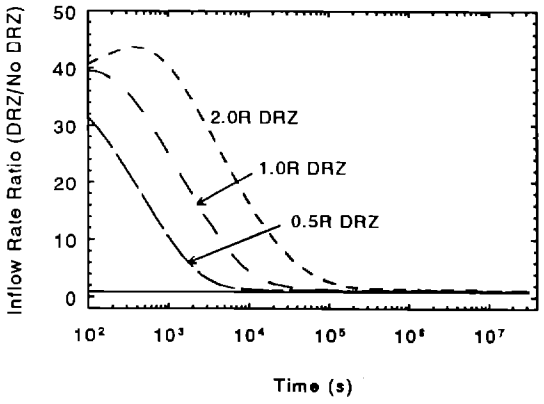

6-G2

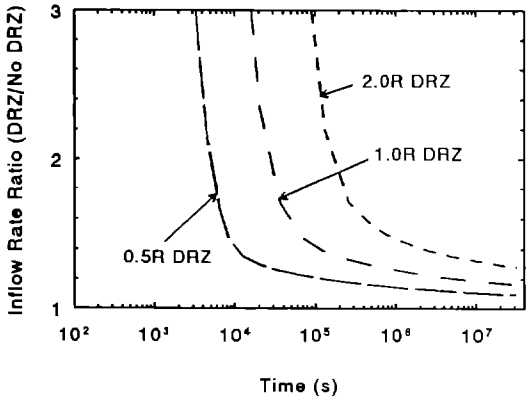

6-G3

Figure 6-G. Results from variation in DRZ distance for two-phase brine inflow.

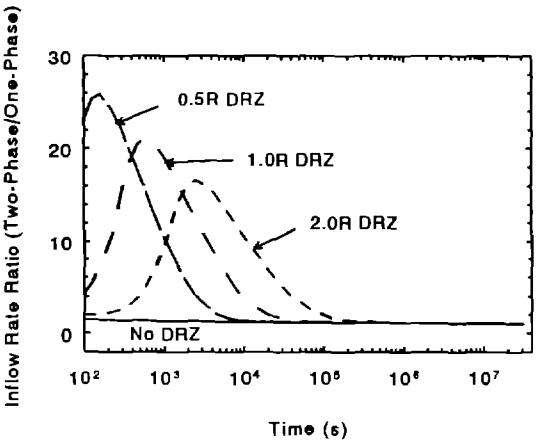

6-G4

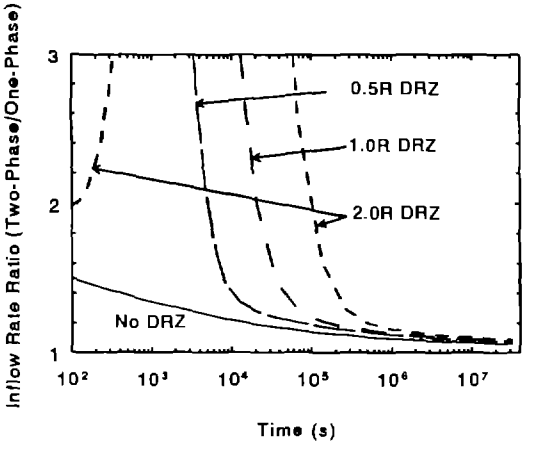

6-G5

Figure 6-G. Results from variation in DRZ distance for two-phase brine inflow (continued).

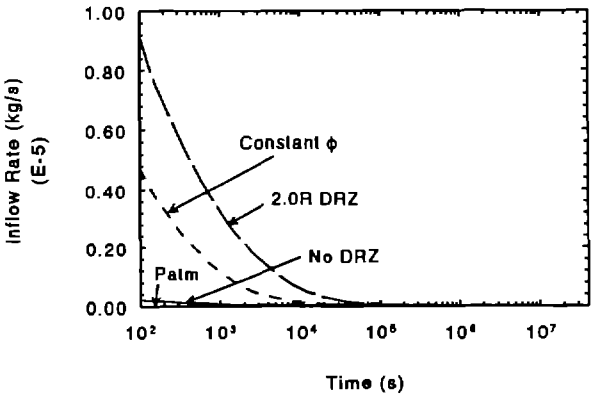

6-H1

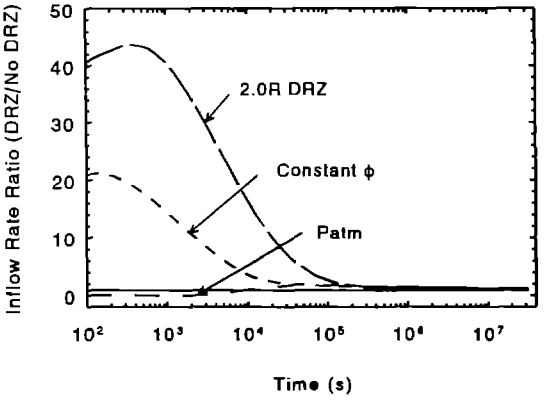

6-H2

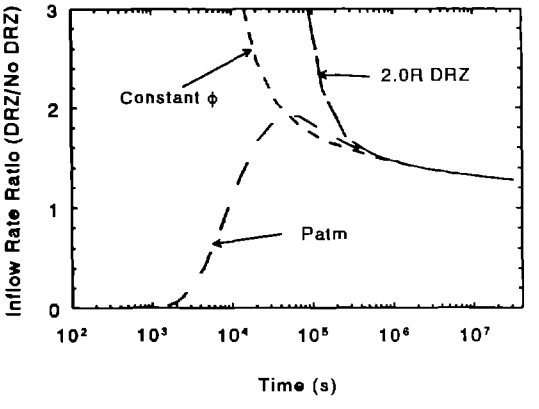

6-H3

Figure 6-H. Results from variation in DRZ porosity and pressure for two-phase brine inflow.

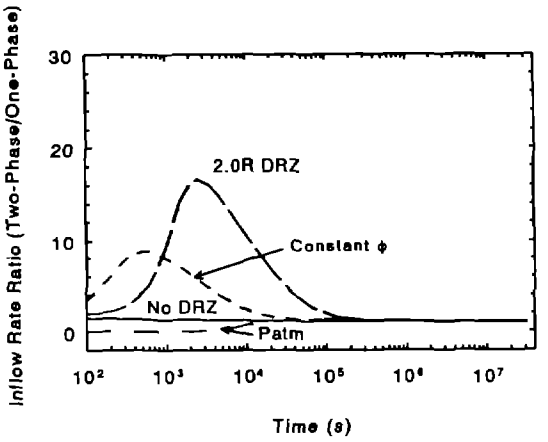

6-H4

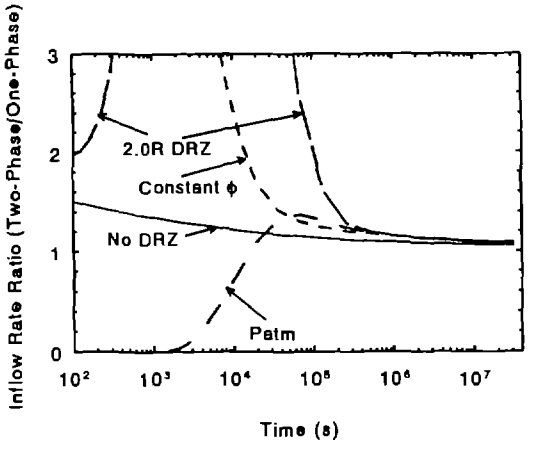

6-H5

Figure 6-H. Results from variation in DRZ porosity and pressure for two-phase brine inflow (continued).

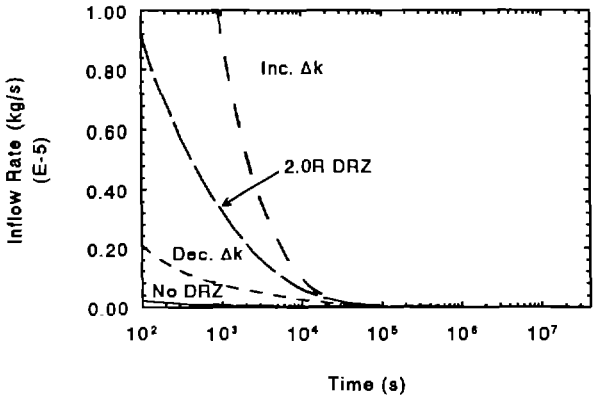

6-I1

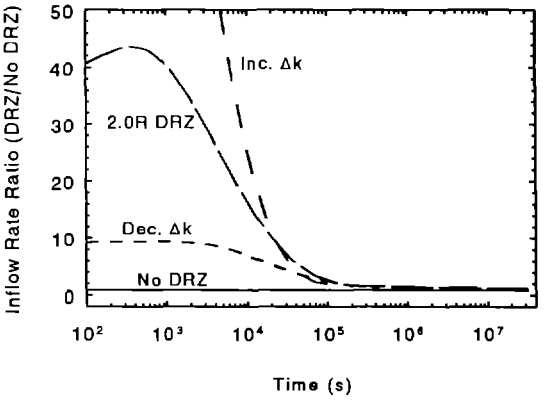

6-I2

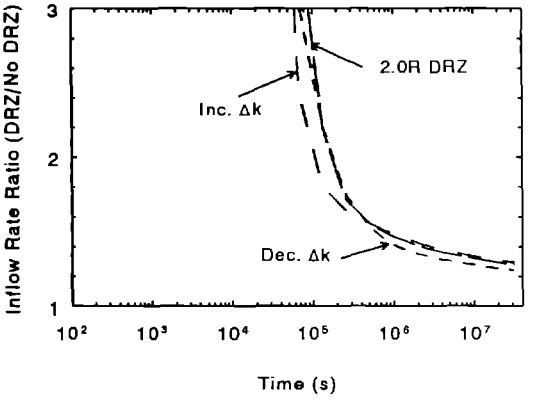

6-I3

Figure 6-I. Results from variation in DRZ permeability contrast for two-phase brine inflow.

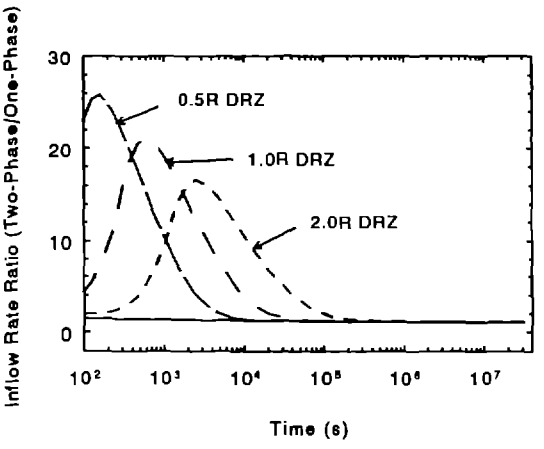

6-I4

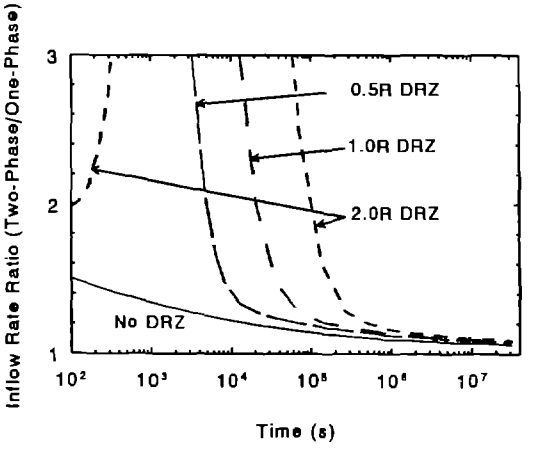

6-I5

Figure 6-I. Results from variation in DRZ permeability contrast for two-phase brine inflow (continued).

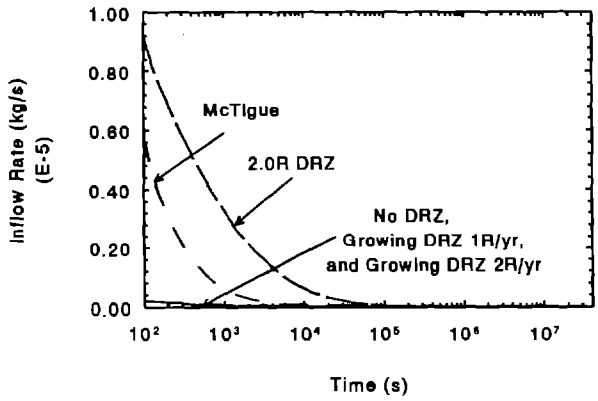

6-J1

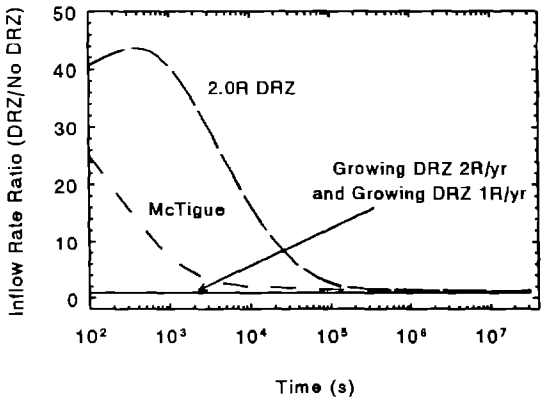

6-J2

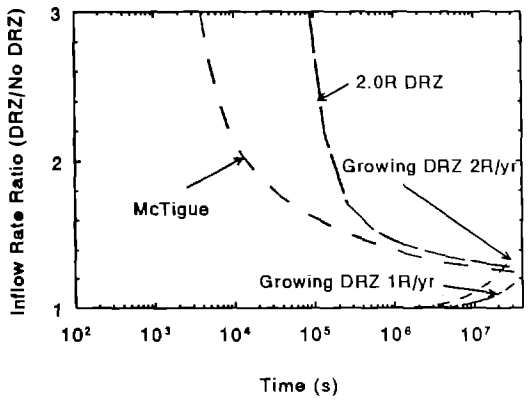

6-J3

Figure 6-J. Results from variation in DRZ permeability distribution for two-phase brine inflow.

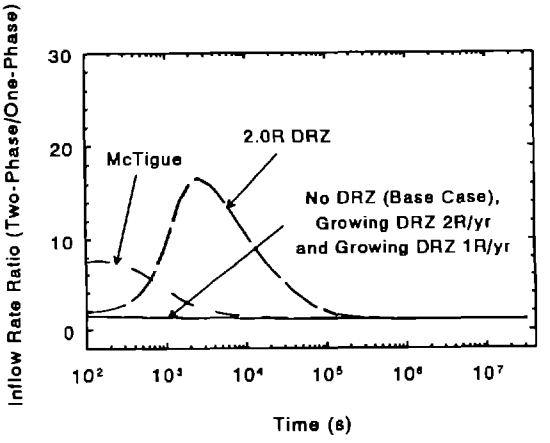

6-J4

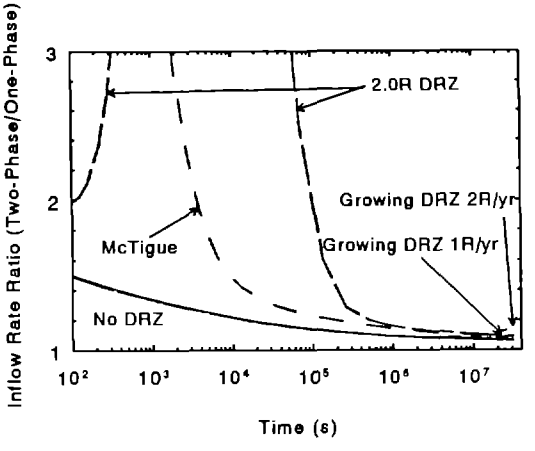

6-J5

Figure 6-J. Results from variation in DRZ permeability distribution for two-phase brine inflow (continued).

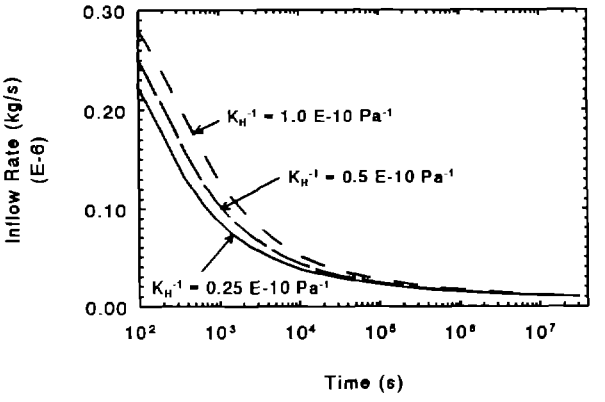

6-K1

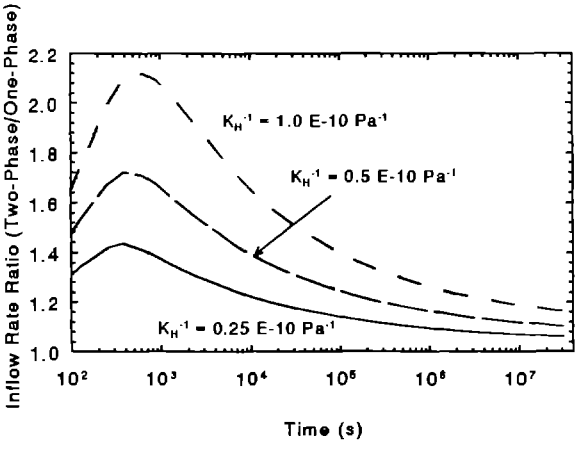

6-K2

Figure 6-K. Results from variation in gas solubility for two-phase brine inflow.

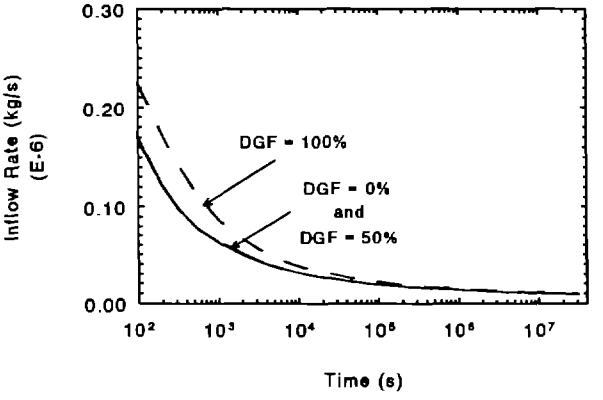

6-L1

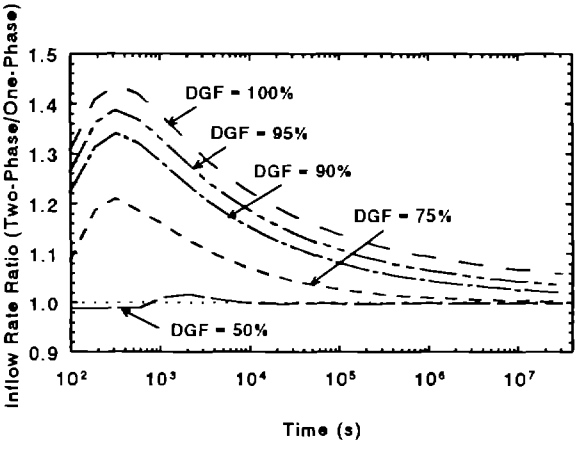

6-L2

Figure 6-L. Results from variation in initial dissolved gas fraction for two-phase brine inflow.

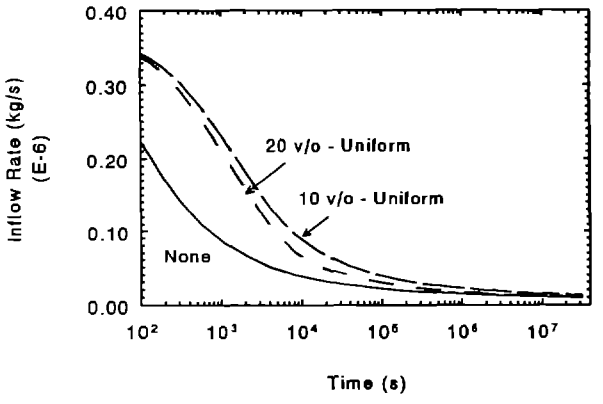

6-M1

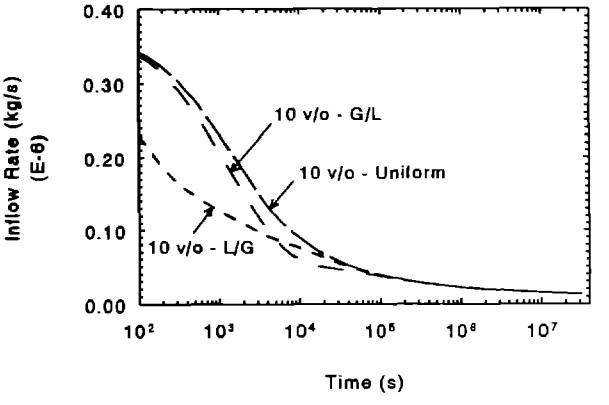

6-M2

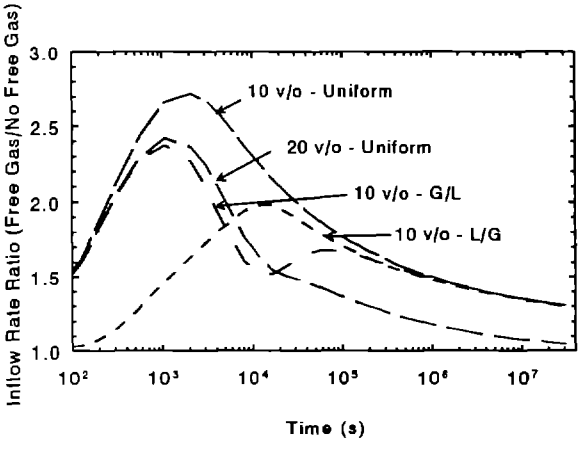

6-M3

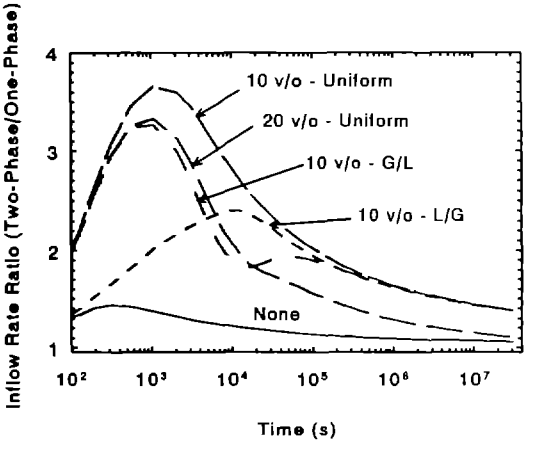

6-M4

Figure 6-M. Results from variation in free gas fraction for two-phase brine inflow.

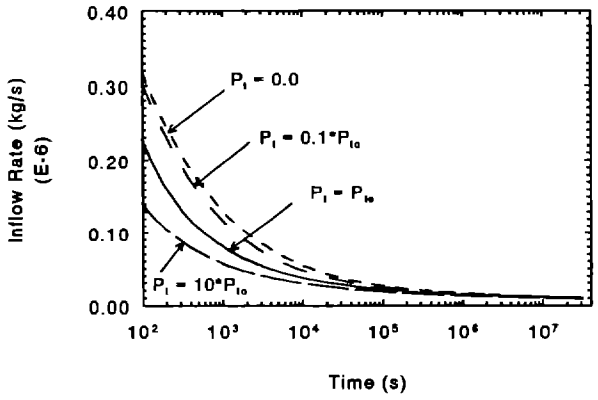

6-N1

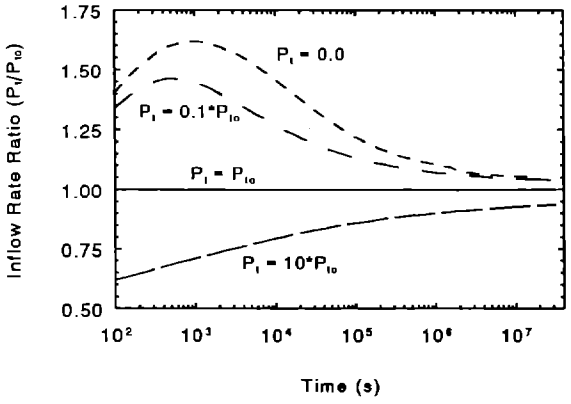

6-N2

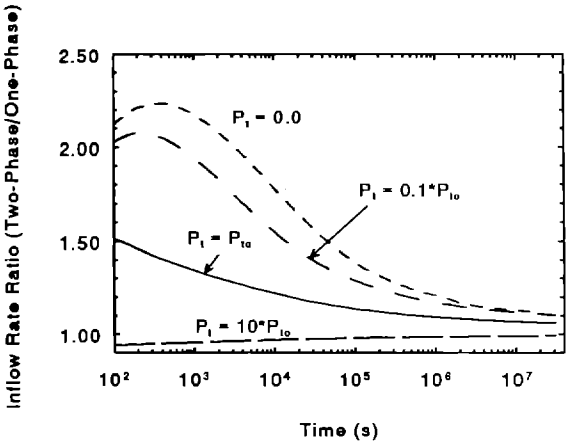

6-N3

Figure 6-N. Results from variation in capillary pressure magnitude for two-phase brine inflow.

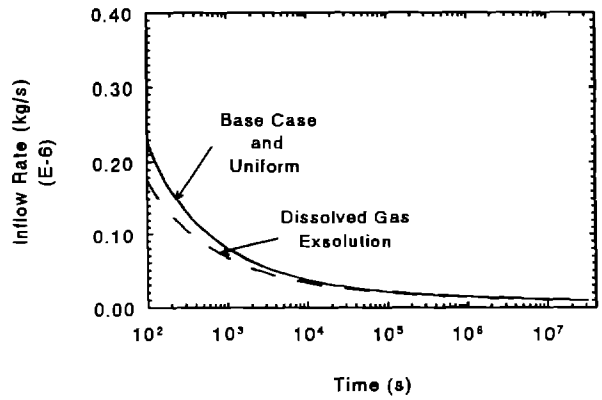

6-01

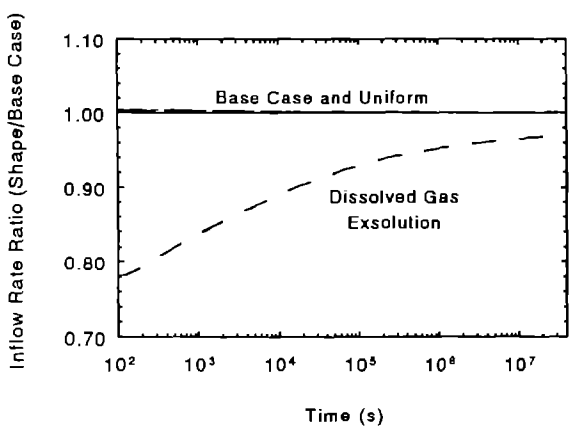

6-02

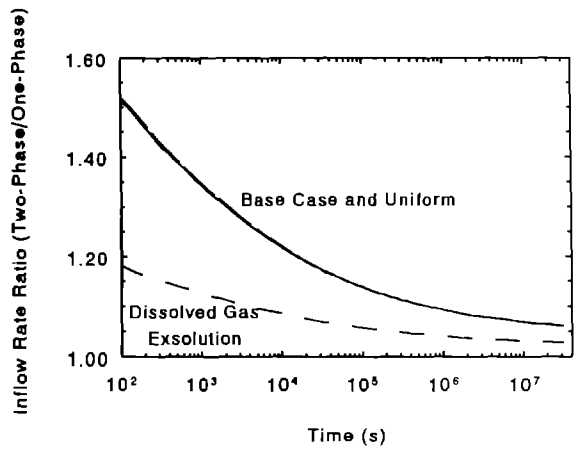

6-03

Figure 6-0. Results from variation in capillary pressure shape for two-phase brine inflow.

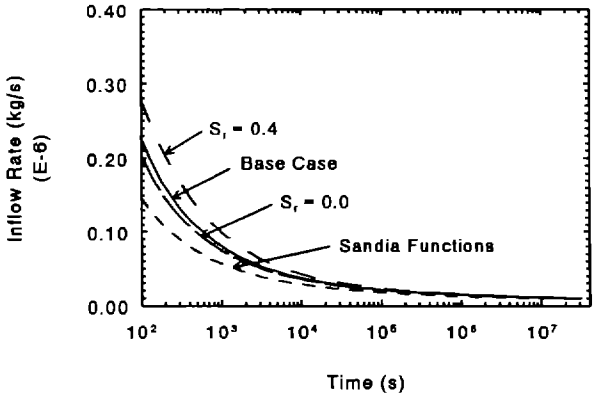

6-P1

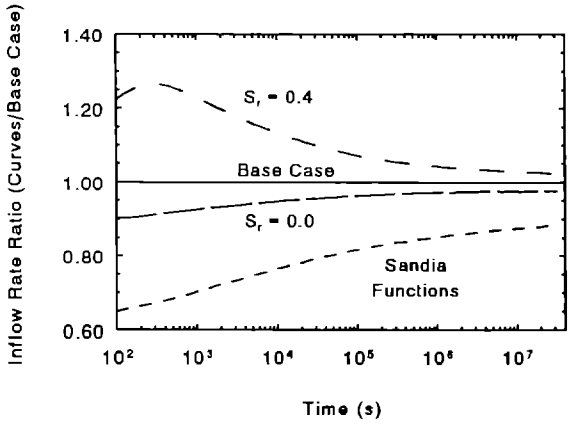

6-P2

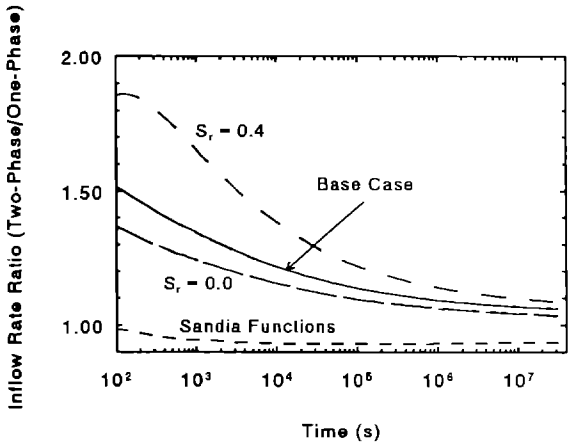

6-P3

Figure 6-P. Results from variation in two-phase characteristic curves for two-phase brine inflow.

Two-Phase Inferred Parameters

The straight-line fits to the inverse of the two-phase brine inflow are shown in this section. Figures 7-A to 7-E present the results for variations in the borehole radius, permeability, pore pressure (dissolved gas and free gas), formation compressibility, and porosity. The results for all these cases are essentially the same as for single-phase flow. The straight-line fits work well for these two-phase cases, even though the fit is only strictly applicable to single-phase conditions. The time of applicability of the straight-line fit is essentially the same as for single-phase conditions. Quantitative information on the inferred formation parameters will be presented later in this section.

Figure 7-F presents the results for the limited brine source. Although the results for an infinite source and a 5.0-m brine source are about the same as for single-phase flow, the smaller source radii of 1.0 and 0.2 m are somewhat different. As can be seen in Figure 7-F3, the fit to the two-phase data for the 1.0-m source radius looks reasonable. It is based on 4 points and has an R^2 of 0.97 (the single-phase fit was for 3 points with an R^2 of 0.92). Even though only a small number of points are involved, the time period involved is up to 7 months. For the 0.2-m radius as shown in Figure 7-F4, the results are similar to the single-phase case in that the fit is meaningless as it is only based on two points.

Figure 7-G shows the fits for different DRZ distances. The applicability of the fits in the two-phase case are essentially the same as for single-phase flow; however, other behavior is different. In single-phase flow, the inverse brine flux data always approaches the final straight line from above. In contrast, the two-phase data for the 1.0R and 2.0R DRZ cases (Figures 7-G3 and 7-G4), the data goes from above the line to below the line before settling down. If the data were progressively fit as acquired, the fit would be steeper early on and get shallower before finally settling down.

The fits for the initial condition variations of the DRZ are given in Figure 7-H. The cases of initial atmospheric pressure and constant porosity are very similar to the single-phase results. These two variations do not show the behavior noted in Figure 7-G4. Therefore, that different behavior is probably related to the porosity variation in the standard DRZ model specification.

The results of changing the permeability contrast in the DRZ are given in Figures 7-I1 and 7-I2 for increasing and decreasing contrast, respectively. The "dip" in the plot seems to get more pronounced with a smaller permeability contrast. In addition, as the dip gets larger (decreasing Δk in this case), the applicability of the fit gets later and later. For a

permeability contrast of 1000, the fit applies after 10^5 seconds (1 day), while for a permeability contrast of 10, the time period is after about 10^6 seconds (10 days).

Figure 7-J shows the plots for the McTigue DRZ specification, as well as for the growing DRZ cases. While the fit to the McTigue approach in Figure 7-J1 is good, the time period of applicability is much later than for single-phase flow, increasing from about 10^5 seconds (1 day) to about 10^6 seconds (10 days). No dip is seen for the data. As with single-phase flow, the data for the growing DRZ cases in Figures 7-J2 and 7-J3 could not be fit by the asymptotic approach.

The gas solubility fits are presented in Figure 7-K. The data is well behaved and is easily fit by the straight-line approach. The initial applicability of the fit increases for the higher gas solubility (higher K_H^{-1}). The time in Figure 7-K1 for the lowest solubility is about 10^5 seconds (1 day) compared to about 5×10^5 seconds (5 days) for the higher solubility case in Figure 7-K2.

Figures 7-L1 and 7-L2 present the dissolved gas fraction results for 50 and 100% dissolved gas fractions, respectively; the 0% dissolved gas fraction is simply single-phase conditions. The fits for the 50 and 100% dissolved gas cases are similar and represent the data quite well.

Free gas variations are fit by the straight-line asymptotic approach in Figure 7-M. For uniform free gas (10 and 20 v/o), the fits in Figures 7-M1 and 7-M2 are applicable after about 10^5 seconds (1 day), and the data show no peculiar behavior. For 10 v/o nonuniform gas distributions, the G/L case (free gas pocket right next to the borehole) in Figure 7-M3 has a kink in the data, while the L/G case (free gas pocket 1 node back from the borehole) in Figure 7-M4 shows no such behavior.

Figure 7-N shows the capillary pressure magnitude variations for the two-phase characteristics case. The results for zero capillary pressure and 10 times the nominal capillary pressure are given in Figures 7-N1 and 7-N2. No significant difference in the fits for the two capillary pressure cases is noted. The fits for the capillary pressure shape are presented in Figure 7-O1 and 7-O2. Again, straight-line behavior is seen in both cases of uniform and dissolved gas exsolution shapes. Figure 7-P gives the results for the variation in the residual saturations (Figures 7-P1 and 7-P2) and in the shape of the characteristic curves (Figure 7-P3). As with the other variations, the data behavior is consistent with the asymptotic approach. Changes in the two-phase parameters are not reflected in these plots.

Table 6 summarizes the quantitative information on the straight-line fits as to their prediction of the formation parameters. In those cases where there was a single-phase analogue, single-phase results were obtained using the two-phase model for reference purposes.

From Table 6, the formation permeability is seen to be well predicted (within about 10%) except in the case of a limited brine source and for the growing DRZ cases where no fit was generated; these results are consistent with those for single-phase conditions. Even for the case of free gas, the formation permeability is well predicted using the single-phase approach at 20 v/o. However, note that in the case of 50 v/o free gas, no fit was obtained because the net brine inflow rate was zero. Also note that 20 v/o is the default residual gas saturation. Therefore, this conclusion may only be appropriate if the gas is immobile.

For the diffusivity, the same general comments apply as for single-phase fits. In general, the two-phase inferred values are about a factor of 2 lower than their single-phase counterparts. Prediction of the permeability is much more reliable than prediction of the diffusivity. The diffusivity for the free gas cases are considerably in error by about an order of magnitude. In this situation, the inferred diffusivity values are unreliable. Prediction of diffusivity for the DRZ cases is also poor; however, use of an effective radius considerably improves the predictions as shown in Table 7.

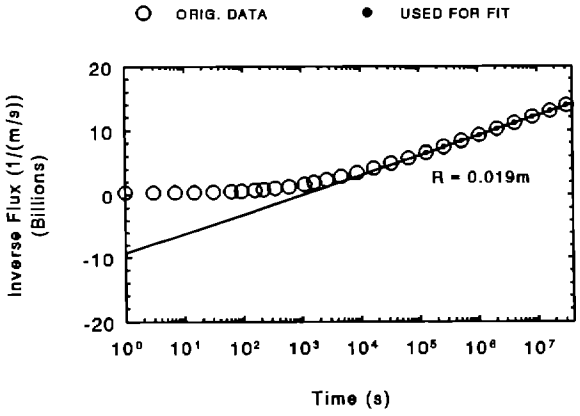

7-A1

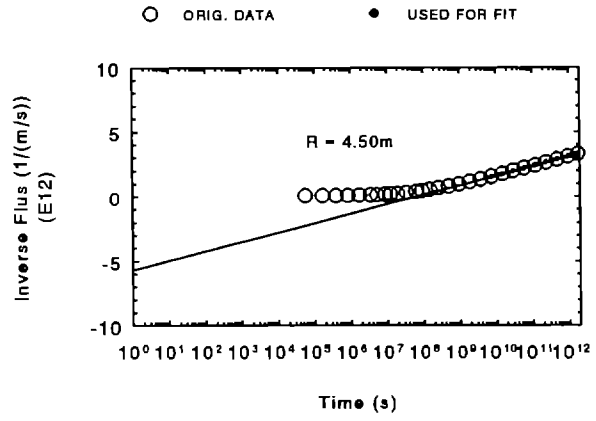

7-A2

Figure 7-A. Results from variation in borehole radius for two-phase gas inflow.

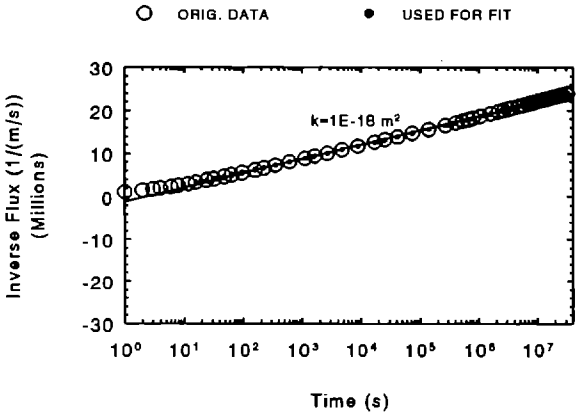

7-B1

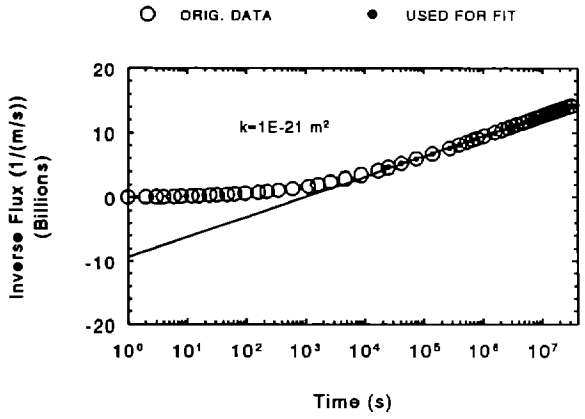

7-B2

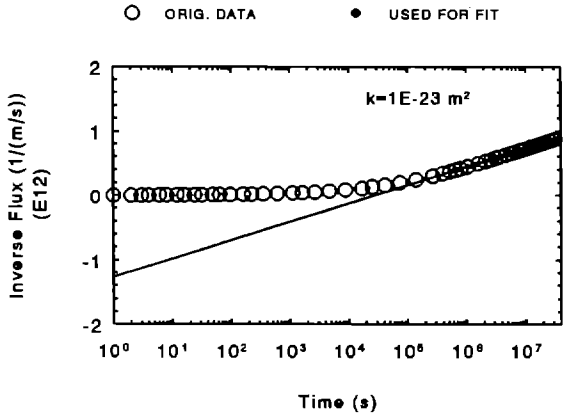

7-B3

Figure 7-B. Results from variation in permeability for two-phase gas inflow.

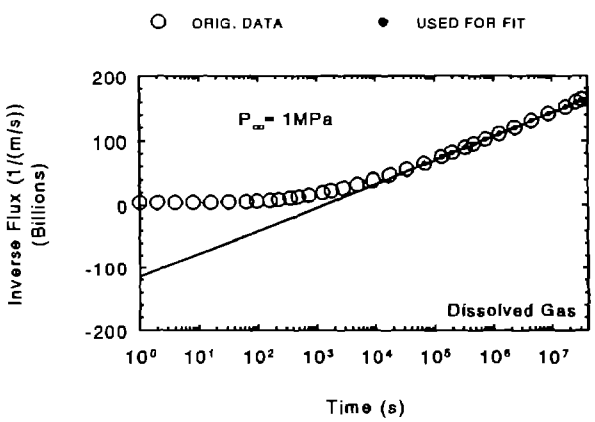

7-C1

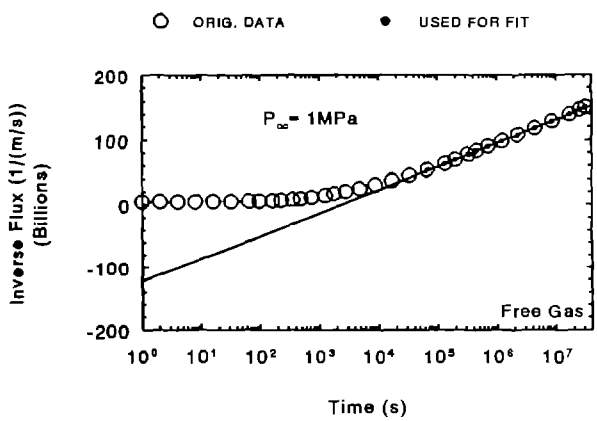

7-C2

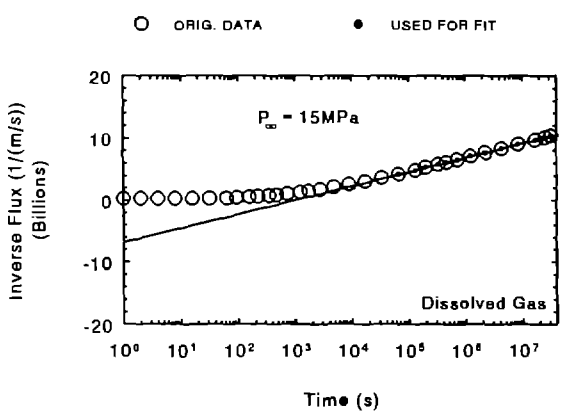

7-C3

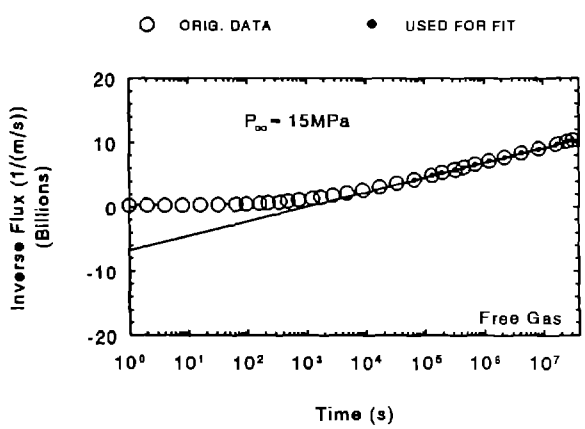

7-C4

Figure 7-C. Results from variation in pore pressure for two-phase gas inflow.

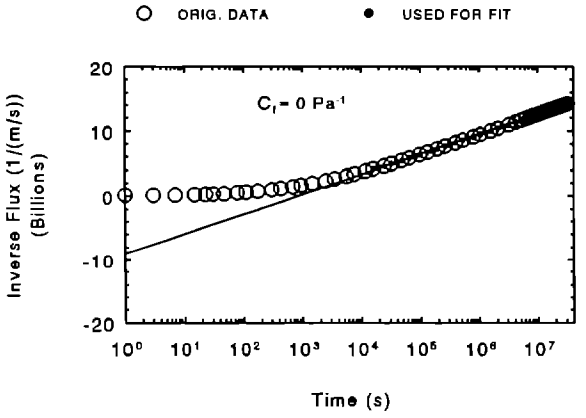

7-D1

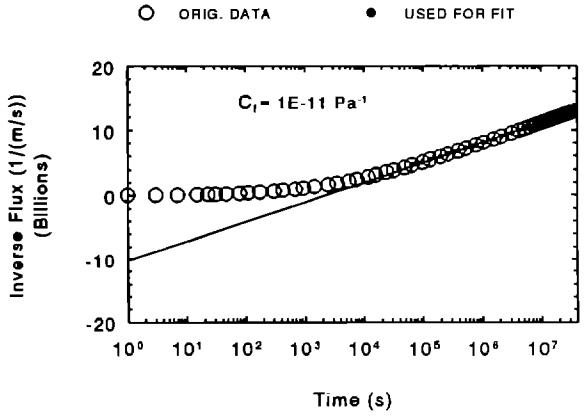

7-D2

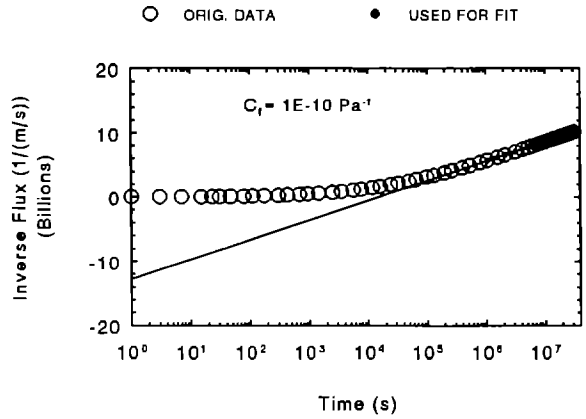

7-D3

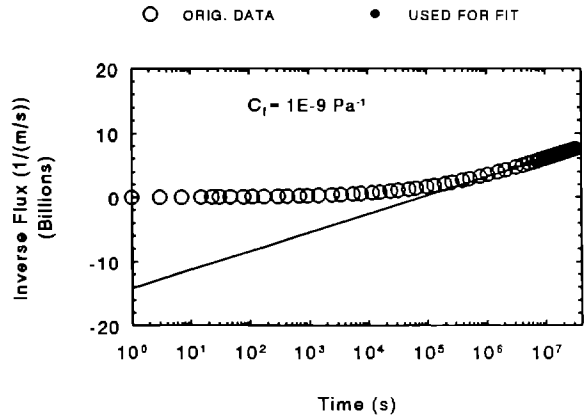

7-D4

Figure 7-D. Results from variation in formation compressibility for two-phase inverse brine flux.

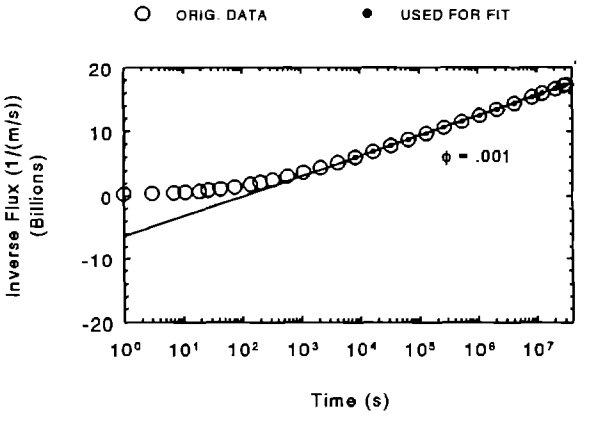

7-E1

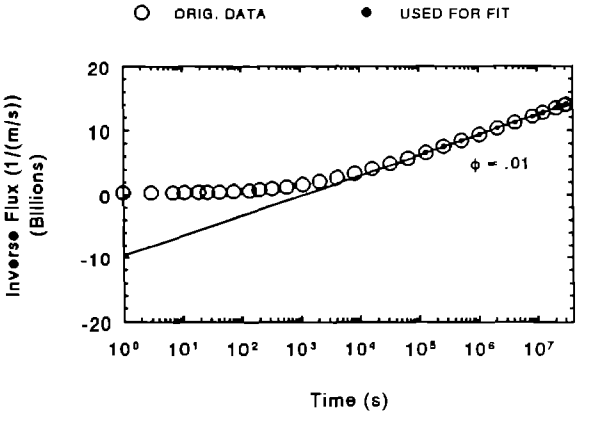

7-E2

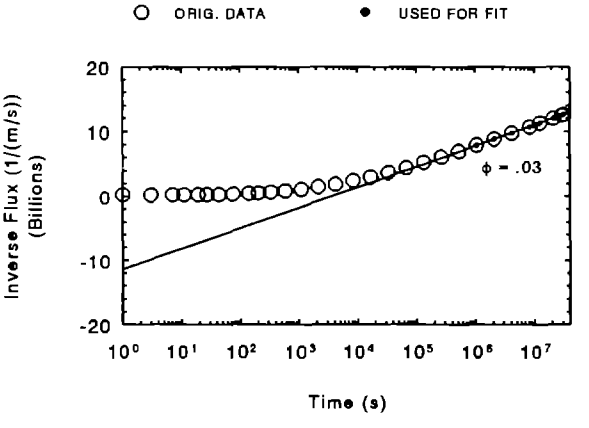

7-E3

Figure 7-E. Results from variation in porosity for two-phase gas inflow.

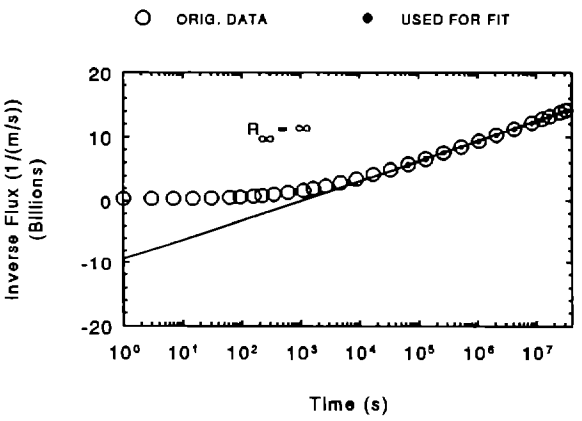

7-F1

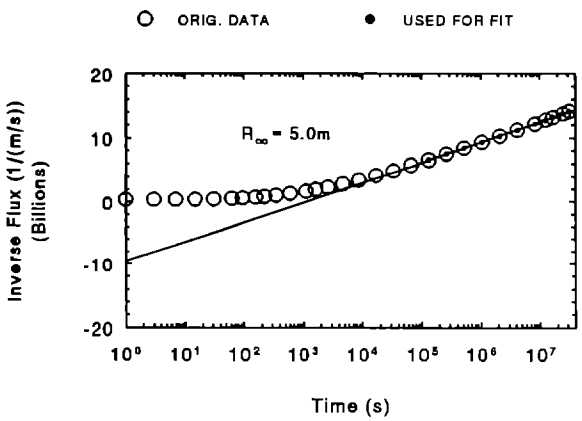

7-F2

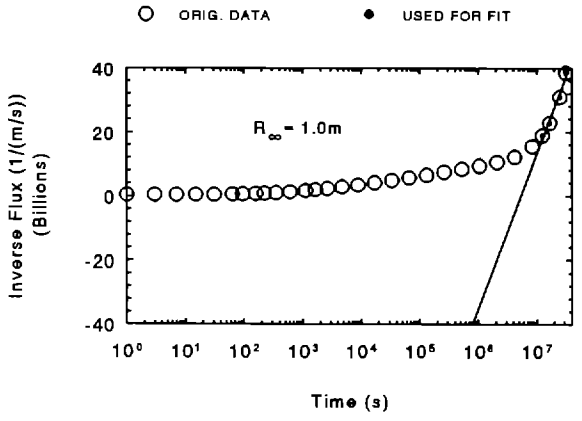

7-F3

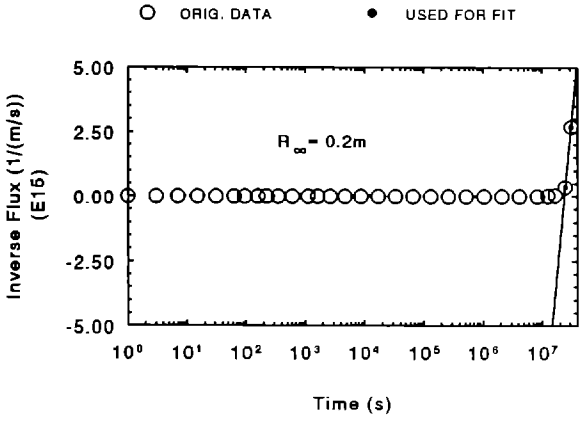

7-F4

Figure 7-F. Results from variation in source radius for two-phase gas inflow.

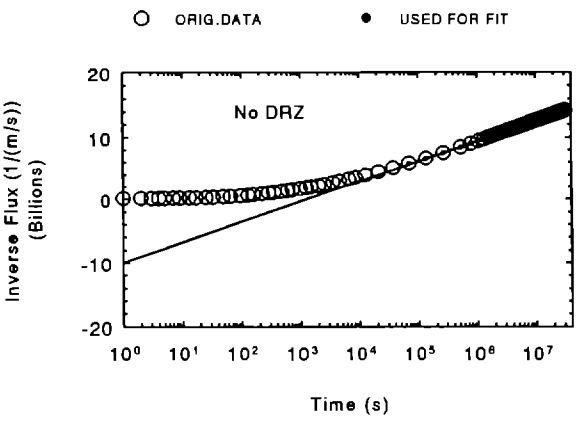

7-G1

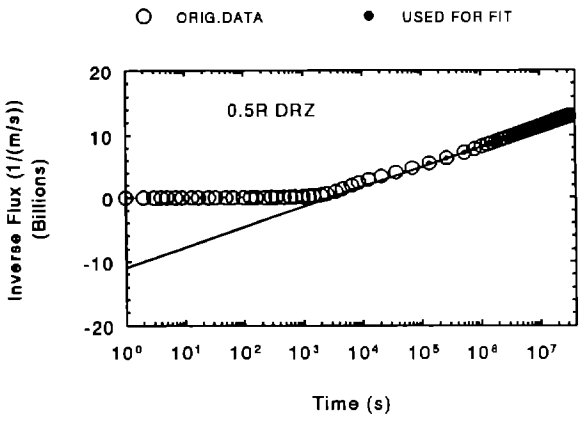

7-G2

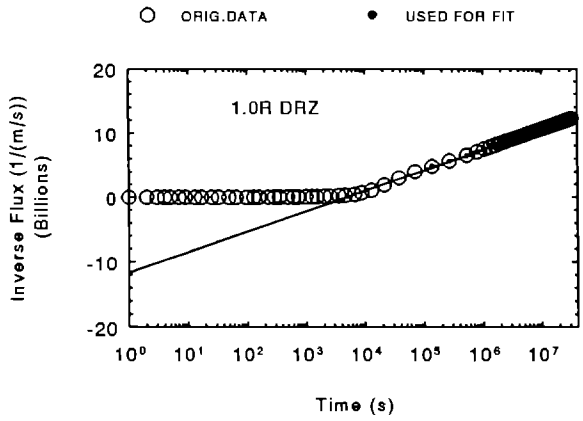

7-G3

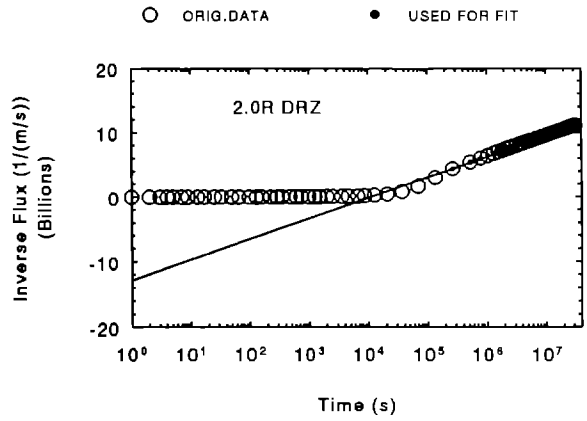

7-G4

Figure 7-G. Results from variation in DRZ distance for two-phase gas inflow.

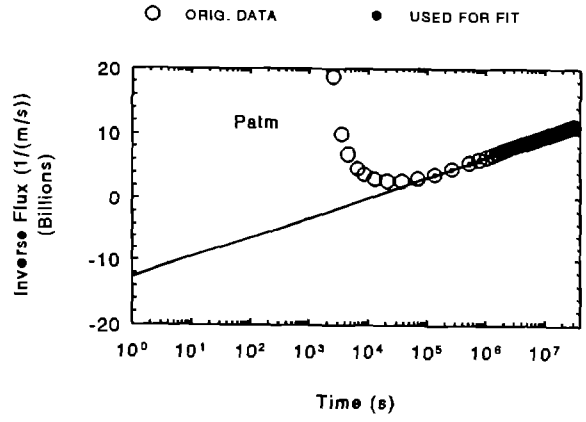

7-H1

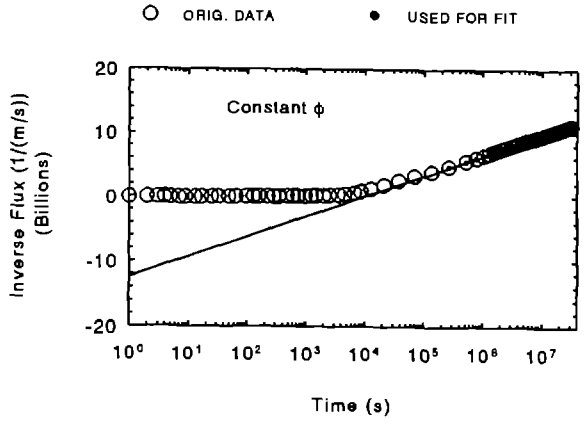

7-H2

Figure 7-H. Results from variation in DRZ porosity and pressure for two-phase inverse brine flux.

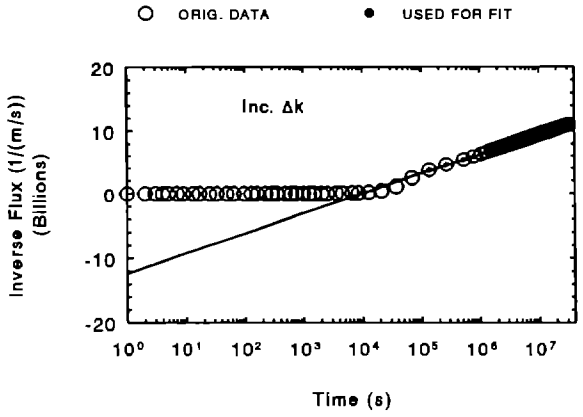

7-I1

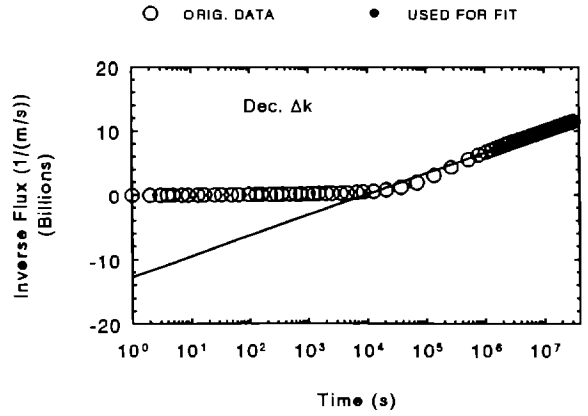

7-I2

Figure 7-I. Results from variation in DRZ permeability contrast for two-phase inverse brine flux.

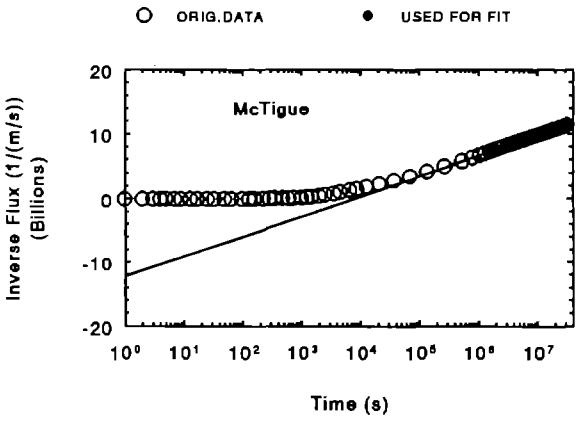

7-J1

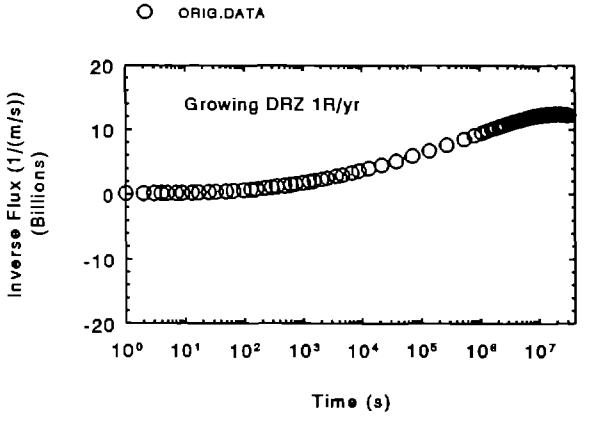

7-J2

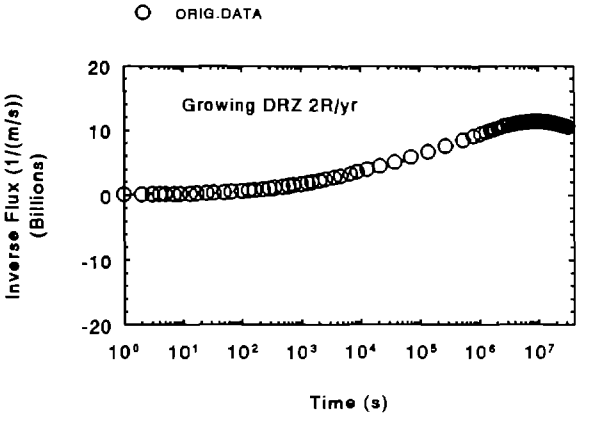

7-J3

Figure 7-J. Results from variation in DRZ permeability distribution for two-phase inverse brine flux.

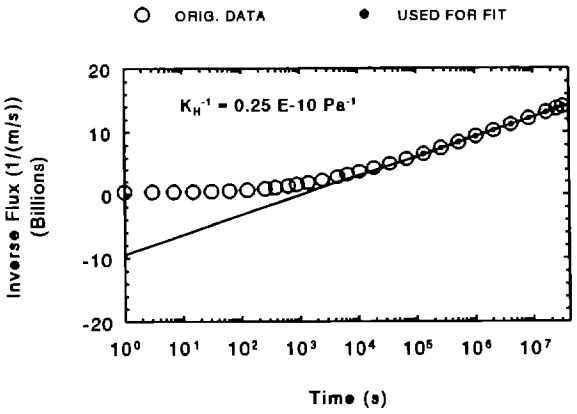

7-K1

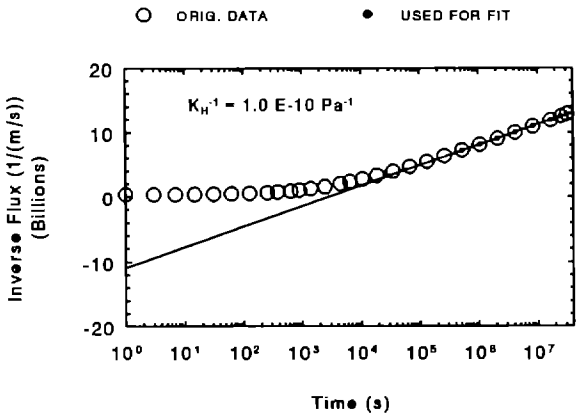

7-K2

Figure 7-K. Results from variation in gas solubility for two-phase gas inflow.

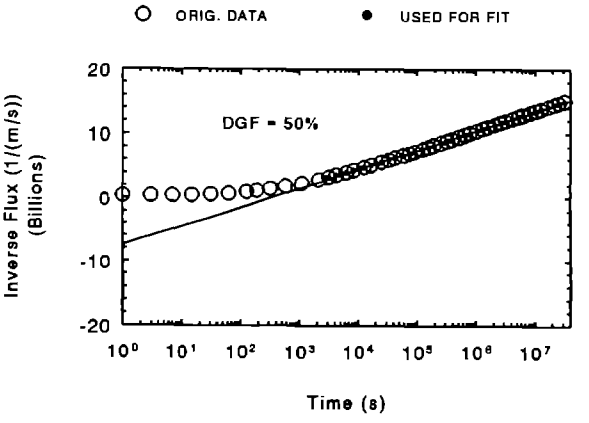

7-L1

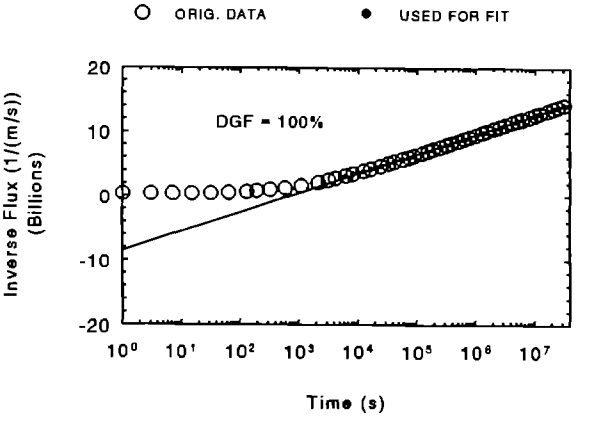

7-L2

Figure 7-L. Results from variation in initial dissolved gas fraction for two-phase inverse brine flux.

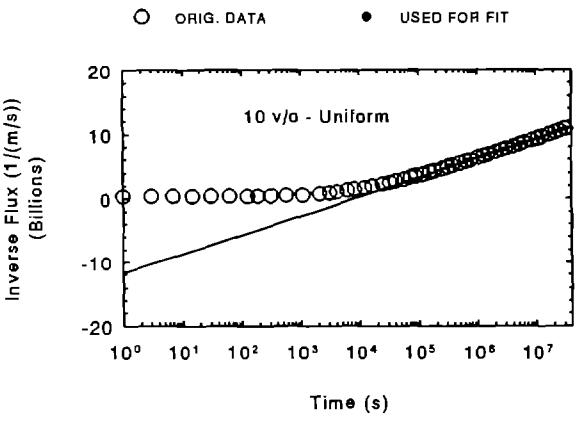

7-M1

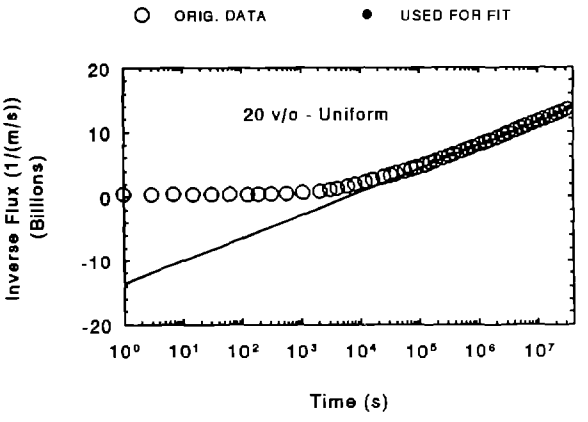

7-M2

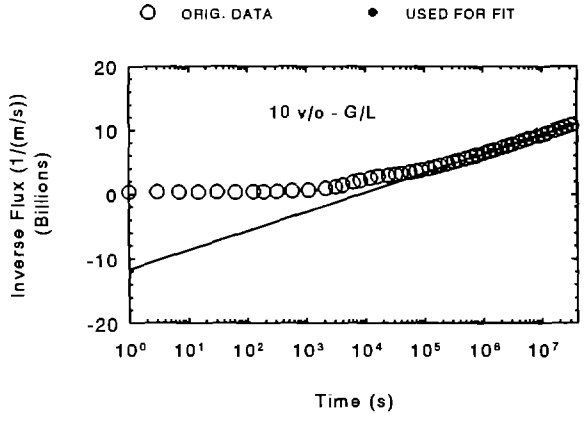

7-M3

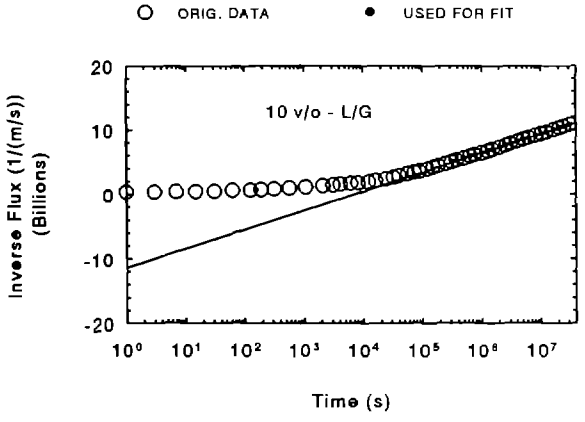

7-M4

Figure 7-M. Results from variation in free gas fraction for two-phase gas inflow.

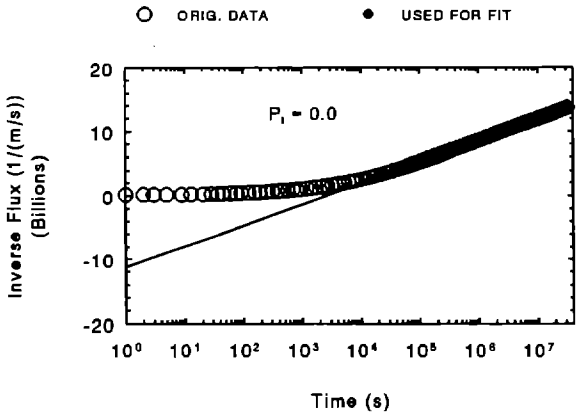

7-N1

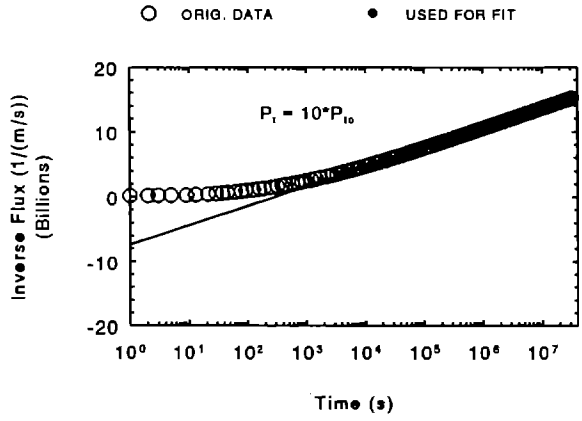

7-N2

Figure 7-N. Results from variation in capillary pressure magnitude for two-phase inverse brine flux.

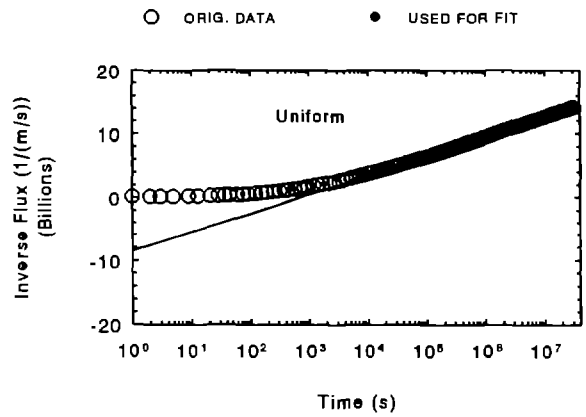

7-01

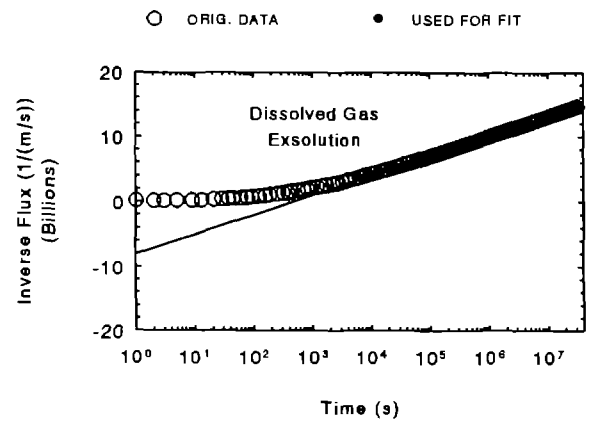

7-02

Figure 7-0. Results from variation in capillary pressure shape for two-phase inverse brine flux.

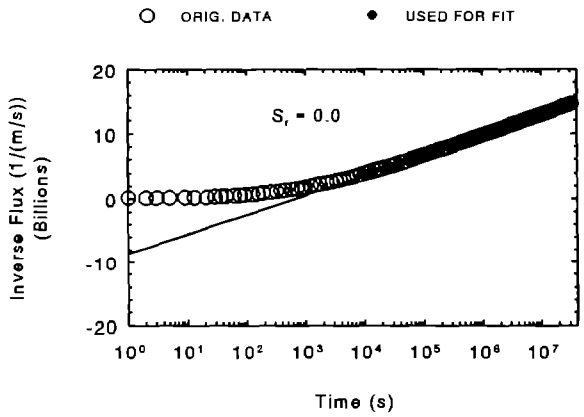

7-P1

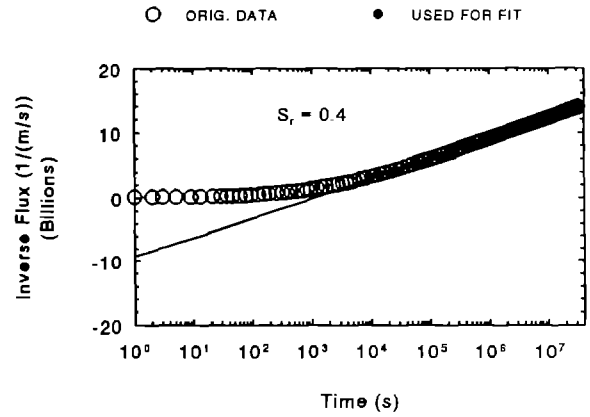

7-P2

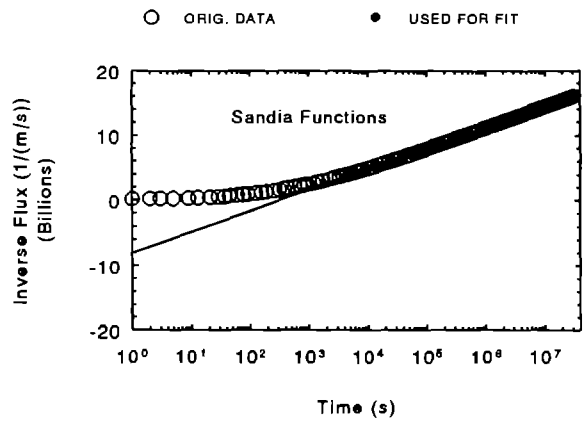

7-P3

Figure 7-P. Results from variation in two-phase characteristic curves for two-phase inverse brine flux.

Table 6. Two-Phase Inferred Parameters

Permeability (m^2)		
Actual	Inferred	Error
1.0×10^{-21} (except as noted)		
Borehole Radius		
R=all	1.03×10^{-21}	+3%
Permeability		
10^{-18} m^2	0.96×10^{-18}	-4%
10^{-21} m^2	1.02×10^{-21}	+2%
10^{-23} m^2	1.12×10^{-23}	+12%
Pore Pressure (dissolved gas)		
1 MPa	0.95×10^{-21}	-5%
15 MPa	1.03×10^{-21}	+3%
Pore Pressure (free gas)		
1 MPa	0.97×10^{-21}	-3%
15 MPa	1.03×10^{-21}	+3%
Formation Compressibility		
0 Pa^{-1}	1.03×10^{-21}	+3%
10^{-13} Pa^{-1}	1.03×10^{-21}	+3%
10^{-12} Pa^{-1}	1.02×10^{-21}	+2%
10^{-11} Pa^{-1}	1.04×10^{-21}	+4%
10^{-10} Pa^{-1}	1.04×10^{-21}	+4%
10^{-9} Pa^{-1}	1.10×10^{-21}	+10%
Porosity		
0.001	1.00×10^{-21}	<0.5%
0.01	1.00×10^{-21}	<0.5%
0.03	0.99×10^{-21}	-1%
Brine Source		
Infinity	1.02×10^{-21}	+2%
5.0 m	1.01×10^{-21}	+1%
1.0 m	6.6×10^{-23}	-93%
0.2 m	1.4×10^{-28}	-100%
DRZ Characteristics		
No DRZ	0.99×10^{-21}	-1%
0.5R DRZ	1.00×10^{-21}	<-0.5%
1.0R DRZ	1.00×10^{-21}	<+0.5%
2.0R DRZ	1.00×10^{-21}	<-0.5%
Patm	1.01×10^{-21}	+1%
Constant ϕ	1.02×10^{-21}	+2%
McTigue	1.02×10^{-21}	+2%
Inc. Δk	1.03×10^{-21}	+3%
Dec. Δk	0.99×10^{-21}	-1%
Growing DRZ - 1R/yr	No Fit	No Fit
Growing DRZ - 2R/yr	No Fit	No Fit

Table 6. Two-Phase Inferred Parameters (Continued)

Gas Solubility		
single-phase	1.02×10^{-21}	+2%
K_H^l = 0.25E-10 Pa^{-1}	1.02×10^{-21}	+2%
= 0.50E-10 Pa^{-1}	1.01×10^{-21}	+1%
= 1.00E-10 Pa^{-1}	1.01×10^{-21}	+1%
Dissolved Gas		
single-phase	1.05×10^{-21}	+5%
DGF = 50%	1.05×10^{-21}	+5%
= 75%	1.03×10^{-21}	+3%
= 90%	1.01×10^{-21}	+1%
= 95%	1.02×10^{-21}	+2%
= 100%	1.04×10^{-21}	+4%
Free Gas		
free gas fraction		
None	1.04×10^{-21}	+4%
10 v/o - uniform	1.06×10^{-21}	+6%
10 v/o - G/L	1.07×10^{-21}	+7%
10 v/o - L/G	1.08×10^{-21}	+8%
20 v/o - uniform	0.88×10^{-21}	-12%
50 v/o - uniform	N/A	N/A
Two-Phase Characteristic Curves		
single-phase	1.02×10^{-21}	+2%
two-phase		
Brooks & Corey	1.05×10^{-21}	+5%
$10*P_{to}$	1.07×10^{-21}	+7%
$0.1*P_{to}$	1.02×10^{-21}	+2%
Zero P_t	0.96×10^{-21}	-4%
Uniform P_{cap}	1.05×10^{-21}	+5%
Dissolved Gas Exsolution	1.06×10^{-21}	+6%
$S_r = 0.0$	1.04×10^{-21}	+4%
$S_r = 0.4$	1.04×10^{-21}	+4%
Sandia functions	1.00×10^{-21}	<-.5%

Diffusivity (m^2/sec)

Actual	Inferred	Error
2.1×10^{-7} (except as noted)		
Borehole Radius		
R=all	1.6×10^{-7}	-20%
Permeability		
10^{-18} m^2		
(2.1×10^{-4})	7.6×10^{-5}	-60%
10^{-21} m^2		
(2.1×10^{-7})	1.7×10^{-7}	-20%
10^{-23} m^2		
(2.1×10^{-9})	5.5×10^{-9}	+160%

Table 6. Two-Phase Inferred Parameters (Continued)

Diffusivity (m^2/sec)

Actual	Inferred	Error
Pore Pressure (dissolved gas)		
1 MPa	1.3×10^{-7}	-40%
15 MPa	1.8×10^{-7}	-10%
Pore Pressure (free gas)		
1 MPa	7.0×10^{-8}	-70%
15 MPa	1.8×10^{-7}	-70%
Formation Compressibility		
0 Pa^{-1}		
(2.1×10^{-7})	1.9×10^{-7}	-10%
10^{-13} Pa^{-1}		
(2.0×10^{-7})	1.9×10^{-7}	-5%
10^{-12} Pa^{-1}		
(1.6×10^{-7})	1.5×10^{-7}	-10%
10^{-11} Pa^{-1}		
(4.8×10^{-8})	7.3×10^{-8}	+50%
10^{-10} Pa^{-1}		
(6.1×10^{-9})	1.1×10^{-8}	+80%
10^{-9} Pa^{-1}		
(6.2×10^{-10})	2.0×10^{-9}	+220%
Porosity		
0.001		
(2.1×10^{-6})	1.5×10^{-6}	-30%
0.01		
(2.1×10^{-7})	1.6×10^{-7}	-20%
0.03		
(6.9×10^{-8})	4.7×10^{-8}	-30%
Brine Source		
Infinity	1.6×10^{-7}	-25%
5.0 m	1.4×10^{-7}	-30%
1.0 m	3.0×10^{-11}	-100%
0.2 m	6.6×10^{-12}	-100%
DRZ Characteristics		
No DRZ	1.4×10^{-7}	-30%
0.5R DRZ	6.1×10^{-8}	-70%
1.0R DRZ	3.6×10^{-8}	-80%
2.0R DRZ	1.6×10^{-8}	-90%
Patm	1.7×10^{-8}	-90%
Constant ϕ	1.8×10^{-8}	-90%
McTigue	2.3×10^{-8}	-90%
Inc. Δk	1.8×10^{-8}	-90%
Dec. Δk	1.9×10^{-8}	-90%

Table 6. Two-Phase Inferred Parameters (Continued)

Growing DRZ - 1R/yr	No Fit	No Fit
Growing DRZ - 2R/yr	No Fit	No Fit
Gas Solubility		
single-phase	3.1×10^{-7}	+50%
two-phase		
K_H^{-1} = 0.25E-10 Pa^{-1}	1.5×10^{-7}	-30%
= 0.50E-10 Pa^{-1}	1.0×10^{-7}	-50%
= 1.00E-10 Pa^{-1}	0.6×10^{-7}	-70%
Dissolved Gas Fraction		
single-phase	4.4×10^{-7}	+110%
two-phase		
DGF = 50%	4.4×10^{-7}	+110%
= 75%	3.3×10^{-7}	+60%
= 90%	2.3×10^{-7}	+10%
= 95%	2.1×10^{-7}	+0%
= 100%	2.0×10^{-7}	-5%
Free Gas		
free gas fraction		
None	2.0×10^{-7}	-5%
10 v/o - uniform	2.0×10^{-8}	-90%
10 v/o - G/L	2.1×10^{-8}	-90%
10 v/o - L/G	2.4×10^{-8}	-90%
20 v/o - uniform	2.8×10^{-8}	-90%
50 v/o - uniform	N/A	N/A
Two-Phase Characteristic Curves		
single-phase	3.1×10^{-7}	+50%
two-phase		
Brooks & Corey	2.4×10^{-7}	+10%
$10*P_{to}$	5.9×10^{-7}	+180%
$0.1*P_{to}$	1.1×10^{-7}	-50%
Zero P_t	6.6×10^{-8}	-70%
Uniform P_{cap}	2.4×10^{-7}	+10%
Dissolved Gas Exsolution	3.7×10^{-7}	+70%
$S_r = 0.0$	4.8×10^{-7}	+130%
$S_r = 0.4$	2.8×10^{-7}	+30%
Sandia functions	9.3×10^{-7}	+340%

Table 7. Inferred Two-Phase Diffusivity Using Effective Radius

Diffusivity (m^2/sec)		
Actual	Inferred	Error
2.1×10^{-7}		
Borehole Radius		
R=all	1.6×10^{-7}	-20%
No DRZ	1.4×10^{-7}	-30%
0.5R DRZ	1.4×10^{-7}	-40%
1.0R DRZ	1.4×10^{-7}	-30%
2.0R DRZ	1.4×10^{-7}	-30%
Patm	1.5×10^{-7}	-30%
Constant ϕ	1.7×10^{-7}	-20%
McTigue	2.1×10^{-7}	-1%
Inc. Δk	1.6×10^{-7}	-20%
Dec. Δk	1.7×10^{-7}	-20%
Growing DRZ - 1R/yr	No Fit	No Fit
Growing DRZ - 2R/yr	No Fit	No Fit

Two-Phase Gas Inflow

Gas inflow rates for the two-phase cases are presented in this section. In addition, the inflowing gas saturation (ratio of gas volume flowing in to total volume flowing in) at the borehole condition of 0.1 MPa is given.

The gas inflow rate for the case of varying the borehole radius is given in Figure 8-A1. Note that the gas mass inflow scale is three orders of magnitude less than the corresponding brine mass inflow scale. Thus, the gas mass inflow rate is insignificant compared to the brine mass inflow rate. Figure 8-A2 gives the gas inflow rate using the normalized time. All the curves fall on top of each other, so the borehole radius scaling for brine inflow also applies to gas inflow, at least for the dissolved gas scenario. Figure 8-A3 gives the gas saturation of the inflowing mixture using the normalized time; this parameter is a measure of the volumetric fraction of the gas to the total. While the gas mass inflow rate is negligible compared to the brine value, the gas saturation (or gas volume fraction) is significant, starting at about 0.36 and decreasing to about 0.25.

Figure 8-B shows the gas inflow and saturation for the permeability variation. The magnitude of the gas inflow rate increases for higher permeabilities as seen in Figures 8-B1 to 8-B3. Figures 8-B4 and 8-B5 show the gas inflow rate divided by the permeability. As with the brine inflow rate, the behavior does not simply scale with the permeability because the shape of the curve also changes. Figure 8-B6 depicts the gas saturation of the inflowing fluid. The gas saturation is a strong function of the formation permeability. For the lowest permeability (10^{-23} m^2), the gas saturation is about 0.6, while for the highest permeability (10^{-18} m^2), the gas saturation is about 0.1. The increase in the 10^{-18} m^2 gas saturation and gas inflow rate at late time is due to mobile free gas; otherwise, all gas inflow is due to transported dissolved gas. The reason for the difference with permeability is the variation of the capillary pressure with permeability. For the lower permeability, the capillary pressure is much higher, and much more dissolved gas is present in the brine than for a lower permeability. Therefore, the gas saturation will be much higher for a lower permeability.

The pore pressure results are given in Figure 8-C. The dissolved gas and free gas results in Figures 8-C1 and 8-C3 show a strong dependence on the pore pressure that can be essentially normalized within a factor of 2 by dividing by the pressure difference (Figures 8-C2 and 8-C4). The ratio of the gas inflow rate for the free gas variation to that for the dissolved gas case is given in Figure 8-C5. The ratio is a strong function of the pore pressure with a maximum value of about 1.5 for 1 MPA pressure. The ratio is exactly 1.0 for a pore pressure of 15 MPa because the dissolved gas and free

gas cases are the same. The gas saturation variation is given in Figures 8-C6 and 8-C7. The values vary from about 0.4 to about 0.2; the higher pressures have the higher values.

Figure 8-D presents the formation compressibility results. The variation in the gas inflow rate in Figures 8-D1 and 8-D2 is consistent with the two-phase brine inflow rate. In fact, as shown in Figure 8-D3, the gas saturation is surprisingly insensitive to the formation compressibility.

The plots for the porosity case are given in Figure 8-E. Again, there are no surprises as the gas inflow rates and normalized values in Figures 8-E1 and 8-E2 closely resemble the brine inflow results. Figure 8-E3 gives the gas inflow rate as a function of normalized time (t/ϕ); the curves are very close to each other except that the value for the highest porosity is below the others at early time. The gas saturation values as a function of normalized time in Figure 8-E4 are also consistent with each other except for the highest porosity results, which are lower than the others; this difference may be due to nodalization effects.

The limited brine source results are shown in Figure 8-F. The gas inflow rate in Figures 8-F1 and 8-F2 behaves just like the brine inflow rate, except at lower values. The normalized values in Figure 8-F3 are also similar to the two-phase brine inflow rate results. The gas saturation values in Figure 8-F4 are insensitive to the brine source radius except for a slight variation in the later portions of the simulation.

Figure 8-G gives the results for the DRZ distance variation. The gas inflow for the different DRZ distances in Figure 8-G1 increases for larger DRZs. However, note that the gas inflow for no DRZ crosses that for a finite DRZ. This behavior is emphasized in Figure 8-G2, where the gas inflow rate has been normalized to the value with no DRZ. The values for a finite DRZ start above the no DRZ case but quickly fall below it and stay below it. The reason for this trend is that the DRZ is a low pressure region like the borehole. When the gas-saturated brine flows into the DRZ, much of the dissolved gas comes out of solution in the DRZ and is trapped until it becomes mobile. The brine, with much lower dissolved gas content due to the lower pressure, continues through the DRZ into the borehole. Thus, the gas saturation is much lower for a DRZ because much of the gas is trapped in the DRZ region. This behavior will be seen in the next section when pressure and gas saturation profiles at the end of the simulation are presented. This situation is also reflected in the inflowing gas saturation in Figure 8-G3; while the no DRZ value is about 0.25, the finite DRZ values are around 0.06.

Figure 8-H summarizes the gas inflow rate and gas saturation values for the DRZ characteristics variation. The results for the gas inflow rate in

Figure 8-H1 and the ratio to the no DRZ results in Figure 8-H2 are consistent with the brine inflow rate and the DRZ gas-trapping behavior mentioned above. The gas saturation values in Figure 8-H3 merge quickly after the initial transient is over.

Figure 8-I presents the results for different DRZ permeability contrasts. While the brine inflow rate for an increased Δk is higher early on than the standard model, the gas inflow rate in Figure 8-I1 for this early time period is about the same. This change is due to increased gas-trapping for the larger Δk. Since the DRZ permeability is higher in this case, the DRZ pressure is lower. More gas comes out of solution in the DRZ and is trapped there, so less makes it to the borehole. Likewise, the difference between the standard model and the decreased Δk is smaller than for the brine inflow rate. The ratio to the no DRZ case is given in Figure 8-I2. This gas trapping behavior is also shown in the gas saturation variation in Figure 8-I3. Considering the no DRZ case as a further decreased Δk ($\Delta k=0$), the gas saturation values decrease with increasing permeability contrast. For contrasts of 0 (no DRZ), 10, 100, and 1000, the late-time gas saturation values are approximately 0.23, 0.12, 0.06, and 0.03, respectively.

The McTigue and growing DRZ results are contained in Figure 8-J. The gas inflow rate for the McTigue model in Figure 8-J1 is similar to the brine inflow results. For the growing DRZ cases, the initial gas inflow rate in Figure 8-J1 is like the no DRZ rate because the DRZ extent is very small and the permeability contrast is limited. The ratio to the no DRZ case is shown in Figure 8-J2 which reflects gas trapping. For the growing DRZ cases, as the DRZ extent grows, the gas inflow rate ratio drops from the no DRZ values to the finite DRZ values. However, the rate suddenly increases for the 2R/yr case as the gas phase becomes mobile, probably due to the lower permeability contrast than for the McTigue approach. The gas saturation values in Figure 8-J3 show a similar trend. The McTigue value is about 0.04, below that for the standard DRZ model. The growing DRZ results start out at a higher value similar to that for no DRZ but decrease toward the finite DRZ values. However, for the 2R/yr case, the free gas suddenly becomes mobile, and the gas saturation value increases dramatically.

The gas solubility results are shown in Figure 8-K. The gas inflow rate is higher for higher gas solubilities as given in Figure 8-K1. As shown in Figure 8-K2, the increase is slightly more than the increase in the solubility. The gas saturation values shown in Figure 8-K3 are higher for the higher gas solubility, varying from about 0.23 for the standard case, to 0.38 for the solubility increased by 2, and to 0.57 for the solubility increased by 4.

Figure 8-L gives the gas inflow and gas saturation results for variation of the dissolved gas fraction. The variation in the gas inflow in Figure 8-L1 and in the ratio to 100% dissolved gas in Figure 8-L2 is a strong function of the dissolved gas fraction, especially at early time. Initially, the inflow rate ratio is very close to the initial dissolved gas fraction. As time goes on, the values all approach 1.0. The gas saturation shown in Figure 8-L3 also reflects this behavior as after 1000 seconds, minimal effect of the initial dissolved gas fraction is noted.

The free gas fraction results are given in Figure 8-M. Unlike the other cases, the gas inflow rate in Figures 8-M1 to 8-M4 varies significantly with free gas fraction apparently unrelated to the brine inflow rate because the gas is often mobile (note the 20 v/o residual gas saturation). Therefore, while the no gas and 10 v/o gas cases follow the brine inflow rate trends, the 20 and 50 v/o are completely different. In addition, the non-uniform cases also involve mobile free gas because the gas pockets are at 20 v/o. Figure 8-M1 gives the gas flow rates for uniform free gas. The values for no free gas and 10 v/o are shown; the rates for 20 v/o and 50 v/o are off the scale. Similarly, the nonuniform rates are given in Figure 8-M2. The 10 v/o L/G case is lower than the uniform case, while the 10 v/o G/L variation is off the scale high. The ratio of the inflow rate to that with no free gas is given in Figure 8-M3. For 50 v/o free gas, the ratio is about 30,000; for 20 v/o, the value is around 100; and for 10 v/o, the ratio is about 2. For nonuniform gas, the ratio of nonuniform to uniform gas inflow shown in Figure 8-M4 is a strong function of time and can vary between 0.3 and 100 for the cases analyzed. Figure 8-M5 gives the gas saturation for these situations. The values vary considerably from a low of about 0.2 (10 v/o L/G) all the way up to essentially 1.0 (50 v/o).

The capillary pressure magnitude results are plotted in Figure 8-N. In contrast to the brine inflow rate, the gas inflow rate increases with increasing capillary pressure magnitude, as given in Figure 8-N1. The ratio of the flow rate compared to the base case is presented in Figure 8-N2; the ratio diverges and reaches an asymptotic value approximately equal to the multiplier on the capillary pressure. The gas saturation results in Figure 8-N3 reflect this trend as the high capillary pressure has a gas saturation of about 0.75, while the zero capillary pressure value approaches zero. As with the permeability case, this variation is caused by more gas in solution for the higher capillary pressures.

Figure 8-O has the plots for variation in the shape of the capillary pressure curve. The uniform results in Figure 8-O1 are essentially the same as the base case, probably because there are minor differences in the two curves in the high liquid saturation region encountered in this simulation.

The dissolved gas exsolution results tend toward the high capillary pressure results, which are again expected due to the difference in the curves. The maximum gas inflow ratio in Figure 8-02 approaches 3. The gas saturation varies from 0.22 for the base case to 0.45 for dissolved gas exsolution as shown in Figure 8-03.

The shape of the characteristic curves has been investigated and the results are shown in Figure 8-P. For a decreased residual saturation, additional gas flow is expected and is seen in Figure 8-P1 and in the ratio to the base case in Figure 8-P2; the results are the opposite for increased residual saturation. The difference in the rates from the base case is between 0.4 and 1.5. However, if the Sandia functions are used with a significantly different gas relative permeability curve, the flow rate is much higher and the ratio is about 500. Thus, the gas inflow rate is a strong function of the shape of the curves in contrast to the brine inflow rate. The gas saturations in Figure 8-P3 show similar variation, varying from about 0.1 for the high residual saturation to 0.99 for the Sandia functions.

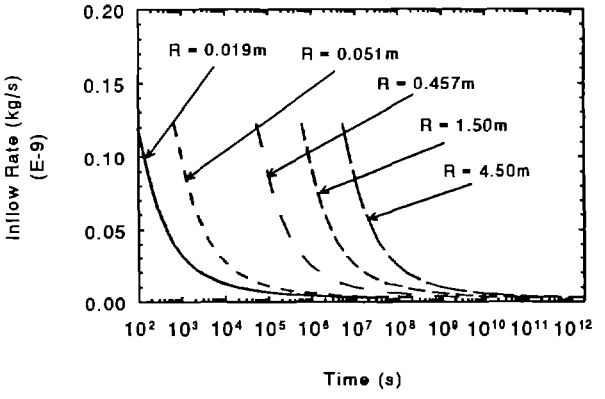

8-A1

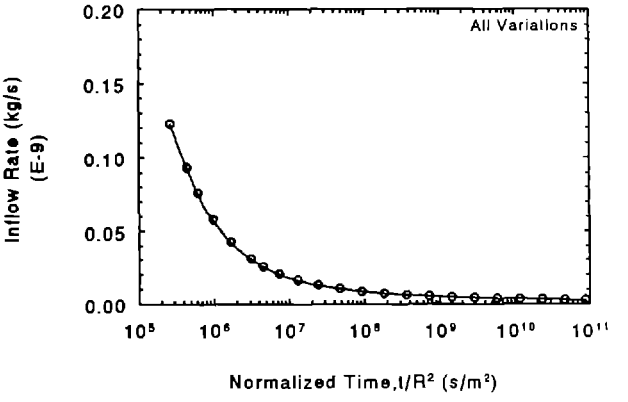

8-A2

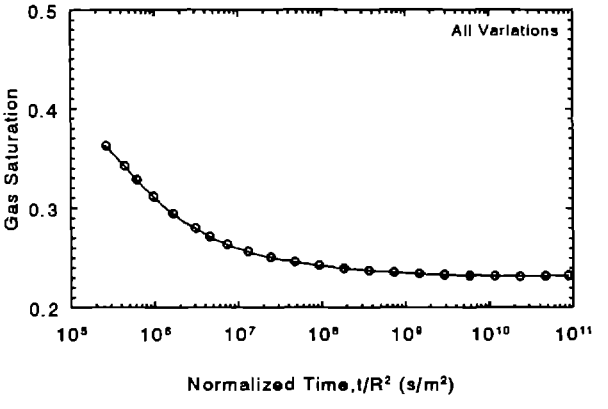

8-A3

Figure 8-A. Results from variation in borehole radius for two-phase gas inflow.

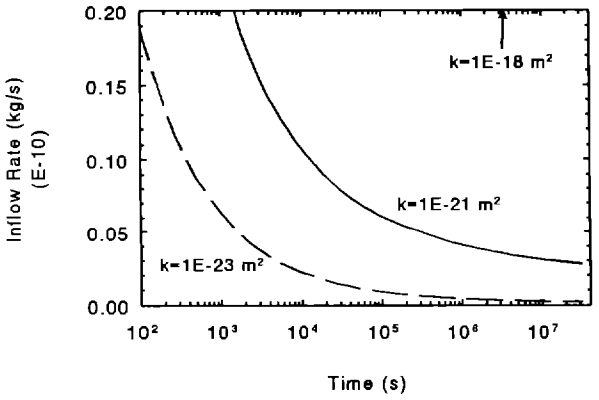

8-B1

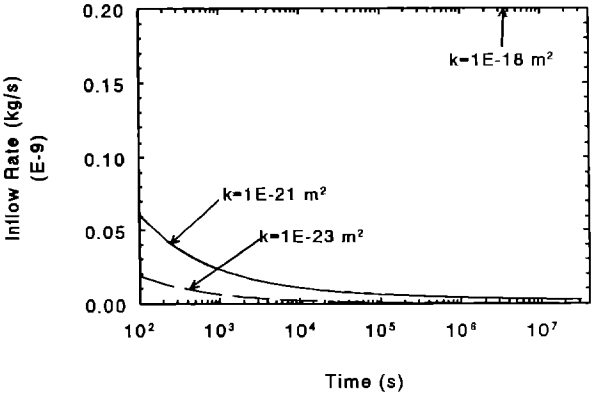

8-B2

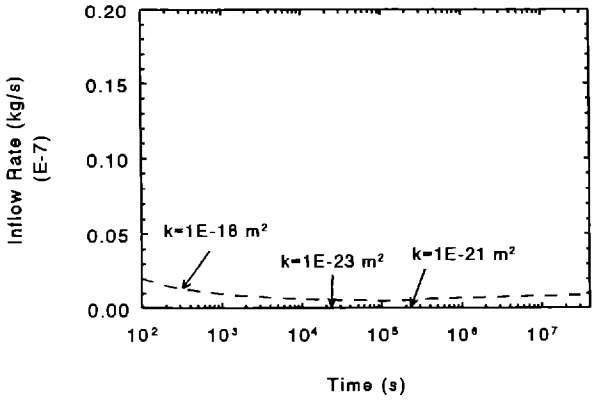

8-B3

Figure 8-B. Results from variation in permeability for two-phase gas inflow.

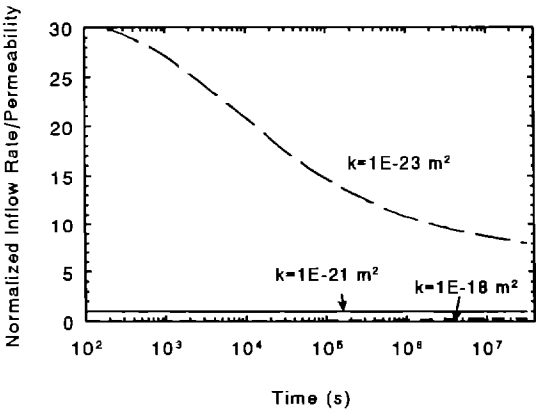

8-B4

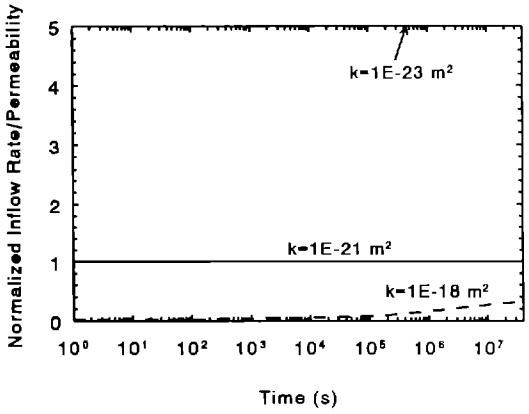

8-B5

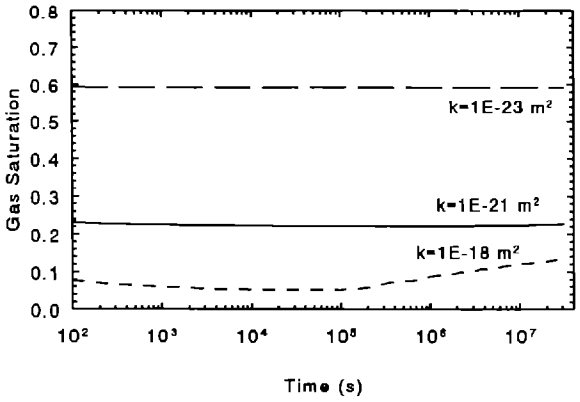

8-B6

Figure 8-B. Results from variation in permeability for two-phase gas inflow (continued).

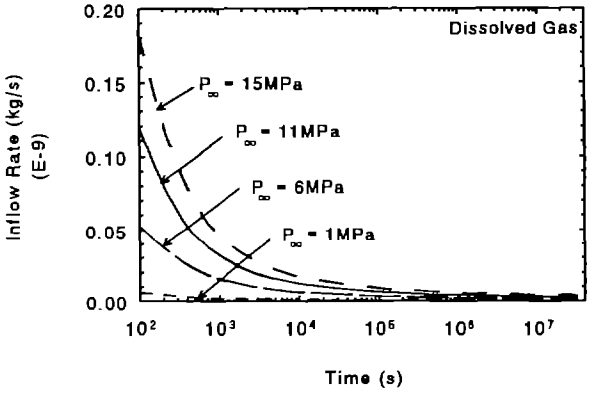

8-C1

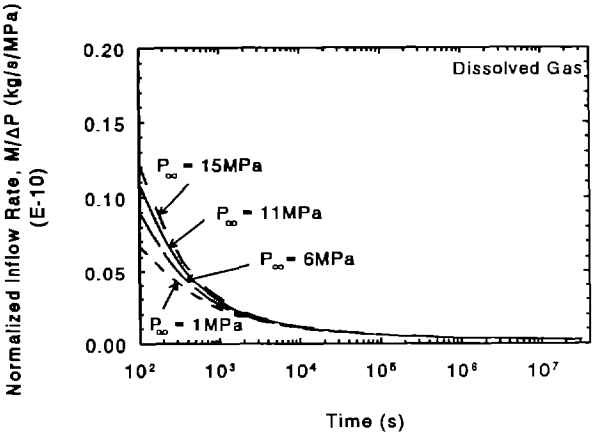

8-C2

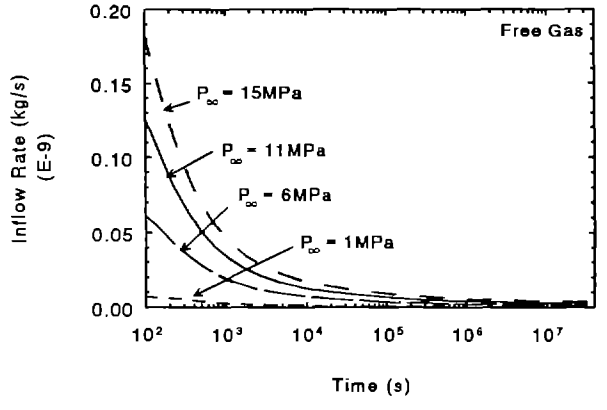

8-C3

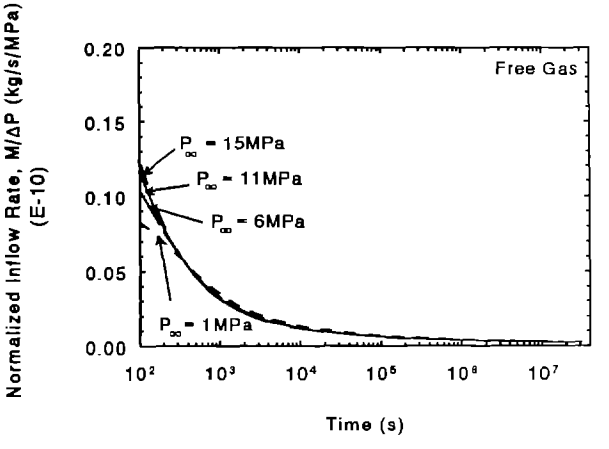

8-C4

Figure 8-C. Results from variation in pore pressure for two-phase gas inflow.

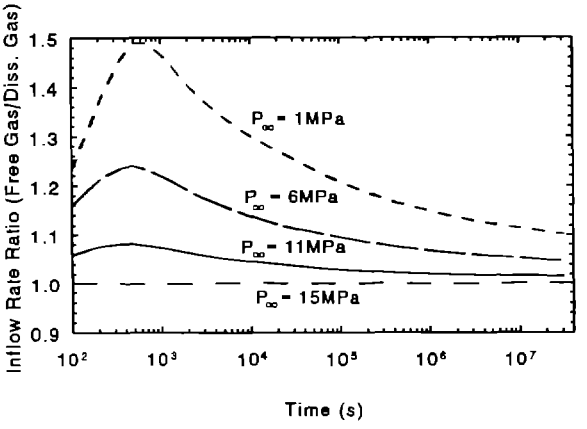

8-C5

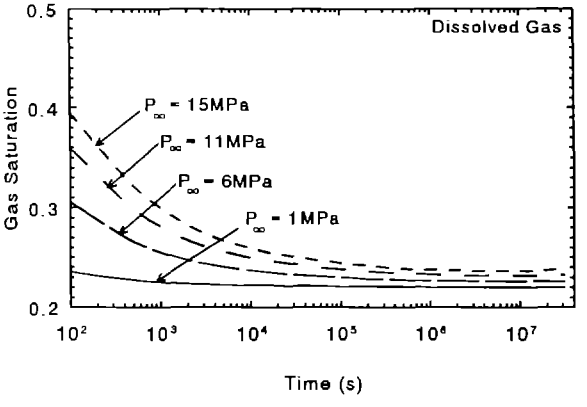

8-C6

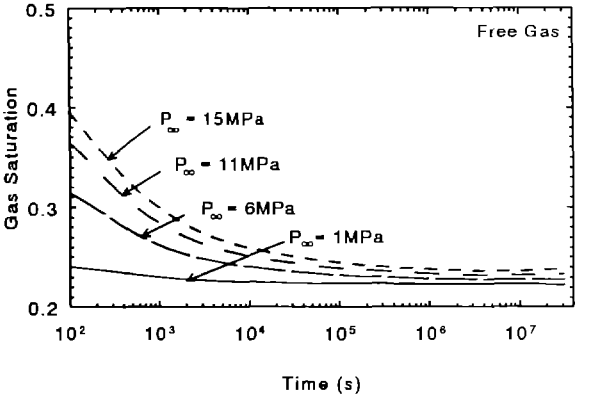

8-C7

Figure 8-C. Results from variation in pore pressure for two-phase gas inflow (continued).

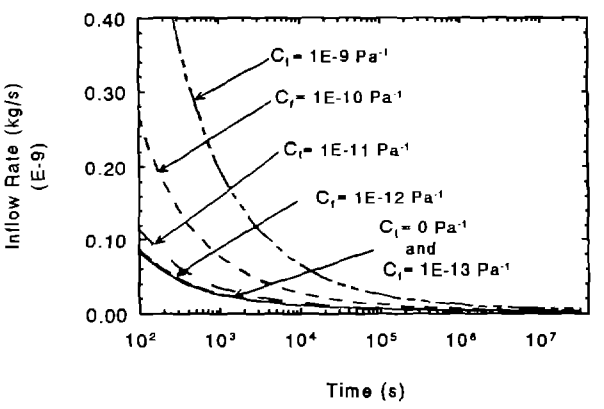

8-D1

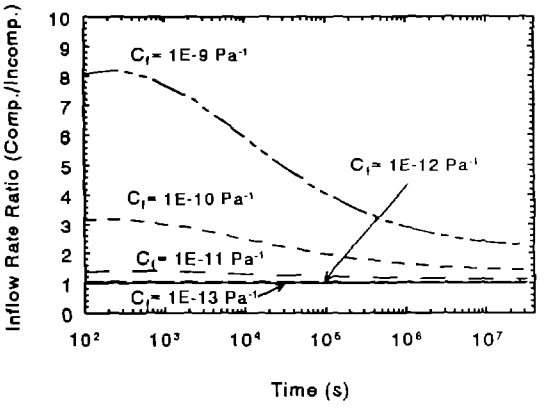

8-D2

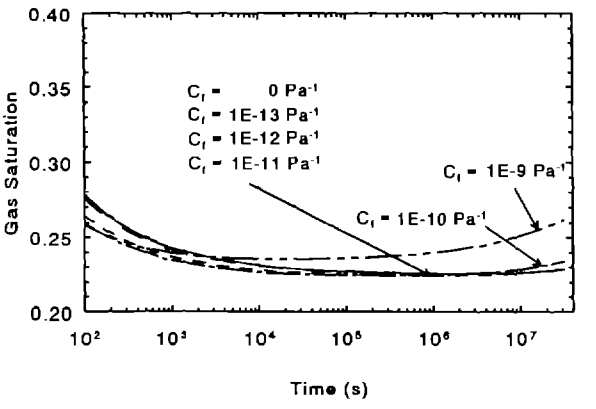

8-D3

Figure 8-D. Results from variation in formation compressibility for two-phase gas inflow.

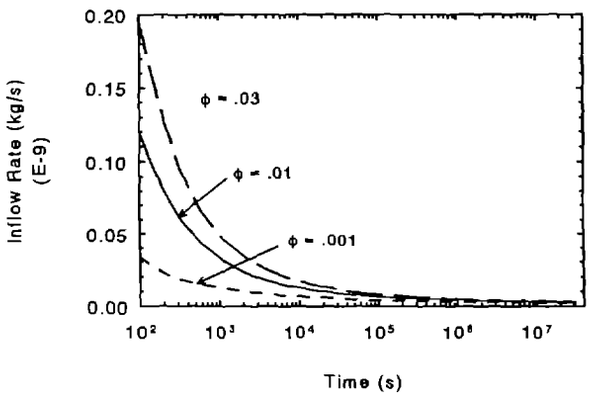

8-E1

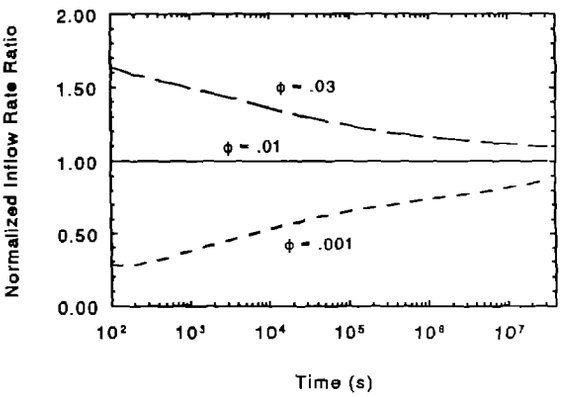

8-E2

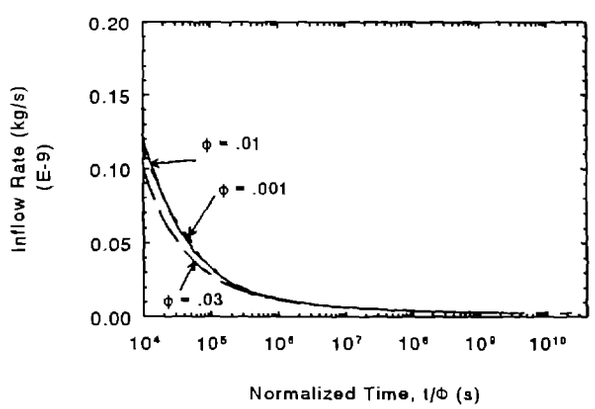

8-E3

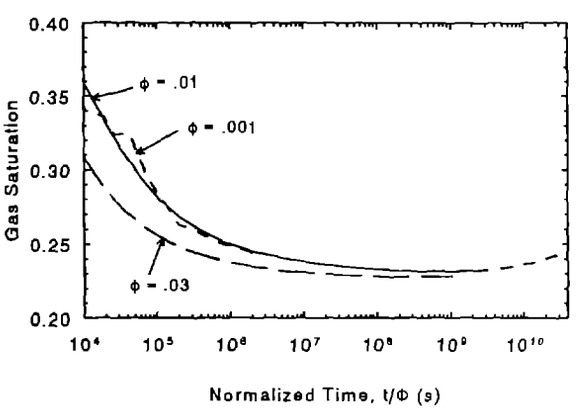

8-E4

Figure 8-E. Results from variation in porosity for two-phase gas inflow.

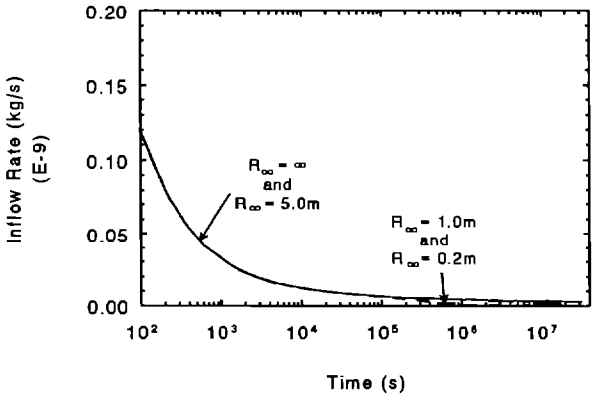

8-F1

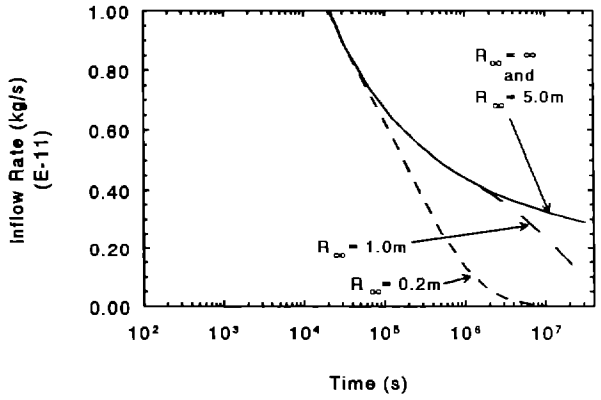

8-F2

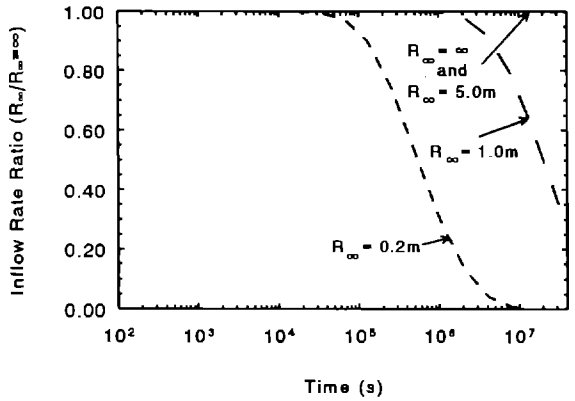

8-F3

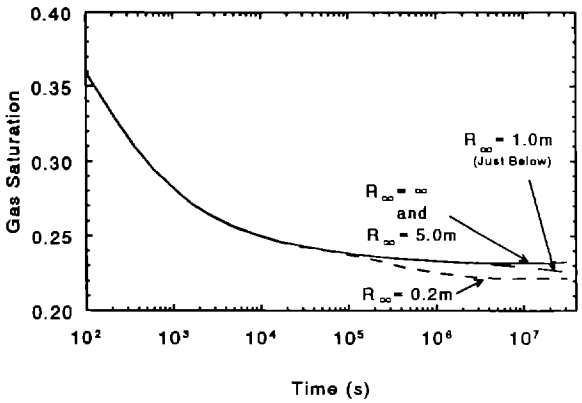

8-F4

Figure 8-F. Results from variation in source radius for two-phase gas inflow.

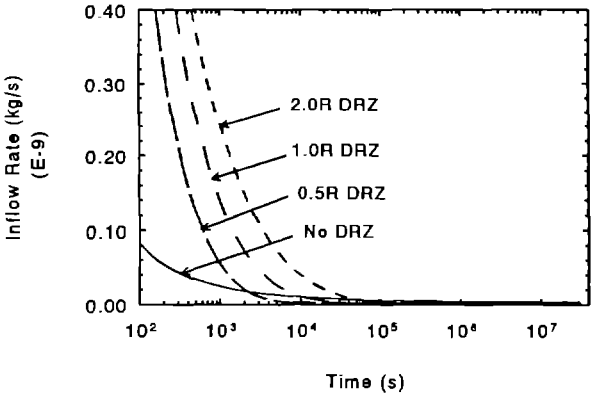

8-G1

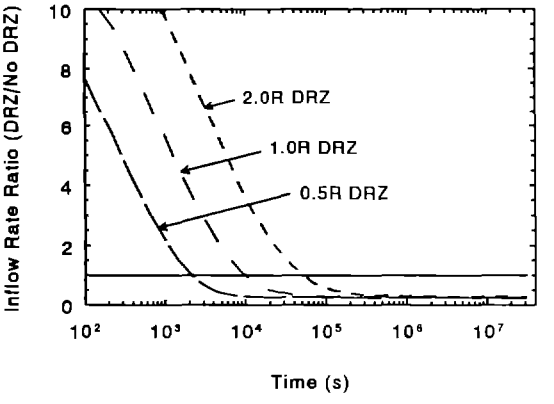

8-G2

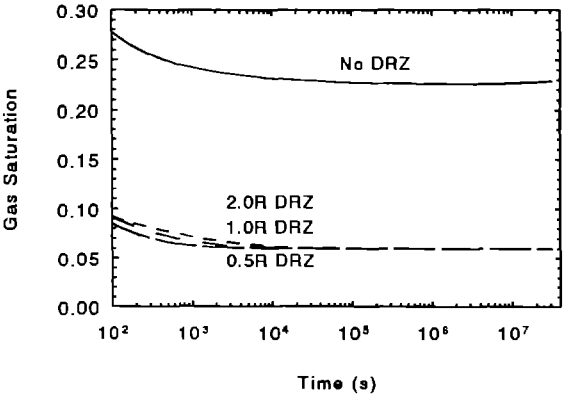

8-G3

Figure 8-G. Results from variation in DRZ distance for two-phase gas inflow.

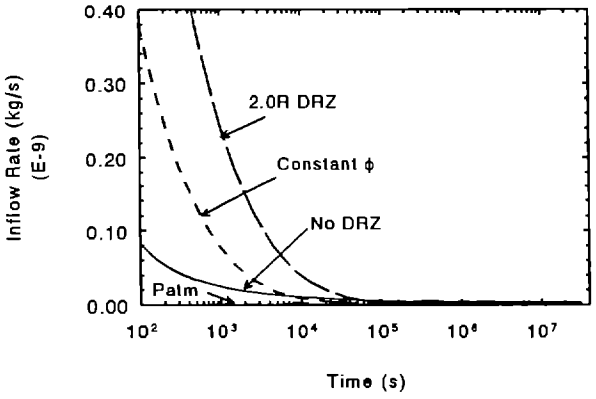

8-H1

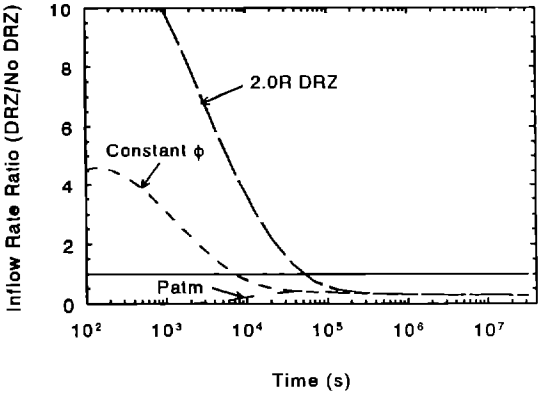

8-H2

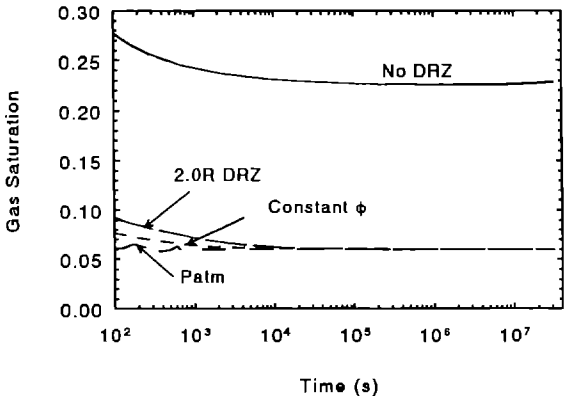

8-H3

Figure 8-H. Results from variation in DRZ porosity and pressure for two-phase gas inflow.

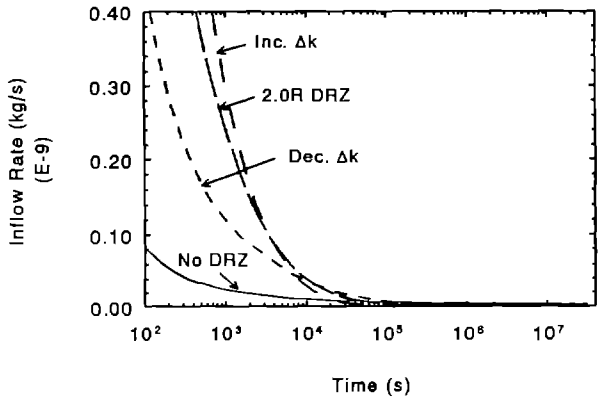

8-I1

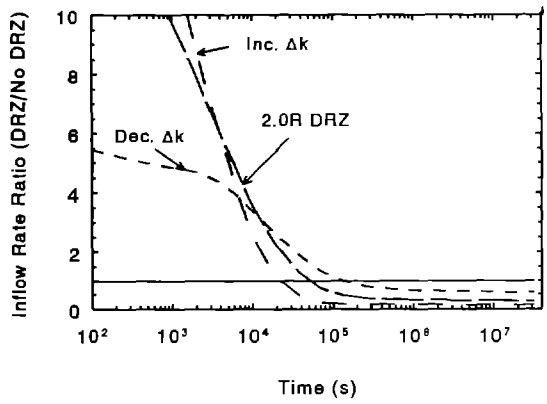

8-I2

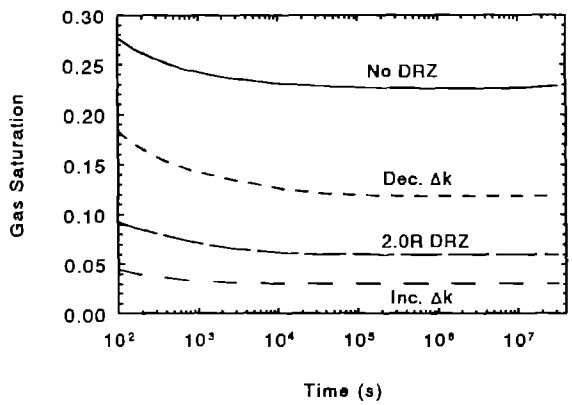

8-I3

Figure 8-I. Results from variation in DRZ permeability contrast for two-phase gas inflow.

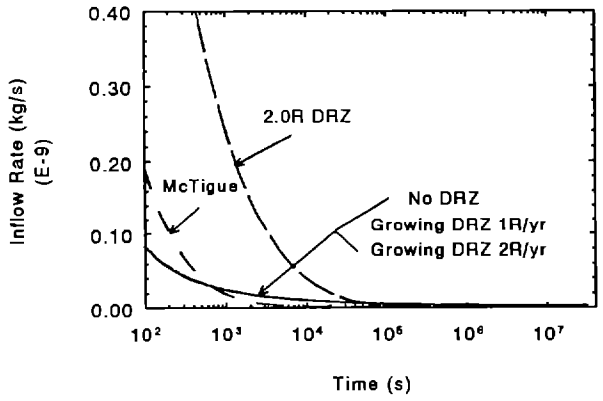

8-J1

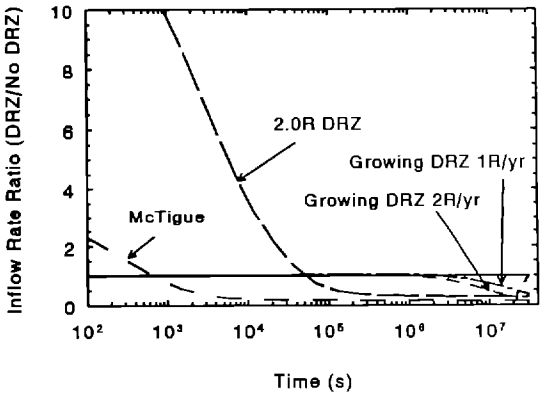

8-J2

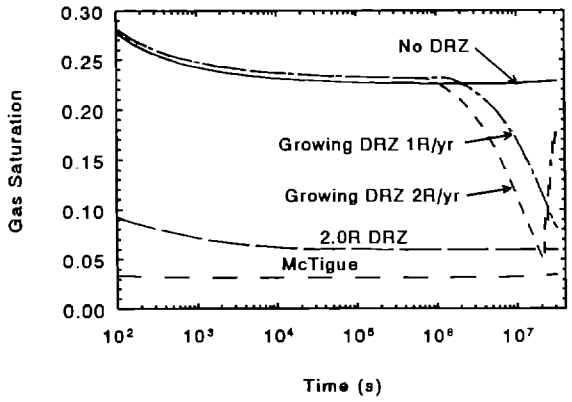

8-J3

Figure 8-J. Results from variation in DRZ permeability distribution for two-phase gas inflow.

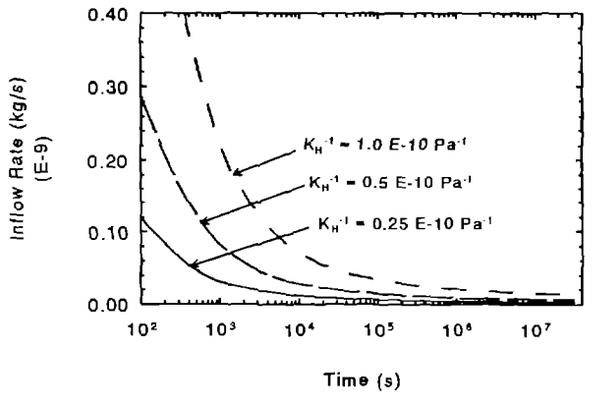

8-K1

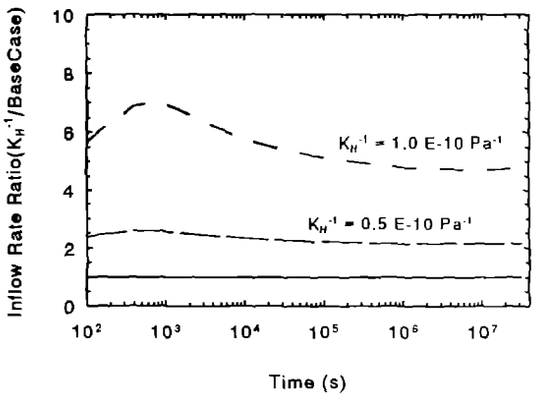

8-K2

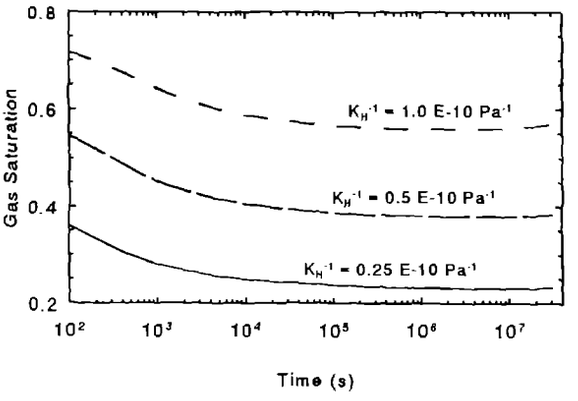

8-K3

Figure 8-K. Results from variation in gas solubility for two-phase gas inflow.

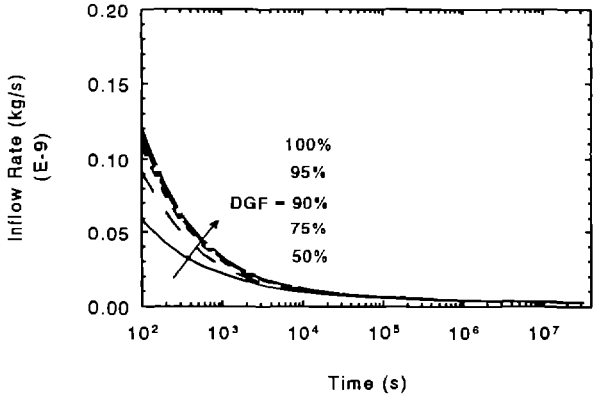

8-L1

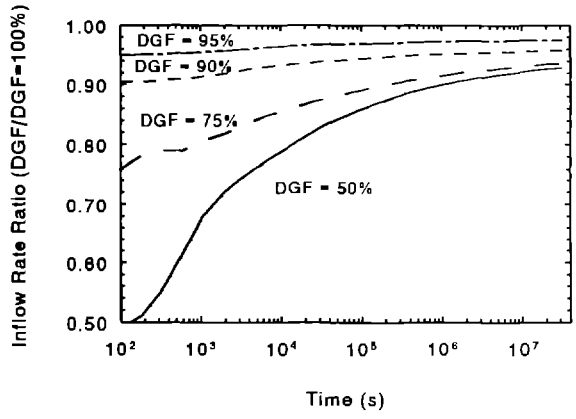

8-L2

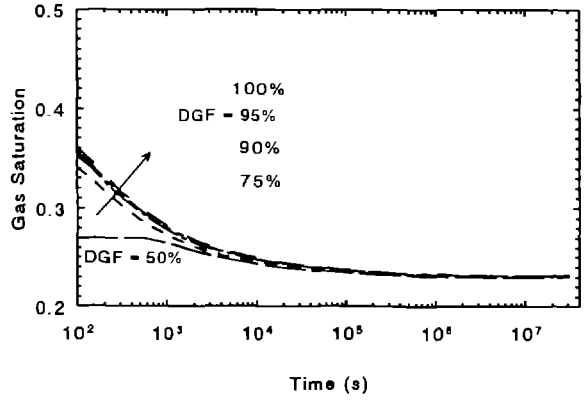

8-L3

Figure 8-L. Results from variation in initial dissolved gas fraction for two-phase gas inflow.

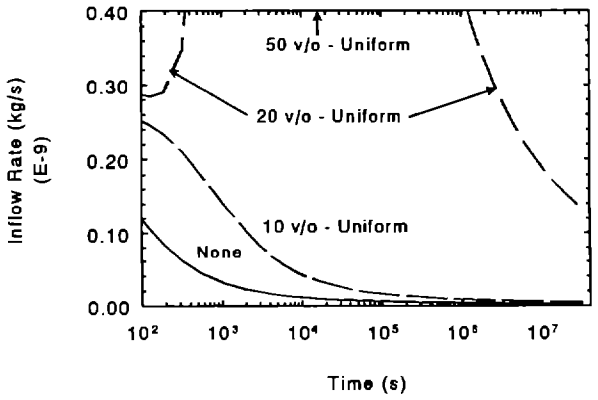

8-M1

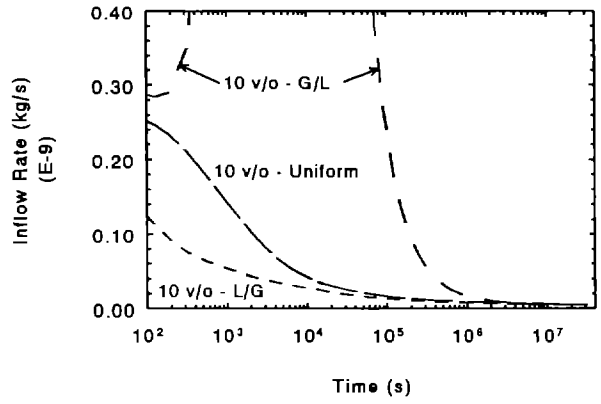

8-M2

Figure 8-M. Results from variation in free gas fraction for two-phase gas inflow.

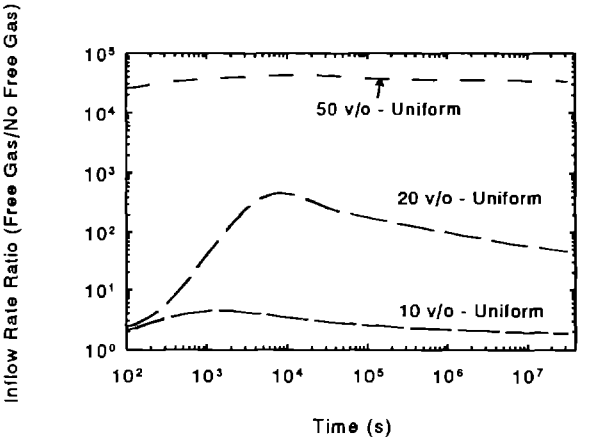

8-M3

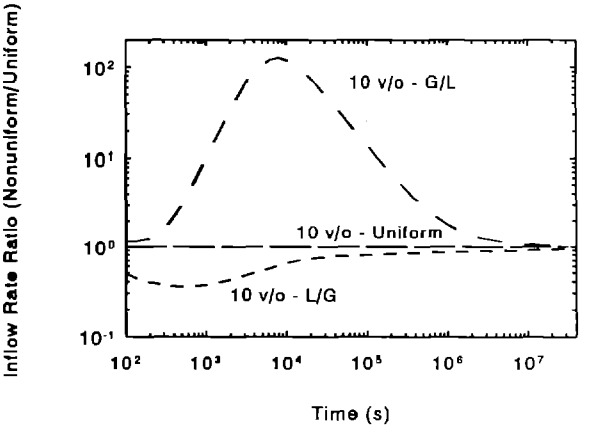

8-M4

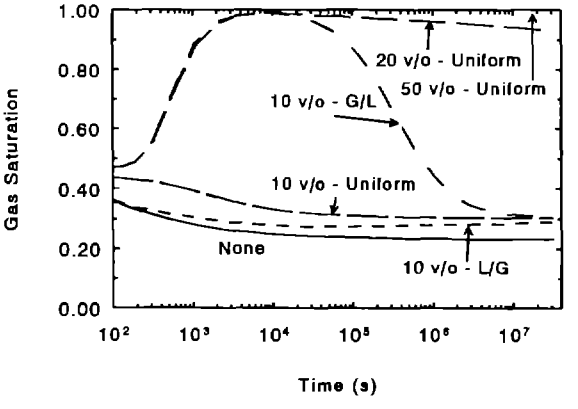

8-M5

Figure 8-M. Results from variation in free gas fraction for two-phase gas inflow (continued).

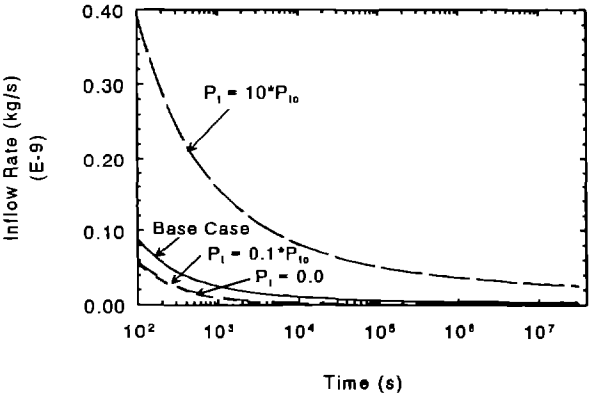

8-N1

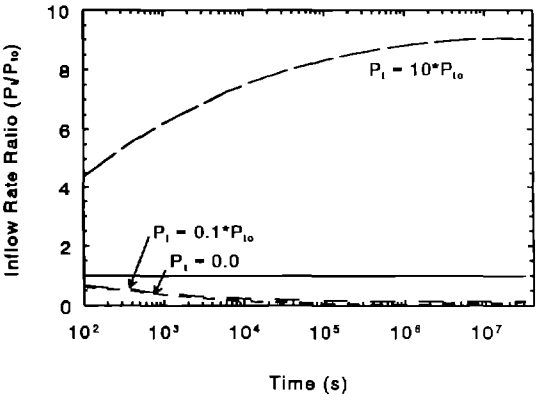

8-N2

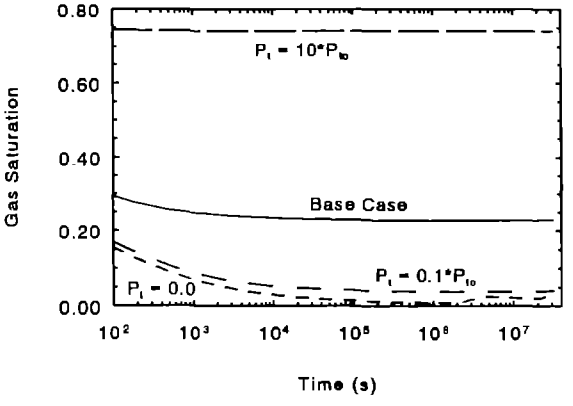

8-N3

Figure 8-N. Results from variation in capillary pressure magnitude for two-phase gas inflow.

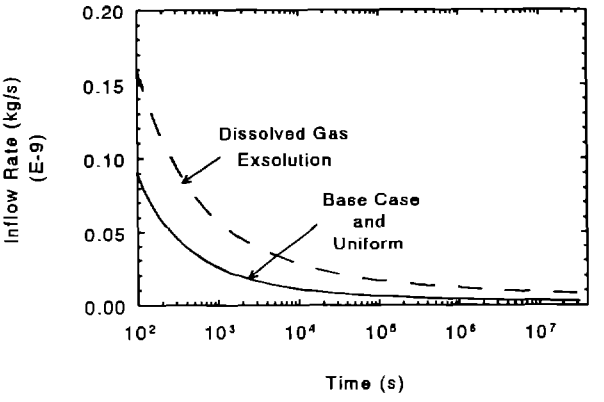

8-01

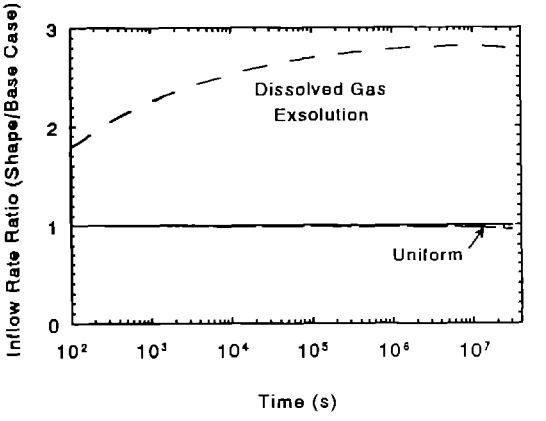

8-02

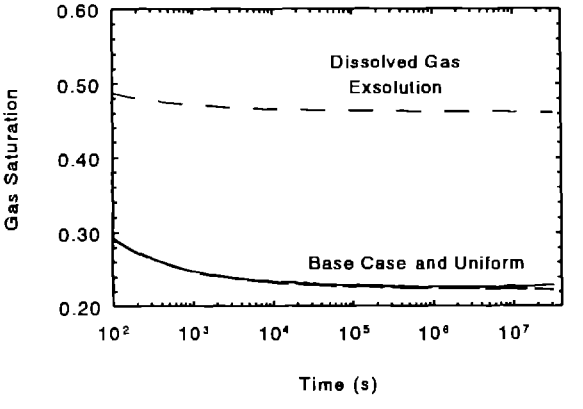

8-03

Figure 8-0. Results from variation in capillary pressure shape for two-phase gas inflow.

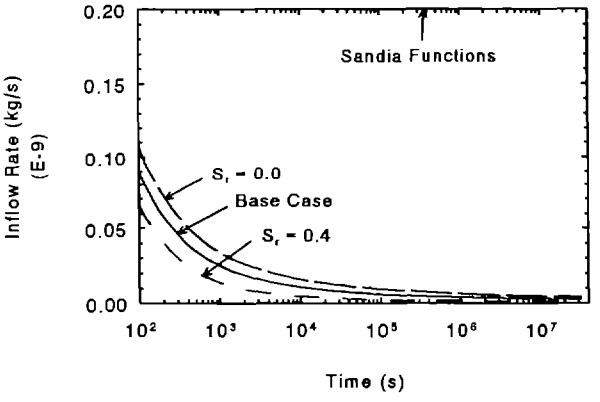

8-P1

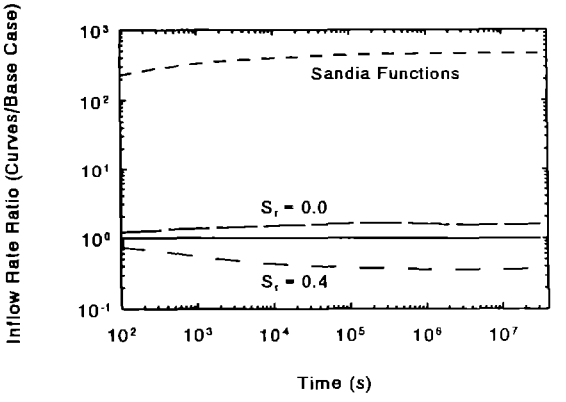

8-P2

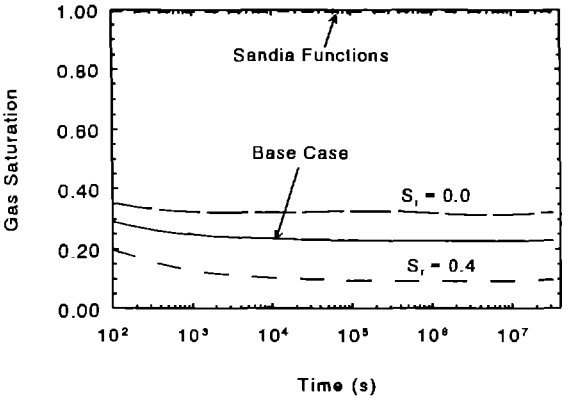

8-P3

Figure 8-P. Results from variation in two-phase characteristic curves for two-phase gas inflow.

Pressure and Gas Saturation Distributions

The brine and gas pressure and free gas saturation distributions in the formation are presented in this section. Only the distributions at the end of the simulation (nominally 1 year) are given. The only exception to the 1-year value is for the borehole radius variation. In that case, as discussed earlier, a constant value of $t^*=t/R^2$ was used. The approximate end time values are:

Borehole Radius	Simulation End Time
0.019 m	1 year
0.051 m	7.2 years
0.457 m	580 years
1.5 m	6200 years
4.5 m	56000 years

Figure 9-A1 shows the single-phase brine pressure profile for the radius variation as a function of normalized radius. The curves for all the borehole radii lie on top of each other. The local pressure reaches 95% of the far-field value at about 200 times the borehole radius, or about 4 m for a 0.019 m radius borehole. For two-phase conditions, as shown in Figure 9-A2, the far-field value is reached at 150 times the borehole radius, or around 3 m for a 0.019 m radius borehole. Figure 9-A3 shows the gas pressure normalized to the far-field brine pressure; the results are greater than 1.0 due to the capillary pressure. The gas pressure reaches the far-field value much sooner than the brine pressure. Figure 9-A4 presents the free gas values. The largest free gas saturation is less than 2%, which drops rapidly with the first 5 borehole radii and slows thereafter.

The distributions at the end of 1 year for the permeability variation are given in Figure 9-B. The pressure is affected over a much smaller distance for the lower permeability, as shown in Figure 9-B1 for single-phase flow. For a permeability of 10^{-23} m^2, the pressure is only disturbed about 1 m out from the borehole, while this distance is over 100 m for a permeability of 10^{-18} m^2. The two-phase brine pressure profile shows similar results, as given in Figure 9-B2. The gas pressure profile is presented in Figure 9-B3. The magnitudes are much different due to the differences in capillary pressure; the extent of the pressure change is in accordance with the brine pressure profiles. The gas saturation distribution in Figure 9-B4 also reflects the capillary pressure as the low permeability, high capillary pressure case has the lowest final gas saturation. The 10^{-18} m^2 permeability gas saturation values near the

borehole are slightly above 0.20, the residual gas saturation, indicating mobile free gas as was observed in the gas flow results.

The pore pressure variation results are shown in Figure 9-C. The single-phase pressure profile for the highest and lowest pore pressures are shown in Figure 9-C1; the results do not overlay because the correct normalization is the pressure difference relative to the borehole pressure, not just the pressure. When the correct normalization is used, the results overlay as shown in Figure 9-C2. Similar results for the two-phase brine pressure are shown in Figures 9-C3 and 9-C4 for dissolved gas. The two-phase results do not overlay but are reasonably close. In all cases, the pressure is affected out to about 4 m at the end of the simulation. The free gas profiles and normalization are shown in Figures 9-C5 and 9-C6. The results are similar although the normalization is not as successful as for the dissolved gas case. The gas pressure profile is shown in Figure 9-C7; the large spread in the values is due to the normalization with the far-field brine pressure. The gas saturation profile given in Figure 9-C8 shows that the gas saturation is higher for higher initial pressures. The maximum gas saturation is about 0.03, and most of the increase in the free gas is within the first 0.2 m. For the free gas case, the gas pressure profile is very similar, as given in Figure 9-C9. However, the gas saturation profiles in Figure 9-C10 are considerably different due to the initial free gas. Still, the free gas values are low and the larger valves are confined to regions very close to the borehole.

Formation compressibility effects are presented in Figure 9-D. The brine pressure profile (single-phase and two-phase) gets steeper as the formation compressibility increases, as shown in Figures 9-D1 and 9-D2. For an incompressible formation, the pressure penetrates about 4 m into the formation. For a formation compressibility of 10^{-9} Pa^{-1}, the penetration is reduced to around 0.5 m. Similar trends are shown in the gas pressure profiles in Figure 9-D3. The free gas saturation profiles in Figure 9-D4 also reflect this behavior in that for the higher compressibility cases, the free gas in concentrated much closer to the borehole and has a much higher value.

Figure 9-E gives the results of the porosity variation. The single-phase pressure profile in Figure 9-E1 extends much deeper into the formation for lower porosities, i.e., about 2.5 m for a 0.03 porosity, about 4 m for a 0.01 porosity, and about 12 m for a 0.001 porosity; similar results are shown in Figure 9-E2 for two-phase conditions. The effect is simply related to the amount of brine available. For a higher porosity, there is more brine available in the pore space, so the depressurization does not penetrate as deeply. The gas pressure in Figure 9-E3 is similar. The free gas saturation in Figure 9-E4 shows the penetration effect plus the fact

that there is less free volume. The brine inflow rates are very similar for the different porosities, as seen earlier. Therefore, approximately the same amount of gas will come out of solution. For the small porosity, the pore space is much less, so the gas saturation is much higher.

Figures 9-F1 and 9-F2 show the brine pressure profiles for the limited brine source radius variation for single- and two-phase conditions, respectively. In both cases, the infinite and 5.0-m radius profiles are close to each other; the effect of a limited radius of 5.0 m is just beginning to impact the behavior at 1 year. For the 1.0-m radius, the entire zone is essentially depressurized for single-phase conditions, while it is well on its way for two-phase. The 0.2-m radius case is completely depressurized in both cases. The same features are seen for the gas-pressure profile in Figure 9-F3. The free gas saturation profile for a radius of 0.2 m in Figure 9-F4 shows that a significant amount of brine is retained in the formation even when fully depressurized; the free gas saturation is less than 1%.

The DRZ distance plots are shown in Figure 9-G. The brine pressure plots in Figure 9-G1 and 9-G2 for single- and two-phase flow, respectively, show that the DRZ zone is almost completely depressurized; thus, the use of an effective radius equal to the outer edge of the DRZ is appropriate as suggested earlier. Similar results are noted for the gas pressure profile in Figure 9-G3. The free gas saturation profile in Figure 9-G4 shows the dissolved gas exsolution and gas trapping occurring at the outer edge of the DRZ as discussed in the previous section. Due to the low pressure in the DRZ, dissolved gas comes out of solution in the DRZ and is trapped in the formation rather than flowing into the borehole. Therefore, the gas inflow rate is much lower with a DRZ than without one. When the gas saturation in the DRZ reaches the mobile gas limit, the gas inflow will suddenly increase.

The DRZ porosity and initial pressure results are given in Figure 9-H. The pressure profiles (brine and gas) in Figures 9-H1 to 9-H3 are the same for all three cases at the end of 1 year. The free gas saturation profiles in Figure 9-H4 have a minor difference; the gas saturation is higher for the lower porosity case simply due to the smaller amount of available pore space. Otherwise, the results are the same.

Figure 9-I summarizes the profiles for the different DRZ permeability contrasts studied. The brine pressures in Figures 9-I1 and 9-I2 are the same for the standard model and for an increased permeability contrast; the pressure is a little higher for the reduced contrast due to the lower DRZ permeability and the slightly larger pressure drop. The gas pressure in Figure 9-I3 shows a difference in the DRZ region because the capillary pressure is a function of the local permeability; the values in the

formation are very similar. The differences in the free gas saturation profiles in Figure 9-I4 are caused by the difference in the gas pressures; a higher gas pressure leads to a smaller gas volume and gas saturation.

The McTigue and growing DRZ cases are presented in Figure 9-J. The brine pressure profiles in Figures 9-J1 and 9-J2 generally reflect the end state distance of the DRZ, i.e., for a DRZ growing at 1R/yr, the entire 1R zone is depressurized. The McTigue and 2R/yr profiles are slightly higher than the 2.0R DRZ due to the permeability variation in both cases. The gas pressure profiles in Figure 9-J3 are considerably different due to the different permeabilities and resulting different capillary pressure values in the DRZ. The gas saturation profiles in Figure 9-J4 show considerably different behavior for the different models as shown in Figure 9-J5. The McTigue variation gradually increases toward the borehole due to the permeability behavior in this region. The growing DRZ cases have a much steeper increase because the region of dissolved gas exsolution continually moves. In early time, when the brine inflow is the highest, the DRZ is very small, and the gas that comes out of solution is trapped very near the borehole. While this zone eventually spreads out, there is still dissolved gas exsolution in the entire DRZ due to the permeability variation. Finally, the mobile gas saturation value is reached for the 2R/yr growing DRZ case, as shown in this profile and as seen earlier in the gas inflow rate results.

The profiles are presented in Figure 9-K for the gas solubility case. The single-phase brine pressure in Figure 9-K1 is for the base case and is included simply for comparison purposes. The two-phase brine pressure in Figure 9-K2 is slightly higher as the gas solubility increases because the fluid system is able to expand more due to the higher fraction of gas. The same trend is seen in the gas pressure profile in Figure 9-K3. The free gas saturation profile in Figure 9-K4 has similar results as the values are higher for the higher gas solubilities.

The dissolved gas profiles are shown in Figure 9-L. Again, Figure 9-L1 is the single-phase base case results for comparison purposes. The brine and gas pressures in Figures 9-L2 and 9-L3 increase slightly with increasing fraction of dissolved gas. The free gas saturation profiles in Figure 9-L4 show the same trend. For a low dissolved gas fraction, the free gas is confined to a very narrow zone around the borehole; as the dissolved gas fraction increases, so does the size of the zone.

Figure 9-M presents the free gas fraction profiles. The two-phase brine pressure in Figure 9-M2 is significantly higher as more free gas is present up to the mobile gas limit. The distance where the pressure is 95% of the far-field value is about 4, 3, 1, and 0.7 m for gas fractions of single-phase, dissolved gas only, 10 and 20 v/o. For 50 v/o free gas, the brine

pressure is lower because the gas is mobile and flows, thereby reducing the system pressure. The non-uniform free gas brine pressure profiles are equivalent to the uniform values. The gas pressure profiles in Figure 9-M3 reflect the increase in the capillary pressure with increasing free gas. The free gas saturation profiles in Figure 9-M5 reflect the initial condition and the mobility of the gas phase. The value near the borehole tends toward the 20 v/o value for mobility; the far-field is the initial condition. The increase in the 20 v/o case toward the borehole is due to the decreased gas pressure and the small relative permeability near 20 v/o. For the non-uniform distributions, the gas pressures and gas saturations in Figures 9-M4 and 9-M6 are naturally erratic due to the local conditions. However, they average out close to the uniform profiles.

The effect of the magnitude of the capillary pressure on the profiles is given in Figure 9-N. The differences in the brine pressure profiles in Figure 9-N2 are a result of the volume of the gas which is reduced at higher capillary pressures. For higher capillary pressures, the effect of any dissolved gas exsolution is small due to the small volume, so the behavior is more like single-phase. The gas pressures in Figure 9-N3 reflect the large differences in the capillary pressure magnitude. Figure 9-N4 presents the free gas saturation values, which are much lower for higher capillary pressure.

The effect of the capillary pressure shape is shown in Figure 9-O. Again, the dissolved gas exsolution case has a higher capillary pressure than the uniform case and the base case. Therefore, the gas volumes will be smaller, and the effect of two-phase conditions will be reduced. This trend is reflected in the brine pressure profiles, the gas pressure profiles, and the free gas saturation variation shown in Figures 9-O2 to 9-O4. Only small differences are seen between the base case and the uniform capillary pressure case since the curves are very similar for the low gas saturation (high liquid saturation) values encountered in this simulation.

Figure 9-P presents the differences due to the shapes of the curves. Minor variations are noted in the brine pressure profiles in Figure 9-P2. The gas pressure discrepancies in Figure 9-P3 reflect the different capillary pressure curves. The free gas saturation profiles in Figure 9-P4 follow the capillary pressure and relative permeability trends. For variation in the residual saturations, the highest residual saturation (S_r = 0.4) has the highest free gas saturation. The low value of the free gas saturation for the Sandia functions reflects the gas-phase relative permeability curve, which permits significant gas flow immediately after exsolution.

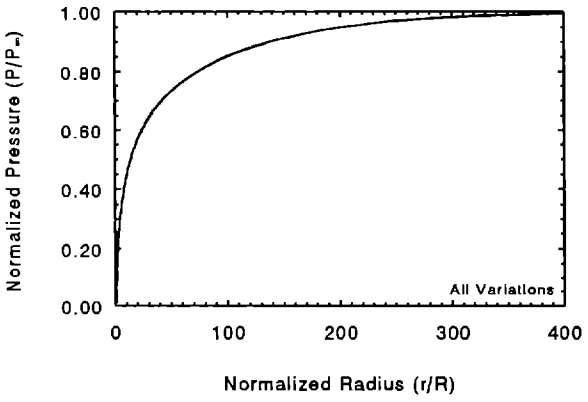

9-A1. Single-phase brine pressure profiles.

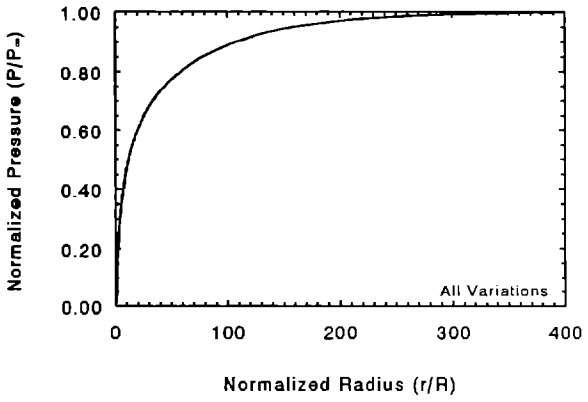

9-A2. Two-phase brine pressure profiles.

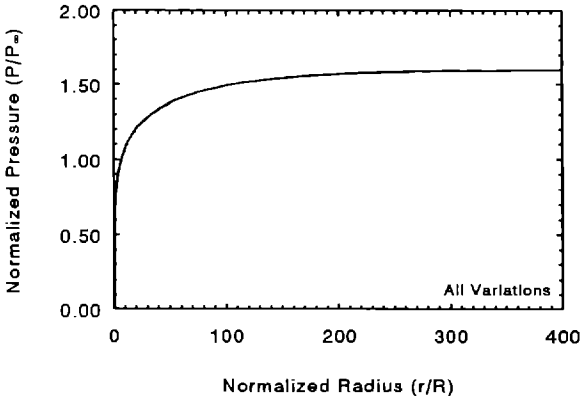

9-A3. Two-phase gas pressure profiles.

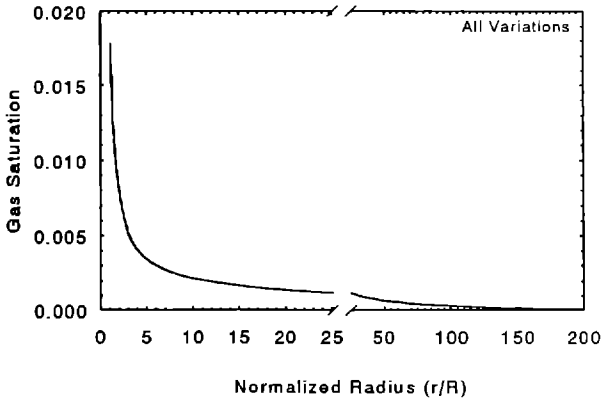

9-A4. Two-phase gas saturation profiles.

Figure 9-A. Results from variation in borehole radius at 1 year.

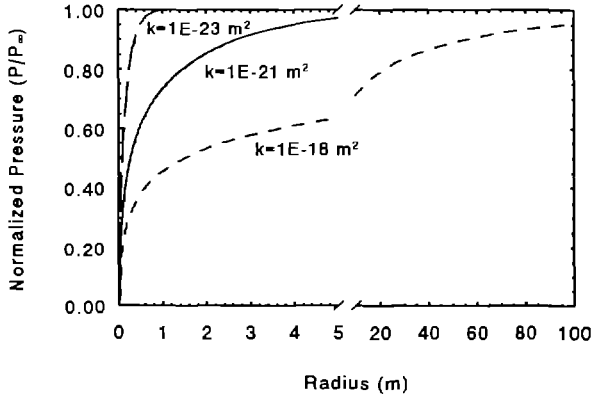

9-B1. Single-phase brine pressure profiles.

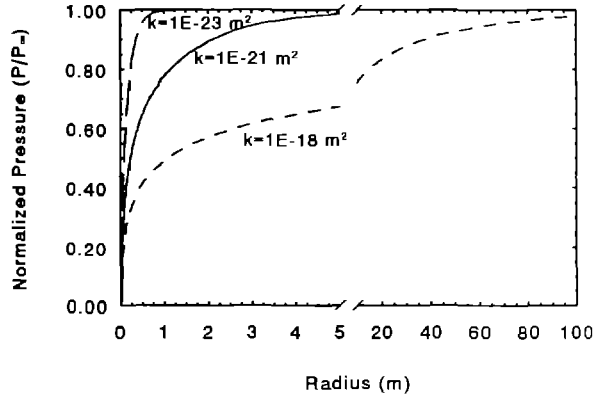

9-B2. Two-phase brine pressure profiles.

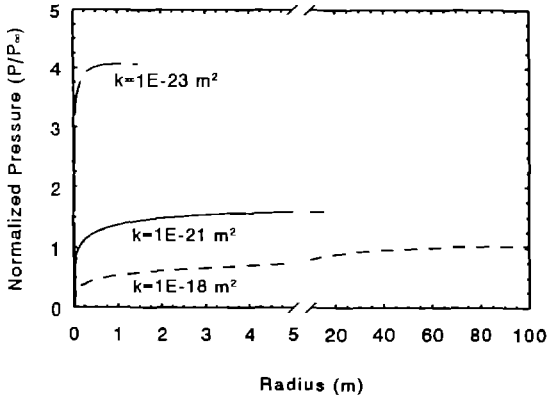

3

9-B3. Two-phase gas pressure profiles.

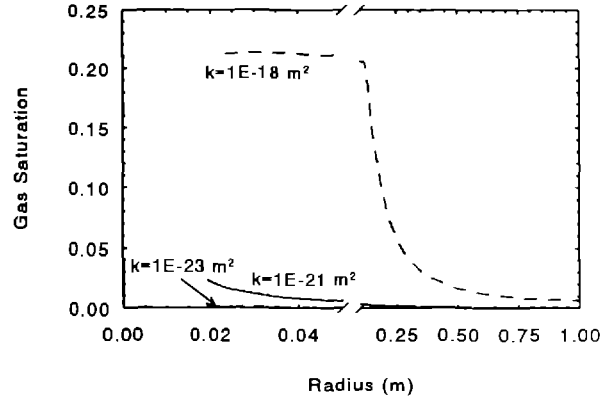

4

9-B4. Two-phase gas saturation profiles.

Figure 9-B. Results from variation in permeability at 1 year.

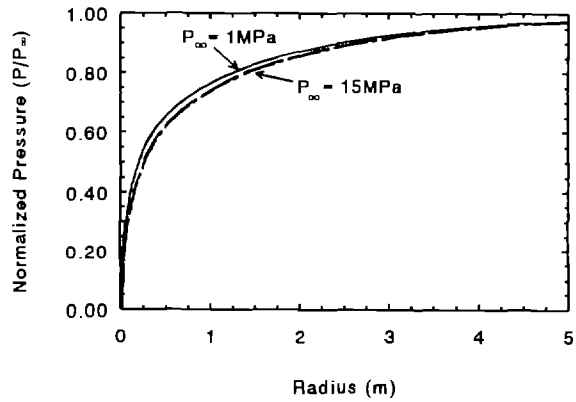

9-C1. Single-phase brine pressure profiles.

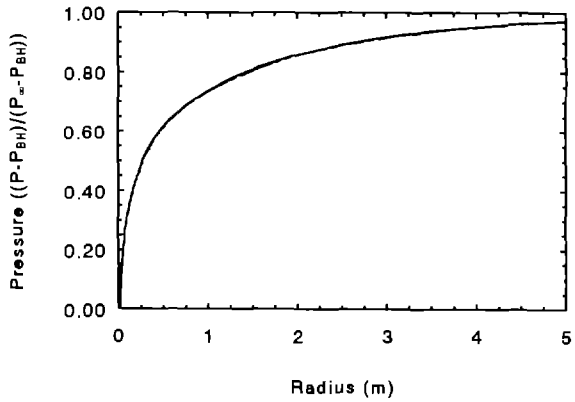

9-C2. Single-phase brine pressure profiles.

Figure 9-C. Results from variation in pore pressure at 1 year.

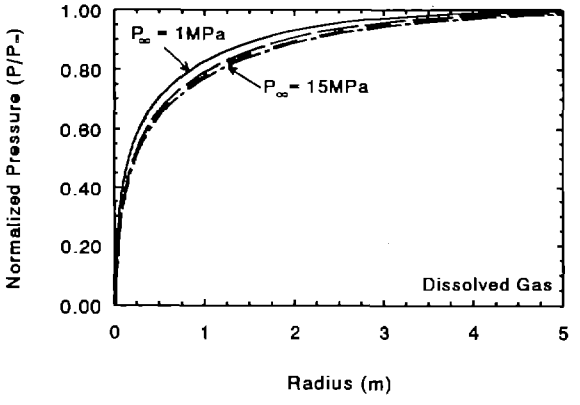

9-C3. Two-phase (dissolved gas) brine pressure profiles.

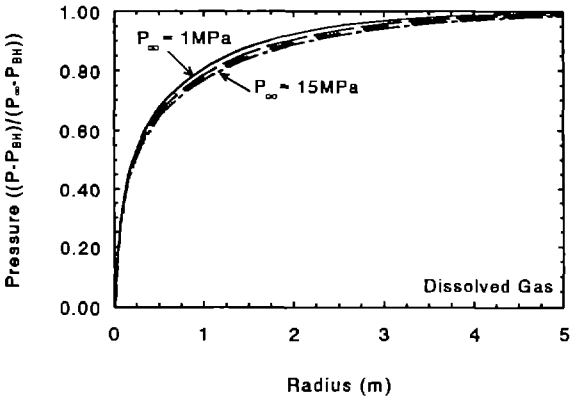

9-C4. Two-phase (dissolved gas) brine pressure profiles.

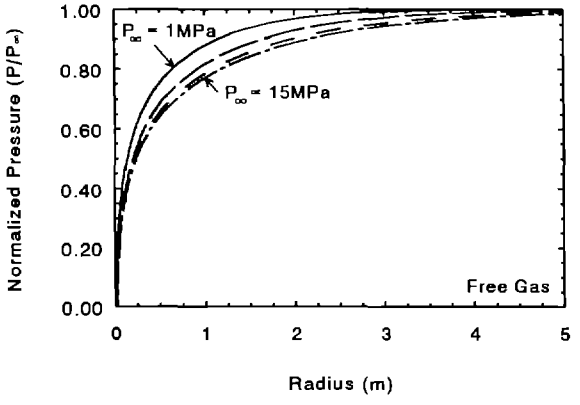

9-C5. Two-phase (free gas) brine pressure profiles.

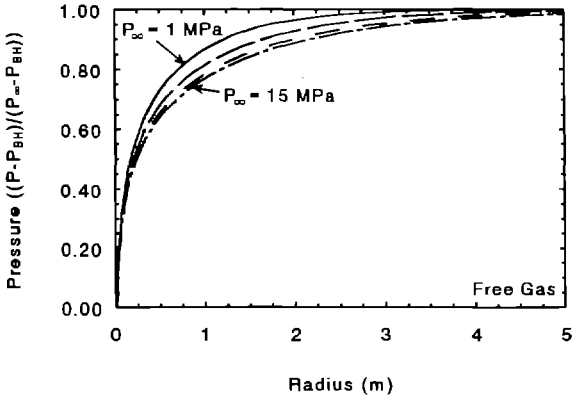

9-C6. Two-phase (free gas) brine pressure profiles.

Figure 9-C. Results from variation in pore pressure at 1 year (continued).

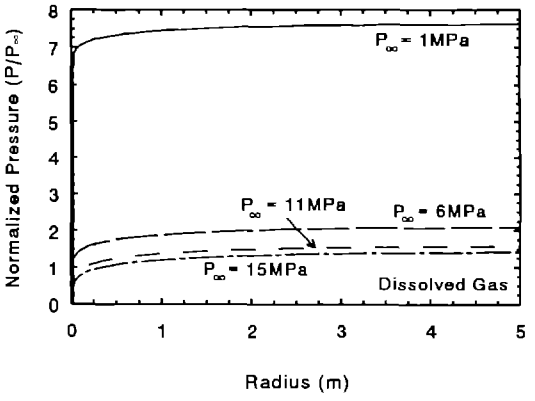

9-C7. Two-phase gas pressure profiles.

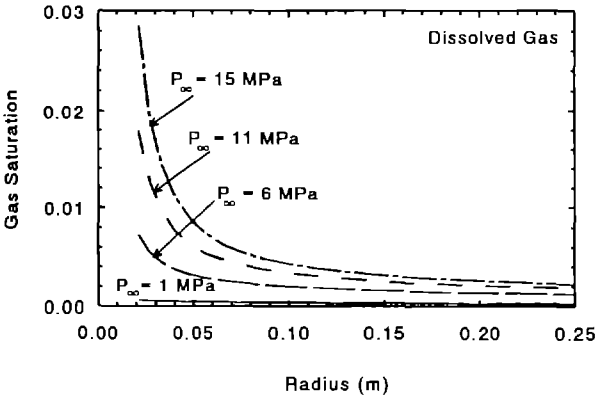

9-C8. Two-phase gas saturation profiles.

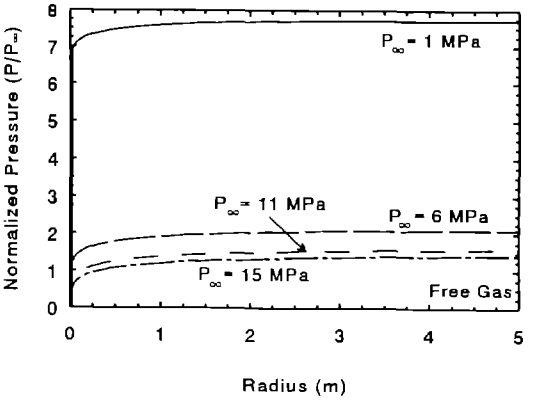

9-C9. Two-phase gas pressure profiles.

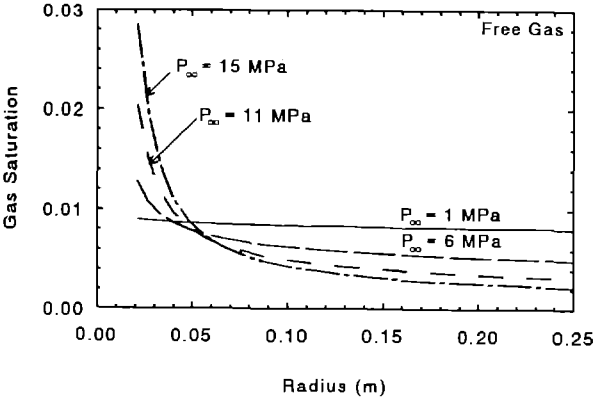

9-C10. Two-phase gas saturation profiles.

Figure 9-C. Results from variation in pore pressure at 1 year (continued).

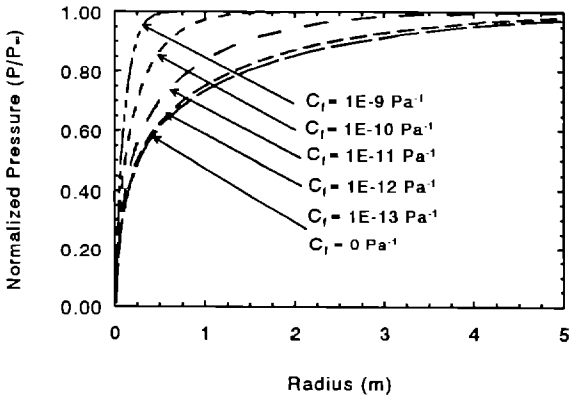

9-D1. Single-phase brine pressure profiles.

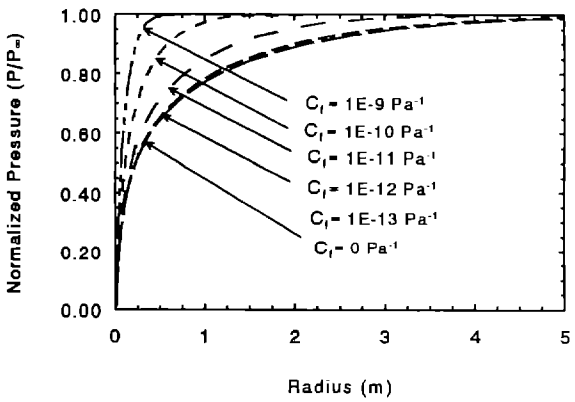

9-D2. Two-phase brine pressure profiles.

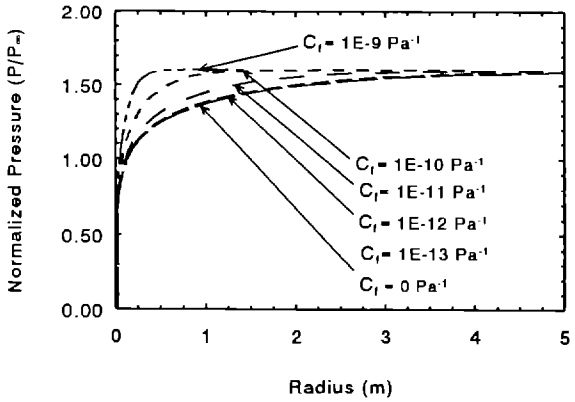

9-D3. Two-phase gas pressure profiles.

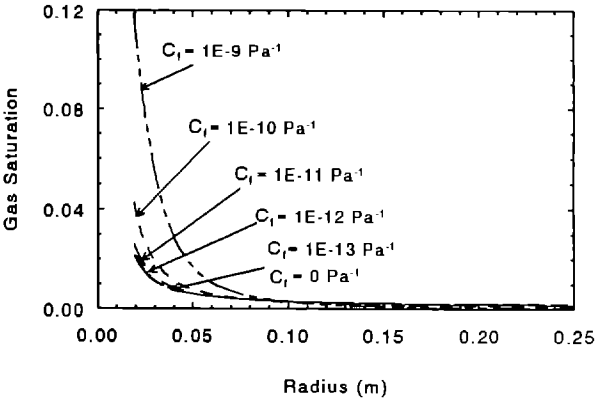

9-D4. Two-phase gas saturation profiles.

Figure 9-D. Results from variation in formation compressibility at 1 year.

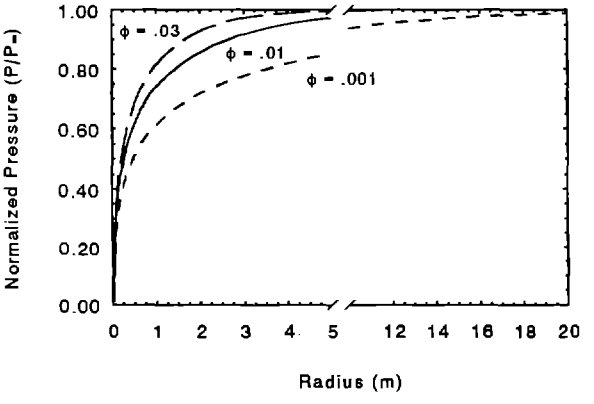

9-E1. Single-phase brine pressure profiles.

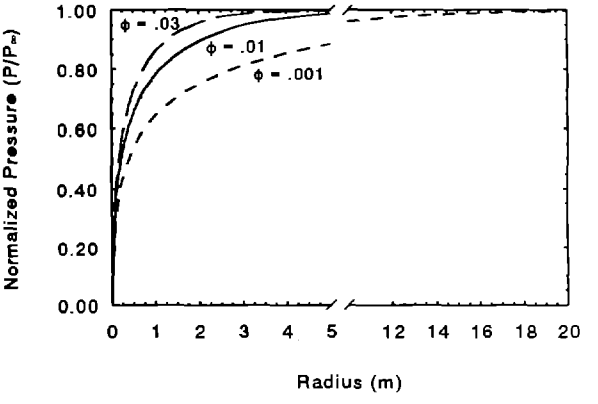

9-E2. Two-phase brine pressure profiles.

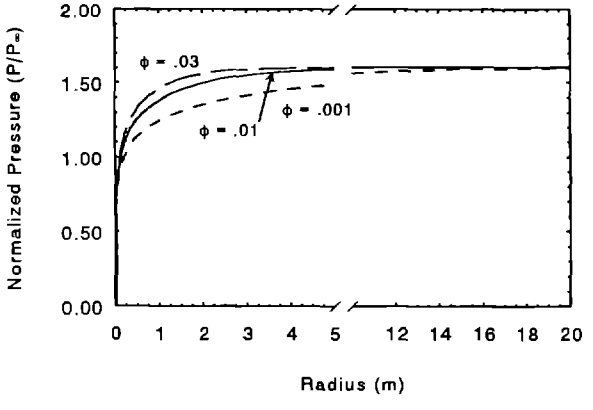

9-E3. Two-phase gas pressure profiles.

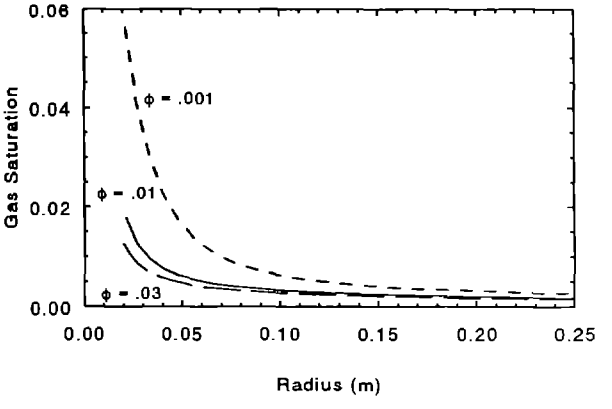

9-E4. Two-phase gas saturation profiles.

Figure 9-E. Results from variation in porosity at 1 year.

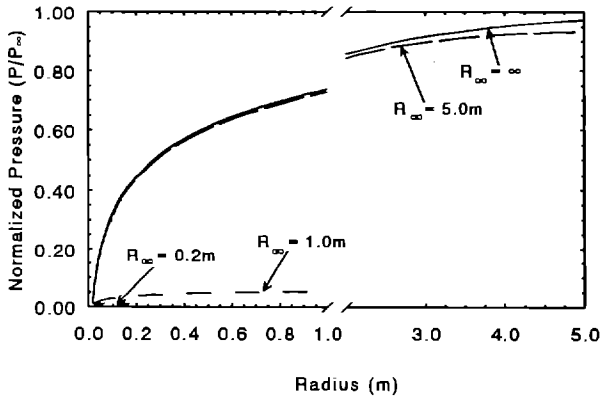

9-F1. Single-phase brine pressure profiles.

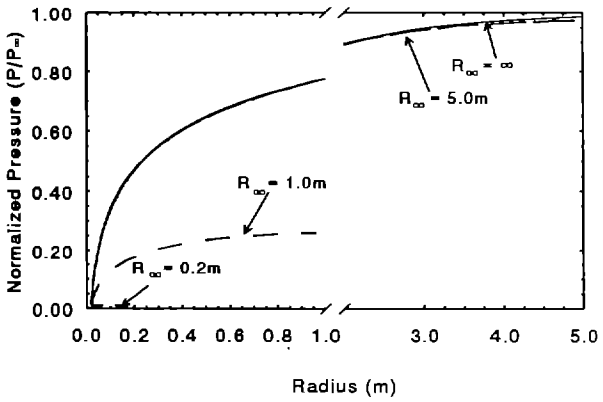

9-F2. Two-phase brine pressure profiles.

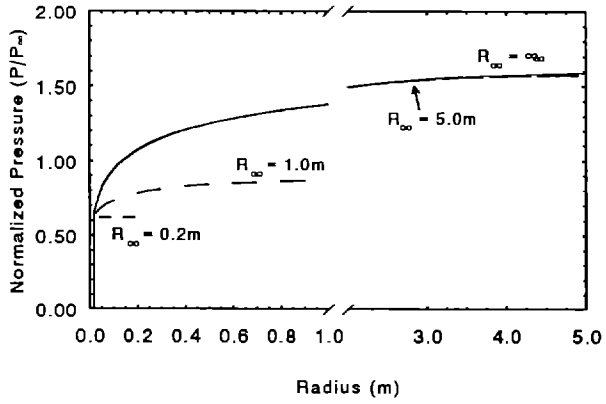

9-F3. Two-phase gas pressure profiles.

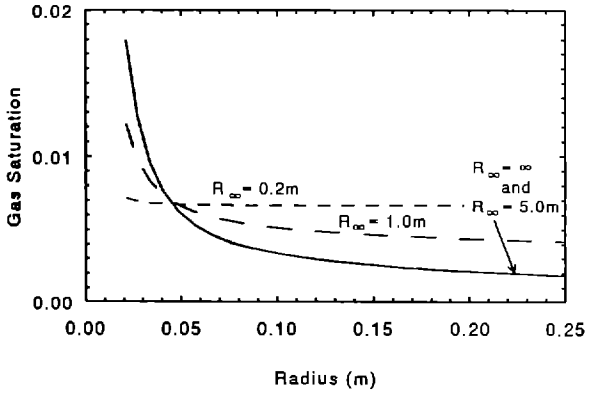

9-F4. Two-phase gas saturation profiles.

Figure 9-F. Results from variation in source radius at 1 year.

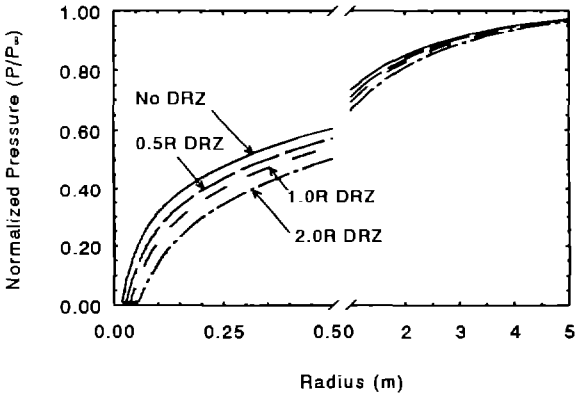

9-G1. Single-phase brine pressure profiles.

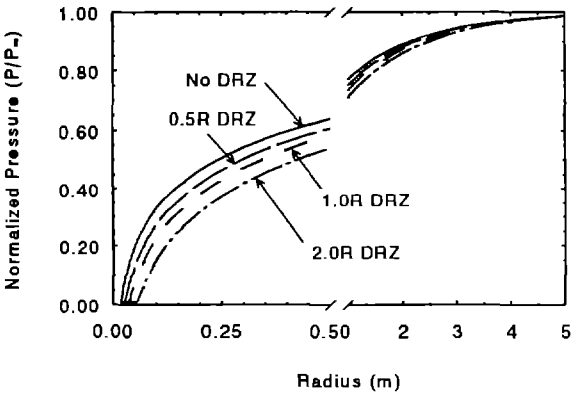

9-G2. Two-phase brine pressure profiles.

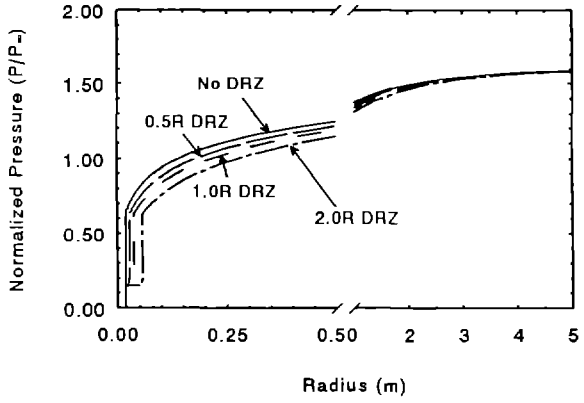

9-G3. Two-phase gas pressure profiles.

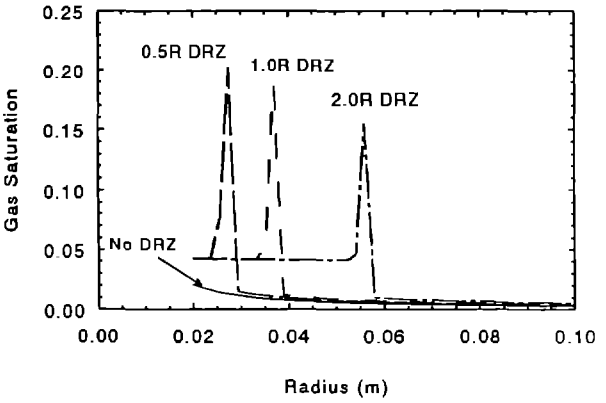

9-G4. Two-phase gas saturation profiles.

Figure 9-G. Results from variation in DRZ distance at 1 year.

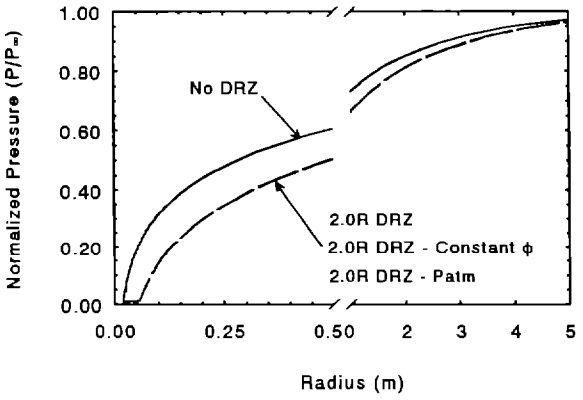

9-H1. Single-phase brine pressure profiles.

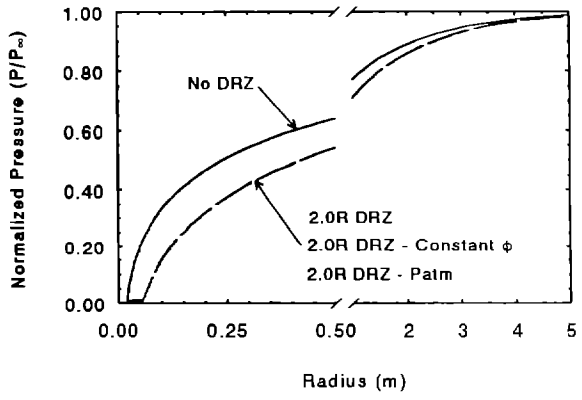

9-H2. Two-phase brine pressure profiles.

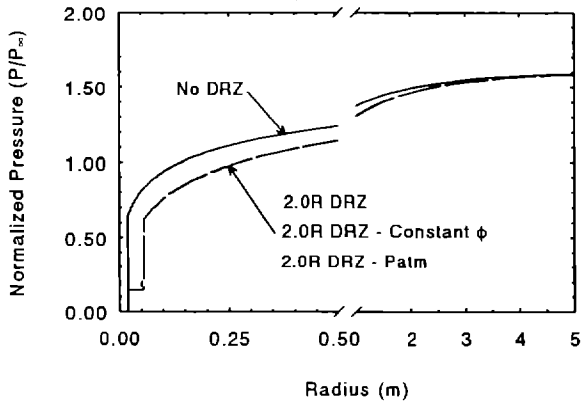

9-H3. Two-phase gas pressure profiles.

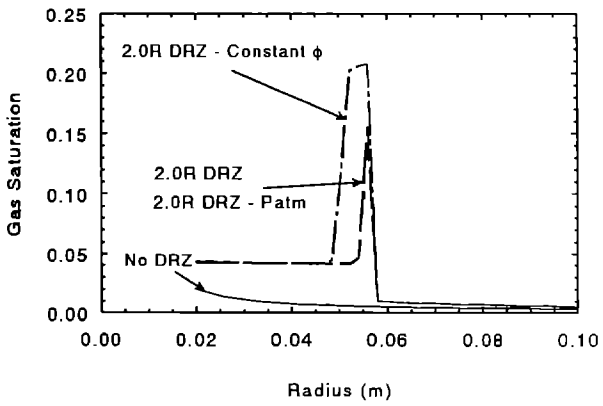

9-H4. Two-phase gas saturation profiles.

Figure 9-H. Results from variation in DRZ porosity and pressure at 1 year.

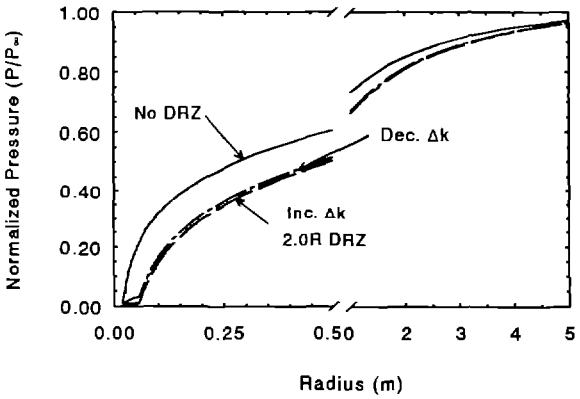

9-I1. Single-phase brine pressure profiles.

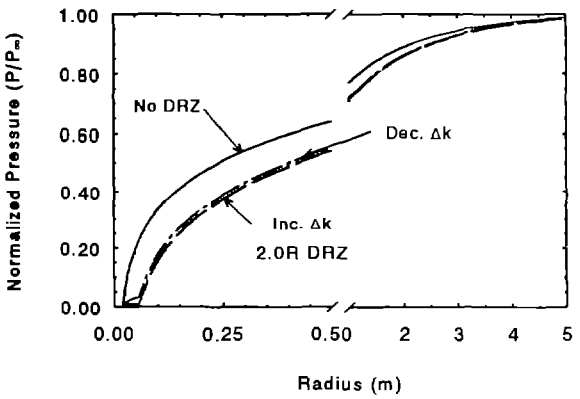

9-I2. Two-phase brine pressure profiles.

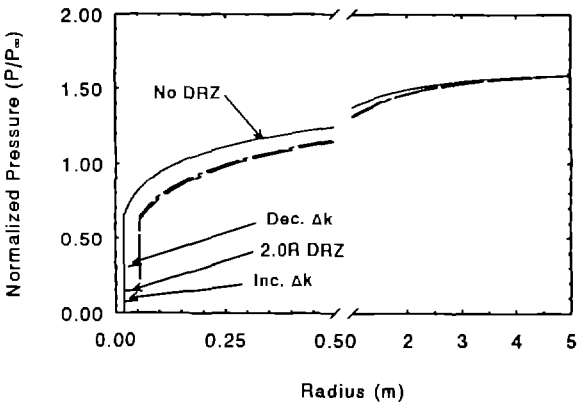

9-I3. Two-phase gas pressure profiles.

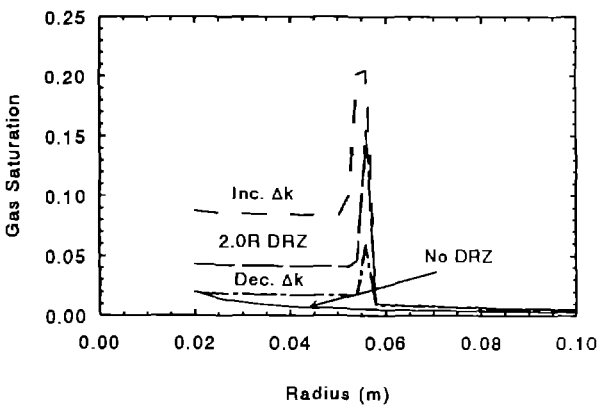

9-I4. Two-phase gas saturation profiles.

Figure 9-I. Results from variation in DRZ permeability contrast at 1 year.

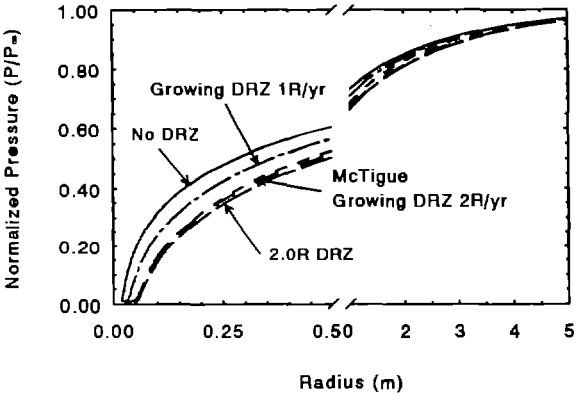

9-J1. Single-phase brine pressure profiles.

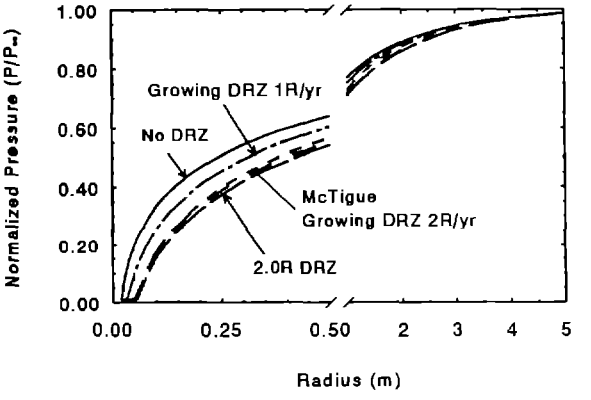

9-J2. Two-phase brine pressure profiles.

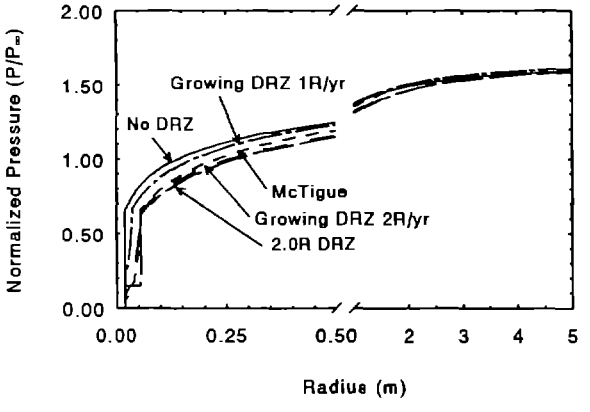

9-J3. Two-phase gas pressure profiles.

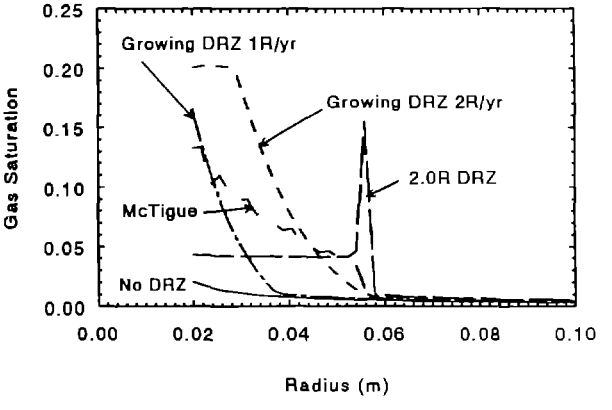

9-J4. Two-phase gas saturation profiles.

Figure 9-J. Results from variation in DRZ permeability distribution at 1 year.

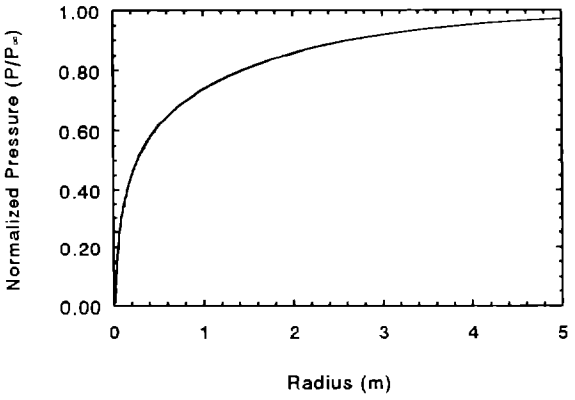

9-K1. Single-phase brine pressure profile.

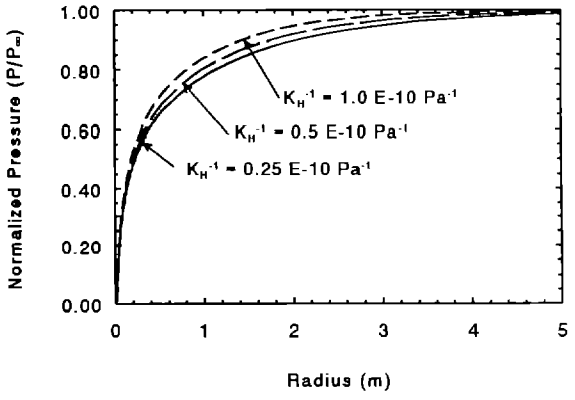

9-K2. Two-phase brine pressure profiles.

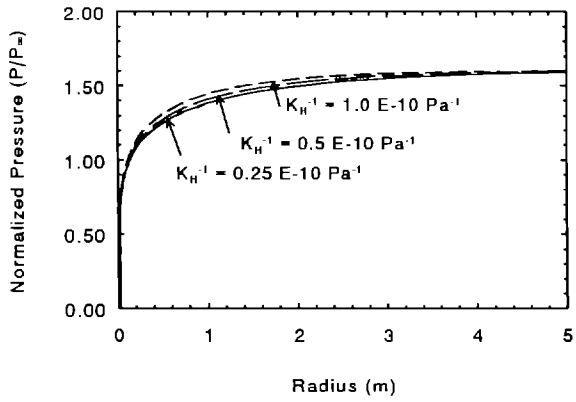

9-K3. Two-phase gas pressure profiles.

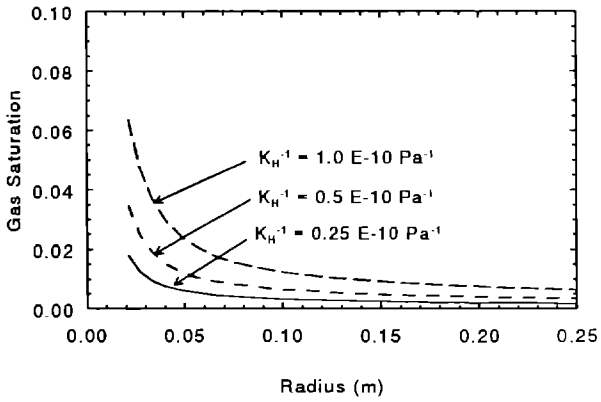

9-K4. Two-phase gas saturation profiles.

Figure 9-K. Results from variation in gas solubility at 1 year.

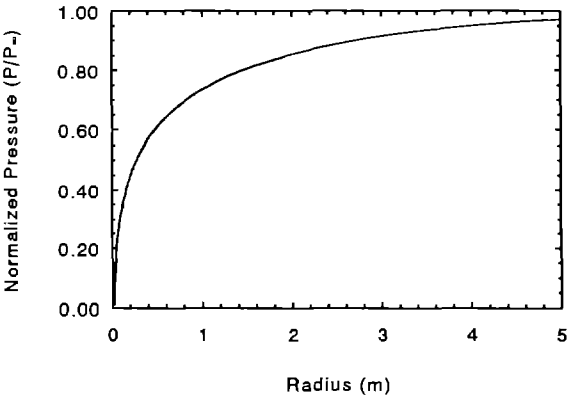

9-L1. Single-phase brine pressure profile.

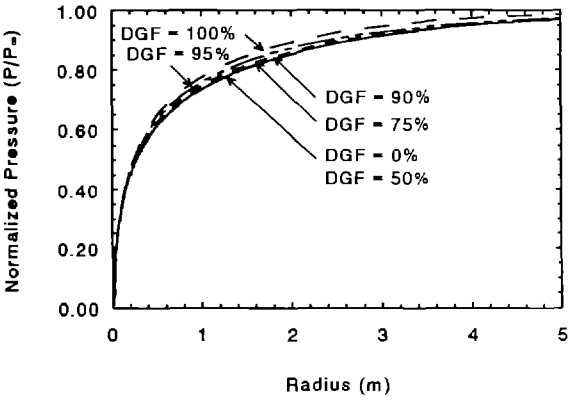

9-L2. Two-phase brine pressure profiles.

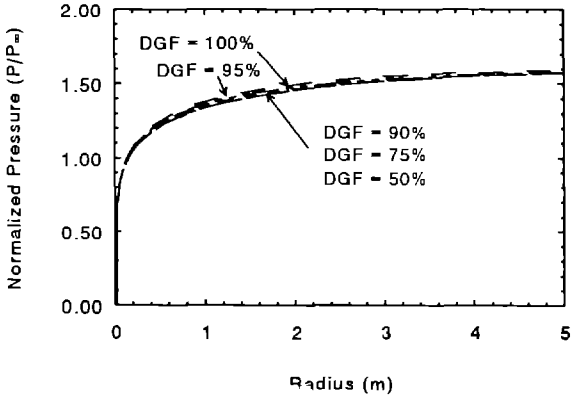

9-L3. Two-phase gas pressure profiles.

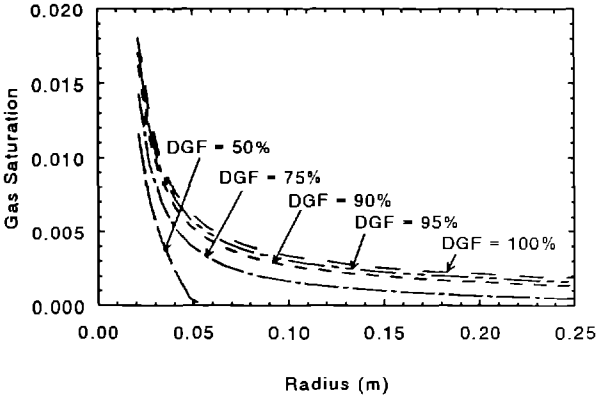

9-L4. Two-phase gas saturation profiles.

Figure 9-L. Results from variation in initial dissolved gas fraction at 1 year.

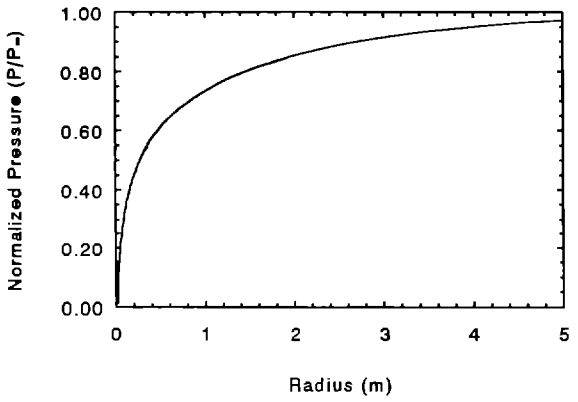

9-M1. Single-phase brine pressure profile.

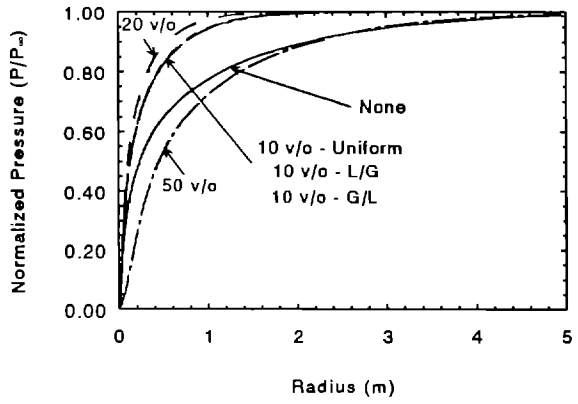

9-M2. Two-phase brine pressure profiles.

Figure 9-M. Results from variation in free gas fraction at 1 year.

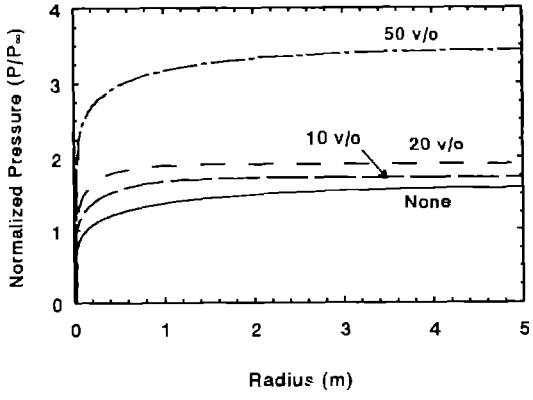

9-M3. Two-phase gas pressure profiles.

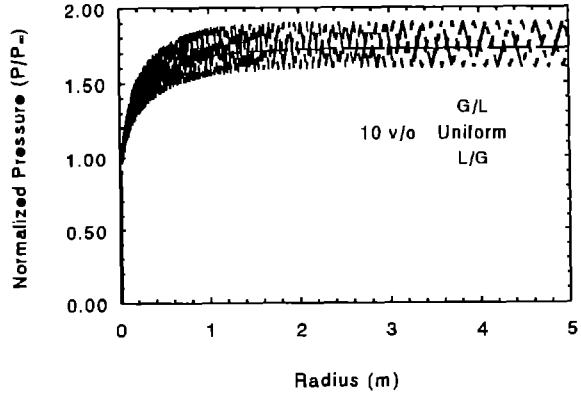

9-M4. Two-phase gas pressure profiles.

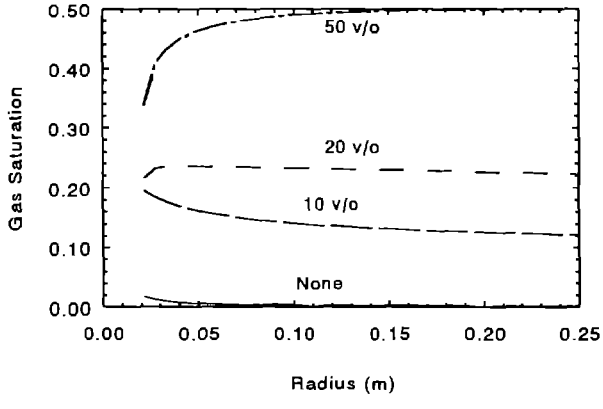

9-M5. Two-phase gas saturation profiles.

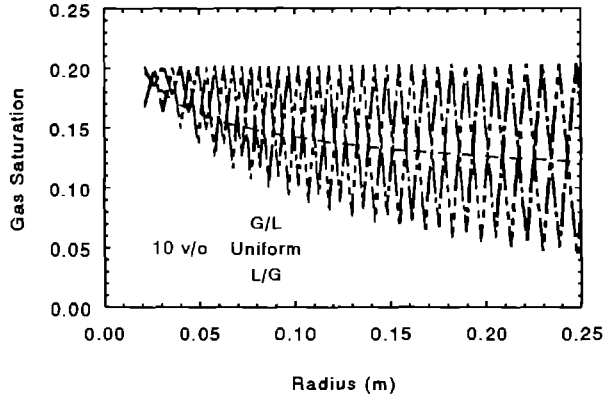

9-M6. Two-phase gas saturation profiles.

Figure 9-M. Results from variation in free gas fraction at 1 year (continued).

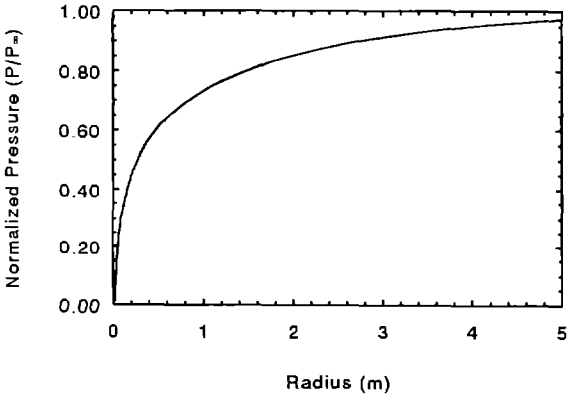

9-N1. Single-phase brine pressure profile.

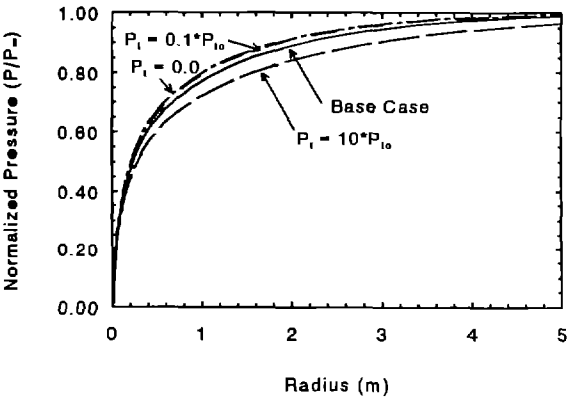

9-N2. Two-phase brine pressure profiles.

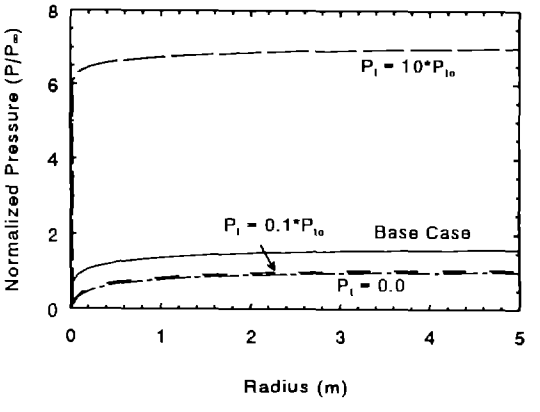

9-N3. Two-phase gas pressure profiles.

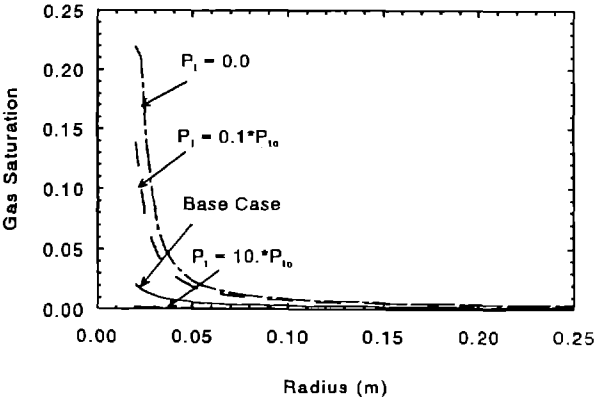

9-N4. Two-phase gas saturation profiles.

Figure 9-N. Results from variation in capillary pressure magnitude at 1 year.

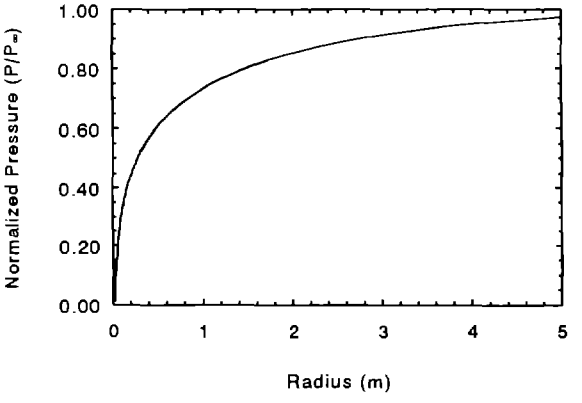

9-01. Single-phase brine pressure profile.

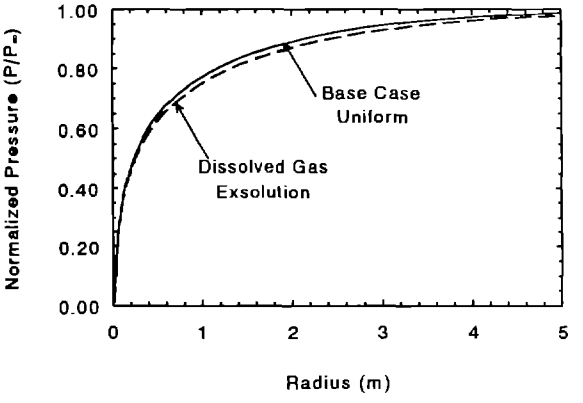

9-02. Two-phase brine pressure profiles.

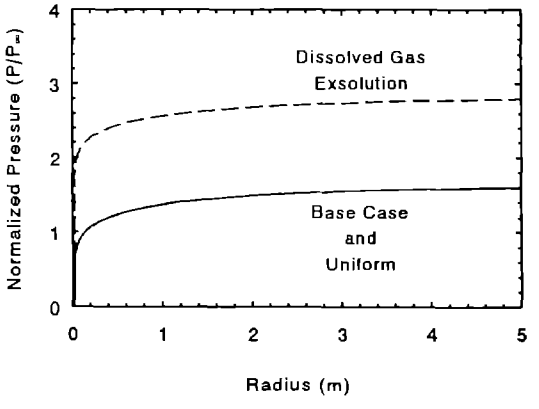

9-03. Two-phase gas pressure profiles.

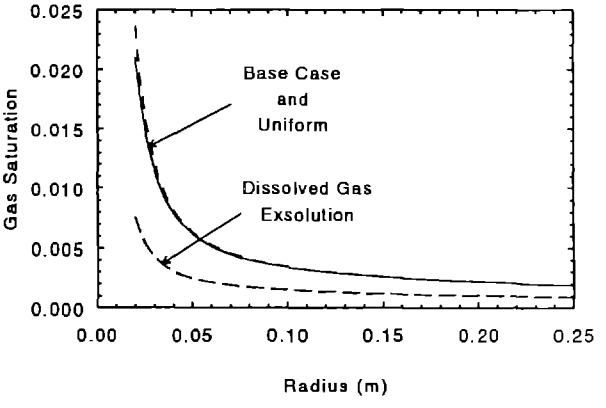

9-04. Two-phase gas saturation profiles.

Figure 9-0. Results from variation in capillary pressure shape at 1 year.

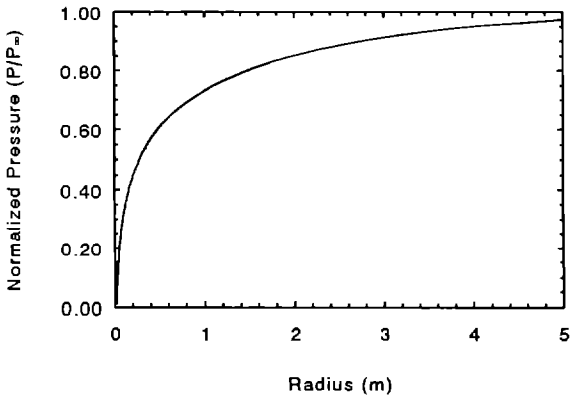

9-P1. Single-phase brine pressure profile.

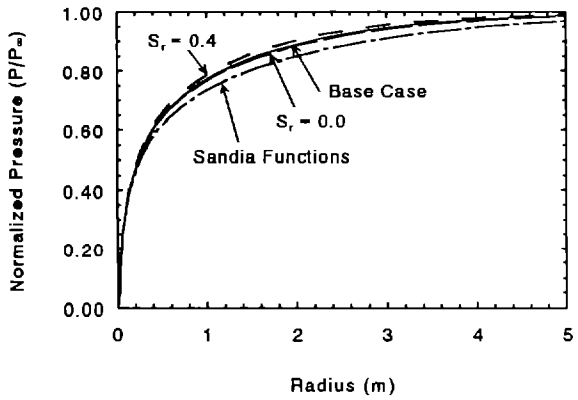

9-P2. Two-phase brine pressure profiles.

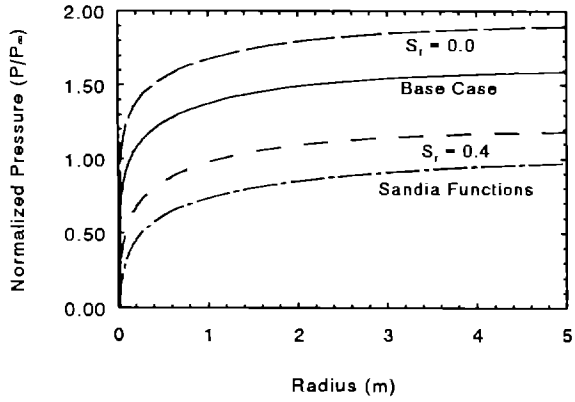

9-P3. Two-phase gas pressure profiles.

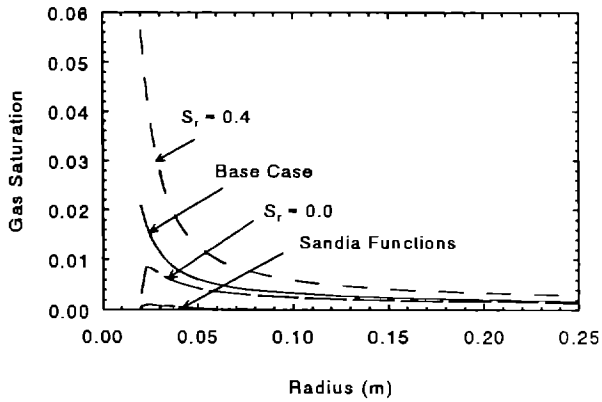

9-P4. Two-phase gas saturation profiles.

Figure 9-P. Results from variation in two-phase characteristic curves at 1 year.

SUMMARY AND DISCUSSION

Single-Phase Brine Inflow

As was discussed in detail in the Introduction, the single-phase brine inflow rate for uniform properties should and does scale directly with the borehole radius, pressure difference, and porosity. The scaling is more complicated for the other cases including permeability, formation compressibility, source radius, and the presence of a DRZ. The single-phase brine inflow rate can have a large range of values, especially if a DRZ is present, although the significant differences from the base case results are generally confined to times less than 10^4 seconds (3 hours); this time translates into about 18 years on the repository scale (R=4.5 m). Because this behavior occurs so early, the values may be additionally influenced by the borehole drilling process.

The only variation that leads to an increasing brine inflow rate with time, which is commonly observed in the WIPP underground, is a growing DRZ. While the observed rate of increase over the last six months of the simulation is small (<1% and 4% for 1R/yr and 2R/yr, respectively), the rate could be enhanced by increasing the growth rate or other modifications.

Single-Phase Inferred Parameters

Straight-line fits to the inverse brine inflow data were generally good representations of the synthetic "data" generated by the simulations. The fits were often applicable after only one day, although the minimum time period increased to about 1 month for the high formation compressibility case. The fit is also applicable for the case of a constant distance DRZ. The fit for the DRZ cases seems to have a "kink" in the inverse flux plot, which may be a mechanism to identify the presence of a DRZ. A fit could not be generated for the growing DRZ cases because the inverse brine inflow data decreases with time toward the end of the simulation. The fit generated for a limited source radius is questionable late in time.

The inferred permeability from these straight-line fits is generally good (within 10%) except for the growing DRZ and limited brine source cases. The diffusivity values have a much larger error, generally within a factor of 2, for the above problem variations plus situations with a DRZ. The values can be considerably improved if the outside radius of the DRZ is used to infer the diffusivity.

Accurate prediction of the permeability is much more important than the diffusivity as far as the brine inflow rate is concerned. As discussed in Appendix E, the brine inflow rate varies linearly with the permeability for a constant value of the diffusivity. However, in the reverse case, an order of magnitude change in the diffusivity for a constant permeability only changes the brine inflow rate by about 30%. Thus, the more important parameter, the permeability, is well predicted in all the cases considered.

Two-Phase Brine Inflow

The single-phase brine inflow rate could be normalized by a number of factors including borehole radius, pressure difference, and porosity. While the borehole radius scaling still seems to work for two-phase (dissolved gas) conditions, the pressure difference and porosity scalings are only approximate.

The ratio of the two-phase to single-phase brine inflow rate varies considerably. For a highly compressible formation ($C_f = 10^{-9}$ Pa^{-1}), the maximum ratio is close to 1.0, while the maximum value increases to about 1.5 for the incompressible base case. The maximum ratio is about 20 with a DRZ, and 10^4 or greater for a limited brine source. These maximum ratios occur at early time ($<10^4$ seconds) except for a limited brine source which occurs at 1 year.

As for single-phase conditions, the only variation with an increasing brine inflow rate with time is a growing DRZ. No other two-phase conditions analyzed resulted in an increasing brine inflow situation.

For variation of the initial free gas fraction, the maximum two-phase brine inflow rate is largest at 10 v/o; the inflow rate was lower for no free gas, 20 v/o free gas, and 50 v/o free gas. This behavior is tied closely to the assumed 20 v/o residual gas saturation before the gas phase becomes mobile. At 20 v/o, flow of gas reduces the driving force, so the inflow rate of brine is reduced. For 50 v/o, another mechanism dominates. As the gas flows into the borehole, it expands and becomes unsaturated, and all the inflowing brine is evaporated by the gas. Thus, the brine inflow rate for 50 v/o free gas is zero.

The effect of the two-phase characteristic curves on the two-phase brine inflow rate is minor. As will be discussed later, the same is not true for the effect on the gas inflow rate.

Finally, some relatively minor limitations in TOUGH have been identified regarding the density of the flowing fluid. The liquid (brine) density is evaluated at the gas pressure, and the mass of dissolved gas is neglected in

the mass flowing between volumes. These limitations are not a concern for analyses typically conducted for the WIPP. However, they should be kept in mind when trying to compare cases with minor differences.

Two-Phase Inferred Parameters

Although the straight-line fits are only directly applicable to single-phase conditions, the fits work quite well for most two-phase (dissolved gas) situations. The "kink" that was seen for the single-phase fits indicative of a DRZ is also present for two-phase conditions. In addition, this "kink" has other features that seem to indicate variation of the porosity in the DRZ. Whether this behavior can be used as a measure of the formation characteristics remains to be seen.

As with single-phase conditions, the inferred permeability is well predicted, while significant errors exist for the diffusivity. In general, the inferred diffusivity values are a factor of 2 lower than the single-phase counterparts. The actual values of the diffusivity are based on single-phase conditions.

Problems with the inferred parameters are seen for limited brine source and, of course, the growing DRZ variation. The DRZ diffusivity predictions are considerably low, which can be improved if the outside DRZ radius is used. Values of the diffusivity are also low by about an order of magnitude if significant free gas is present. No fit could be generated for the 50 v/o free gas case because the net brine inflow rate is zero.

Two-Phase Gas Inflow

In many cases, the two-phase gas inflow rate is smaller by about three orders of magnitude than the brine inflow rate in terms of mass. However, at the assumed borehole conditions of 0.1 MPa, the volume ratio is much greater, and gas saturation values for the inflowing fluid vary from 0.36 to 0.25 for the base case.

The variation of two-phase parameters, especially the two-phase characteristic curves and the amount of free gas, give a wide range in the gas mass inflow and gas saturation values. While many of the gas inflow rates are reasonably consistent with the two-phase brine inflow variation, others are dramatically different. In the case of 50 v/o free gas, the gas inflow rate is about 30,000 times greater than for no free gas, while the net brine inflow rate is zero for the 50 v/o free gas case. An order of magnitude increase in the capillary pressure causes about an order of

magnitude increase in the gas inflow rate compared to the base case, while the brine inflow rate is only slightly lower. The gas saturation of the inflowing fluid also shows dramatic changes for these cases. Thus, gas inflow cannot be directly inferred from brine inflow measurements alone. Conversely, measurement of brine inflow and gas inflow does not uniquely determine the two-phase parameters; other measurements such as the free gas fraction and the two-phase characteristic curves are needed as well.

The presence of a DRZ causes an interesting modification of the gas inflow rate. While the brine inflow rate is higher if a DRZ is present, the gas inflow rate decreases after initially being higher. This behavior is caused by gas being trapped in the DRZ. As the brine flows into the DRZ, the lower pressure causes gas to come out of solution in the DRZ before reaching the borehole. If the gas saturation is less than the mobile limit, this gas becomes trapped, and the gas inflow rate to the borehole is lower until the gas phase becomes mobile. This behavior is also noted in the gas saturation profiles.

Pressure and Gas Saturation Distributions

The pressure and gas saturation profiles in the formation show that, for the base case, the radius of influence is about 4 m at one year for a 0.019 m radius borehole. This radius of influence is affected by a number of parameters including the formation compressibility, porosity, and two-phase conditions. For a high formation compressibility ($C_f = 10^{-9}$ Pa^{-1}), the radius is reduced to about 0.5 m. Porosity values of 0.001, 0.01 (base case), and 0.03 have a radius of influence of 12, 4, and 2.5 m, respectively. For two-phase conditions, the radius is reduced to 3 m for brine saturated with dissolved gas, to 1 m with 10 v/o free gas, to 0.7 m with 20 v/o free gas. For 50 v/o free gas, the radius increases to about 4 m because the free gas is mobile.

The gas saturation profiles show the DRZ gas-trapping behavior noted in the gas inflow section. The gas saturation values are much greater at the outer edge of the DRZ since gas is trapped in the DRZ until it becomes mobile. In cases without a DRZ, the gas saturation peaks at the borehole wall, and most of the free gas is present within a few centimeters of the borehole. This behavior of the gas saturation profile may be useful in determining the presence of a DRZ if significant dissolved gas is present in the resident brine.

CONCLUSIONS

Brine inflow sensitivity studies have been conducted using a one-dimensional model to try to identify the effect of different parameter variations including two-phase conditions on brine inflow measurements. Many of the effects were expected, such as the effect of permeability on the brine inflow rate, and the usefulness of the late-time asymptotic technique in inferring formation permeabilities and diffusivities for single-phase flow. Some of the other effects were a pleasant surprise such as the applicability of the asymptotic method in inferring formation characteristics for two-phase (dissolved gas and some free gas) conditions. Finally, some results indicate that many parameters only influence brine inflow to boreholes at very small times (<1 day).

The general conclusions from this investigation are:

- The late-time asymptotic approach for inferring formation parameters from brine inflow data is reliable (within 10%) in predicting the formation permeability for most single-phase and two-phase conditions. Problems occur for limited brine sources, high initial free gas fractions, and growing DRZs.

- The late-time asymptotic approach is less reliable in evaluating the formation diffusivity, although this parameter is not as crucial as the permeability. Typical errors are within a factor of 2. Again, problems occur for limited brine sources, high initial free gas fractions, and growing DRZs. In addition, for cases with a stationary DRZ, the error in the inferred diffusivity can be about a factor of 10. Use of the outer radius of the DRZ in evaluating the formation diffusivity improves the predictive capability to within a factor of 2.

- Gas inflow rates vary orders of magnitude with variations in the two-phase characteristic curves and free gas fractions. Note that the brine inflow rate variation for these conditions is minimal (within a factor of 2). Therefore, any inference on the free gas conditions in the formation must include knowledge of the two-phase characteristic curves. The presence of a DRZ also affects the gas inflow rate and the distribution of gas in the formation.

- The zone of influence that the borehole measures is often small. After 1 year, for a 0.019-m radius borehole, this distance could be as small as 0.5 m from the center of the borehole for a highly compressible formation or about 1.0 m if there is a significant amount of free gas present.

- The only situation that resulted in the commonly observed increasing brine inflow rate with time is a growing DRZ. Unfortunately, this also is a case where the late-time asymptotic approach did not work and formation parameters can not be inferred.

- Additional two-dimensional simulations are planned to address other effects such as excavation-borehole interactions and the influence of stratigraphy.

NOMENCLATURE

A	curve fit parameter, borehole surface area
B	curve fit parameter
c	diffusivity
C_f	formation compressibility
D	natural log of DRZ permeability ratio
DGF	dissolved gas fraction
DRZ	disturbed rock zone
G/L	gas/liquid
J_o	Bessel function
k	permeability
Δk	DRZ permeability contrast
k_a	undisturbed formation permeability
k_{rg}	gas phase relative permeability
k_{rl}	liquid phase relative permeability
K	hydraulic conductivity
K_H	Henry's constant
L	length of borehole
L/G	liquid/gas
$\dot{m}$	mass flow rate
P	pressure
P_{atm}	atmospheric pressure
P_c	capillary pressure
P_{cmax}	maximum value of capillary pressure
P_o	initial brine pressure
P_t	threshold pressure
P_{to}	base case threshold pressure
P_∞	far-field brine pore pressure
q	brine flux
r	radial distance from borehole centerline
R	borehole radius, square root of correlation coefficient
R^*	effective borehole radius
R_∞	far-field effective radius
S	storativity
S_e	effective liquid saturation (equation (F-4))
S_{gr}	residual gas saturation
S_{lr}	residual liquid saturation
S_{ls}	complete liquid saturation
S_r	residual saturation for both gas and liquid
S_s	specific storage (S/L)
S^*	effective liquid saturation (equation (F-8))
t	time
t_*	dimensionless time, ct/R^2
T	transmissivity

u	dummy variable
v/o	volume percent
V_p	pore volume
Y_o	Bessel function
z	characteristic distance for DRZ permeability variation

Greek

α	porous medium compressibility
α_p	pore compressibility
β_l	liquid compressibility
β_s	solid compressibility
γ	Euler's constant = 0.5772...
Γ	$\exp(\gamma)$
λ	pore-size distribution parameter
ρ	brine density
μ	brine viscosity
ϕ	porosity

REFERENCES

Beauheim, R.L., G.J. Saulnier, Jr., and J.D. Avis. 1991. *Interpretation of Brine-Permeability Tests of the Salado Formation at the Waste Isolation Pilot Plant Site: First Interim Report*. SAND90-0083. Albuquerque, NM: Sandia National Laboratories.

Cygan, R.T. 1991. *The Solubility of Gases in NaCl Brine and a Critical Evaluation of Available Data*. SAND90-1946. Albuquerque, NM: Sandia National Laboratories.

Davies, P.B. 1991. *Evaluation of the Role of Threshold Pressure in Controlling Flow of Waste-Generated Gas into Bedded Salt at the Waste Isolation Pilot Plant*. SAND90-3246. Albuquerque, NM: Sandia National Laboratories.

de Marsily, G. 1986. *Quantitative Hydrology*. Academic Press, Inc. Orlando, FL: 1986.

Finley, S.J., D.J. Hanson, and R. Parsons. 1992. "Small-Scale Brine Inflow Experiments--Data Report through 6/6/91." SAND91-1956. Albuquerque, NM: Sandia National Laboratories.

Lappin, A.R., R.L. Hunter, eds., D.P. Garber, P.B. Davies, assoc. eds. 1989. *Systems Analysis, Long-Term Radionuclide Transport, and Dose Assessments, Waste Isolation Pilot Plant (WIPP), Southeastern New Mexico; March 1989*. SAND89-0462. Albuquerque, NM: Sandia National Laboratories.

McTigue, D.F. 1989. "Appendix A.8: Increased Permeability Near Storage Rooms: Effect on Brine Inflow Computed with a Darcy Model," *Systems Analysis, Long-Term Radionuclide Transport, and Dose Assessments, Waste Isolation Pilot Plant (WIPP), Southeastern New Mexico; March 1989*. Eds. A.R. Lappin, R.L. Hunter, D.P. Garber, and P.B. Davies. SAND89-0462. Albuquerque, NM: Sandia National Laboratories. A-105 through A-115.

McTigue, D.F., S.J. Finley, J.H. Gieske, and K.L. Robinson. 1991. Appendix A: "Compressibility Measurements on WIPP Brines," *Preliminary Comparison with 40 CFR Part 191, Subpart B for the Waste Isolation Pilot Plant, December 1991; Volume 3: Reference Data*. WIPP Performance Assessment Division. SAND91-0893/3. Albuquerque, NM: Sandia National Laboratories. A-79 through A-98.

Nowak, E.J., and D.F. McTigue. 1987. *Interim Results of Brine Transport Studies in the Waste Isolation Pilot Plant (WIPP)*. SAND87-0880. Albuquerque, NM: Sandia National Laboratories.

Nowak, E.J., D.F. McTigue, and R. Beraun. 1988. *Brine Inflow to WIPP Disposal Rooms: Data, Modeling, and Assessment*. SAND88-0112. Albuquerque, NM: Sandia National Laboratories.

Pruess, K. 1987. *TOUGH User's Guide*. NUREG/CR-4645. SAND86-7104. LBL-20700, August 1987.

Pruess, K. 1991. *TOUGH2 - A General-Purpose Numerical Simulator for Multiphase Fluid and Heat Flow*. LBL-29400, May 1991.

Stormont, J.C. 1990. *Summary of 1988 WIPP Facility Horizon Gas Flow Measurements*. SAND89-2497. Albuquerque, NM: Sandia National Laboratories.

Weast, R.C. 1984. *CRC Handbook of Chemistry and Physics*, 65th edition, CRC Press, Inc., Boca Raton, FL: 1984.

Webb, S.W., and J.C. Chen. 1990. "Phasic Pressure Difference Effects in Two-Phase Flow For Dissolved Gas Exsolution." *Proceedings of the TOUGH Workshop*. Berkeley, CA: Lawrence Berkeley Laboratory. September 13-14, 1990, pp. 107-112, LBL-29710, September 1990.

APPENDIX A:
ANALYTICAL SOLUTION FOR SEEPAGE TO A BOREHOLE

Sandia National Laboratories
Albuquerque, New Mexico 87185

date: March 6, 1991

to: Distribution

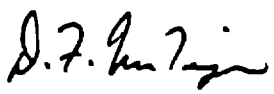

from: D. F. McTigue, 1511

subject: Analytical Solution for Seepage to a Borehole

Introduction

One of the simplest conceptual models for the seepage of brine in salt assumes that the salt is a brine-saturated porous medium. Analytical solutions exist for simple flow configurations in such a system [*e.g.*, 1, 2], and serve as useful tools for the interpretation of data. In particular, the solution for the flow rate to an open borehole can be fit to data to estimate two critical parameters, *e.g.*, the initial formation pressure and the hydraulic diffusivity (given an independent estimate of the capacitance). Analytical solutions are also used as "benchmarks" for the verification of computer codes designed to solve a broader class of problems.

Radial flow to a borehole has been discussed extensively in previous reports [1, 2]. However, the practical importance of this problem has been highlighted by its recent application to both data interpretation and code benchmarking. This has prompted a more exhaustive study of the exact solution, its numerical evaluation, and its asymptotic behavior.

This memo reports the results of a detailed examination of the exact solution for radial seepage to an open borehole in a homogeneous medium. The study reveals some inaccuracies in previous evaluations of the solution and identifies means to correct these errors. Updated pressure profiles and flux histories are provided for reference. Also, a higher-order approximation to the flux at late time is derived, and the applicability of the asymptotic solution is discussed.

Model Description

The standard, linearized, hydrological model for flow in a porous medium represents the evolution of the excess pore pressure by a diffusion equation. A detailed development is given, for example in [1]. An open, circular hole introduced into an unbounded, homogeneous medium at some initial pressure p_0 results in radial flow toward the hole, associated with relaxation of the pressure in a zone that grows diffusively outward from

the hole. The exact statement of the initial-value problem is:

$$\frac{\partial p}{\partial t} - \frac{c}{r}\frac{\partial}{\partial r}\left(r\frac{\partial p}{\partial r}\right) = 0, \tag{1}$$

$$p(r,t) = p_0, \tag{2}$$

$$p(a,t) = 0, \tag{3}$$

$$\lim_{r\to\infty} p(r,t) = p_0, \tag{4}$$

where c is the hydraulic diffusivity and a is the radius of the borehole. An analytical solution to (1)–(4) is well known [*e.g.*, 3, pp. 87–88]:

$$\frac{p}{p_0} = -\frac{2}{\pi}\int_0^\infty \exp(-u^2 t_*) f(u;\, r_*)\frac{du}{u}, \tag{5}$$

where

$$f(u;\, r_*) = \frac{J_0(ur_*)Y_0(u) - Y_0(ur_*)J_0(u)}{J_0^2(u) + Y_0^2(u)}, \tag{6}$$

and where $t_* = ct/a^2$, $r_* = r/a$, and J_0 and Y_0 are Bessel functions of the first and second kind of order zero, respectively.

Although (5) is a closed-form solution to the problem of interest, it proves to be difficult to evaluate accurately. The source of the difficulty is that the integrand is singular at the lower limit of integration. However, the singularity is integrable, so that (5) can be evaluated accurately if appropriate care is taken. Proper account of this was not taken in the calculations shown in [1] and [2]; one purpose of this memo is to provide corrected calculations.

In order to isolate the singular part of the integrand, one can partition the integral in (5) into two parts:

$$\frac{p}{p_0} = -\frac{2}{\pi}\int_0^\epsilon \exp(-u^2 t_*)\, f(u;\, r_*)\frac{du}{u} - \frac{2}{\pi}\int_\epsilon^\infty \exp(-u^2 t_*)\, f(u;\, r_*)\frac{du}{u}, \tag{7}$$

where ϵ can be chosen to be arbitrarily small. The expansions of $J_0(\zeta)$ and $Y_0(\zeta)$ for small argument are given by:

$$J_0(\zeta) = 1 - \frac{\zeta^2}{4} + \cdots, \tag{8}$$

$$Y_0(\zeta) = \frac{2}{\pi}\left(1 - \frac{\zeta^2}{4}\right)\ln\left(\frac{C\zeta}{2}\right) + \cdots, \tag{9}$$

where $C = \exp(\gamma)$, and $\gamma = 0.5772\ldots$ is Euler's constant. Substitution of (8) and (9) into the first integral in (7) and expansion about $u = 0$ gives, to leading order:

$$\lim_{u\to 0} -\frac{2}{\pi}\int_0^\epsilon \exp(-u^2 t_*)\, f(u, r_*)\frac{du}{u} = \ln r_* \int_0^\epsilon \frac{\exp(-u^2 t_*)}{\ln^2(Cu/2)}\frac{du}{u} + \cdots \quad . \tag{10}$$

This can be integrated by parts to yield

$$\lim_{u\to 0} -\frac{2}{\pi}\int_0^{\epsilon} \exp(-u^2 t_*)\, f(u, r_*)\frac{du}{u} = -\frac{\exp(-\epsilon^2 t_*)\ln r_*}{\ln(C\epsilon/2)} + O\left(\frac{\epsilon^2 t_*}{\ln \epsilon}\right) \quad . \tag{11}$$

Thus, (5) can be evaluated accurately by separating the singular part of the integrand, integrating it analytically, and evaluating the remainder by numerical quadrature. Substitution of (11) into (7) gives the final form used:

$$\frac{p}{p_0} \simeq -\frac{\exp(-\epsilon^2 t_*)\ln r_*}{\ln(C\epsilon/2)} - \frac{2}{\pi}\int_{\epsilon}^{\infty} \exp(-u^2 t_*)\, f(u;\, r_*)\frac{du}{u}. \tag{12}$$

Evaluations of (12) have been carried out, setting $\epsilon = 10^{-8}$, and performing the integral by the Gauss quadrature routine DGAUS8 in the SLATEC subroutine package. The error tolerance in the numerical integrator was set to ERR = 10^{-6}, and the calculations were carried out on a VAX 8650 using double-precision arithmetic. Figure 1 shows equation (12) evaluated for $1 \le r_* \le 5$ and $t_* = 0.01, 0.1, 0.5, 1.0, 5.0, 10.0, 50.0$. This figure is identical in scope to Figure 20 in [1]. The most significant differences in the corrected version shown here are evident at later time and larger radius, where the pressures are typically somewhat larger than in the original calculations. Thus, it appears that the numerical quadrature applied to (5) directly tends to underestimate the contribution near the singularity.

The exact numerical values on which Figure 1 is based are reproduced in Table 1 for reference. Note that the integration scheme appears to have some difficulty in resolving values asymptotically close to unity. For example, at $t_* = 0.01$, the dimensionless pressure reaches a maximum value of 0.9986 at $r_* = 1.6$, and *decreases* monotonically to 0.9952 at $r_* = 5.0$, rather than continuing to approach 1.0. No attempt has been made here to resolve this problem, as it appears to have little practical consequence.

Fluid Flux at the Borehole

The easiest quantity to measure in the field is the flux into the hole, $q_r(a,t)$, which can be obtained from (5) by application of Darcy's law:

$$q_r(a,t) = -\frac{k}{\mu}\frac{\partial p}{\partial r}(a,t) \quad , \tag{13}$$

where k is the permeability and μ is the brine viscosity. The resulting expression has been noted previously [1]:[1]

$$q_* = \frac{4}{\pi^2}\int_0^{\infty} \frac{\exp(-u^2 t_*)}{J_0^2(u) + Y_0^2(u)}\frac{du}{u}, \tag{14}$$

[1]There is a typographical error in equation (28) of reference [1]; the coefficient $4/\pi$ should read $4/\pi^2$.

where q_* is the magnitude of the normalized flux at the borehole, $q_* = |q_r|(a,t)/q_0 = -q_r(a,t)/q_0$, and the scale of the flux, q_0, is given by $q_0 = kp_0/\mu a$.

Equation (14) encounters the same difficulty discussed above in the context of the pressure profiles: the integrand is singular at $u = 0$, and numerical quadrature routines cannot easily resolve this. However, the singularity is of the same form as that in (5), and is therefore integrable. The identical procedure can be applied to (14). However, the same result can be achieved by differentiating (12) directly, giving:

$$q_* = -\frac{\exp(-\epsilon^2 t)}{\ln(C\epsilon/2)} + \frac{4}{\pi^2}\int_\epsilon^\infty \frac{\exp(-cu^2t/a^2)}{J_0^2(u)+Y_0^2(u)}\frac{du}{u}. \tag{15}$$

Evaluations of (15) have been carried out in the same fashion as those of (12) described above, again taking $\epsilon = 10^{-8}$, and ERR $= 10^{-6}$. The results are shown in Table 2 and in Figure 2. These results replace Figure 18 in [1] and Figure 1 in [2] (which was simply reproduced from the former reference). The fluxes computed here are slightly higher than those obtained in the older calculations, again because numerical quadrature applied directly to (14) underestimates the contribution near the singularity.

Late-Time, Asymptotic Flux

The asymptotic expansion of (14) for $t_* \gg 1$ takes a particularly simple form useful for fitting data. The development is reproduced here in detail because some care must be taken in order to obtain consistent higher-order corrections.

In order to find the late-time, asymptotic expansion of the fluid flux (14), let $\eta^2 = u^2 t_*$, so that large t_* corresponds to small arguments of the Bessel functions. Introduce the appropriate expansions for small argument (8–9), and expand the integrand:

$$\begin{aligned}\lim_{t_*\to\infty} q_* = & \int_0^\infty \frac{\exp(-\eta^2)}{\left[\ln\left(C\eta/2t_*^{1/2}\right)\right]^2}\left\{1 - \frac{\pi^2/4}{\left[\ln\left(C\eta/2t_*^{1/2}\right)\right]^2} + \cdots\right\}\frac{d\eta}{\eta} \\ & + \frac{1}{2t_*}\int_0^\infty \frac{\eta\exp(-\eta^2)}{\left[\ln\left(C\eta/2t_*^{1/2}\right)\right]^2}d\eta + \cdots\end{aligned} \tag{16}$$

where $C = \exp(\gamma)$, and $\gamma = 0.5772\ldots$ is Euler's constant. Integration of each term in (16) by parts yields:

$$\begin{aligned}\lim_{t_*\to\infty} q_* = & -2\int_0^\infty \frac{\eta\exp(-\eta^2)}{\ln(C\eta/2t_*^{1/2})}\left[1 - \frac{\pi^2}{6}(\eta^4 - 3\eta^2 + 1) + \cdots\right]d\eta \\ & - \frac{1}{t_*}\int_0^\infty \frac{\eta(\eta^2-1)\exp(-\eta^2)}{\ln(C\eta/2t_*^{1/2})}d\eta + \cdots\end{aligned} \tag{17}$$

Expansion of $1/\ln(C\eta/2t_*^{1/2})$ in powers of $1/\ln(4t_*/C^2)$ gives:

$$\frac{1}{\ln(C\eta/2t_*^{1/2})} = -\frac{2}{\ln(4t_*/C^2)}\left\{1 + \frac{2\ln\eta}{\ln(4t_*/C^2)} + \frac{4(\ln\eta)^2}{[\ln(4t_*/C^2)]^2} + \cdots\right\} \tag{18}$$

Substitution of (18) into (17) and integration term by term yields:

$$\begin{aligned}\lim_{t_*\to\infty} q_* = \; & \frac{2}{\ln(4t_*/C^2)}\left[1 - \frac{\gamma}{[\ln(4t_*/C^2)]} + \frac{\left(\frac{\pi^2}{6} + \gamma^2\right)}{[\ln(4t_*/C^2)]^2} + \cdots\right] \\ & -\frac{2\pi^2/3}{\ln(4t_*/C^2)}\left[0 + 0 + \frac{1}{[\ln(4t_*/C^2)]^2} + \cdots\right] \\ & +\frac{2/t_*}{\ln(4t_*/C^2)}\left[0 + \frac{1/2}{\ln(4t_*/C^2)} + \cdots\right]\end{aligned} \tag{19}$$

Combination of the first four nonzero terms in (19) and neglect of the smaller term of order $t_*^{-1}\ln^{-2}(t_*)$ yields the final result:

$$\lim_{t_*\to\infty} q_* = \frac{2}{\ln(4t_*/C^2)}\left[1 - \frac{\gamma}{\ln(4t_*/C^2)} - \frac{\left(\frac{\pi^2}{6} - \gamma^2\right)}{[\ln(4t_*/C^2)]^2} + \cdots\right] \tag{20}$$

Figure 3 shows an evaluation of the full integral solution for the flux (15) along with the late-time approximations based on (20). It is evident by inspection of Figure 3 that one or two terms of the series given by (20) capture the general trend of the exact solution at late time, but overestimate the flux somewhat. The two-term expansion yields a flux 5% too high at $t_* = 100$ and 3% too high at $t_* = 1000$. The three-term expansion is very close (less than 2% error) for $t_* > 100$.

A simple scheme for fitting data in order to extract hydraulic properties is suggested by taking the inverse of (20):

$$\lim_{t_*\to\infty} q_*^{-1} = \frac{1}{2}\ln\left(\frac{4t_*}{C^2}\right)\left\{1 + \frac{\gamma}{\ln(4t_*/C^2)} + \frac{\pi^2/6}{[\ln(4t_*/C^2)]^2} + \cdots\right\} \tag{21}$$

Retaining the first two terms in (21) (*i.e.*, neglecting the term of $O(\ln^{-1}(4t_*/C^2))$, and returning to dimensional variables, this takes the convenient form:

$$\lim_{t_*\to\infty} |q_r|^{-1}(a,t) = A\ln t + B, \tag{22}$$

where

$$A = \frac{\mu a}{2kp_0}, \tag{23}$$

and

$$B = A \ln\left(\frac{4c}{a^2 C}\right). \tag{24}$$

Thus, a plot of the inverse flux at the borehole *versus* $\ln t$ is approximately linear at sufficiently late time. The slope, A, is an indicator of the permeability, and the intercept, B, is an indicator of the hydraulic diffusivity through the simple relations:

$$k = \frac{\mu a}{2 p_0 A}, \tag{25}$$

and

$$c = \frac{a^2 C}{4} \exp\left(\frac{B}{A}\right) \quad (\text{two} - \text{term expansion}). \tag{26}$$

Note that, if only the first term of the expansion given in (20) or (21) is retained, (26) is replaced by

$$c = \frac{a^2 C^2}{4} \exp\left(\frac{B}{A}\right) \quad (\text{leading order}). \tag{27}$$

Thus, the higher-order approximation simply shifts the curve upward by a constant, $A\gamma$. As a result, a fit based on only the first term in (20) or (21) will yield an estimate for the diffusivity (27) that is a factor of $C \simeq 1.78$ times greater than that obtained in view of the two-term expansion (26).

Figure 4 shows a plot of inverse flux *versus* the logarithm of time for $t_* > 10$. The open symbols are computed from evaluations of the exact, integral solution (15). The lines show one, two, and three terms of equation (21). As noted above, both the leading-order approximation and the next, higher-order approximation are linear on this plot, with the latter simply shifted upward by a constant. It is evident from this plot that (26) will give a better estimate of the hydraulic diffusivity than will (27), but (26) still tends to overestimate c. A nonlinear fit of the three-term series given in (21) would give a much better result, and, although more involved than a linear regression based on the first two terms, is still far easier to perform than a fit requiring numerical quadrature on (15).

The inverse-flux fitting method was tested recently [4, 5] using synthetic data generated by numerical simulations of radial flow. Although the permeabilities used in the simulations were recovered with very good accuracy (typically within a few percent), the diffusivities estimated using (27) were consistently overestimated by factors of about 2 to 3. It is well known from the heat-transfer literature [*e.g.*, 6] that this difficulty is inherent in the method because extrapolation of the late-time fit back to $\ln t = 0$ introduces significant error. Nonetheless, the above considerations indicate that some of the discrepancy is removed simply by accounting for one higher-order term in the late-time expansion. When the same fits are interpreted using equation (26) rather than (27), the errors are reduced to the order of 50%. Thus, the simple linear fit to late time data gives a reasonably good approximation to the diffusivity.

Summary

The principal results reported in this memo are:

1. Previous evaluations of the integral solution for flow to an open borehole were inaccurate, particularly for large radius and long time.
2. The inaccuracy arose because direct application of a standard numerical quadrature scheme to the integral solution did not take careful account of the singular nature of the integrand at the lower limit of integration.
3. The singularity is exactly integrable, which allows more accurate evaluation of the pressure profiles and flux history. Results are provided in tabular and graphical forms.
4. The late-time asymptotic solution for the borehole flux has been extended to order $\ln^{-3} t_*$.
5. The late-time expansion for the *inverse* of the flux is linear in $\ln t$ when one considers either the leading-order term alone or the first higher-order correction, as well. Inclusion of the higher-order correction has no effect on the permeability inferred from a linear fit to late-time data, but results in an estimate for the hydraulic diffusivity that is smaller by a factor of 1.8.

References

1. Nowak, E. J., and D. F. McTigue, Interim Results of Brine Transport Studies in the Waste Isolation Pilot Plant (WIPP), **SAND87–0880**, Sandia National Laboratories, Albuquerque, NM, May 1987.
2. Nowak, E. J., D. F. McTigue, and R. Beraun, Brine Inflow to WIPP Disposal Rooms: Data, Modeling, and Assessment, **SAND88–0112**, Sandia National Laboratories, Albuquerque, NM, September 1988.
3. Crank, J., *The Mathematics of Diffusion*, Clarendon Press, Oxford, 1979.
4. Webb, S. W., and D. B. Barber, "Brine Inflow Sensitivity Studies — Results of Permeability Variation," memo to E. D. Gorham, Sandia National Laboratories, February 11, 1991.
5. Webb, S. W., and D. B. Barber, "Brine Inflow Sensitivity Studies — Results of Porosity Variation," memo to E. D. Gorham, Sandia National Laboratories, February 22, 1991.
6. Jaeger, J. C., The measurement of thermal conductivity and diffusivity with cylindrical probes, *EOS Transactions, American Geophysical Union*, **39**, 1958, 708–710.

Table 1. Pressure Profiles at Various Times.

r_*	$t_* = 0.01$	$t_* = 0.1$	$t_* = 0.5$	$t_* = 1.0$	$t_* = 5.0$	$t_* = 10.0$	$t_* = 50.0$
1.0	0.0000	0.0000	0.0000	0.0000	0.0000	0.0000	0.0000
1.2	0.8557	0.3987	0.2234	0.1785	0.1139	0.0968	0.0702
1.4	0.9950	0.6830	0.4067	0.3273	0.2101	0.1785	0.1296
1.6	0.9986	0.8553	0.5558	0.4525	0.2930	0.2492	0.1810
1.8	0.9982	0.9428	0.6749	0.5580	0.3656	0.3113	0.2263
2.0	0.9979	0.9798	0.7679	0.6466	0.4298	0.3666	0.2668
2.2	0.9977	0.9927	0.8384	0.7203	0.4871	0.4164	0.3035
2.4	0.9974	0.9962	0.8904	0.7812	0.5386	0.4614	0.3368
2.6	0.9972	0.9969	0.9274	0.8308	0.5850	0.5025	0.3675
2.8	0.9969	0.9969	0.9529	0.8706	0.6270	0.5401	0.3959
3.0	0.9967	0.9967	0.9698	0.9022	0.6650	0.5747	0.4222
3.2	0.9965	0.9965	0.9806	0.9269	0.6994	0.6066	0.4468
3.4	0.9963	0.9963	0.9872	0.9458	0.7306	0.6360	0.4698
3.6	0.9962	0.9961	0.9912	0.9600	0.7590	0.6633	0.4914
3.8	0.9960	0.9960	0.9934	0.9706	0.7847	0.6886	0.5118
4.0	0.9959	0.9958	0.9945	0.9783	0.8079	0.7121	0.5311
4.2	0.9957	0.9957	0.9951	0.9838	0.8289	0.7340	0.5494
4.4	0.9956	0.9955	0.9953	0.9876	0.8479	0.7542	0.5668
4.6	0.9954	0.9954	0.9953	0.9902	0.8650	0.7731	0.5833
4.8	0.9953	0.9953	0.9953	0.9919	0.8804	0.7906	0.5990
5.0	0.9952	0.9951	0.9952	0.9931	0.8942	0.8069	0.6140

Table 2. Fluid Flux at the Borehole for Selected Times; Evaluated from "Exact" Solution, Equation (15).

t_*	q_*
$0.1E-01$	6.1291
$0.2E-01$	4.4718
$0.4E-01$	3.2969
$0.6E-01$	2.7748
$0.8E-01$	2.4625
0.1E+00	2.2489
0.2E+00	1.7154
0.4E+00	1.3326
0.6E+00	1.1601
0.8E+00	1.0559
0.1E+01	0.9839
0.2E+01	0.8007
0.4E+01	0.6645
0.6E+01	0.6010
0.8E+01	0.5617
0.1E+02	0.5340
0.2E+02	0.4613
0.4E+02	0.4041
0.6E+02	0.3762
0.8E+02	0.3584
0.1E+03	0.3457
0.2E+03	0.3109
0.4E+03	0.2822
0.6E+03	0.2676
0.8E+03	0.2580
0.1E+04	0.2511
0.2E+04	0.2316
0.4E+04	0.2149
0.6E+04	0.2061
0.8E+04	0.2003
0.1E+05	0.1961

Table 3. Fluid Flux at the Borehole for Selected Times; Comparison of Late-Time Approximations (Eq. 20) and "Exact" Solution (Eq. 15).

t_*	q_*			
	Late-time Approx.			"Exact"
	1 Term	2 Terms	3 Terms	
10	0.7891	0.6094	0.4483	0.5340
50	0.4826	0.4154	0.3785	0.3883
100	0.4135	0.3641	0.3410	0.3457
500	0.3102	0.2825	0.2727	0.2739
1000	0.2801	0.2575	0.2503	0.2511
5000	0.2286	0.2135	0.2096	0.2100
10000	0.2118	0.1989	0.1957	0.1961

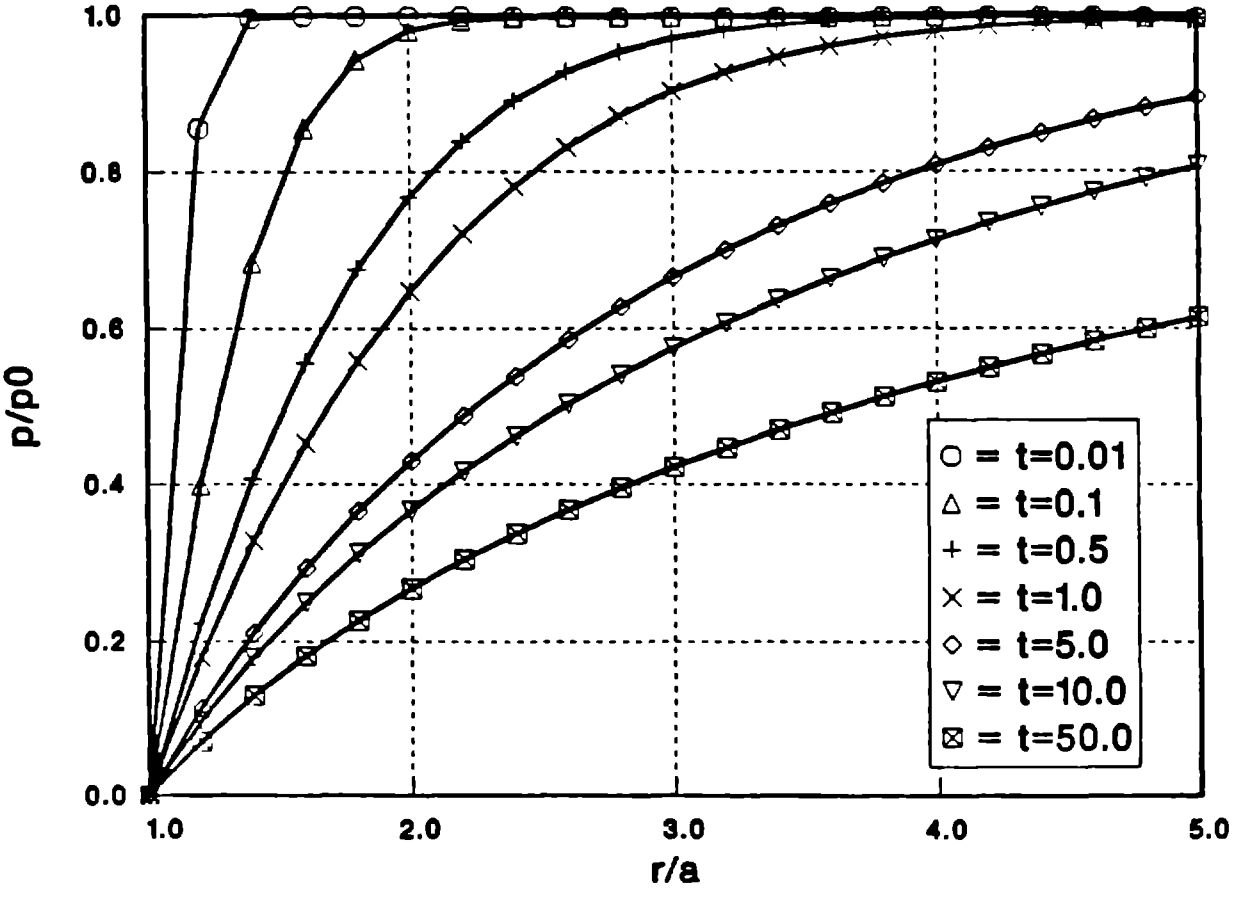

Figure 1. Pressure profiles based on equation (12); radial coordinate, r, is normalized by borehole radius, a; pressure, p, is normalized by initial value, p_0. This figure replaces Figure 18 in [1].

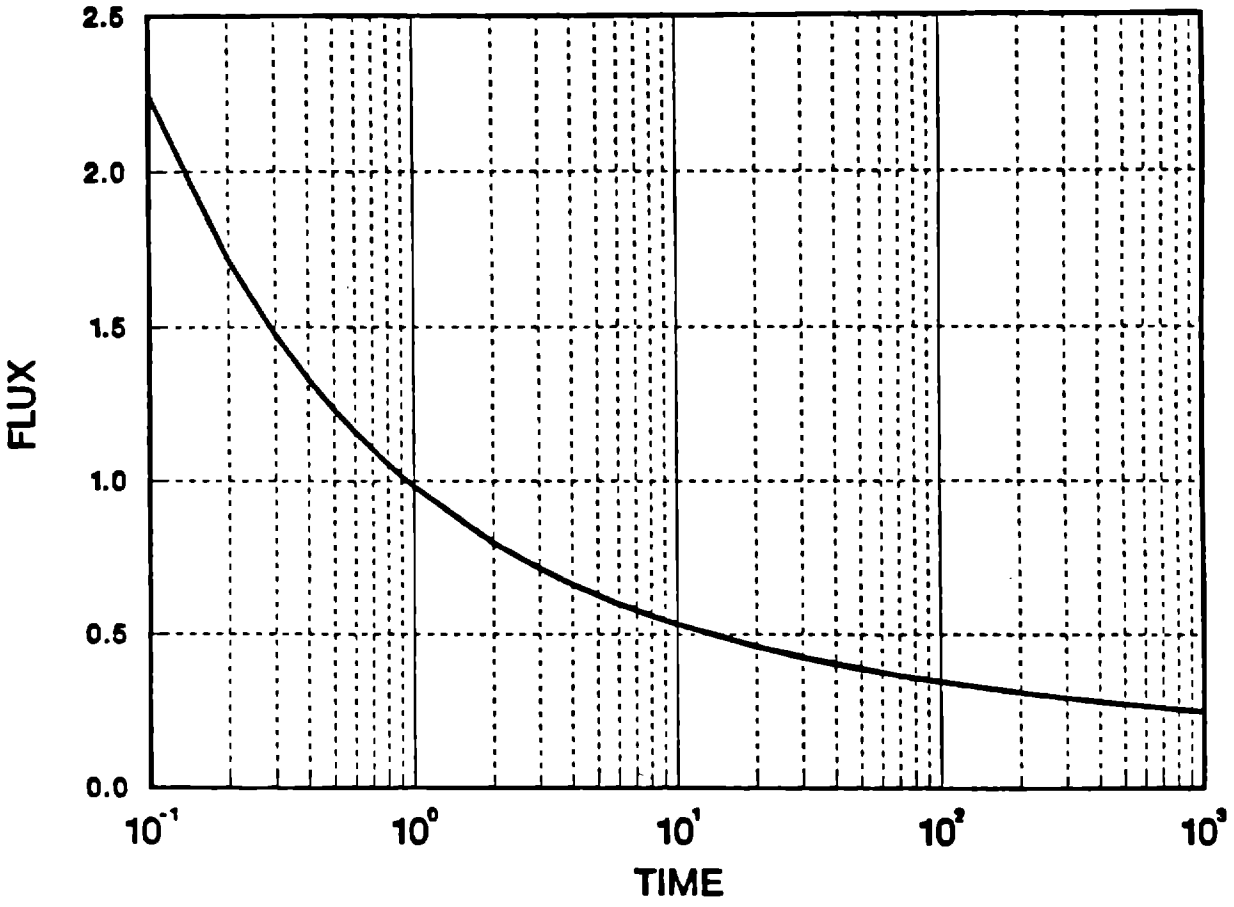

Figure 2. Flux history based on equation (15); time, t, is normalized by characteristic diffusion time, a^2/c; flux, $|q_r|(a,t)$, is normalized by $q_0 = kp_0/\mu a$. This figure replaces Figure 20 in [1] and Figure 1 in [2].

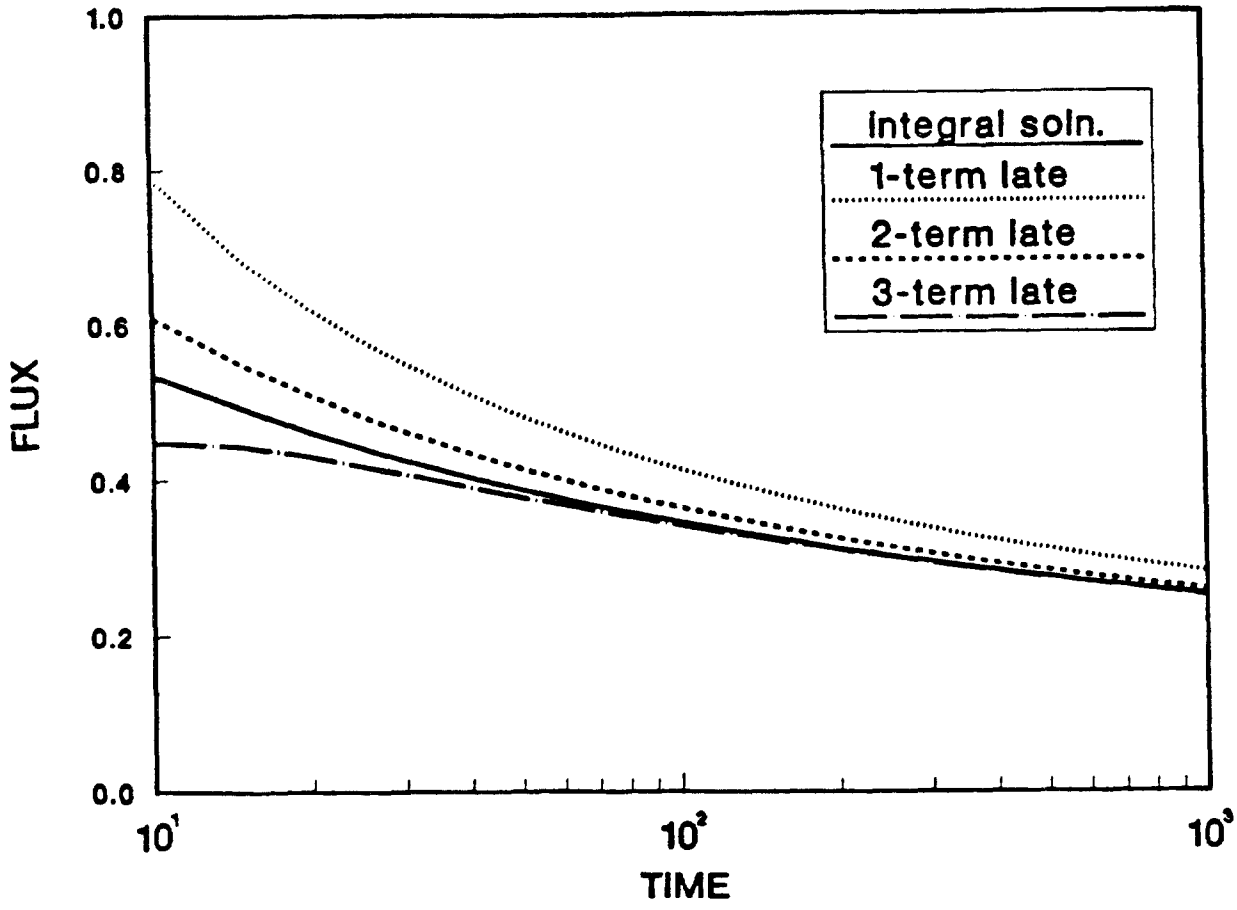

Figure 3. Comparison of "exact" integral solution (15) and late-time, asymptotic solution (20); time, t, is normalized by characteristic diffusion time, a^2/c; flux, $|q_r|(a,t)$, is normalized by $q_0 = kp_0/\mu a$.

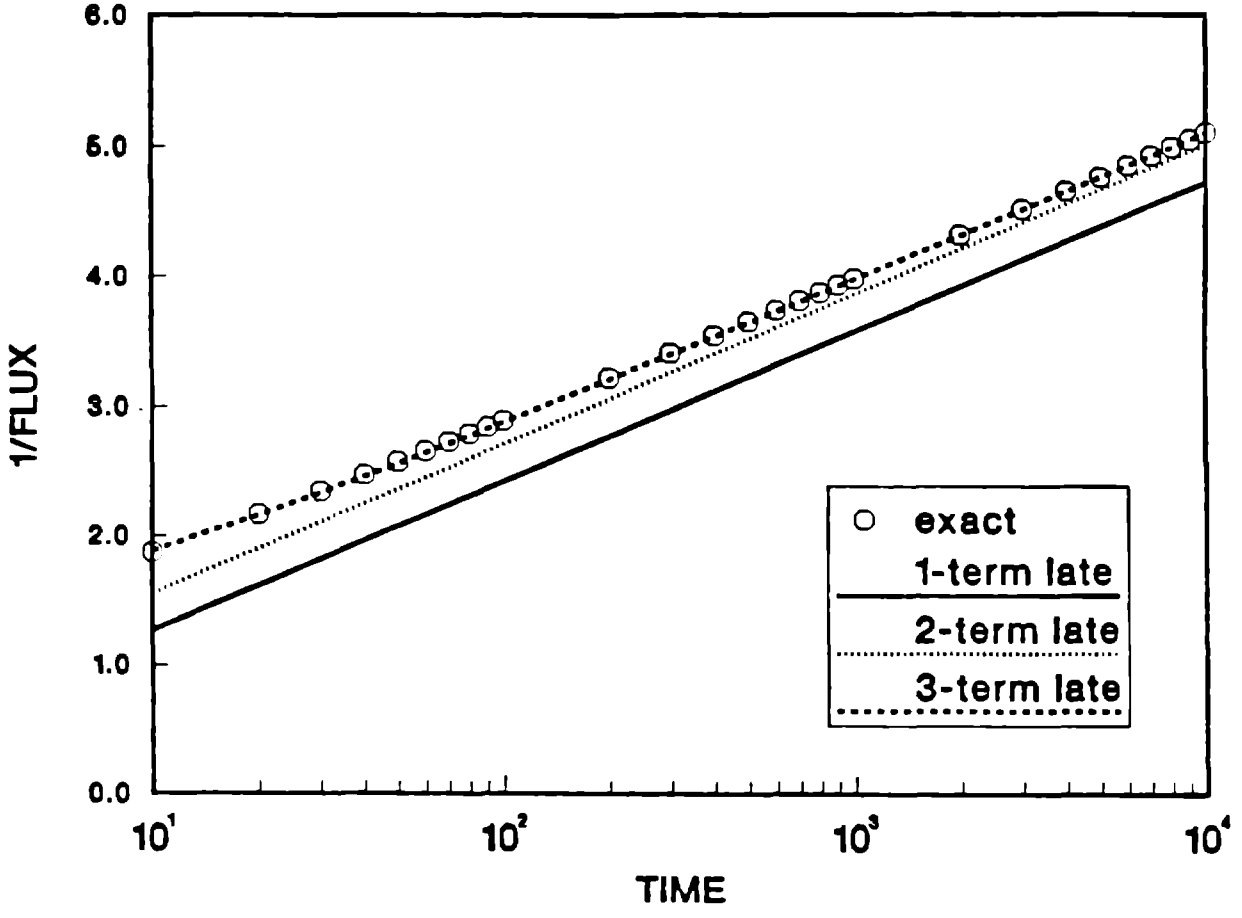

Figure 4. Comparison of "exact" integral solution (15) and late-time, asymptotic solution (21) for inverse of borehole flux; time, t, is normalized by characteristic diffusion time, a^2/c; flux, $|q_r|(a,t)$, is normalized by $q_0 = kp_0/\mu a$.

Distribution *March 6, 1991*

DFM:1511

Key Words: **Waste Isolation Pilot Plant, Darcy flow, seepage, hydraulic diffusivity, permeability**

Copy to:

1510 J. C. Cummings
DKG 1511 D. K. Gartling
1511 D. F. McTigue (day file)
1512 A. C. Ratzel
1513 Acting supervisor
1513 C. E. Hickox
1514 H. S. Morgan
1514 J. G. Arguello, Jr.
1514 C. M. Stone
1514 J. R. Weatherby
1540 J. R. Asay
1550 C. W. Peterson, Jr.
6340 W. D. Weart
6340 A. R. Lappin
6340 S. Y. Pickering
6341 R. C. Lincoln
6342 D. R. Anderson
6344 E. D. Gorham
6344 D. B. Barber
6344 R. L. Beauheim
6344 P. B. Davies
6344 S. J. Finley
6344 S. M. Howarth
6344 S. W. Webb
6345 B. M. Butcher
6345 F. T. Mendenhall
6346 J. R. Tillerson
6346 E. J. Nowak
6346 J. C. Stormont

APPENDIX B:
MEASUREMENT OF WIPP BRINE HUMIDITIES

Sandia National Laboratories

Albuquerque, New Mexico 87185

date: March 26, 1990

to: E. D. Gorham, 6344

from: S. J. Finley, 6344 and W. F. DeYonge, RE/SPEC

subject: Measurement of WIPP Brine Humidities

Introduction and Objectives

Relative humidity data has been collected as part of the Room D brine inflow experiment since September, 1987. Recent data reduction indicates that the relative humidity in the 10 sealed, brine inflow boreholes ranges from roughly 55% to 70%. In order to determine the integrity of the borehole seals in Room D and use the Room D humidity data to compliment the brine inflow data, the equilibrium relative humidity of WIPP brines is needed. In addition to the Room D experiments, relative humidity is also being monitored in the L4 brine inflow experiments and in Room Q, the Cylindrical Brine Room. Knowledge of the equilibrium relative humidity for WIPP brines is also necessary for the analysis and interpretation of the data from these experiments. Well beyond the scope of the brine inflow experiments, the equilibrium relative humidity value for WIPP brines is also needed as input for the prediction of metal corrosion and biogenic gas generation from the waste.

The National Bureau of Standards (NBS) has approved the use of saturated salt solutions as fixed points for relative humidity and reports an equilibrium relative humidity of approximately 75% for a chemically pure, saturated sodium chloride solution. (See Table 1 for exact NBS values.) WIPP brines are saturated sodium chloride solutions; however, there are other chemical constituents that may affect the vapor pressure and, consequently, the relative humidity in equilibrium with these brines. The objective of this test was to develop a means of determining the WIPP brine equilibrium relative humidity.

Test Method

WIPP QA Procedure No. 285 entitled "Testing Brine Humidities" was developed to specifically identify the equilibrium relative humidity or humidities associated with WIPP brines. In summary, Procedure No. 285 involves transferring a sufficient quantity of WIPP brine to a new, unused calibration cell and measuring the relative humidity with a recently calibrated, capacitance-type sensor at a constant temperature of 75°F. Table 2 lists the test dates, dates the sensors were calibrated,

and the error in relative humidity at the 75.3% calibration step after adjustment. The 75.3% calibration step is the closest step to the range of test data obtained. The humidity sensors used were calibrated according to WIPP QA Procedure No. 157.

The relative humidity measurements were conducted in 12/89 and 2/90. In December, 1989, all four samples were tested twice with the same humidity sensor. In February, 1990, the humidity measurements were conducted again using two different humidity sensors. A total of sixteen relative humidity measurements were completed. The sensors used were HYCAL, model CT-827-D. The calibration cells used were also manufactured by HYCAL, and the model designation is HC-60. These HYCAL humidity sensors are currently used for the brine inflow experiments in Rooms D, L4, and Q.

The WIPP brine samples used for this test were selected from the brine sample inventory from the brine inflow experiments in Rooms D, L4, and Q. In the course of these experiments, brine has accumulated in boreholes. The accumulated brine is periodically extracted and stored according to WIPP QA Procedure No. 154. In summary, brine is extracted by using an 110V portable pump to pump the brine through Inconel and Tygon tubing into a plastic vacuum flask. After extraction, the brine is weighed and then transferred to a plastic sample bottle and stored in metal cabinets underground at WIPP.

The brine sample designations used for this test indicate the borehole number, that the brine was extracted from, and the date the brine was extracted. The two samples designated DBT10-A are from the same vertical borehole collared in the invert of Room D, but the samples were extracted on different dates. The sample designated L4B01-A (6/8/89) came from a sub-horizontal borehole collared in the face of Room L4. The sample designated QPB02-A (5/24/89) came from one of the five vertical brine inflow boreholes drilled in the invert of the Q entry drift.

Discussion of Results

The detailed test results are included in Appendix A; however, the test results are summarized in Table 3. Equilibrium relative humidity values for the WIPP brines tested range from 72.4% to 75.6%. The mean for all 16 measurements is 73.8% with a standard deviation of 1.1%. These values calculated from actual measurements are consistent with the equilibrium relative humidity of ~73% calculated by L. H. Brush, 6345 (Brush, 1990). L. H. Brush calculated an average activity of water of ~73% in intergranular Salado brines from the waste facility horizon with the speciation and solubility code EQ3NR. The average activity of water in these brines is numerically equal to the relative humidity, if water vapor is in equilibrium with water in the brine according to Brush.

Moreover, the data suggests that different equilibrium relative humidity values are associated with different brine samples. The variability of the equilibrium relative humidity measurements for a particular brine sample is significantly less than the variability of humidity measurements for all four brine samples. Figure 1 shows the range in relative humidity values for each of the different WIPP brine samples used. Although the ranges overlap to some extent, the range of values for each individual brine sample is considerably smaller than the range of values for the entire data set. Variations in equilibrium relative humidity could be a result of the variations in WIPP brine chemistry reported by Stein and Krumhansl (1988).

References

Brush, L. H. (1990), personal communication

Hasegawa, S. (1985), National Basis of Accuracy in Humidity Measurements, Proceedings of the 1985 International Symposium on Moisture and Humidity, Washington, D.C., 4/1985, p15-28.

Stein, C. L., and Krumhansl, J. L. (1988), A Model for the Evolution of Brines in Salt from the Lower Salado Formation, Southeastern New Mexico. Geochim. Cosmochim. Acta, 52:1037-1046.

Copy to:
6340 W. D. Weart
6340 S. Y. Pickering
6340 SWCF/590PS/BT
6341 R. C. Lincoln
6342 D. R. Anderson
6343 T. M. Schultheis
6344 E. D. Gorham
6344 Staff
6345 A. R. Lappin
6345 L. H. Brush
6345 M. A. Molecke
6346 J. R. Tillerson
W. DeYonge, RE/SPEC
B. Stenson, Re/SPEC
G. Baird, RE/SPEC
J. Trone, Tech Reps
R. Jones, Tech Reps

Table 1: Equilibrium Relative Humidity of Selected Saturated Salt Solution from 0 to 100°C

T °C	Relative Humidity, %								
	Lithium Chloride	Potassium Acetate	Magnesium Chloride	Potassium Carbonate	Magnesium Nitrite	Sodium Chloride	Potassium Chloride	Potassium Nitrate	Potassium Sulfate
0	11.23 ± 0.54		33.66 ± 0.33	43.13 ± 0.66	60.35 ± 0.55	75.51 ± 0.34	88.61 ± 0.53	96.33 ± 2.9	98.77 ± 1.1
5	11.26 ± 0.47		33.60 ± 0.28	43.13 ± 0.50	58.86 ± 0.43	75.65 ± 0.27	87.67 ± 0.45	96.27 ± 2.1	98.48 ± 0.91
10	11.29 ± 0.41	23.28 ± 0.53	33.47 ± 0.24	43.14 ± 0.39	57.36 ± 0.33	75.67 ± 0.22	86.77 ± 0.39	95.96 ± 1.4	98.18 ± 0.76
15	11.30 ± 0.35	23.40 ± 0.32	33.30 ± 0.21	43.15 ± 0.33	55.87 ± 0.27	75.61 ± 0.18	85.92 ± 0.33	95.41 ± 0.96	97.89 ± 0.63
20	11.31 ± 0.31	23.11 ± 0.25	33.07 ± 0.18	43.16 ± 0.33	54.38 ± 0.23	75.47 ± 0.14	85.11 ± 0.29	94.62 ± 0.66	97.59 ± 0.53
25	11.30 ± 0.27	22.51 ± 0.32	32.78 ± 0.16	43.16 ± 0.39	52.89 ± 0.22	75.29 ± 0.12	84.34 ± 0.26	93.58 ± 0.55	97.30 ± 0.45
30	11.28 ± 0.24	21.61 ± 0.53	32.44 ± 0.14	43.17 ± 0.50	51.40 ± 0.24	75.09 ± 0.11	83.62 ± 0.25	92.31 ± 0.60	97.00 ± 0.40
35	11.25 ± 0.22		32.05 ± 0.13		49.91 ± 0.29	74.87 ± 0.12	82.95 ± 0.25	90.79 ± 0.83	96.71 ± 0.38
40	11.21 ± 0.21		31.60 ± 0.13		48.42 ± 0.37	74.68 ± 0.13	82.32 ± 0.25	89.03 ± 1.2	96.41 ± 0.38
45	11.16 ± 0.21		31.10 ± 0.13		46.93 ± 0.47	74.52 ± 0.16	81.74 ± 0.28	87.03 ± 1.8	96.12 ± 0.40
50	11.10 ± 0.22		30.54 ± 0.14		45.44 ± 0.60	74.43 ± 0.19	81.20 ± 0.31	84.78 ± 2.5	95.82 ± 0.45
55	11.03 ± 0.23		29.93 ± 0.16			74.41 ± 0.24	80.70 ± 0.35		
60	10.95 ± 0.26		29.26 ± 0.18			74.50 ± 0.30	80.25 ± 0.41		
65	10.86 ± 0.29		28.54 ± 0.21			74.71 ± 0.37	79.85 ± 0.48		
70	10.75 ± 0.33		27.77 ± 0.25			75.06 ± 0.45	79.49 ± 0.57		
75	10.64 ± 0.38		26.94 ± 0.29			75.58 ± 0.55	79.17 ± 0.66		
80	10.51 ± 0.44		26.05 ± 0.34			76.29 ± 0.65	78.90 ± 0.77		
85	10.38 ± 0.51		25.11 ± 0.39				78.68 ± 0.89		
90	10.23 ± 0.59		24.12 ± 0.46				78.50 ± 1.0		
95	10.07 ± 0.67		23.07 ± 0.52						
100	9.90 ± 0.77		21.97 ± 0.60						

(Hasegawa, S., 1985)

Table 2: Calibration Information for Humidity Sensors Used for WIPP Brine Tests

Humidity Sensor Serial Number	Test Date(s)	Calibration Date	Δ Relative Humidity at 75.3% Calibration Step after Adjustment
178921	12/22 - 12/27/89	12/18/89	0.0
179088	2/19 - 2/20/90	2/14/90	+0.3%
178921	2/19 - 2/20/90	2/14/90	+0.6%

Table 3: Summarized Equilibrium Relative Humidity (RH) Measurement Results for WIPP Brines

Brine Sample Designation	SN 178921* RH Measured in %	SN 178921* RH Measured in %	SN 179088* RH Measured in %	SN 178921* RH Measured in %
DBT10-A 10/7/87	74.9	74.2	74.0	73.8
DBT10-A 12/6/89	72.5	72.6	72.4	72.6
L4B01-A 6/8/89	72.8	73.8	73.7	73.0
QPB02-A 5/24/89	74.4	75.4	75.6	75.6

* The serial number of the RH sensor used for the measurements listed.

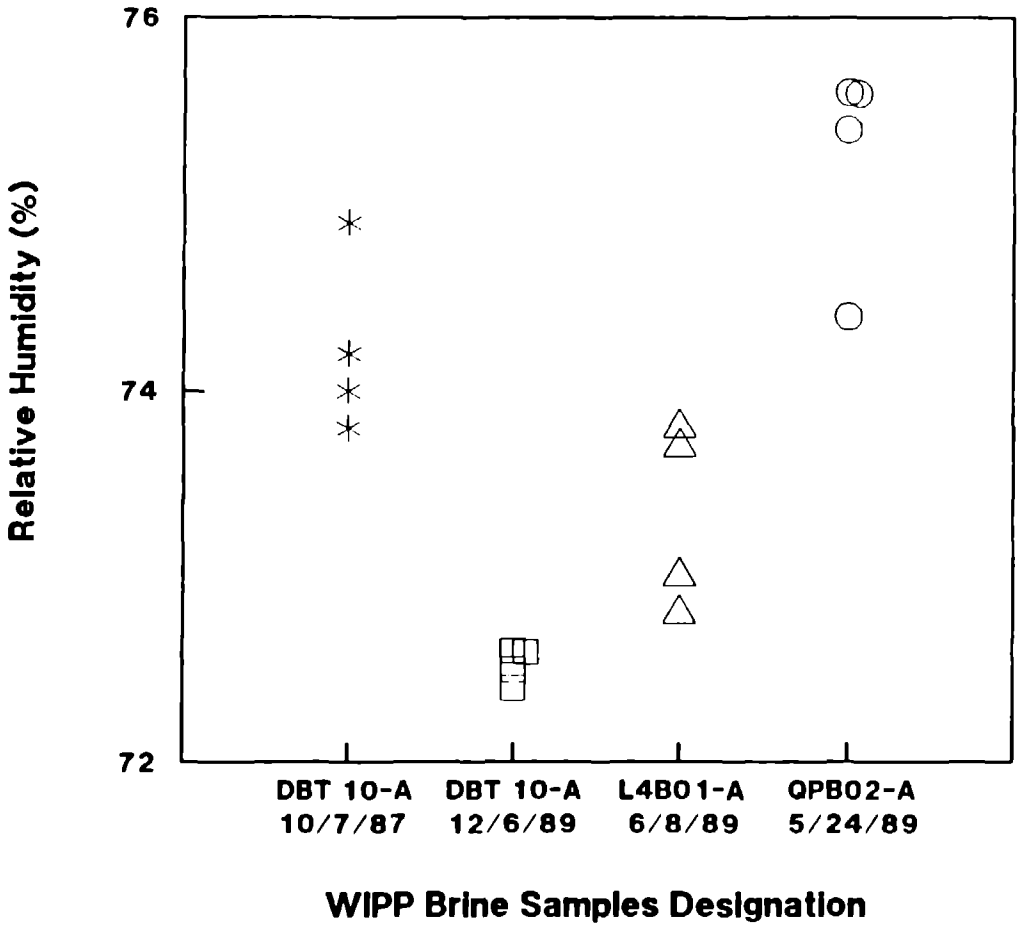

Fig. 1: Measured relative humidity in equilibrium with WIPP brine samples @ 75°F

APPENDIX A

WIPP BRINE TESTING RESULTS

WASTE ISOLATION PILOT PLANT	WIPP BRINE HUMIDITIES	SANDIA NATIONAL LABORATORIES
GAGE USED: HY-CAL MODEL CT-827-D HUMIDITY GAGE, S/N: 178921, CAL'D: 12/18/89	PROCEDURE: 285 FORM: 130	DATE: 12/27/89-12/28/89 EXCIT: 30.00 VDC
ELECTRICAL CONNECTIONS: E= +EXC., F= -EXC. DWR. NO.: 590-016-00-A G= +MON., H= -MON.		OPERATOR: D. BARTON

CERTIFICATION: MODEL: HP-3467A
DESCRIPTION: LOGGING MULTIMETER
S/N: 1821A0236 CAL. DUE: 02/28/90

CERTIFICATION: MODEL: HP-6114A
DESCRIPTION: PRECISION POWER SUPPLY
S/N: 2437AO4024 CAL. DUE: N/A

CERTIFICATION: MODEL: DATRON 1081
DESCRIPTION: AUTOCAL STANDARDS MULTIMETER
S/N: 10940 CAL. DUE: 02/28/90

CERTIFICATION: MODEL: SDL PRT 100
DESCRIPTION: PLATINUM RESISTANCE THERMOMETER
S/N: R100/262 CAL. DUE: 07/25/90

SOLN. FIXTURE: MODEL: HY-CAL HC-60 SERIES
DESCRIPTION: BRINE HUMIDITY CELLS
DATE PREPARED: 12/20/89

REMARKS: LOAD RESISTOR #63= 499.970 OHMS APPROVAL: WBJ, 2/7/90
SOLUTION FIXTURES WERE PREPARED FROM WIPP BRINE SAMPLES
SECOND TEST RUN, USING SAME GAGE

BRINE SAMPLE (DATE COLLECTED)	V Read	R.H. Calc (%)
DBT 10-A (10/07/87)	7.844	74.2
DBT 10-A (12/06/89)	7.702	72.6
L4 B01-A (06/08/89)	7.811	73.8
QPB 02-A (05/24/89)	7.949	75.4
AVERAGE:	N/A	74.0

	BRINE SAMPLE	ENDING TEMP.(C)
TEMPERATURES DURING RUN	DBT 10-A (10/07/87)	24.111
	DBT 10-A (12/06/89)	24.066
	L4 B01-A (06/08/89)	24.092
	QPB 02-A (05/24/89)	24.099
	AVG.	24.092

WASTE ISOLATION PILOT PLANT	WIPP BRINE HUMIDITIES	SANDIA NATIONAL LABORATORIES
GAGE TYPE: HY-CAL MODEL NO. CT-827-D HUMIDITY GAGE	S/N: 178921 CAL DUE: 01/18/90	DATE: 12/22/89- 12/27/89 EXCIT: 30.00 VDC
ELECTRICAL CONNECTIONS: DWR. NO.: 590-016-00-A	E= +EXC., F= -EXC. G= +MON., H= -MON.	OPERATOR: D. BARTON

CERTIFICATION: MODEL: HP-3467A
DESCRIPTION: LOGGING MULTIMETER
S/N: 1821A0236 CAL. DUE: 02/28/90

CERTIFICATION: MODEL: HP-6114A
DESCRIPTION: PRECISION POWER SUPPLY
S/N: 2437A04024 CAL. DUE: N/A

CERTIFICATION: MODEL: DATRON 1081
DESCRIPTION: AUTOCAL STANDARDS MULTIMETER
S/N: 10940 CAL. DUE: 02/28/90

CERTIFICATION: MODEL: SDL PRT 100
DESCRIPTION: PLATINUM RESISTANCE THERMOMETER
S/N: R100/262 CAL. DUE: 07/25/90

SOLN. FIXTURE: MODEL: HY-CAL HC-60 SERIES
DESCRIPTION: BRINE HUMIDITY CELLS
DATE PREPARED: 12/20/89

REMARKS: LOAD RESISTOR #63= 499.970 OHMS APPROVAL: WJS 2/7/90
SOLUTION FIXTURES WERE PREPARED FROM WIPP BRINE SAMPLES

BRINE (DATE) SAMPLE (COLLECTED)	V Read	R.H. Calc
DBT 10 (10/07/87)	7.906	74.9
DBT 10 (12/06/89)	7.696	72.5
L4 B01 (06/08/89)	7.725	72.8
QPB 02 (05/24/89)	7.862	74.4
AVERAGE:	N/A	73.6

	BRINE SAMPLE	ENDING TEMP.(C)
TEMPERATURES DURING RUN	DBT 10 (10/07/87)	24.054
	DBT 10 (12/06/89)	24.091
	L4 B01 (06/08/89)	24.120
	QPB 02 (05/24/89)	24.279
	AVG.	24.136

WASTE ISOLATION PILOT PLANT	WIPP BRINE HUMIDITIES	SANDIA NATIONAL LABORATORIES
GAGE USED: HY-CAL MODEL CT-627-D HUMIDITY GAGE, S/N: 178921, CAL'D: 02/14/90	PROCEDURE: 285 FORM: 130	DATE: 02/19/90-02/20/90 EXCIT: 30.00 VDC
ELECTRICAL CONNECTIONS: E= +EXC., F= -EXC. DWR. NO.: 590-016-00-A G= +MON., H= -MON.		OPERATOR: D. BARTON

CERTIFICATION: MODEL: HP-3467A
DESCRIPTION: LOGGING MULTIMETER
S/N: 1821A02039 CAL. DUE: 04/09/90

CERTIFICATION: MODEL: HP-6114A
DESCRIPTION: PRECISION POWER SUPPLY
S/N: 2437A04024 CAL. DUE: N/A

CERTIFICATION: MODEL: HP-3456A
DESCRIPTION: DIGITAL MULTIMETER
S/N: 2201A08614 CAL. DUE: 06/05/90

CERTIFICATION: MODEL: SDL PRT 100
DESCRIPTION: PLATINUM RESISTANCE THERMOMETER
S/N: R100/262 CAL. DUE: 07/25/90

SOLN. FIXTURE: MODEL: HY-CAL HC-60 SERIES
DESCRIPTION: BRINE HUMIDITY CELLS
DATE PREPARED: 12/20/89, 02/08/90

REMARKS: LOAD RESISTOR #63= 499.970 OHMS APPROVAL: WJP, 2/23/90
SOLUTION FIXTURES WERE PREPARED FROM WIPP BRINE SAMPLES
SECOND SERIES OF TEST

BRINE SAMPLE (DATE COLLECTED)	V Read	R.H. Calc (%)
DBT 10-A (10/07/87)	7.813	73.8
DBT 10-A (12/06/89)	7.709	72.6
L4 B01-A (06/08/89)	7.737	73.0
QPB 02-A (05/24/89)	7.966	75.6
MB1-1 (02/08/90)	8.042	76.4
AVERAGE:	N/A	74.3

TEMPERATURES DURING RUN:

BRINE SAMPLE	OHM VALUE	ENDING TEMP.(C)
DBT 10-A (10/07/87)	109.350	23.927
DBT 10-A (12/06/89)	109.412	24.087
L4 B01-A (06/08/89)	109.312	23.831
QPB 02-A (05/24/89)	109.339	23.900
MB1-1 (02/08/90)	109.305	23.810
AVERAGE CALCULATED TEMPERATURE=		23.911

WASTE ISOLATION PILOT PLANT	WIPP BRINE HUMIDITIES	SANDIA NATIONAL LABORATORIES
GAGE USED: HY-CAL MODEL CT-827-D HUMIDITY GAGE, S/N: 179088, CAL'D: 02/14/90	PROCEDURE: 285 FORM: 130	DATE: 02/19/90-02/20/90 EXCIT: 30.00 VDC
ELECTRICAL CONNECTIONS: E= +EXC., F= -EXC. DWR. NO.: 590-016-00-A G= +MON., H= -MON.		OPERATOR: D. BARTON

CERTIFICATION: MODEL: HP-3467A
DESCRIPTION: LOGGING MULTIMETER
S/N: 1821A02039 CAL. DUE: 04/09/90

CERTIFICATION: MODEL: HP-6114A
DESCRIPTION: PRECISION POWER SUPPLY
S/N: 2437A04024 CAL. DUE: N/A

CERTIFICATION: MODEL: HP-3456A
DESCRIPTION: DIGITAL MULTIMETER
S/N: 2201A08614 CAL. DUE: 06/05/90

CERTIFICATION: MODEL: SDL PRT 100
DESCRIPTION: PLATINUM RESISTANCE THERMOMETER
S/N: R100/262 CAL. DUE: 07/25/90

SOLN. FIXTURE: MODEL: HY-CAL HC-60 SERIES
DESCRIPTION: BRINE HUMIDITY CELLS
DATE PREPARED: 12/20/89, 02/08/90

REMARKS: LOAD RESISTOR #52= 499.985 OHMS APPROVAL: WBS, 2/23/90
SOLUTION FIXTURES WERE PREPARED FROM WIPP BRINE SAMPLES
SECOND SERIES OF TEST

BRINE SAMPLE (DATE COLLECTED)	V Read	R.H. Calc (%)
DBT 10-A (10/07/87)	7.826	74.0
DBT 10-A (12/06/89)	7.692	72.4
L4 B01-A (06/08/89)	7.802	73.7
QPB 02-A (05/24/89)	7.966	75.6
MB1-1 (02/08/90)	8.021	76.2
AVERAGE:	N/A	74.4

TEMPERATURES DURING RUN:

BRINE SAMPLE	OHM VALUE	ENDING TEMP.(C)
DBT 10-A (10/07/87)	109.412	24.087
DBT 10-A (12/06/89)	109.312	23.831
L4 B01-A (06/08/89)	109.339	23.900
QPB 02-A (05/24/89)	109.305	23.810
MB1-1 (02/08/90)	109.386	24.021
AVERAGE CALCULATED TEMPERATURE=		23.930

APPENDIX C:
SENSITIVITY SIMULATIONS

Appendix C: Sensitivity Simulations

The following is a list of the sensitivity simulations performed in this study. As mentioned in the main part of the report, each parameter was varied around the base case which is

Borehole Radius	0.019 m
Borehole Depth	1.0 m
Permeability	10^{-21} m^2
Porosity	0.01
Pore Pressure	11 MPa
Effective Radius	Infinite
Compressibility	Fluid Only
	Incompressible Formation
Dissolved Gas	Air
Dissolved Gas Fraction	0 and 100%
Free Gas	None
Capillary Pressure	Brooks and Corey
Relative Permeability	Brooks and Corey
DRZ	None

The variations and the logic behind them are discussed below. These parameters are based on those summarized by Rechard et al. (1990) unless otherwise noted. The base case values are marked with an "*".

1. Borehole Radius

* 1.9 cm (1.5 in diameter) - Room Q Boreholes (Howarth et al., 1991)
5.1 cm (4.0 in diameter) - Beauheim et al. (1991) and Finley et al. (1992) Boreholes
45.7 cm (36. in diameter) - Finley et al. (1992) Boreholes
1.5 m - Radius of Room Q
4.5 m - Simple 1-D model of Repository (Nowak et al., 1988)

2. Permeability

10^{-23} m^2 - Low range of Salado permeability
*10^{-21} m^2 - Rounded off value of expected Salado permeability
10^{-18} m^2 - High range of Salado permeability

3. Porosity (initial value)

0.001 - Low measured value
*0.01 - Median value
0.03 - High measured value

4. Pore Pressure

1 MPa - low arbitrary value
6 MPa - value between 1 MPa and 11 MPa
*11 MPa - maximum measured far-field pore pressure.
15 MPa - lithostatic pressure

Two sets of two-phase conditions were selected for this variation. The first set is brine saturated with dissolved gas at this pore pressure. The second set is brine saturated with dissolved gas at 15 MPa which is then depressurized to the respective pore pressure. This second set is a rough approximation of the local depressurization that might occur due to an excavation.

5. Effective Radius of Brine Source

*infinite - standard model
5.0 m - arbitrary value
1.0 m - arbitrary value
0.2 m - arbitrary value

6. Compressibility

The values of the vertical formation compressibility used by Beauheim et al. (1991) range from 4.8×10^{-12} to 1.4×10^{-10} Pa^{-1}. The formation compressibilities selected are orders of magnitude which contain these values and include the incompressible limit.

*incompressible formation
10^{-13} Pa^{-1}
10^{-12} Pa^{-1}
10^{-11} Pa^{-1}
10^{-10} Pa^{-1}
10^{-9} Pa^{-1}

7. Solubility

*nominal - based on Cygan (1991)
multiplied by two - enhances effect
multiplied by four - further enhancement - similar to air-water

8. Dissolved Gas Fraction

* 0%
50%
75%
90%
95%
*100%

9. Free Gas Fraction

* 0%
10% by volume - uniform distribution - arbitrary
- gas pockets (gas next to borehole - arbitrary
(brine next to borehole - arbitrary
20% by volume - uniform - default residual gas saturation
50% by volume - uniform - arbitrary

10. Capillary Pressure and Relative Permeability

*Brooks and Corey Model
Capillary Pressure * 10 - arbitrary
Capillary Pressure ÷ 10 - arbitrary
Capillary Pressure = 0. - arbitrary
Uniform Capillary Pressure - arbitrary
Dissolved Gas Exsolution Shape - Webb (1990)
Residual Saturations = 0.0 (Default = 0.2) - arbitrary
Residual Saturations = 0.4 (Default = 0.2) - arbitrary
Sandia functions - Pruess (1987)

11. Disturbed Rock Zone Characteristics

*none
DRZ of 0.5 R
DRZ of 1.0 R

DRZ of 2.0 R - range typical of those studied by McTigue (1989)
Initial DRZ P = Patm - uncertainty in initial pressure in DRZ
No increase in porosity - uncertainty in porosity in DRZ
increase Δk (decreased DRZ k) - k uncertainty
decrease Δk (increased DRZ k) - k uncertainty
McTigue approach - McTigue (1989)
Growing DRZ - possible variation
1R/yr
2R/yr

The details of the DRZ characteristics are summarized Table 3 of the main report.

References for Appendix C

Beauheim, R.L., G.J. Saulnier, Jr., and J.D. Avis. 1991. ***Interpretation of Brine-Permeability Tests of the Salado Formation at the Waste Isolation Pilot Plant Site: First Interim Report***. SAND90-0083. Albuquerque, NM: Sandia National Laboratories.

Cygan, R.T. 1991. ***The Solubility of Gases in NaCl Brine and a Critical Evaluation of Available Data***. SAND90-1946. Albuquerque, NM: Sandia National Laboratories.

Finley, S.J., D.J. Hanson, and R. Parsons. 1992. "Small-Scale Brine Inflow Experiments--Data Report through 6/6/91." SAND91-1956. Albuquerque, NM: Sandia National Laboratories.

Howarth, S.M., E.W. Peterson, P.L. Lagus, K. Lie, S.J. Finley, and J.E. Nowak. 1991. "Interpretation of In-Situ Pressure and Flow Measurements of the Salado Formation at the Waste Isolation Pilot Plant," SPE paper No. 21840, 1991.

McTigue, D.F. 1989. "Appendix A.8: Increased Permeability Near Storage Rooms: Effect on Brine Inflow Computed with a Darcy Model," ***Systems Analysis, Long-Term Radionuclide Transport, and Dose Assessments, Waste Isolation Pilot Plant (WIPP), Southeastern New Mexico; March 1989.*** Eds. A.R. Lappin, R.L. Hunter, D.P. Garber, and P.B. Davies. SAND89-0462. Albuquerque, NM: Sandia National Laboratories. A-105 through A-115.

McTigue, D.F., S.J. Finley, J.H. Gieske, and K.L. Robinson. 1991. Appendix A: "Compressibility Measurements on WIPP Brines," ***Preliminary Comparison with 40 CFR Part 191, Subpart B for the Waste Isolation Pilot Plant, December 1991; Volume 3: Reference Data.*** WIPP Performance Assessment Division. SAND91-0893/3. Albuquerque, NM: Sandia National Laboratories. A-79 through A-98.

Nowak, E.J., D.F. McTigue, and R. Beraun. 1988. ***Brine Inflow to WIPP Disposal Rooms: Data, Modeling, and Assessment***. SAND88-0112. Albuquerque, NM: Sandia National Laboratories.

Pruess, K. 1987. ***TOUGH User's Guide***. NUREG/CR-4645. SAND86-7104. LBL-20700, August 1987.

Rechard, R.P., H. Iuzzolino, and J.S. Sandha. 1990. ***Data Used in Preliminary Performance Assessment of the Waste Isolation Pilot Plant (1990)***. SAND89-2408. Albuquerque, NM: Sandia National Laboratories.

Webb, S.W., and J.C. Chen. 1990. "Phasic Pressure Difference Effects in Two-Phase Flow For Dissolved Gas Exsolution," ***Proceedings of the TOUGH Workshop, Lawrence Berkeley Laboratory, Berkeley, CA, September 13-14, 1990***, pp. 107-112, LBL-29710, September 1990.

APPENDIX D:
BASE CASE NODALIZATION EFFECTS

Appendix D: Base Case Nodalization Effects

The sensitivity study has been conducted with the TOUGH computer code. Typical nodalization of the formation resulted in 63 nodes out to 20 meters. The initial node spacing was 0.0055 m at the borehole with a telescoping (multiplication) factor of 1.1. Initially, the results seemed adequate with this nodalization. However, after the study was essentially completed, it was determined that finer nodalization was necessary in some situations, and as many as 94 nodes out to 20 m were employed with an initial spacing of 0.0019 m. The effect of the different nodalizations is discussed in this appendix.

The results from the different nodalizations are presented in Figures D-1 to D-4. The single-phase brine inflow rate is given in Figure D-1, while Figure D-2 presents the two-phase brine inflow rate (brine saturated with dissolved gas, no free gas). The differences between the various nodalizations are confined predominantly to the period up to 100 seconds; minor differences can be seen up to 1000 seconds. Figure D-3 gives the gas inflow rate with the same regions of disagreement. The gas saturation of the inflowing brine is shown in Figure D-4. While differences exist for the entire simulation for this parameter, the magnitude is less than 0.02 after about 10^4 seconds. Based on these comparisons, the effect of the nodalization is small after 10^4 seconds (3 hours) or less. Since this time period is small compared to the total simulation time, and the actual borehole drilling procedure is not simulated, these differences are not generally significant. Note that the results in the main report are only presented for time periods greater than 100 seconds in order to minimize differences due to nodalization. Even so, it should be kept in mind that small differences in results between cases may be due to nodalization effects and should be examined closely.

The effect of the nodalization is also reflected in the values of the inferred formation parameters. In addition, the number and distribution of the "data" due to time step differences will affect the late-time asymptotic fit used in the inferring procedure. The variation in the inferred parameters for the base case due to differences in the nodalization and in the time steps is summarized in Table D-1 for two different nodalizations, each with two different sets of time steps. As can be noted, the finer nodalization does not necessarily lead to better prediction of the inferred parameters; in fact, the variation due to the nodalization and due to the different time steps seem to be about the same. The total variability in the

permeability is about 4% while the diffusivity range is about 40%. Note that the late-time asymptotic fit is only applicable after about 10^5 seconds, or well after the nodalization effects are minimal.

Based on these results, nodalization effects are small and will not significantly alter the results presented in this report. In those instances where the effect is apparent, it will be noted.

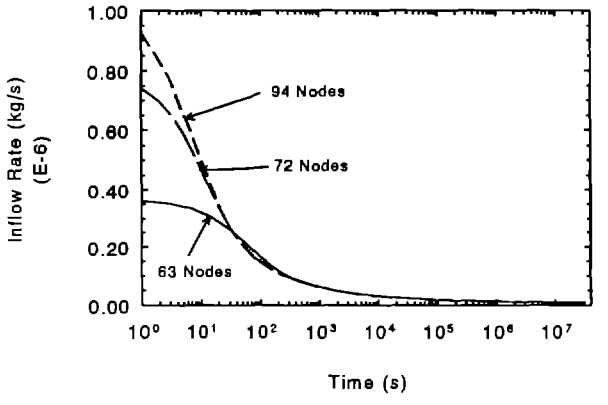

D-1. Single-phase brine inflow.

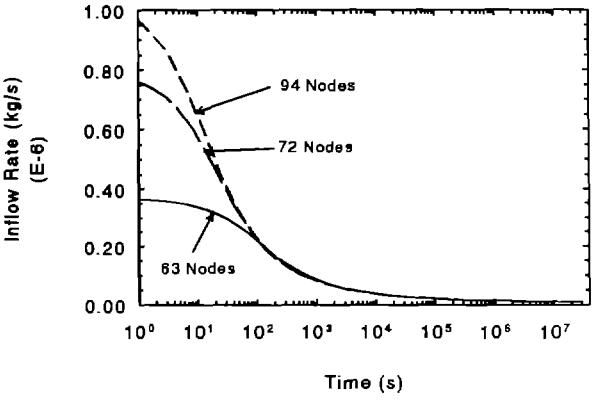

D-2. Two-phase brine inflow.

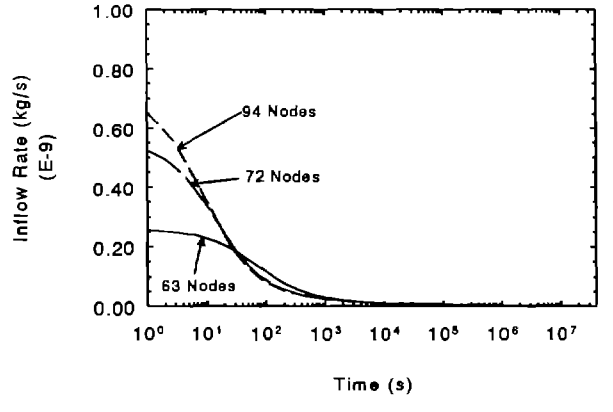

D-3. Two-phase gas inflow.

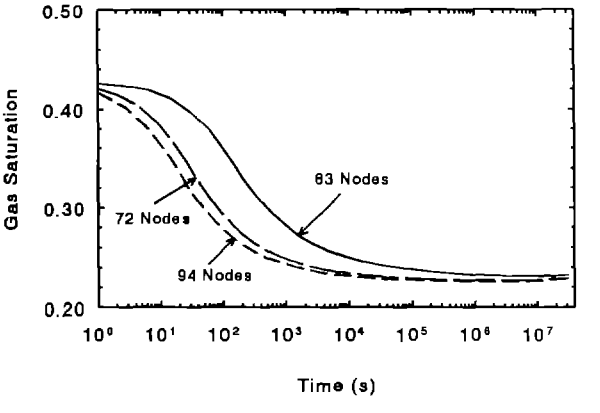

D-4. Gas saturation of inflowing brine.

Figure D. Results from varying the nodalization.

Table D-1. Nodalization and Time Step Results

Permeability (m2)		
Actual	Inferred	Error
1.0×10^{-21}		
single-phase		
63 Nodes - Radius	1.04×10^{-21}	+4%
- Perm.	1.01×10^{-21}	+1%
94 Nodes - Matrix Comp.	1.03×10^{-21}	+3%
- DRZ	1.00×10^{-21}	<-1%
two-phase		
63 Nodes - Radius	1.03×10^{-21}	+3%
- Perm.	1.02×10^{-21}	+2%
94 Nodes - Matrix Comp.	1.03×10^{-21}	+3%
- DRZ	0.99×10^{-21}	-1%

Diffusivity (m2/sec)		
Actual	Inferred	Error
2.1×10^{-7}		
single-phase		
63 Nodes - Radius	3.2×10^{-7}	+50%
- Perm.	3.1×10^{-7}	+50%
94 Nodes - Matrix Comp.	3.9×10^{-7}	+90%
- DRZ	2.7×10^{-7}	+30%
two-phase		
63 Nodes - Radius	1.6×10^{-7}	-20%
- Perm.	1.7×10^{-7}	-20%
94 Nodes - Matrix Comp.	1.9×10^{-7}	-10%
- DRZ	1.4×10^{-7}	-30%

APPENDIX E:
BRINE INFLOW PERMEABILITY-DIFFUSIVITY MAPS AND INFERRED PARAMETERS

Sandia National Laboratories

Albuquerque, New Mexico 87185

date: January 3, 1992

to: E. D. Gorham, 6344

from: S. W. Webb, 6344

subject: Brine Inflow Permeability-Diffusivity Maps and Inferred Parameters

Brine inflow into a borehole is a function of the permeability and the diffusivity. At the current time, the data reduction procedure used to infer the formation parameters is a simplified one-dimensional, uniform property, single-phase Darcy flow model (Nowak et al. (1988)). The brine inflow rate per unit length to an open borehole as prescribed by this simplified model is

$$\dot{m} / L = \rho\, q\, A / L = 2\,\pi\,\rho\, r\, q$$

$$= \frac{\rho\, k\, P_o}{\mu}\,\frac{8}{\pi}\int_0^{\infty}\frac{\exp\left(-cu^2 t/r^2\right)}{J_o^2(u) + Y_o^2(u)}\,\frac{du}{u} \qquad (1)$$

where ρ, k, P_o, μ, r, and c are the brine density, permeability, initial brine pressure, brine viscosity, borehole radius, and diffusivity, respectively, and u is a dummy variable. From the above relationship, the brine inflow per unit length scales linearly with the permeability and in a more complex fashion with the diffusivity through the integral. The diffusivity can be written as (Webb, 1991b)

$$c = \frac{T}{S} = \frac{k}{\mu}\,\frac{1}{\phi\left[\beta_1 + \alpha_p\right]} \qquad (2)$$

where T, S, ϕ, β_1, and α_p are the transmissivity, storativity, porosity, liquid compressibility, and pore compressibility coefficient, respectively. While the diffusivity and permeability are coupled from the above expression, the permeability and diffusivity will be individually specified in the present study.

In data reduction of brine inflow into a borehole (McTigue, 1991), uncertainties in the inferred values of permeability and diffusivity exist. In order to ascertain the relative importance of these two factors, maps of the single-phase brine inflow rate and the cumulative brine inflow as a function of permeability and diffusivity for various times have been generated for a 0.019 m radius borehole using the TOUGH code (Webb, 1991a).

TOUGH was used since it is the current code being used for brine inflow studies by Webb (1991b). Note that as discussed by Webb (1991b), these results are also applicable to other size boreholes if the appropriate scaling criteria are employed.

Figures 1 and 2 present the mappings for brine inflow rate and cumulative brine inflow, respectively, for times of 1 month, 6 months, 1 year, and 2 years after borehole drilling. The numbers on the figures are the brine inflow rate (or cumulative mass) relative to the value for the reference case, which is for a diffusivity and permeability of 10^{-9} m^2/s and 10^{-21} m^2, respectively. The parameters used in the analysis are listed below. Lines are drawn on each figure to indicate the approximate location of constant inflow rate or cumulative mass.

Study Parameters

Borehole Radius	0.019 m
Formation Depth	1.0 m
Permeability	Varied
Porosity	0.01
Pore Pressure	11 MPa
Effective Radius	Infinite
Compressibility (Fluid)	3.0×10^{-10} Pa^{-1}
(Matrix)	Calculated from Diffusivity
Dissolved Gas	None
Free Gas	None

Note that the linear scaling predicted by equation (1) is not seen in all cases, especially for low values of the diffusivity (more compressible porous medium). This discrepancy is due to temporal and spatial variations of the porosity (and the diffusivity (equation 2)) as the porous medium depressurizes. In most cases, this variation is insignificant, but it becomes more important as the diffusivity decreases.

As can be seen from the figures, a factor of 3 increase in the permeability is approximately equivalent to an increase of 3 orders of magnitude in the diffusivity, and the slope of the constant parameter lines changes very little with time. Variation of the ratio at any given set of conditions is about 20% from 1 month to 1 year. Note, however, that this variation is similar to those seen by Webb (1991b) in his sensitivity studies of, for example, porosity changes, the presence of a DRZ, or dissolved gas exsolution. In addition, multi-dimensional effects (stratification, finite length borehole) cause additional deviations from the model.

Attempts to fit the entire brine inflow history to determine the diffusivity are difficult since the brine inflow rate and cumulative mass are relatively insensitive to diffusivity compared to permeability. Additional complications arise from non-uniform properties, if the parameters are different than assumed, i.e., porosity, and from multi-dimensional effects. Therefore, large variation in the inferred diffusivity for different boreholes is expected; variation of the inferred values of the permeability is much more significant for brine inflow purposes.

References

McTigue, D. F. (1991), memo to Distribution, "Analytical Solution for Seepage to a Borehole," March 6, 1991.

Nowak, E. J., D. F. McTigue, and R. Beraun (1988), "Brine Inflow to WIPP Disposal Rooms: Data, Modeling, and Assessment," SAND88-0112, September 1988.

Webb, S. W. (1991a), memo to E. D. Gorham, "Brine Inflow Sensitivity Studies - General Methodology," February 8, 1991.

Webb, S. W. (1991b), "Brine Inflow Sensitivity Study: Results of 1-D Simulations," SAND91-2296 DRAFT, October 15, 1991.

Copy to:
1511 D. F. McTigue
1514 C. M. Stone
1514 J. R Weatherby
6340 W. D. Weart
6342 D. R. Anderson
6342 P. Vaughn
6344 R. L. Beauheim
6344 T. F. Corbet
6344 P. B. Davies
6344 C. F. Novak
6345 A. R. Lappin
6345 F. T. Mendenhall
6346 J. R. Tillerson
6344 File 7.4.4
DOE B. Becker
DOE P. Higgins

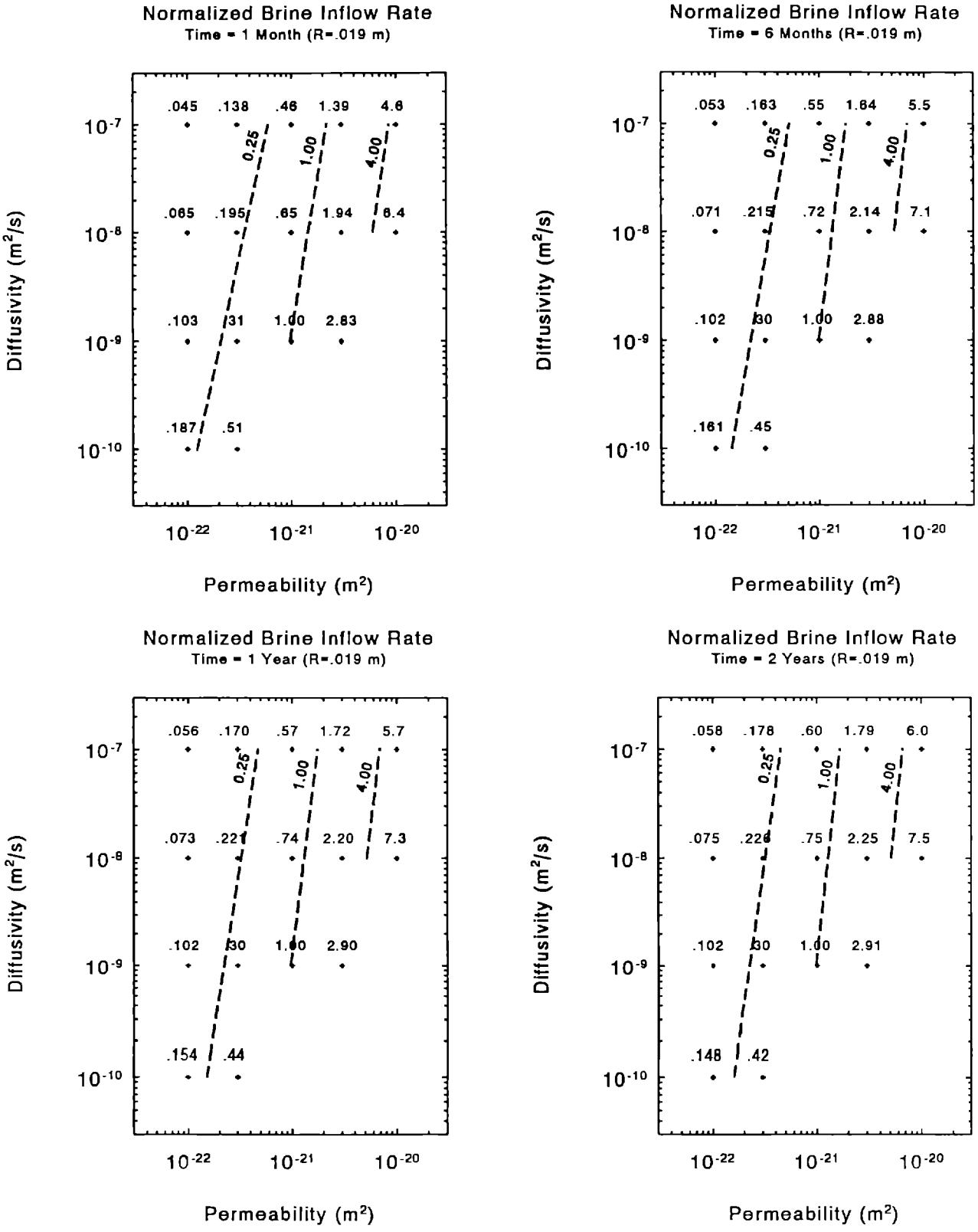

Figure 1. Brine Inflow Rate Mapping

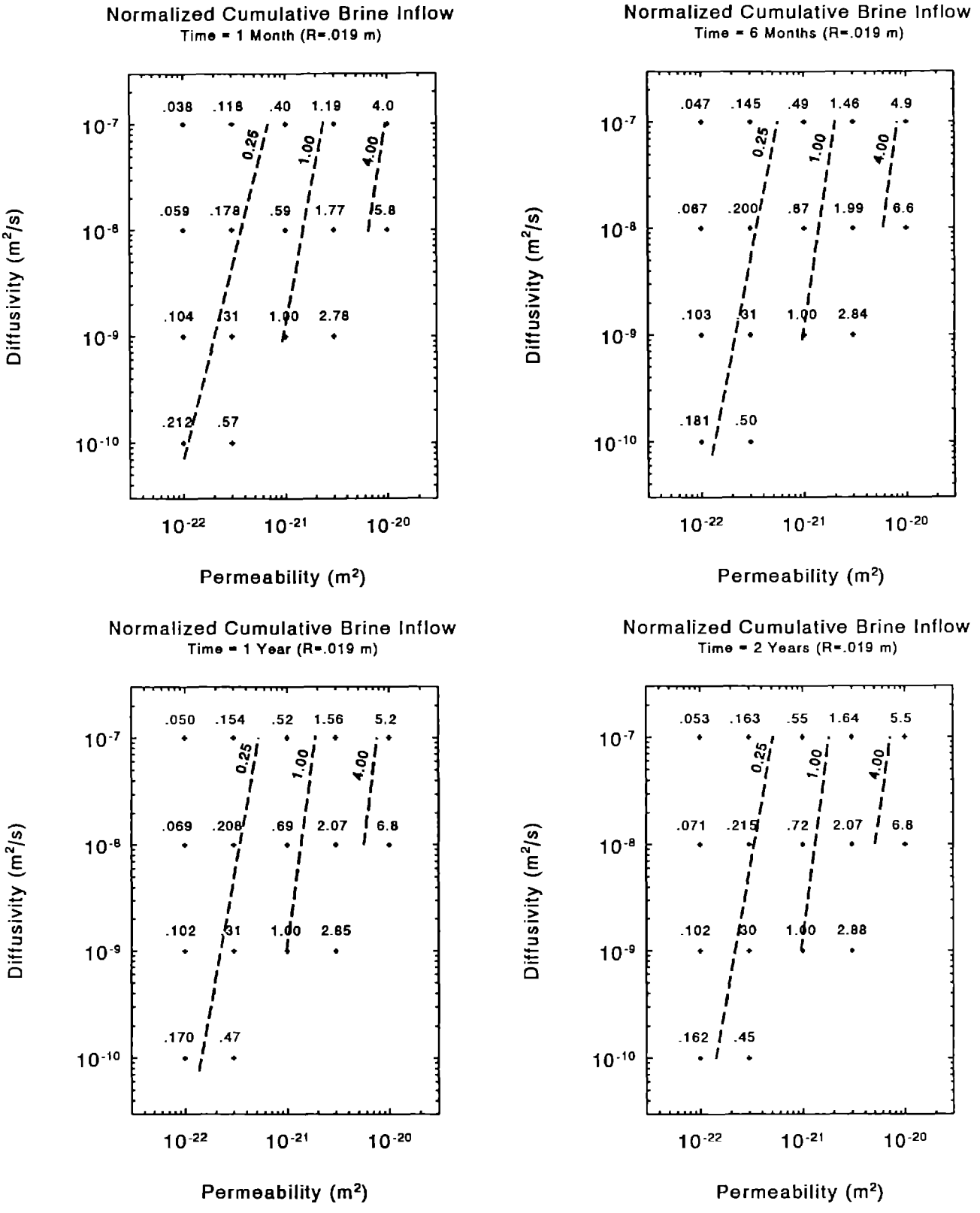

Figure 2. Cumulative Brine Inflow Mapping

APPENDIX F:
TWO-PHASE CHARACTERISTIC CURVES

Appendix F: Two-Phase Characteristic Curves

Brooks and Corey

According to Davies and LaVenue (1990), a modified Brooks and Corey (1964) model has been used for the relative permeability and capillary pressure curves in the preliminary analysis of the Salado. This model was also used in the recent Performance Assessment calculations (Rechard et al., 1990). From Davies and LaVenue (1990), the appropriate relationships are:

Capillary Pressure

$$P_c = \frac{P_t}{S_e^{1/\lambda}} \tag{F-1}$$

Relative Permeability

$$k_{rl} = S_e^{(2+3\lambda)/\lambda} \tag{F-2}$$

$$k_{rg} = \left(1 - S_e\right)^2 \left[1 - S_e^{(2+\lambda)/\lambda}\right] \tag{F-3}$$

where

$$S_e = \frac{S_l - S_{lr}}{1 - S_{gr} - S_{lr}} \tag{F-4}$$

and

P_c = capillary pressure
P_t = threshold pressure
S_e = effective liquid saturation
λ = pore-size distribution parameter
k_{rl} = relative permeability of liquid
k_{rg} = relative permeability of gas
S_l = liquid saturation
S_{lr} = residual liquid saturation
S_{gr} = residual gas saturation.

In the current implementation, the capillary pressure relationship, Equation F-1, is used throughout the entire saturation region. As discussed by Corey (1986), this relationship does not represent the data for $P_c < P_t$, where P_t is the threshold pressure for displacement ($k_{rg} > 0$). Note that the figures presented by Davies and LaVenue (1990) seem to continue to use Equation F-1 for $P_c < P_t$ while Rechard et al. (1990) use a constant value of P_c in this region.

Sandia Functions

The Sandia functions are based on the work of van Genuchten (1980) and are an option in the TOUGH code (Pruess, 1987). The equations are:

Capillary Pressure

$$P_c = P_o \left(S^{*-1/\lambda} - 1 \right)^{1 - \lambda} \tag{F-5}$$

Relative Permeability

$$k_{rl} = S^{*1/2} \left[1 - \left(1 - S^{*1/\lambda} \right)^{\lambda} \right]^2 \tag{F-6}$$

$$k_{rg} = 1. - k_{rl} \tag{F-7}$$

where

$$S^* = \frac{S_l - S_{lr}}{S_{ls} - S_{lr}} \tag{F-8}$$

and S_{ls} is complete liquid saturation.

Table F-1. Two-Phase Characteristic Curve Variations

Case	Capillary Pressure	Relative Permeability
Base	Brooks & Corey $\lambda = 0.7$, $S_{lr} = S_{gr} = 0.2$, $P_t = 10.$ MPa, $P_{cmax} = 120.$ Mpa	Brooks & Corey
$10*P_{cap}$	Brooks & Corey $P_t = 100.$ MPa	Brooks & Corey
$0.1*P_{cap}$	Brooks & Corey $P_t = 1.$ MPa	Brooks & Corey
Zero P_{cap}	Brooks & Corey $P_t = 0.$ MPa	Brooks & Corey
Uniform P_{cap}	Brooks & Corey $P_{cap} = 6.63$ MPa	Brooks & Corey
Dissolved Gas Exsolution Shape	Brooks & Corey with Webb and Chen (1990) Mods	Brooks & Corey
$S_r = 0.0$	Brooks & Corey $S_{lr} = S_{gr} = 0.0$	Brooks & Corey
$S_r = 0.4$	Brooks & Corey $S_{lr} = S_{gr} = 0.4$	Brooks & Corey
Sandia functions	Sandia functions $\lambda = .45$, $P_o = 10.63$ MPa chosen to be consistent with Brooks & Corey at $S_l = 0.8$; $S_{lr} = 0.2$, $S_{ls} = 1.0$, $P_{max} = 120.$ MPA.	Sandia functions

References for Appendix F

Brooks, R.H., and A.T. Corey. 1964. "Hydraulic Properties of Porous Media," Colorado State University Hydrology Paper No. 3, Fort Collins, Colorado, 1964.

Corey, A.T. 1986. *Mechanics of Immiscible Fluids in Porous Media,* Water Resources Publications, Littleton, CO: 1986.

Davies, P., and A.M. LaVenue. 1990. Memo to R. P. Rechard, "Additional Data for Characterizing 2-Phase Flow Behavior in Waste-Generated Gas Simulations and Pilot Point Information for Final Culebra 2-D Model (SAND89-7068/1)," November 19, 1990, contained in Rechard et al. (1990), pp. A-141.

Pruess, K. 1987. *TOUGH User's Guide*. NUREG/CR-4645. SAND86-7104. LBL-20700, August 1987.

Rechard, R.P., H. Iuzzolino, and J.S. Sandha. 1990. *Data Used in Preliminary Performance Assessment of the Waste Isolation Pilot Plant (1990)*. SAND89-2408. Albuquerque, NM: Sandia National Laboratories.

van Genuchten, M.T. 1980. "A Closed-Form Equation for Predicting the Hydraulic Conductivity of Unsaturated Soils," *Soil Sci. Am. J.*, Vol. 44, pp. 892-898, 1980.

Webb, S.W., and J.C. Chen. 1990. "Phasic Pressure Difference Effects in Two-Phase Flow For Dissolved Gas Exsolution." *Proceedings of the TOUGH Workshop. Lawrence Berkeley Laboratory, Berkeley, CA, September 13-14, 1990,* pp. 107-112, LBL-29710, September 1990.

DISTRIBUTION

Federal Agencies

US Department of Energy, (5)
Office of Civilian Radioactive Waste Management
Attn: Deputy Director, RW-2
Associate Director, RW-10
Office of Program Administration and Resources Management
Associate Director, RW-20
Office of Facilities Siting and Development
Associate Director, RW-30
Office of Systems Integration and Regulations
Associate Director, RW-40
Office of External Relations and Policy
Forrestal Building
Washington, DC 20585

US Department of Energy (4)
WIPP Project Integration Office
Attn: W.J. Arthur III
L.W. Gage
P.J. Higgins
D.A. Olona
PO Box 5400
Albuquerque, NM 87115-5400

US Department of Energy
Attn: National Atomic Museum Library
Albuquerque Operations Office
PO Box 5400
Albuquerque, NM 87185-5400

US Department of Energy (4)
WIPP Project Site Office (Carlsbad)
Attn: R. Becker
V. Daub
J. Lippis
J.A. Mewhinney
PO Box 3090
Carlsbad, NM 88221

US Department of Energy
Research & Waste Management Division
Attn: Director
PO Box E
Oak Ridge, TN 37831

US Department of Energy
Attn: E. Young
Room E-178
GAO/RCED/GTN
Washington, DC 20545

US Department of Energy
Office of Environmental Restoration and Waste Management
Attn: J. Lytle, EM-30 (Trevion II)
Washington, DC 20585-0002

US Department of Energy (3)
Office of Environmental Restoration and Waste Management
Attn: M. Frei, EM-34 (Trevion II)
Washington, DC 20585-0002

US Department of Energy
Office of Environmental Restoration and Waste Management
Attn: S. Schneider, EM-342 (Trevion II)
Washington, DC 20585-0002

US Department of Energy (3)
Office of Environment, Safety and Health
Attn: C. Borgstrom, EH-25
R. Pelletier, EH-231
Washington, DC 20585

US Department of Energy (2)
Idaho Operations Office
Fuel Processing and Waste Management Division
785 DOE Place
Idaho Falls, ID 83402

US Environmental Protection Agency (2)
Radiation Programs (ANR-460)
Attn: R. Guimond
Washington, DC 20460

US Geological Survey (2)
Water Resources Division
Attn: R. Livingston
Suite 200
4501 Indian School, NE
Albuquerque, NM 87110

US Nuclear Regulatory Commission
Attn: H. Marson
Mail Stop 623SS
Washington, DC 20555

Boards

Defense Nuclear Facilities Safety Board
Attn: D. Winters
Suite 700
625 Indiana Ave., NW
Washington, DC 20004

Nuclear Waste Technical Review Board (2)
Attn: D.A. Deere
S.J.S. Parry
Suite 910
1100 Wilson Blvd.
Arlington, VA 22209-2297

Advisory Committee on Nuclear Waste
Nuclear Regulatory Commission
Attn: R. Major
7920 Norfolk Ave.
Bethesda, MD 20814

State Agencies

Environmental Evaluation Group (3)
Attn: Library
Suite F-2
7007 Wyoming, NE
Albuquerque, NM 87109

NM Bureau of Mines and Mineral Resources
Socorro, NM 87801

NM Energy, Minerals, and Natural Resources Department
Attn: Library
2040 S. Pacheco
Santa Fe, NM 87505

NM Environment Department (3)
Secretary of the Environment
Attn: J. Espinosa
1190 St. Francis Drive
Santa Fe, NM 87503-0968

NM Environment Department
WIPP Project Site
Attn: P. McCasland
PO Box 3090
Carlsbad, NM 88221

Laboratories/Corporations

Battelle Pacific Northwest Laboratories (2)
Attn: H.C. Burkholder, P7-41
R.E. Westerman, P8-37
Battelle Blvd.
Richland, WA 99352

Savannah River Laboratory (3)
Attn: N. Bibler
M.J. Plodinec
G.G. Wicks
Aiken, SC 29801

INTERA Inc.
Attn: J.F. Pickens
Suite 300
6850 Austin Center Blvd.
Austin, TX 78731

INTERA Inc.
Attn: W. Stensrud
PO Box 2123
Carlsbad, NM 88221

IT Corporation
Attn: R.F. McKinney
Regional Office - Suite 700
5301 Central, NE
Albuquerque, NM 87108

Los Alamos National Laboratory
Attn: B. Erdal, CNC-11
PO Box 1663
Los Alamos, NM 87544

RE/SPEC, Inc.
Attn: W. Coons
Suite 300
4775 Indian School, NE
Albuquerque, NM 87110-3927

RE/SPEC, Inc.
Attn: J.L. Ratigan
PO Box 725
Rapid City, SD 57709

Southwest Research Institute (2)
Center for Nuclear Waste Regulatory Analysis
Attn: P.K. Nair
6220 Culebra Road
San Antonio, TX 78228-0510

SAIC
Attn: G. Dymmel
101 Convention Center Dr.
Las Vegas, NV 89109

SAIC
Attn: H.R. Pratt,
10260 Campus Point Dr.
San Diego, CA 92121

SAIC (2)
Attn: M. Davis
J. Tollison
2109 Air Park Rd., SE
Albuquerque, NM 87106

Tech Reps Inc. (3)
Attn: J. Chapman
R. Jones
E. Lorusso
5000 Marble, NE
Albuquerque, NM 87110

Westinghouse Electric Corporation (5)
Attn: Library
C. Cox
L. Fitch
R. Kehrman
L. Trego
PO Box 2078
Carlsbad, NM 88221

Universities

University of New Mexico
Geology Department
Attn: Library
Albuquerque, NM 87131

University of Washington
Attn: G.R. Heath
College of Ocean
and Fishery Sciences
583 Henderson Hall
Seattle, WA 98195

Individuals

P. Drez
8816 Cherry Hills Rd., NE
Albuquerque, NM 87111

D.W. Powers
Star Route Box 87
Anthony, TX 79821

Libraries

Thomas Brannigan Library
Attn: D. Dresp
106 W. Hadley St.
Las Cruces, NM 88001

Hobbs Public Library
Attn: M. Lewis
509 N. Ship St.
Hobbs, NM 88248

New Mexico State Library
Attn: N. McCallan
325 Don Gaspar
Santa Fe, NM 87503

New Mexico Tech
Martin Speere Memorial Library
Campus Street
Socorro, NM 87810

New Mexico Junior College
Pannell Library
Attn: R. Hill
Lovington Highway
Hobbs, NM 88240

WIPP Public Reading Room
Carlsbad Public Library
Attn: Director
101 S. Halagueno St.
Carlsbad, NM 88220

Government Publications Department
General Library
University of New Mexico
Albuquerque, NM 87131

National Academy of Sciences, WIPP Panel

Charles Fairhurst, Chairman
Department of Civil and
Mineral Engineering
University of Minnesota
500 Pillsbury Dr., SE
Minneapolis, MN 55455-0220

Howard Adler
Oak Ridge Associated Universities
Medical Sciences Division
PO Box 117
Oak Ridge, TN 37831-0117

John D. Bredehoeft
Western Region Hydrologist
Water Resources Division
US Geological Survey (M/S 439)
345 Middlefield Road
Menlo Park, CA 94025

Fred M. Ernsberger
250 Old Mill Road
Pittsburgh, PA 15238

Rodney C. Ewing
Department of Geology
University of New Mexico
Albuquerque, NM 87131

B. John Garrick
PLG, Inc.
Suite 400
4590 MacArthur Blvd.
Newport Beach, CA 92660-2027

Leonard F. Konikow
US Geological Survey
431 National Center
Reston, VA 22092

Jeremiah O'Driscoll
Jody Incorporated
505 Valley Hill Drive
Atlanta, GA 30350

Christopher G. Whipple
Clement International
Suite 1380
160 Spear St.
San Francisco, CA 94105

Peter B. Myers
National Academy of Sciences
Board on Radioactive
Waste Management
2101 Constitution Ave.
Washington, DC 20418

Ina Alterman
Board on Radioactive
Waste Management
GF456
2101 Constitution Ave.
Washington, DC 20418

Foreign Addresses

Studiecentrum Voor Kernenergie
Centre D'Energie Nucleaire
Attn: A. Bonne
SCK/CEN
Boeretang 200
B-2400 Mol, BELGIUM

Atomic Energy of Canada, Ltd. (3)
Whiteshell Research Estab.
Attn: B. Goodwin
M. Stevens
D. Wushke
Pinewa, Manitoba, CANADA R0E 1L0

Francois Chenevier, Director (2)
ANDRA
Route du Panorama Robert Schumann
B.P.38
92266 Fontenay-aux-Roses Cedex
FRANCE

Jean-Pierre Olivier
OECD Nuclear Energy Agency
Division of Radiation Protection
and Waste Management
38, Boulevard Suchet
75016 Paris, FRANCE

Claude Sombret
Centre D'Etudes Nucleaires
De La Vallee Rhone
CEN/VALRHO
S.D.H.A. BP 171
30205 Bagnols-Sur-Ceze, FRANCE

Bundesministerium fur Forschung und
Technologie
Postfach 200 706
5300 Bonn 2, GERMANY

Gesellschaft fur Reaktorsicherheit
(GRS) (2)
Attn: B. Baltes
W. Muller
Schwertnergasse 1
D-5000 Cologne, GERMANY

Bundesanstalt fur Geowissenschaften
und Rohstoffe
Attn: M. Langer
Postfach 510 153
3000 Hanover 51, GERMANY

Hahn-Meitner-Institut fur
Kernforschung
Attn: W. Lutze
Glienicker Strasse 100
100 Berlin 39, GERMANY

Institut fur Tieflagerung (2)
Attn: K. Kuhn
Theodor-Heuss-Strasse 4
D-3300 Braunschweig, GERMANY

Physikalisch-Technische Bundesanstalt
Attn: P. Brenneke
Postfach 3345
D-3300 Braunschweig, GERMANY

D.R. Knowles
British Nuclear Fuels, plc
Risley, Warrington, Cheshire WA3 6AS
1002607 UNITED KINGDOM

AEA Technology
Attn: J.H. Rees
D5W/29 Culham Laboratory
Abington, Oxfordshire OX14 3DB
UNITED KINGDOM

AEA Technology
Attn: W.R. Rodwell
044/A31 Winfrith Technical Centre
Dorchester, Dorset DT2 8DH
UNITED KINGDOM

AEA Technology
Attn: J.E. Tinson
B4244 Harwell Laboratory
Didcot, Oxfordshire OX11 0RA
UNITED KINGDOM

Nationale Genossenschaft fur die
Lagerung Radioaktiver Abfalle (2)
Attn: S. Vomvoris
P. Zuidema
Hardstrasse 73
CH-5430 Wettingen, SWITZERLAND

Shingo Tashiro
Japan Atomic Energy Research Inst.
Tokai-Mura, Ibaraki-Ken
319-11 JAPAN

Netherlands Energy Research
Foundation ECN
Attn: L.H. Vons
3 Westerduinweg
PO Box 1
1755 ZG Petten, THE NETHERLANDS

Svensk Karnbransleforsorjning AB
Attn: F. Karlsson
Project KBS
Karnbranslesakerhet, Box 5864
10248 Stockholm, SWEDEN

Sandia Internal

1502	J.C. Cummings
6000	D.L. Hartley
6100	R.W. Lynch
6101	P.J. Hommert
6119	E.D. Gorham
6119	S.W. Webb (10)
6119	Staff (14)
6121	J.R. Tillerson
6121	Staff (7)
6300	D.E. Miller
6302	T.E. Blejwas, Acting
6303	W.D. Weart
6303	S.Y. Pickering
6305	S.A. Goldstein
6341	A.L. Stevens
6341	Staff (6)
6341	WIPP Central Files (10)
6342	D.R. Anderson
6342	Staff (20)
6343	T.M. Schultheis
6343	Staff (2)
6345	R.C. Lincoln
6345	Staff (9)
6347	D.R. Schafer
7141	Technical Library (5)
7151	Technical Publications
7613-2	Document Processing for DOE/OSTI (10)
8523-2	Central Technical Files
9300	J.E. Powell

☆ U.S. GOVERNMENT PRINTING OFFICE 1992—774-122/80052